First Principles Investigations of Nanomaterials for Electronic, Spintronic and Gas Storage Applications.

A Thesis
Submitted For the Degree of
Doctor of Philosophy
in the Faculty of Science

by

Kanchan Ulman

Theoretical Sciences Unit
Jawaharlal Nehru Centre for Advanced Scientific Research
Bangalore – 560 064

FEBRUARY 2015

To my Parents

DECLARATION

I hereby declare that the matter embodied in the thesis entitled “**First Principles Investigations of Nanomaterials for Electronic, Spintronic and Gas Storage Applications.**” is the result of investigations carried out by me at the Theoretical Sciences Unit, Jawaharlal Nehru Centre for Advanced Scientific Research, Bangalore, India under the supervision of Prof. Shobhana Narasimhan and that it has not been submitted elsewhere for the award of any degree or diploma.

In keeping with the general practice in reporting scientific observations, due acknowledgement has been made whenever the work described is based on the findings of other investigators.

Kanchan Ulman

CERTIFICATE

I hereby certify that the matter embodied in this thesis entitled "**First Principles Investigations of Nanomaterials for Electronic, Spintronic and Gas Storage Applications.**" has been carried out by Mr. Kanchan Ulman at the Theoretical Sciences Unit, Jawaharlal Nehru Centre for Advanced Scientific Research, Bangalore, India under my supervision and that it has not been submitted elsewhere for the award of any degree or diploma.

Prof. Shobhana Narasimhan
(Research Supervisor)

Acknowledgements

First of all, I would like to thank my Ph.D. advisor, Prof. Shobhana Narasimhan, for her constant support and guidance regarding my academic as well as non-academic activities throughout my Ph.D. tenure. She not only helped shape up my scientific career and inspired me to become a good scientist, but she also gave me valuable advice as to be a better person. She gave me plenty of opportunities and time to help me explore through my Ph.D. work, and at the same time showed tremendous patience towards my progress. She provided me opportunities to travel to many renowned scientific institutions throughout the world, and to work with the masters in our field. I would miss the intense scientific discussions I had with her, regarding my work as well as other problems in our field, which made my Ph.D. work so much fun. Not to forget the wonderful cakes she baked for me and my labmates, and the new delicacies she cooked for us. Most importantly, she created such a wonderful research atmosphere in our group, making my Ph.D. time as enjoyable as possible.

I would like to thank my collaborators, Prof. Anna Delin and Dr. Anders Odell at KTH Stockholm, Dr. Rajesh Sathiyanarayanan, Dr. R. K. Pandey and Dr. K. V. R. M. Murali at IBM India, for fruitful discussions and collaborative work. I would sincerely like to thank Prof. Anna Delin for providing me the best facilities for my work as well as for making my stay in Stockholm as homely as possible. I would also like to sincerely thank Dr. Rajesh Sathiyanarayanan for all the scientific as well as administrative help, he provided me throughout my internship with IBM India.

I would like to thank my course instructors for the scientific courses they taught me: Prof. U. Waghmare, Prof. S. Pati, Prof. N. S. Vidhyadhiraja, Prof. S. K. Das, and Prof. V. Shenoy. I would also like to acknowledge the educative and helpful lectures from Prof. S. Baroni, Prof. S. de Gironcoli, Prof. R. Gebauer, Prof. S. Scandolo, Prof. M. Weinert, which I got an opportunity to learn from. I would like to acknowledge helpful discussions with Prof. S. Baroni, Prof. S. de Gironcoli, Prof. S. Piccinin, Prof. P. Umari, Prof. V. Repain, Prof. R. Gebuaer, Prof. S. Scandolo, Dr. Ivan Rungger, and Prof. M. Weinert. I would like to thank Prof. M. S. Narasimhan for the helpful discussions regarding certain mathematical problems I faced during my Ph.D. work.

I would like to thank all my past and present labmates - Jaita, Mighfar, Madhura, Nisha, Sananda, Deboshruti, Brandon, Chakra, Vasudevan, Lakshmi, Bulumoni, Debarati, Debdipto, Sukanya, Rajdeep, Rajiv, Nurapati, Aruna, for maintaining the lively lab atmosphere, for all the fun activities as well as the interactive discussions we had in our group. I would like to thank Mighfar and Madhura for listening patiently to all the silly questions I posed before them, and helping me develop my basic understanding in my work. I would like to thank Madhura for finding time out of her busy schedule to proof read my thesis. I would like to acknowledge Nisha and Sananda for providing me with helpful comments and their ideas regarding my work.

I would like to acknowledge the funding from CSIR, Indo-Swedish SRL Grant, IBM Internship, ICMS-SISSA Grant, DST Nanomission, and last but not the least, JNCASR for supporting me when my regular Ph.D. funding was stopped. I would like to acknowledge computation facilities from TUE-CMS (Amit, Ershad, Bharti, Vijay), Akka/Abisko (HPC2N), CURIE; these machines made the time consuming computations in this thesis possible.

I would like to thank the Academic Section (Dr. Princy and Sukanya Madam) and Administrative section (Mr. Jayachandra, Mr. Gururaj, Ms. Jayamangala) for providing effective and timely solutions to our academic and administrative problems, and making all the procedures involved as simple as possible.

I would like to thank all my friends. Sanved, Varun Watharkar, and Pradyot provided me an escape from my Ph.D. routine by pulling me to wonderful trips to different parts of India (though our long treasured wish to visit Lakshadweep together never materialized). We had a lot of new experiences in these trips and wonderful memories to cherish. I would also thank them for their constant support as well as constructive criticism about my work. I would like to thank Deepashri for the wonderful time I had with her in JNC, and her enthusiasm helped introduce me to new hobbies like bird watching and photography. I would like to thank Nisha for the beautiful songs, as well as the memorable trips and wonderful activities we did together. I would like to thank Kaustuv for the weekly escapes from work and the trips we had together. My thanks to Sumanta for the warm welcoming atmosphere in Uppsala away from home, and the wonderful times we had together in our unplanned adventurous trips in the Alps. Thanks to my friends Pramod, Varun Thakur, and Sananda for the wonderful time we had cooking, exploring new food junctions and traveling around in Bangalore, and sometimes just idling. I would like to thank my friends Sharmila, Arun, Dinesh, Saumik, Sirisha, Supriyo, Nikhil, Ronak, and all others, for making my time in JNC just wonderful.

Finally, I would like to acknowledge my family: my parents and my brother, and my Sadguru, for their constant support, love and blessings throughout my life.

Synopsis

The broad aim of this thesis is to design materials for technological applications using first-principles methods. In this thesis, we have focused on materials which may be used for applications in three broad areas: (1) electronics, (2) on-board vehicular gas storage, and (3) spintronics. We use first principles density functional theory (DFT) based calculations to both design novel nanomaterials with enhanced properties that make them suitable for these applications, as well as to get insight into the underlying mechanisms governing the physical, chemical and magnetic properties of these materials. Wherever possible, we also develop simple models that not only enable us to understand the underlying complex phenomena, but also allow us to supplement time-consuming calculations that invoke the full machinery of *ab initio* calculations, with quicker alternatives that can be used to obtain estimates of desired quantities. A brief introduction to the thesis is given in Chapter 1.

For electronic applications, we have studied two systems. First we look at the dielectric properties of ternary silicon germanium nitride and silicon carbon nitride materials, where we explore the possibility of tuning the dielectric properties of these materials by changing the concentration of germanium and carbon. Next, we study how the electronic, magnetic and structural properties of Twisted Bilayer Graphene (TBLG) are affected by the presence of point defects. In TBLG, the weak interlayer coupling presumably plays a crucial role, and we therefore incorporate the van der Waals interactions into our DFT calculations and compare our results with those obtained using conventional DFT functionals. For on-board vehicular gas storage, we try to enhance the uptake of hydrogen gas in carbon nanostructures by chemical functionalization. As the binding between hydrogen and the substrate is weak, the incorporation of van der Waals interactions is mandatory. For spintronics applications, we try to design a molecule-lead geometry with the aim of enhancing the magnetoresistance.

In Chapter 2 of the thesis, the theoretical background of different methods used in this thesis is discussed – density functional theory, density functional perturbation theory, and the non-equilibrium Green's functions technique for quantum transport. Grimme's method of incorporating van der Waals interactions in DFT is also described.

In Chapter 3, we have studied the dielectric properties of crystalline α- and β-phase silicon germanium nitrides and silicon carbon nitrides, $A_{3-\xi}B_{\xi}N_4$ (A=Si, B=Ge or C, ξ =0,1,2,3). In silicon germanium nitrides, both the high-frequency and static dielectric constants increase monotonically with increasing germanium concentration, providing a straightforward way to tune the dielectric constant of these materials. In the case of silicon carbon nitrides, the high-frequency dielectric constant increases monotonically with increasing carbon concentration, but a more complex non-monotonic trend is observed for the static dielectric constant, which can be understood in terms of competition between changes in the unit-cell volume and the average oscillator strength. The computed static dielectric constants of C_3N_4, Si_3N_4 and Ge_3N_4 are 7.13, 7.70 and 9.74, respectively.

In Chapter 4, we have used DFT incorporating van der Waals corrections, to study twisted bilayer graphene (TBLG) where Stone-Wales defects or monovacancies are introduced in one of the layers. We compare these results to those for defects in single layer graphene or Bernal stacked graphene. The energetics of defect formation is not very sensitive to the stacking of the layers or the specific site at which the defect is created, suggesting a weak interlayer coupling. However signatures of the interlayer coupling are manifested clearly in the electronic band structure. For the "$\gamma\gamma$" Stone Wales defect in TBLG, we observe two Dirac cones that are shifted in both momentum space and energy. This up/down shift in energy results from the combined effect of a charge transfer between the two graphene layers, and a chemical interaction between the layers, which mimics the effects of a transverse electric field. Charge density plots show that states near the Dirac points have significant admixture between the two layers. For Stone Wales defects at other sites in TBLG, this basic structure is modified by the creation of mini gaps at energy crossings. For a monovacancy, the Dirac cone of the pristine layer is shifted up in energy by ~ 0.25 eV due to a combination of the requirements of the equilibration of Fermi energy between the two layers with different numbers of electrons, charge transfer, and chemical interactions. Both kinds of defects increase the density of states at the Fermi level. The monovacancy also results in spin polarization, with magnetic moments on the defect of $1.2 - 1.8\ \mu_B$.

In Chapter 5, we have performed *ab initio* density functional theory calculations, incorporating van der Waals corrections, to study the absorption of molecular hydrogen on zigzag graphene nanoribbons whose edges have been functionalized by OH, NH_2, COOH, NO_2, or H_2PO_3. We find that hydrogen molecules always preferentially bind at or near the functionalized edge, and display induced dipole moments. Binding is generally enhanced by the presence of polar functional groups. The largest gains are observed for groups with oxygen lone pairs that can facilitate local charge reorganization, with the biggest single enhancement in adsorption energy found for "strong functionalization" by H_2PO_3 (115 meV/H_2 versus 52 meV/H_2 on bare graphene). We show that for binding on the "outer edge" near the functional group, the presence of the group can introduce appreciable contributions from Debye interactions and higher-order multipole electrostatic terms, in addition to the dominant London dispersion interactions. For those functional groups that contain the OH moiety, the adsorption energy is linearly proportional to the number of lone pairs on oxygen atoms. Mixed functionalization with two different functional groups on a graphene edge can also have a synergistic effect, particularly when electron-donating and electron-withdrawing groups are combined. For binding on the "inner edge" somewhat farther from the functional group, most of the binding again arises from London interactions; however, there is also significant charge redistribution in the π manifold, which directly reflects the electron donating or withdrawing capacity of the functional group. Our results offer insight into the specific origins of weak binding of gas molecules on graphene, and suggest that edge functionalization could perhaps be used in combination with other strategies to increase the uptake of hydrogen in graphene. They also have relevance for the storage of hydrogen in porous carbon materials, such as activated carbons.

In Chapter 6, we perform *ab initio* calculations, combining the non-equilibrium Green's function method with density functional theory, on a dithienylethene molecule placed between spin-polarized nickel leads of varying geometries, with the aim of understanding how the magnetoresistance is affected by the lead geometries. We find that, in general, the magnetoresistance is significantly higher when the contact is made to sharp tips than to flat surfaces. Interestingly, this holds true for both resonant and tunneling conduction regimes, i.e., when the molecule is in its 'closed' and 'open' conformations, respectively. We find that changing the lead geometry can increase the magnetoresistance by up to a factor of $\sim$5. We also introduce a simple model that, despite requiring minimal computational time, can recapture our *ab initio* results for the behavior of magnetoresistance as a function of bias voltage. This model requires as its input only the density of states on the anchoring atoms, at zero bias voltage.

In Chapter 7, the main findings of the thesis are summarized and an outlook for possible directions of future research is presented.

List of Publications

Included in thesis

1. “Point Defects in twisted bilayer graphene: A density functional study”, Kanchan Ulman and Shobhana Narasimhan, Phys. Rev. B. **89**, 245429 (2014).
2. “Hydrogen Adsorption on Chemically Functionalized Carbon Nanostructures: Ab initio calculations on Graphene Nanoribbons”, Kanchan Ulman, D. Bhaumik, B. Wood, and Shobhana Narasimhan, Journal of Chem. Phys. **140**, 174708 (2014).
3. “Tuning Spin Transport Properties and Molecular Magnetoresistance Through Contact Geometry”, Kanchan Ulman, Shobhana Narasimhan, and Anna Delin, Journal of Chemical Physics, **140**, 044716 (2014).
4. “Theoretical Study of Spin Conduction in the Ni/DTE/Ni nanohybrid”, Kanchan Ulman, M. Imam, Shobhana Narasimhan, A. Odell, and Anna Delin, Nano Hybrids Vol. **4**, 1-20 (2013).
5. “Dielectric properties of $Si_{3-\xi}Ge_{\xi}N_4$ and $Si_{3-\xi}C_{\xi}N_4$: A density functional study”, Kanchan Ulman, Rajesh Sathiyanarayanan, R. K. Pandey, K. V. R. M. Murali, and Shobhana Narasimhan, Journal of Applied Physics **113**, 234102 (2013).

Not included in thesis

- “Graphene oxide as a candidate system for methane storage”, R. Chouhan, Kanchan Ulman and Shobhana Narasimhan. (In preparation)
- “Functionalizing graphene for enhanced binding of methane by decorating with metal adatoms”, Nurapati Pantha, Kanchan Ulman and Shobhana Narasimhan. (In preparation)
- “Comparison between s- and d-electron mediated transport in a photoswitching dithienylethene molecule using *ab initio* transport methods”, Anders Odell, Anna Delin, Börje Johansson, Kanchan Ulman, Shobhana Narasimhan, Ivan Rungger and Stefano Sanvito, Phys. Rev. B **84**, 165402 (2011).

List of Abbreviations

E_F	Fermi Energy
ϵ_0	Static dielectric constant
ϵ_∞	High-frequency dielectric constant
μ_B	Bohr Magneton
m_e	Mass of a free electron
0D	Zero dimensional
1D	One dimensional
2D	Two dimensional
3D	Three dimensional
AB-BLG	AB-stacked bilayer graphene
AFM	Atomic Force Microscopy
BZ	Brillouin Zone
DFPT	Density Functional Perturbation Theory
DFT	Density Functional Theory
DFZGNR	Dilute Functionalized Zigzag Graphene Nanoribbon
DOS	Density of States
DTE	Dithienylethene
eV	electron volt
FZGNR	Functionalized Zigzag Graphene Nanoribbon
GEA	Gradient Expansion Approximation
GGA	Generalized Gradient Approximation
GMR	Giant Magnetoresistance

HOMO	Highest Occupied Molecular Orbitals
IBZ	Irreducible Brillouin Zone
IFC	Interatomic Force Constant
IP	in plane
KS	Kohn-Sham
LDA	Local Density Approximation
LUMO	Lowest Unoccupied Molecular Orbitals
MBE	Molecular Beam Epitaxy
MEMS	Microelectromechanical system
meV	milli-electron volt
MFZGNR	Mixed Functionalized Zigzag Graphene Nanoribbon
MR	Magnetoresistance
NEGF	Non Equilibrium Green's Function Theory
OP	out of plane
PBE	Perdew Burke Ernzerhof
PDOS	Projected Density of States
PZ	Perdew Zunger
Ry	Rydberg
SC	Scattering Center
SFZGNR	Strong Functionalized Zigzag Graphene Nanoribbon
SiCN	Silicon Carbon Nitride
SiGeN	Silicon Germanium Nitride
SLG	Single layer graphene
STM	Scanning Tunneling Microscopy
SW	Stone Wales
TBLG	Twisted bilayer graphene
XC	Exchange Correlation
ZGNR	Zigzag Graphene Nanoribbon

List of Figures

2.1 Flow chart showing the self-consistency loop for the iterative solution of the Kohn-Sham equation . . . 15

2.2 A typical two terminal transport setup. . . . 34

2.3 Flowchart showing the self-consistency loop for the iterative solution of the NEGF formalism . . . 37

3.1 Optimized structures of α-$Si_{3-\xi}Ge_{\xi}N_4$ and β-$Si_{3-\xi}Ge_{\xi}N_4$ for different values of ξ . . . 44

3.2 Variation of static and high-frequency dielectric constants with germanium concentration for α-$Si_{3-\xi}Ge_{\xi}N_4$ and β-$Si_{3-\xi}Ge_{\xi}N_4$ . . . 48

3.3 Contribution of various phonon modes to the ionic part of the dielectric constant (ϵ_{ion}) of α-$Si_{3-\xi}Ge_{\xi}N_4$ and β-$Si_{3-\xi}Ge_{\xi}N_4$ . . . 51

3.4 Optimized α-$Si_{3-\xi}C_{\xi}N_4$ and β-$Si_{3-\xi}C_{\xi}N_4$ structures for different values of ξ 52

3.5 Variation of static and high-frequency dielectric constants with carbon concentration for α-$Si_{3-\xi}C_{\xi}N_4$ and β-$Si_{3-\xi}C_{\xi}N_4$ . . . 55

4.1 Twisted Bilayer Graphene (TBLG) with a twist angle of 38.213° . . . 61

4.2 The first Brillouin zone corresponding to the unrotated graphene layer, the rotated graphene layer, and TBLG . . . 65

4.3 Simulated STM images for (a) Single layer of graphene (SLG), (b) AB-stacked BLG (AB-BLG), and (c) TBLG. . . . 69

4.4 Comparison of band structure of SLG, pristine TBLG, and AB-BLG . . . 70

4.5 Band structure of pristine TBLG in the vicinity of $\mathbf{K}_1^{\mathrm{B}}$ . . . 71

4.6 Charge density redistribution for pristine TBLG and AB-BLG . . . 73

4.7 Relaxed geometries for (a) $\alpha\beta$-SW, (b) $\beta\beta$-SW, (c) $\beta\gamma$-SW, and (d) $\gamma\gamma$-SW defects in TBLG . . . 74

4.8 Structure for SW defect in SLG, (a) the top view and (b) the side view . . 76

4.9 (a) FBZ for S_2 supercell of TBLG and (b) the zoomed view of the region showing the position of the Dirac point E_D for SLG with SW defect . . . 78

4.10 Band structure in the vicinity of $\mathbf{K}_1^{\mathrm{B}}$ for (a) the SW defect in SLG, (b) SW defect in AB-BLG, (c) $\gamma\gamma$-SW defect, (d) $\alpha\beta$-SW defect, (e) $\beta\gamma$-SW defect, and (f) $\beta\beta$-SW defect in TBLG 79
4.11 Planar integral of the change in electronic charge density $\Delta\rho_{xy}(z)$ for the SW defect and Monovacancy in TBLG 82
4.12 Distribution of charge density corresponding to the four states that lie just above and below the Dirac points for the case of $\gamma\gamma$-SW defect in TBLG . . 84
4.13 Atomic structures for (a) α-vacancy, (b) β-vacancy, and (c) γ-vacancy in TBLG, and corresponding simulated STM images from the defective side and from the undefective side 87
4.14 Electronic band structure for (a) α-vacancy, (b) β-vacancy, and (c) γ-vacancy in TBLG 90
4.15 Comparison of electronic band structure for pristine SLG, monovacancy in SLG, and α-monovacancy in TBLG 93
4.16 Charge density redistribution in the vicinity of the undefective lower layer of TBLG due to the presence of a monovacancy in the upper layer 94
4.17 Spatial extent of the spin polarized charge density corresponding to the states in an energy window near E_F for the case of monovacancy in TBLG 95

5.1 Chemically functionalized ZGNR used in the calculations 104
5.2 Optimized adsorption geometry for hydrogen adsorption on pristine graphene 105
5.3 Optimal adsorption geometries, and redistribution of electronic charge upon adsorption of hydrogen on the outer edge of the various dilute FZGNRs . . 109
5.4 Energy contributions from the London interaction, the Debye interaction, and the induced multipolar interactions for the outer edge adsorption of dilute FZGNRs 112
5.5 Optimal adsorption geometries, and redistribution of electronic charge upon adsorption of hydrogen, on the inner edge of the various dilute FZGNRs . . 115
5.6 Variation of the induced charges and the tilt angle of the line joining these charges with respect to the normal to the ZGNR plane, as a function of the Hammett parameter of the functional group for inner edge adsorption of H_2 117
5.7 Optimal adsorption geometries, and redistribution of electronic charge upon adsorption of hydrogen, on the outer edge of the various strong FZGNRs . 119
5.8 H_2 Adsorption energy on ZGNRs functionalized with groups containing the OH moiety, as a function of the number of oxygen lone pairs per adsorbate 121
5.9 Energy contributions from the London interaction, the Debye interaction, and the induced multipolar interactions, for the outer edge adsorption of strong FZGNRs. 122

5.10 Optimal adsorption geometries, and redistribution of electronic charge upon adsorption of hydrogen, on the outer edge of the mixed FZGNRs 124
5.11 Energy contributions from the London interaction, the Debye interaction, and the induced multipolar interactions, for the outer edge adsorption of mixed FZGNRs 126

6.1 Geometrical conformations of the dithienylethene (DTE) molecule, 'closed' and 'open' conformation 131
6.2 Front and side views of the geometry for the (a), (b) closed and (c), (d) open conformations of the DTE molecule 134
6.3 Closed and open conformations of the DTE molecule attached to different Ni lead geometries 136
6.4 DOS and frontier Molecular Orbitals for the (a) closed and (b) open conformations of the DTE molecule 138
6.5 PDOS over the different carbon atoms along the C-backbone for (a) closed and (b) open conformation of the DTE molecule 139
6.6 *I*-*V* characteristics for the closed and open conformation of DTE between Ni leads for various Ni lead geometries 141
6.7 The ratio of the current for the closed and the open molecule $\mathrm{I}_{\mathrm{closed}}/\mathrm{I}_{\mathrm{open}}$ for various Ni lead geometries 142
6.8 Transmission Coefficient as a function of energy E, for the closed conformation attached to various Ni lead geometries, at different bias voltages 143
6.9 Transmission Coefficient as a function of energy E, for the open conformation attached to various Ni lead geometries, at different bias voltages 144
6.10 Transmission Coefficients for closed and open conformations of the DTE molecule, when attached to four different lead materials, Au, Ag, non-magnetic Ni, and spin-polarized Ni 145
6.11 Magnetoresistance calculated as a function of applied bias voltage, for various Ni lead geometries. 147
6.12 PDOS over the end sulfur atoms S_1 and S_2 of the closed conformation as a functions of the applied bias voltage for different lead geometries. 149
6.13 PDOS over the end sulfur atoms S_1 and S_2 of the open conformation as a functions of the applied bias voltage for different lead geometries. 150
6.14 A simple model to understand the full bias-dependent MR through the behavior of the PDOS on the anchoring atoms 152

A.1 Non-uniform *k*-point sampling that is dense near the **K** point, but sparse in rest of the BZ. 162
A.2 Comparison of DOS for a non-uniform *k*-mesh and a very dense uniform mesh for graphene 163

List of Tables

3.1 Optimized structural parameters and band gap for α- and β- phases of Si_3N_4, Ge_3N_4 and C_3N_4. 43
3.2 Computed phonon frequencies (cm^{-1}) compared with experimental results and previous calculations for β-Si_3N_4. 45
3.3 Computed phonon frequencies (cm^{-1}) compared with previous calculations for β-Ge_3N_4. 45
3.4 Optimized structural parameters and band gap for α-$Si_{3-\xi}Ge_\xi N_4$ and β-$Si_{3-\xi}Ge_\xi N_4$ 47
3.5 Static dielectric constant (ϵ_0) and high-frequency dielectric constant (ϵ_∞) for α-$Si_{3-\xi}Ge_\xi N_4$ and β-$Si_{3-\xi}Ge_\xi N_4$ materials 49
3.6 Optimized structural parameters and band gap for α-$Si_{3-\xi}C_\xi N_4$ and β-$Si_{3-\xi}C_\xi N_4$ materials. 53
3.7 Static dielectric constant (ϵ_0) and high-frequency dielectric constant (ϵ_∞) for α-$Si_{3-\xi}C_\xi N_4$ and β-$Si_{3-\xi}C_\xi N_4$ materials 54

4.1 A list of a few commensurate integer pairs and twist angles for TBLG . . . 63
4.2 Results for structure and energetics of AB-stacked bilayer graphene and TBLG, as obtained with LDA, PBE, and DFT-D2 approaches 69
4.3 Formation energetics for SW defect in SLG, AB-BLG, and TBLG 77
4.4 Formation energies and net magnetic moments for monovacancy in SLG, AB-BLG and TBLG 89

5.1 H_2 adsorption energies and dipole moments for dilute FZGNRs 107
5.2 H_2 adsorption energies and dipole moments for strong FZGNRs 118
5.3 Mixing energies and H_2 adsorption energies for different combinations of functional groups for mixed FZGNRs 123

Contents

Acknowledgements **v**

Synopsis **vii**

List of Abbreviations **xi**

List of Figures **xii**

List of Tables **xv**

1 Introduction **1**

- 1.1 Nanomaterials for Technological Applications 1
- 1.2 Thesis Outline 4

2 Theoretical Formalism **9**

- 2.1 Density Functional Theory 9
  - 2.1.1 The Many Body Problem 9
  - 2.1.2 Hohenberg-Kohn Theorems 11
  - 2.1.3 The Kohn-Sham Formulation 13
  - 2.1.4 Approximations for Exchange-Correlation Functionals 15
  - 2.1.5 Basis Set 18
  - 2.1.6 Pseudopotential Approximation 19
  - 2.1.7 Force Calculations: Hellmann-Feynman theorem 21
  - 2.1.8 Spin Polarized DFT 22
  - 2.1.9 Incorporation of London Dispersion Interactions 23
- 2.2 Density Functional Perturbation Theory 24
  - 2.2.1 Formalism of DFPT 25
  - 2.2.2 Homogeneous electric fields 27
  - 2.2.3 Phonon modes in crystalline solids 30

2.2.4 Dielectric Constants 31
2.3 Electronic Transport 32
2.3.1 Non Equilibrium Greens Function Technique (NEGF) 33
2.4 Codes Used 38

3 Dielectric properties of crystalline SiGeN and SiCN materials 39
3.1 Introduction 39
3.2 Computational Details 41
3.3 Results and Discussion 42
3.3.1 Pure Phases: Si_3N_4, Ge_3N_4, and C_3N_4. 42
3.3.2 SiGeN Materials 44
3.3.3 SiCN Materials 51
3.4 Summary and Conclusions 56

4 Point Defects in Twisted Bilayer Graphene 57
4.1 Introduction 57
4.2 Computational Details 59
4.3 Twisted Bilayer Graphene 61
4.3.1 Geometric Properties 62
4.3.2 Brillouin Zone 65
4.3.3 Properties of pristine TBLG 68
4.4 Defects in Twisted Bilayer Graphene 72
4.4.1 Stone-Wales Defect 73
4.4.2 Monovacancy Defect 85
4.5 Summary and Conclusions 96

5 Physical Origins of Weak H_2 Binding on Carbon Nanostructures 99
5.1 Introduction 100
5.2 Computational Details 102
5.3 H_2 Adsorption on Graphene 104
5.4 H_2 Adsorption on Edge Functionalized Zigzag Graphene Nanoribbons . . . 106
5.4.1 Dilute Functionalization 107
5.4.2 Strong Functionalization 118
5.4.3 Mixed Functionalization 122
5.5 Summary and Conclusions 126

6 Spin Transport Properties and Molecular Magnetoresistance of Dithienylethene Molecule attached to Magnetic Nickel Leads 129
6.1 Introduction 130
6.2 Computational Details 132

6.3 The Dithienylethene molecule 133
6.4 Systems studied 136
6.5 Results 137
6.5.1 “Closed” molecule v/s “Open” molecule 137
6.5.2 Spin Polarized Conduction 139
6.5.3 Magnetoresistance 146
6.6 Discussion and Analysis 148
6.6.1 A Simple Model for Magnetoresistance 151
6.7 Summary and Conclusions 154

7 Summary and Outlook **157**

A Brillouin zone integrations over a non-uniform k-point mesh. **161**

Bibliography **165**

Chapter 1

Introduction

1.1 Nanomaterials for Technological Applications

Nanomaterials have become a gold mine for research in the field of materials science, owing to the incredible variety of novel and technologically desirable properties that one can get out of materials by a reduction in size. Nanomaterials are materials which are restricted to nanometric size in one, two or three dimensions. These include zero dimensional materials like molecules, clusters and nanoparticles [1, 2], one dimensional materials like nanowires, nanotubes and nanoribbons [3–6], two dimensional materials like graphene and surface alloys [7, 8], as well as three dimensional nanostructured materials like nanocomposites [9]. These nanomaterials present a large scope for finding new properties that might be completely different from those of conventional bulk materials. To cite just a couple of examples, gold nanoparticle suspensions are known to show colors ranging from red to violet depending on the particle size, and gold and palladium metal nanoparticles become magnetic in contrast to the nonmagnetic bulk [10]. Two dimensional (2D) materials like graphene have led to new ways of structuring materials, and have also led to considerable theoretical advances [11, 12]. In nanomaterials like surface alloys, the traditional rules governing the formation of bulk alloys are no longer valid, and the formation of new surface alloy phases, and novel stabilization mechanisms are possible [8]. In the famous words of Prof. R. P. Feynman [13]: “There is plenty of room at the bottom.”

Nanomaterials can be incorporated into the current technologies, as well as raise the possibility of completely new technological paradigms. The silicon based electronics industry requires effective ways of nano-structuring and patterning materials that can lead to a large density of electronic components on a chip [14–16]. Current topics of research include how to effectively tune electronic properties such as the band gap of materials [17]. Graphene based materials are not only attractive from the technological point of view due to their extraordinary material properties like remarkably high electron mobility and thermal conductivity [18], but are also interesting from the viewpoint of fundamental physics, as they show exotic properties like the integer and fractional quantum Hall effects [7,19,20], the possibility of observing the Casimir effect [21], etc. In recent years, research on 2D nanomaterials like graphene has been followed by the development of other two dimensional nanomaterials like silicene, germanene [22], phosphorene [23, 24] and boron-nitrides [25], and van der Waals stacked heterostructures [11, 12] of these materials. It has been suggested that these materials may replace the current silicon based electronics in the near future.

Another field where the current realms of electronics technology are being revolutionized is in the field of molecular electronics [26], where one or more molecules are designed to become electronic components. Conducting wires, switches as well as rectifiers can be designed out of just molecules [27]. The use of organic and biocompatible molecules for electronics is paving the way for new technologies like nanobiotechnology [28]. Further advances can be brought about by using the additional spin degree of freedom of the electron to drive electronics. This leads to the new field of molecular spintronics which combines molecular electronics with spintronics [29, 30]. There is a large scope of research in this field, for developing basic understanding as well as probing and improving spin-dependent properties for applications.

With the advance of experimental techniques, the synthesis of nanomaterials and their manipulation in a desired way is possible. For example, synthesis methods like molecular beam epitaxy (MBE) allow layer-by-layer controlled growth of crystalline as well as nanostructured materials [31]. Techniques like scanning tunneling microscopy (STM) and atomic force microscopy (AFM) allow for an atom-by-atom manipulation, as well as atom-resolved characterization of materials [32–34]. However, despite such advances, the experimental synthesis of nanomaterials can be expensive and difficult to control. Special conditions like ultra-high vacuum and cryogenic temperatures can be required. Large scale synthesis of nanomaterials relevant for technological applications can be very costly. Achieving properties that are most desirable for technology by experimentally exploring a wide range of constituents and compositions is cumbersome, time-consuming and expensive. Given the vast range of possibilities, it can be very difficult to determine just from an experimental search, the nanomaterial that is best suited for a particular application. This is where a first principles theoretical/computational study of nanomaterials becomes almost a necessity. Not only do such calculations frequently offer a quicker and cheaper alternative to experiments, more importantly, they can provide physical and chemical insight that can guide one towards the rational design of novel nanomaterials.

First principles or *ab initio* calculations are calculations that are based on the basic underlying physical laws and theoretical formulations (e.g., the Schrodinger equation or the Dirac equation), which do not require one to provide any input from experiments, or to fit any parameters to empirical data. These calculations are essentially independent from experiments, and can be used to complement experimental results. First principles calculations can be used as a predictive tool for designing materials properties, and can provide insight and guidance in the search for candidate materials for specific applications. Computations based on first principles calculations can be used to model materials efficiently, sidestepping the need for achieving difficult experimental conditions like ultrahigh vacuum or low temperature or the need to have very pristine systems. With the development of state of the art computational technology and new methods, it is now possible to handle real life materials problems starting from just the atomic numbers of the constituent elements of the material. Such calculations can provide a quick and thorough understanding of the underlying mechanisms that give rise to a particular phenomenon or property, and provide guidance as to which interactions can be tuned, and how, for enhancing certain properties needed for applications. One can, for example separate out contributions from different interactions by performing appropriate calculations, which is usually not possible in experiments.

Often computations based on first principles calculations can become rather expensive, and the availability of computational resources can place limitations on how realistic the study can be. However it is still possible to work with prototypical models that capture the essential physics in an experiment. Different first principles methods can be developed which give different levels of accuracy and rigor. One can gain insight into a simple material with an accuracy right up to the atomic level using, e.g., density functional theory based first principles calculations [35]. For more complex properties like transport or excited state properties, it is possible to develop computations based on advanced theories like the non-equilibrium Green's function method or time dependent Schrodinger theory, in combination with first principles density functional theory based computations [36, 37]. One can essentially choose to what level of accuracy a material needs to be understood.

1.2 Thesis Outline

Chapter 1 is a brief introduction to the thesis. The broad aim of this thesis is to design materials for technological applications using first-principles methods. In this thesis, we have focused on materials which may be used for applications in three broad areas: (1) electronics, (2) on-board vehicular gas storage, and (3) spintronics. We use first principles calculations based on density functional theory (DFT), as well as other techniques like density functional perturbation theory (DFPT) and the non-equilibrium Green's function (NEGF) method, to design novel nanomaterials with enhanced properties that make them suitable for these applications, as well as to get insight into the underlying mechanisms governing the physical, chemical and magnetic properties of these materials. Wherever possible, we also develop simple models that not only enable us to understand the underlying complex phenomena, but also allow us to supplement time-consuming calculations that invoke the full machinery of *ab initio* calculations, with quicker alternatives that can be used to obtain estimates of desired quantities.

In Chapter 2 of the thesis, the theoretical background of different methods used in this thesis is discussed – density functional theory, density functional perturbation theory, and the non-equilibrium Green's functions technique for quantum transport. Grimme's method of incorporating van der Waals interactions in DFT is also described.

The next four chapters are about our research work based on first principles calculations for designing nanomaterials for applications. In this thesis, we have tried various ways of tuning the different materials properties for applications. To start with we try to tune the electronic and dielectric properties of silicon nitride by progressive substitution of silicon atoms with either germanium or carbon atoms. Next, we try to either remove atoms or to alter their positions and bonding topology in systems like Twisted Bilayer Graphene (TBLG) to create defects, and see how the electronic and magnetic properties are affected. Next, we add new chemical functional groups to the edges of a graphene nanoribbon and see how the chemical properties are altered, with the objective of enhancing the binding of hydrogen molecules. Finally, we change the geometry of the molecule-lead contact in a molecular spintronics setup, with the aim of tuning the spin-polarized transport and the magnetoresistance. As we will show in the thesis, all four of these attempts at designing materials lead to promising computational results, worthy of future experimental investigations.

For electronics applications, we have studied two systems. First we look at the dielectric properties of ternary silicon germanium nitride and silicon carbon nitride materials. Silicon nitride and germanium nitride find many applications in the electronics industry, e.g., in gate dielectrics, microelectronic cutting tools, optoelectronic devices, and microelectromechanical systems (MEMS) [38–41]. Carbon nitride materials are proposed candidates for super-hard materials [42]. We explore the possibility of tuning the band gap and dielectric properties of crystalline silicon germanium nitride and silicon carbon nitride ternary materials by changing the composition of germanium and carbon. In Chapter 3, we have studied the dielectric properties of crystalline α- and β-phase silicon germanium nitrides and silicon carbon nitrides, $A_{3-\xi}B_{\xi}N_4$ (A=Si, B=Ge or C, ξ =0,1,2,3). We try to understand the origin of the variation in the dielectric constant with the change in chemical composition.

Next, we study how the electronic, magnetic and structural properties of Twisted Bilayer Graphene (TBLG) are affected by the presence of point defects. Graphene has huge potential for applications in electronics, however its properties are drastically affected by the presence of a second layer, especially the manner in which the two layers of graphene are stacked. TBLG can show an array of exotic electronic properties: van Hove singularities near the Fermi energy, tunability of the Fermi velocity with the twist angle, and also the possibility of superconductivity [43]. The weak interlayer coupling between the layers is not very well understood. It is also quite well known that point defects, like monovacancies and Stone-Wales defects can change the properties of graphene [44,45]. These defects can induce magnetic moments in graphene and affect the gas sensing and transport properties of graphene [45–52]. We try to understand how the properties are affected when both the twist as well as the defects are simultaneously present. In TBLG, the weak interlayer coupling presumably plays a crucial role, and we therefore incorporate the van der Waals interactions into our DFT calculations and compare our results with those obtained using conventional DFT functionals. In Chapter 4, we have used DFT incorporating van der Waals corrections, to study twisted bilayer graphene (TBLG) where Stone-Wales defects or monovacancies are introduced in one of the layers. We compare these results to those for defects in single layer graphene (SLG) or Bernal stacked graphene (AB-BLG). We first look at the energetics of defect formation and the structural properties of the defects and compare these with the same defects in SLG and AB-BLG. We then look at the electronic band structure, especially how the band structure in the vicinity of the Fermi energy (E_F) is affected by the presence of defects. In the case of the monovacancy, magnetic moments are known to arise in SLG. We check whether such magnetic moments also arise in TBLG, and if so how their values compare with those in SLG and AB-BLG. We also check if the monovacancy leads to the possibility of having a spin-polarized current. We try to understand the nature of the interlayer interactions by looking at the interlayer charge transfer and chemical interactions, and how these affect the band-structure in the presence of the two kinds of defects.

With applications for on-board vehicular gas storage in mind, we explore the possibility of adsorptive capture of molecular hydrogen in the solid state. The difficulty faced here is that the gas molecules are required to bind optimally on the substrate [53]. The molecules should be bound tightly enough to the substrate that the gas is retained at room temperatures; but at the same time, the binding should be weak enough that the release of gas whenever required is not hindered. Carbon nanostructures are ideal candidates for adsorptive storage due to their large surface to volume ratio [54, 55]. The problem is that adsorption of hydrogen is weak in carbon nanostructures. In this study, we try to enhance the uptake of hydrogen gas in carbon nanostructures by chemical functionalization. For accurately capturing the weak interaction between the hydrogen and the substrate, the incorporation of van der Waals interactions is essential. In Chapter 5, we have performed *ab initio* density functional theory calculations, incorporating van der Waals corrections, to study the adsorption of molecular hydrogen on zigzag graphene nanoribbons whose edges have been functionalized by OH, NH_2, COOH, NO_2, or H_2PO_3. The functional groups used here are either electron withdrawing and electron donating in nature, and we try to see which functional groups work best for enhancing the binding. We also mix various functional groups, and try to see if we see any enhancement due to synergistic combinations of electron withdrawing and electron donating groups. We then wish to understand what are the interactions that lead to the binding, and we try to separate out the different contributions to the adsorption energy due to various interactions between the hydrogen molecules and the substrate. Our results can offer insight into the specific origins of weak binding of gas molecules on graphene, and suggest the possible use of edge functionalization in combination with other strategies to increase the uptake of hydrogen in graphene. This study can also have relevance for the storage of hydrogen in porous carbon materials, such as activated carbons.

For spintronics applications, the important property from the point of view of applications is the magnetoresistance (MR). High magnetoresistance is desirable for technological applications, and materials like multilayered Fe/Cr/Fe sandwiches showing giant magnetoresistance (GMR) have been used extensively in applications for memory storage [56,57].

The discovery of GMR was awarded the Nobel prize in physics in 2007. Beyond GMR, the search for materials for effective spin injection and retaining spin coherence has been the topic of active research [58]. Research has now moved on to include molecular spintronics, especially using organic molecules as they have the advantage of large spin coherence time and length scales [59]. Some of the open problems in molecular spintronics are how to effectively connect molecules to the electrodes, and how to effectively inject spins into the molecules. The molecule-metal interface, and the system geometry, play a vital role in determining conduction properties [60–64]. Here we try to understand whether the magnetoresistance is affected by how the molecule is connected to the leads, and whether we can try to design a molecule-lead geometry with the aim of enhancing the magnetoresistance. In Chapter 6, we perform *ab initio* calculations, combining the non-equilibrium Green's function method with density functional theory, on a non-magnetic dithienylethene molecule placed between spin-polarized nickel leads of varying geometries, with the aim of understanding how the magnetoresistance is affected by the lead geometries. We choose to use this molecule as it has two stable conformations, that are representative of the resonant and tunneling conduction regimes. The non-equilibrium Green's function calculations involved here can become very computationally expensive for the full self-consistent bias dependent study. We try to develop a simple model that can capture the full bias-dependent behavior of the full *ab initio* calculation, with inputs of only the zero-bias density of states of the sulfur atoms connecting the dithienylethene molecule to the nickel leads. This model can give us very useful insight into the spin injection into a molecule. It can also be used as an important predictive tool for magnetoresistance, at minimum computational cost.

In Chapter 7, the main findings of the thesis are summarized and an outlook for possible directions of future research is presented.

Chapter 2

Theoretical Formalism

2.1 Density Functional Theory

The general quantum-mechanical treatment of any material is a problem of many interacting particles. Density Functional Theory (DFT) is a theoretical formalism that enables us to solve this many body problem. It is a highly accurate technique and is one of the most widely used methods for *ab initio* calculations of the structure and properties of atoms, molecules, crystals, surfaces and nanosystems. Here we would like to give an overview as to how DFT works.

2.1.1 The Many Body Problem

The Hamiltonian of a many body system of nuclei and electrons is given by:

$$\hat{H} = -\sum_{I}\frac{\hbar^2}{2M_I}\nabla_I^2 - \frac{\hbar^2}{2m_e}\sum_{i}\nabla_i^2 + \frac{1}{2}\sum_{I\neq J}\frac{Z_I Z_J e^2}{|\mathbf{R}_I - \mathbf{R}_J|} - \sum_{i,I}\frac{Z_I e^2}{|\mathbf{r}_i - \mathbf{R}_I|} + \frac{1}{2}\sum_{i\neq j}\frac{e^2}{|\mathbf{r}_i - \mathbf{r}_j|}, \quad (2.1)$$

where $\mathbf{r}_i$ is the position co-ordinate of the i^{th} electron of mass m_e and charge e; and $\mathbf{R}_I$ is the position co-ordinate of the I^{th} nucleus, with mass M_I and atomic number Z_I. $\hbar$ is Planck's constant, and the indices i, j run over all the electrons in the system, while I, J run over all the nuclei in the system. The first two terms on the right-hand side of Eq.(2.1) are the nuclear and the electronic kinetic energies, respectively. The subsequent terms are the nuclei-nuclei Coulomb repulsion, electron-nuclei Coulomb attraction and the electron-electron Coulomb repulsion, respectively.

Born-Oppenheimer Approximation or Adiabatic Approximation

The Born-Oppenheimer approximation [65] offers a way of separating the nuclear and the electronic degrees of motion. The nuclei being much heavier than the electrons ($M_I \gg m_e$), have much smaller velocities as compared to that of the electron's motion. The electronic time scales are small enough that the electrons can relax to their instantaneous ground states in the time scale required for the nuclear motion. Thus the nuclei can be considered as effectively stationary in the electronic time scale. The electronic Hamiltonian can thus be solved using a time-independent Schrödinger equation for electrons in this stationary external (nuclear) potential.

The electronic part of the many body Hamiltonian that describes a system of interacting electrons acted on by a static external (nuclear) potential is given as:

$$\hat{H}_e = -\sum_i \frac{\hbar^2}{2m_e}\nabla_i^2 + \frac{1}{2}\sum_{i\neq j}\frac{e^2}{|\mathbf{r}_i - \mathbf{r}_j|} - \sum_{i,I}\frac{Z_I e^2}{|\mathbf{r}_i - \mathbf{R}_I|}. \tag{2.2}$$

The (many body) electronic wavefunction $\Psi\big(\{\mathbf{r}_i\};\{\mathbf{R}_I\}\big)$ can be found by solving the time-independent Schrödinger equation for the electronic part of the Hamiltonian, with a particular fixed set of positions of the nuclei,

$$\left[-\sum_i \frac{\hbar^2}{2m_e}\nabla_i^2 + \frac{1}{2}\sum_{i\neq j}\frac{e^2}{|\mathbf{r}_i - \mathbf{r}_j|} - \sum_{i,I}\frac{Z_I e^2}{|\mathbf{r}_i - \mathbf{R}_I|}\right]\Psi\Big(\{\mathbf{r}_i\};\{\mathbf{R}_I\}\Big) = E(\{\mathbf{R}_I\})\Psi\Big(\{\mathbf{r}_i\};\{\mathbf{R}_I\}\Big) \tag{2.3}$$

Here, $E(\{\mathbf{R}_I\})$ is the set of electronic energy eigenvalues, that depend only parametrically on the nuclear positions. Note that the first two terms in Eqs.(2.2) and (2.3) are purely dependent on the electronic positions and are the same for all N-electron systems. Thus, the knowledge of the external nuclear potential ($\hat{V}_{ext}$) is sufficient to determine the ground states as well as the excited states (basically all the properties) of the many electron system. However the solution for the wavefunctions of this many particle equation is practically impossible even for a small number of electrons.

In DFT, the electronic density is treated as the basic variable rather than the many-electron wavefunction. Within DFT, the knowledge of the ground state electronic density is sufficient to determine all the properties of the many electron system. Thus, instead of solving for the many-body wavefunction (which is a function of $3N$ electronic coordinates), we need to only solve for the total electronic density, which is a function of three spatial variables. This drastically simplifies the problem.

The density operator for a system of N electrons is given as,

$$\hat{n}(\mathbf{r}) = \sum_{i=1}^{N} \delta(\mathbf{r} - \mathbf{r}_i).$$

The electronic density is thus determined from the many-electron wavefunction,

$$n(\mathbf{r}) = \frac{\langle \Psi | \hat{n}(\mathbf{r}) | \Psi \rangle}{\langle \Psi | \Psi \rangle} = \frac{\int d\mathbf{r}_1 \; d\mathbf{r}_2 \; \ldots d\mathbf{r}_N \sum_{i=1}^{N} \delta(\mathbf{r} - \mathbf{r}_i) \left| \Psi(\mathbf{r}_1, \mathbf{r}_2, \ldots, \mathbf{r}_N) \right|^2}{\int d\mathbf{r}_1 \; d\mathbf{r}_2 \; \ldots d\mathbf{r}_N \left| \Psi(\mathbf{r}_1, \mathbf{r}_2, \ldots, \mathbf{r}_N) \right|^2}. \tag{2.4}$$

The total energy of the system can then be written as,

$$E = \langle \hat{H}_e \rangle = \Big\langle - \sum_i \frac{\hbar^2}{2m_e} \nabla_i^2 + \frac{1}{2} \sum_{i \neq j} \frac{e^2}{|\mathbf{r}_i - \mathbf{r}_j|} \Big\rangle + \int d\mathbf{r} V_{ext}(\mathbf{r}) n(\mathbf{r}). \tag{2.5}$$

Note that the term in the angular brackets is universal for all electronic systems with a given number of electrons N. Hence, all system-specific properties are completely determined by the second term containing V_{ext} and the electronic density $n(\mathbf{r})$.

2.1.2 Hohenberg-Kohn Theorems

DFT is based on two theorems proposed by Hohenberg and Kohn [66] which are stated as follows.

Theorem I: For any system of interacting particles in an external potential $V_{ext}(\mathbf{r})$, the potential $V_{ext}(\mathbf{r})$ is determined uniquely, up to an additive constant, by the ground state particle density $n_0(\mathbf{r})$.

As a consequence of this first theorem, the external potential is uniquely determined from the knowledge of the ground state electronic density. The density however can be determined from the many-body wavefunction which is a solution of the Schrödinger equation involving the potential. This thus leads to a self-consistent procedure for the determination of the ground state density, which will be more clearly described in the next section.

Theorem II: A universal functional for the energy $E[n]$ in terms of $n(\mathbf{r})$ can be defined, valid for any external potential $V_{ext}(\mathbf{r})$. For any particular $V_{ext}(\mathbf{r})$, the exact ground state energy of the system is the global minimum value of this functional, and the density $n(\mathbf{r})$ that minimizes the functional is the exact ground state density $n_0(\mathbf{r})$.

The kinetic energy and the electron-electron interaction terms in the many body Hamiltonian are the same for all electronic systems. The total energy can thus be written as a functional of the density $n(\mathbf{r})$,

$$E[n] = F[n] + \int d\mathbf{r} V_{ext}(\mathbf{r}) n(\mathbf{r}), \tag{2.6}$$

where the first term $F[n]$ is a universal functional of the density that is the same for all electronic systems. The second term is a linear functional of the density which contains the system-specific information of the electron-nuclei interaction. According to the second Hohenberg-Kohn theorem, that density which minimizes the total energy functional $E[n]$ is the exact ground state density of the system.

However, the exact functional form of the universal functional $F[n]$ is not known. A large part of this functional corresponds to the kinetic energy term, that involves gradients over each electronic coordinate, and it is not possible to write an exact analytical form of the kinetic energy as a functional of the total density. The functional form of the many particle electron-electron interactions is again not known. In principle, DFT is exact, however the lack of knowledge of the exact functional form of $F[n]$ is the main reason for approximations creeping into DFT.

The next most important step is to construct an approximate form for the functional $F[n]$. A very effective approximation for the universal energy functional $F[n]$ was proposed by Kohn and Sham in 1965 [67]. This formulation of the Kohn-Sham equations is the main reason for the success of density functional theory.

2.1.3 The Kohn-Sham Formulation

The Kohn-Sham formulation maps the problem of an interacting N-electron system onto an equivalent problem of N non-interacting fictitious electrons. These N fictitious non-interacting electrons are described by a set of $N/2$ lowest-lying orbital states called the Kohn-Sham (KS) states, so that each state accommodates two electrons of opposite spin. The Kohn-Sham states are given as $\Big\{\psi_1(\mathbf{r}), \psi_2(\mathbf{r}) \ldots \psi_{N/2}(\mathbf{r})\Big\}$ and lead to the true ground state density $n(\mathbf{r})$:

$$n(\mathbf{r}) = 2\sum_{\alpha=1}^{N/2} \psi_\alpha^*(\mathbf{r})\psi_\alpha(\mathbf{r}). \tag{2.7}$$

The functional $F[n]$ can be cast in the form

$$F[n] = T_s[n] + E_H[n] + E_{xc}[n]. \tag{2.8}$$

Here, $T_s[n]$ is the kinetic energy of the fictitious non-interacting electrons, and is given as:

$$T_s[n] = -2\frac{\hbar^2}{2m_e}\sum_{\alpha=1}^{N/2}\int \psi_\alpha^*(\mathbf{r})\nabla^2\psi_\alpha(\mathbf{r})d\mathbf{r}. \tag{2.9}$$

This term captures the majority of the kinetic energy of the many-electron system.

The electron-electron repulsion term has been separated out into the Hartree term E_H (which is a functional of the density) and a residual energy contribution due to the exchange asymmetry and correlations. The Hartree energy E_H is given as,

$$E_H[n] = \frac{e^2}{2}\int \frac{n(\mathbf{r})n(\mathbf{r}')}{|\mathbf{r}-\mathbf{r}'|}d\mathbf{r}d\mathbf{r}'. \tag{2.10}$$

The residual energy contribution due to the exchange asymmetry and correlations can be clubbed together along with the kinetic energy difference into the so-called Exchange-Correlation energy E_{xc}, which is defined as,

$$E_{xc}[n] = \Big\{\Big\langle -\sum_i \frac{\hbar^2}{2m_e}\nabla_i^2\Big\rangle - T_s[n]\Big\} + \Big\{\Big\langle \frac{1}{2}\sum_{i\neq j}\frac{e^2}{|\mathbf{r}_i-\mathbf{r}_j|}\Big\rangle - E_H[n]\Big\}. \tag{2.11}$$

Thus all the terms whose functional forms are not known are now accumulated into the exchange-correlation energy term. There are many levels of approximation proposed for this term, some of which will be described in the next section.

Thus the problem of finding the ground state density of the interacting many-electron system, basically boils down to the minimization problem of the energy functional $E[n]$ of N fictitious non-interacting Kohn-Sham electrons with respect to the density $n(\mathbf{r})$, with the constraint imposed that the total number of electrons in the system is fixed.

Thus, the Kohn-Sham equations are given as,

$$\left\{-\frac{\hbar^2}{2m_e}\nabla^2 + V_{\text{KS}}(\mathbf{r})\right\}\psi_\alpha(\mathbf{r}) = \epsilon_\alpha\psi_\alpha(\mathbf{r}), \tag{2.12}$$

where the first term is the kinetic energy of the fictitious non-interacting electrons and V_{KS} is the potential experienced by the non-interacting Kohn-Sham particles, and is given as:

$$V_{\text{KS}}(\mathbf{r}) = V_{ext}(\mathbf{r}) + e^2\int\frac{n(\mathbf{r}')}{|\mathbf{r}-\mathbf{r}'|}d\mathbf{r}' + V_{xc}(\mathbf{r}). \tag{2.13}$$

Here $V_{xc}(\mathbf{r}) = \frac{\delta E_{xc}}{\delta n(\mathbf{r})}$ is the functional derivative of the exchange-correlation energy, called the exchange-correlation potential.

Equations (2.7), (2.12) and (2.13) form a set of self-consistent equations for the system. A flowchart demonstrating the self-consistent procedure to solve these equations is shown in Fig. 2.1. First, a trial (input) density n^{inp} is obtained (e.g., from a combination of atomic wavefunctions and plane waves). The KS potential is then calculated using this density and the KS equation is solved for the KS orbitals. The new (output) density n^{out} is obtained from these KS orbitals. If the difference between the input and the output densities is lower than a pre-defined tolerance, self-consistency is achieved. Otherwise, this output density is used, after some mixing (defined by the function f) with the input density to speed up the convergence, for a new iteration, and the whole procedure is repeated until convergence is achieved. There exist various mixing schemes to speed up the convergence; in most of our calculations we have used a modified Broyden's mixing

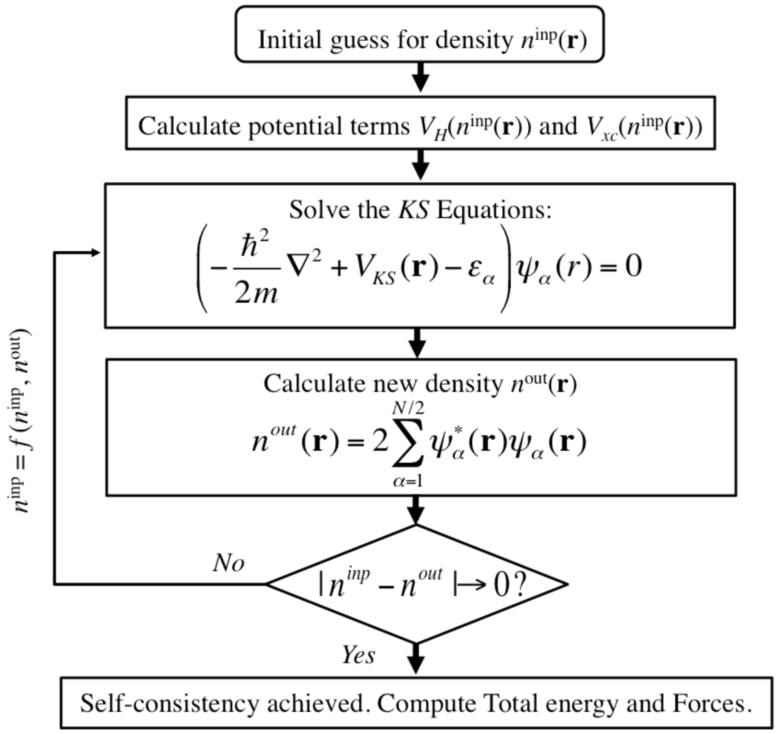

Figure 2.1: *Flow chart showing the self-consistency loop for the iterative solution of the Kohn-Sham equations.*

method [68, 69].

Once convergence is achieved, the total ground state energy is calculated which is given as,

$$E_0 = 2\sum_{\alpha=1}^{N/2}\epsilon_\alpha - \frac{e^2}{2}\int\frac{n(\mathbf{r})n(\mathbf{r}')}{|\mathbf{r}-\mathbf{r}'|}d\mathbf{r}d\mathbf{r}' + E_{xc}[n] - \int d\mathbf{r}\,V_{xc}(\mathbf{r})n(\mathbf{r}) + E_{Ewald} \tag{2.14}$$

where E_{Ewald} is the Coulomb interaction energy between the nuclei, which is calculated using the method suggested by Ewald [35].

2.1.4 Approximations for Exchange-Correlation Functionals

The exchange energy is a result of the fermionic nature of the electrons, due to which the many-body wave-function is anti-symmetric under the exchange of any pair of electrons. The correlation energy is defined as the difference between the exact total energy and collectively the kinetic, Hartree and exchange energy of the system. The correlation energy is a result of complicated many-body interactions between the electrons, so that the electrons screen themselves and try to reduce the Coulombic repulsion between each other. The exact functional form of the exchange-correlation energy is not known, and hence approximate exchange-correlation functionals are used to calculate various properties of the system. In this thesis, we have primarily used two approximations for the exchange correlation functionals. These are described below.

Local Density Approximation

In the Local Density Approximation (LDA), the effect of the exchange and correlation is assumed to be local in nature, so that the exchange-correlation term is solely due to the density at each point in space, independent of other points [67]. The exchange-correlation energy density is assumed to be the same as that in a homogeneous electron gas:

$$E_{xc}^{\mathrm{LDA}}[n] = \int d\mathbf{r}\; n(\mathbf{r})\epsilon_{xc}^{hom}(n(\mathbf{r})), \tag{2.15}$$

where $\epsilon_{xc}^{hom}(n(\mathbf{r}))$ is the exchange-correlation energy density in a homogeneous electron gas with density $n(\mathbf{r})$. The average exchange energy density for the homogeneous electron gas can be calculated analytically,

$$\epsilon_{x}^{hom}(n) = -\frac{3}{4}\left(\frac{6}{\pi}n\right)^{1/3}. \tag{2.16}$$

The correlation energy of a homogeneous electron gas was calculated by accurate quantum Monte-Carlo calculations [70] and parametrized analytic forms were developed. The most commonly used forms are due to Perdew and Zunger (PZ) [71], and Vosko, Wilk, and Nusair (VWN) [72].

Further, the exchange-correlation potential can be written as,

$$V_{xc}^{\mathrm{LDA}}(\mathbf{r}) = \left[\epsilon_{xc} + n\frac{\partial \epsilon_{xc}}{\partial n}\right]_{\mathbf{r}}. \tag{2.17}$$

Though the LDA seems to be a very drastic approximation, it works remarkably well for most solid systems. This is possibly a consequence of the fact that the LDA obeys certain sum rules for the exchange-correlation hole [73]. The LDA generally has a tendency to overbind, and hence typically results in lattice constants that are small, and binding energies that are too large.

Generalized Gradient Approximations

In order to take into account the inhomogeneous nature of the density in real systems, one can include corrections to the functional due to the gradient of the density. However a naive expansion of the exchange correlation functional as a Taylor series, with terms containing the density and the gradient of the density, known as the Gradient Expansion Approximation (GEA), in fact performs even worse than the LDA functional for real systems [74]. Such an expansion violates the sum rules for the exchange-correlation hole that the LDA satisfies. The basic reason is that in real materials, the gradient is so large that the GEA breaks down.

This problem was overcome by modifying the large gradient behavior exchange-correlation functionals so as to obtain the desired properties. A variety of ways were proposed [75–77] to do this and these are collectively known as the Generalized Gradient Approximations (GGA). In the GGA, the exchange correlation functional has the form:

$$E_{xc}^{\mathrm{GGA}}[n] = \int d\mathbf{r}\; n(\mathbf{r})\epsilon_{xc}([n], |\nabla n(\mathbf{r})|), \tag{2.18}$$

where $\epsilon_{xc}([n], |\nabla n(\mathbf{r})|)$ is the exchange-correlation energy per electron, that depends on the local density $n(\mathbf{r})$ as well as the magnitude of the gradient of the density $|\nabla n(\mathbf{r})|$.

Thus the exchange correlation potential is given as

$$V_{xc}^{\mathrm{GGA}}(\mathbf{r}) = \left[\epsilon_{xc} + n\frac{\partial \epsilon_{xc}}{\partial n} - \nabla\left(n\frac{\partial \epsilon_{xc}}{\partial \nabla n}\right)\right]_{\mathbf{r}}. \tag{2.19}$$

The GGA usually corrects the overbinding effect of the LDA. However, the GGA is often known to underbind, which can result in lattice constants that are too large. Some properties, such as magnetic moments, are better estimated using the GGA.

2.1.5 Basis Set

To solve the KS equation, the KS orbitals are generally expanded in terms of a suitable set of basis functions $\Big\{\phi_\beta(\mathbf{r})\Big\}$. A variety of basis functions can be chosen for this expansion, including plane waves [78, 79], gaussians [80], Muffin Tin Orbitals [81], localized atomic orbitals [82], etc. In this thesis, the majority of our calculations are done using a plane wave basis set [78]. For electronic transport calculations, we have done calculations using a basis set of localized atomic-like orbitals [30, 82, 83]. We will briefly describe these two basis sets.

Plane Waves

For extended systems, Bloch's theorem suggests plane waves as a natural choice for the basis set. The KS orbitals can be expanded in terms of plane-waves:

$$\psi_{\alpha,\mathbf{k}}(\mathbf{r}) = \sum_{\mathbf{G}} c_{\alpha,\mathbf{k}+\mathbf{G}} e^{i(\mathbf{k}+\mathbf{G}).\mathbf{r}} \tag{2.20}$$

where $\mathbf{G}$ is a reciprocal lattice vector, and $\mathbf{k}$ is a wavevector in the first Brillouin zone. This expansion is infinite in principle, however it can be truncated at a sufficiently large value of $|\mathbf{k}+\mathbf{G}|$. The truncation of this expansion is possible because the lower values of $|\mathbf{k}+\mathbf{G}|$ contribute most to the wavefunctions. A kinetic energy cutoff is used to specify the truncation of this expansion, and is given as $(\hbar^2/2m)|\mathbf{k}+\mathbf{G}|^2 \leq E_{cut}$. If the charge density is rapidly oscillating or very localized, a large number of Fourier components are required to accurately represent it, and thus a large plane wave cutoff is required.

One advantage of using plane waves as a basis set is that the kinetic energy is a diagonal matrix in this representation. The computational expense depends on the number of plane waves in the expansion; and this can be reduced by using ultrasoft pseudopotentials (explained in the next subsection).

Localized Atomic Orbitals

The atomic orbitals are the solutions for the wavefunctions of the electrons in an isolated atom. The wavefunction in the solid or nanosystem can typically be expanded as a linear combination of the atomic orbitals, which is the general choice used in tight binding calculations. The most common approach is to use atom centered orbitals, that are products of the radial functions and spherical harmonics. For DFT calculations, the basis set of atomic orbitals is tailored with the aim of reducing the number of basis functions, and to ease the computations. These modifications include strictly localizing the radial extent of the orbitals so that the radial orbitals go smoothly to zero at a certain cutoff value of the radius [84, 85]. The KS wavefunctions can then be written as,

$$\psi_\alpha(\mathbf{r}) = \sum_{\beta \equiv \{I,n,l,m\}} c_{\alpha\beta}\phi_{Inl}(|\mathbf{r} - \mathbf{R}_I|)Y_{lm}(\hat{\mathbf{r}_I}), \tag{2.21}$$

where $\phi_{Inl}(|\mathbf{r} - \mathbf{R}_I|)$ are localized atomic like orbitals (these can be numerical orbitals), Y_{lm} are the spherical harmonics, $\mathbf{R}_I$ is the position vector of the I^{th} atom, $n = 1, 2 \ldots,$ is the radial quantum number, $l = 0, \ldots n-1$, is the angular quantum number, and $m = -l, \ldots l$, is the magnetic quantum number. α and β are compound indices composed of I, n, l, and m. Only a small number of basis functions per orbital are required to effectively represent the KS wavefunctions. Depending on the number of basis functions used to expand each KS orbital, the basis set is labeled as the minimal single-ζ or SZ (one radial basis function per orbital), double-ζ or DZ (two radial basis functions per orbital), double-ζ + polarization or DZP (two radial basis functions + one angular basis function per orbital) and so on. The advantage of using such localized orbitals is that the Hamiltonian becomes a sparse matrix in this representation, and hence the computational cost is drastically reduced.

2.1.6 Pseudopotential Approximation

The core-electrons are tightly bound to the nucleus and their wavefunctions are very localized and show rapid oscillations in space. In an all-electron plane wave DFT calculation, a large number of basis functions is required for an accurate description of the core states. For example, a large number of Fourier components is required to expand the wavefunctions of the core electrons, leading to a very high plane-wave cutoff. Also, the orthogonality requirements mean that valence wavefunctions have several oscillations in the core region, which again leads to a high plane-wave cutoff. This leads to huge computational costs and such all-electron calculations of real materials are practically impossible when using a plane wave basis.

However one can get rid of this problem by the pseudopotential approximation [86,87]. The pseudopotential approximation replaces the core region of the atom by a hypothetical potential so that one can neglect the core orbitals completely, at the same time, treating the interactions between the valence electrons and the 'ionic core' with sufficient accuracy. The justification for such a seemingly drastic approximation is that it is generally the valence electrons that determine the chemical bonding and material properties. The pseudopotential is so constructed that the pseudo-wavefunction matches exactly with the true wavefunction in the valence region, i.e., beyond a particular core radius cutoff value. Inside this core radius, the pseudo wavefunction is nodeless and goes smoothly to zero (i.e., all oscillations are removed), so as to get rid of large Fourier components. The core radius value is so chosen that all the nodes of the true wavefunction lie inside the core region, and can be gotten rid of in the pseudization procedure.

The construction of a pseudopotential is not unique, however there are certain conditions obeyed by a good pseudopotential [88]. Firstly, both the pseudo-wavefunction and its first and second derivatives should match smoothly at the core radius cutoff. Secondly, it used to be believed that a good pseudopotential should conserve the electronic charge, such pseudopotentials are called norm-conserving pseudopotentials [88]. Norm-conservation ensures that the scattering properties of the atom are correctly described. Generally the success of a pseudopotential lies in its 'transferability' to different chemical environments. Norm-conserving pseudopotentials generally show good transferability [35].

Although the pseudopotential approximation drastically reduces the computational expense, the constraint of norm-conservation can still force certain large Fourier components to be required in the plane-wave expansion of the wavefunction. If this condition is relaxed, the computational cost is even further reduced. Such a pseudopotential is called an 'ultrasoft pseudopotential' [89]. The loss of charge due to relaxing the norm-conservation condition is compensated for by adding an 'augmentation' charge in the core region of the pseudopotential. One thing to note is that as a result, in an ultrasoft pseudopotential a separate cutoff for the charge density is used in addition to the kinetic energy cutoff for the wavefunction. This charge density cutoff is quite large, typically 8 to 12 times that of the cutoff for the wavefunction, for accurate enough calculation of the augmentation charge. This however adds very minimally to the computational cost.

2.1.7 Force Calculations: Hellmann-Feynman theorem

For obtaining the optimized geometry of the systems, the accurate calculation of the forces is required. The forces acting on the atoms are first derivatives of the total energy of the system, with respect to the atomic positions. A naive approach to find the forces is to basically evaluate the local energy landscape in the parameter space of the atomic positions, and then to take the derivative. This however involves the tedious procedure of performing self-consistent calculations for a large number of different atomic configurations. A way out of this is provided by the Hellmann-Feynman theorem [90], which relates the derivative of the total energy to the expectation value of the derivative of the Hamiltonian, given as:

$$F_I = -\frac{\partial \langle E(\mathbf{R}_I) \rangle}{\partial \mathbf{R}_I} = -\left\langle \frac{\partial H}{\partial \mathbf{R}_I} \right\rangle = -\int \frac{\partial V_{\mathbf{R}_I}(\mathbf{r})}{\partial \mathbf{R}_I} n_{\mathbf{R}_I}(\mathbf{r}) d\mathbf{r}, \tag{2.22}$$

where, $n_{\mathbf{R}_I}(\mathbf{r})$ is the ground state electron density for a given set of nuclear co-ordinates $\{\mathbf{R}_I\}$. The huge advantage of this simple relation is that evaluation of the total energy at many configurations is not necessary, and one can do just a single calculation to evaluate the forces on atoms in a particular configuration. A similar procedure is applied for the evaluation of various response functions which are higher order derivatives of the total energy with respect to certain parameters, as will be seen in the next section describing density functional perturbation theory.

2.1.8 Spin Polarized DFT

So far, we have neglected the spin of the electron. For magnetic and spintronic properties, however, the consideration of the electronic spin is necessary. This is done in spin polarized DFT calculations. The spin up and spin down charge densities are separately evaluated in terms of the spin up and spin down KS orbitals in the same way as in "normal" DFT:

$$n^{\sigma}(\mathbf{r}) = 2\sum_{\alpha=1}^{N^{\sigma}} \psi_{\alpha}^{\sigma *}(\mathbf{r})\psi_{\alpha}^{\sigma}(\mathbf{r}), \tag{2.23}$$

where $\sigma = \{\uparrow, \downarrow\}$, is the spin of the electron, and N^{σ} is the number of orbitals of spin σ. The total electron density is the sum of the density of both the spins, $n(\mathbf{r}) = n^{\uparrow}(\mathbf{r}) + n^{\downarrow}(\mathbf{r})$, and the magnetization density is the difference, given as $m(\mathbf{r}) = n^{\uparrow}(\mathbf{r}) - n^{\downarrow}(\mathbf{r})$. Note that the direction of the magnetization is absent, as we are considering collinear magnetic calculations, and no spin-orbit interactions are present.

The Kohn-Sham equations for spin-polarized calculations are given as:

$$\left\{ -\frac{\hbar^2}{2m_e}\nabla^2 + V_{\mathrm{KS}}^{\sigma}(\mathbf{r}) \right\}\psi_{\alpha}^{\sigma}(\mathbf{r}) = \epsilon_{\alpha}^{\sigma}\psi_{\alpha}^{\sigma}(\mathbf{r}), \tag{2.24}$$

where V_{KS}^{σ} is the Kohn-Sham potential, which is given as:

$$V_{\mathrm{KS}}^{\sigma}(\mathbf{r}) = V_{ext}(\mathbf{r}) + e^2 \int \frac{n(\mathbf{r}')}{|\mathbf{r} - \mathbf{r}'|} d\mathbf{r}' + V_{xc}^{\sigma}(\mathbf{r}), \tag{2.25}$$

where the spin dependence arises only from the exchange-correlation potential. The exchange correlation potential is defined as:

$$V_{xc}^{\sigma}(\mathbf{r}) = \frac{\delta E_{xc}[n(\mathbf{r}), m(\mathbf{r})]}{\delta n^{\sigma}(\mathbf{r})}. \tag{2.26}$$

These equations can be solved in a similar fashion to the non-spin-polarized KS equations, with approximations for the XC functional.

2.1.9 Incorporation of London Dispersion Interactions

The London dispersion interaction arises from the quantum mechanical phenomenon by which the charge fluctuations in one part of an atomic system are electrodynamically correlated with charge fluctuations in the rest of the system [91]. This is an attractive, long range, non-local interaction, and the strength of this interaction decays as a power law as a function of the distance [92].

Exact density functional theory should be able to incorporate the London dispersion interactions, however the local and semilocal approximate functionals (LDA and GGA functionals) used in traditional DFT calculations fail to incorporate these non-local interactions. However, several methods have been developed in recent years to include these dispersive interactions in DFT calculations. These are broadly divided in two classes, (1) one class of methods adds the dispersion interactions as semi-empirical corrections on top of existing local functionals [93, 94], and (2) another class of methods attempts to develop non-local exchange-correlation functionals for DFT that can incorporate the London interactions [95, 96]. In this thesis, to study the weak interactions between layers of graphene (see Chapter 4), as well as to get a correct description of weak binding of gases (see Chapter 5), it is vital to incorporate the London interactions and therefore one should use one of these methods. We have chosen to use the "DFT-D2" treatment of Grimme (which belongs to the first class of methods described above), which gives a fairly accurate treatment of London dispersion interactions at relatively low computational cost [93]. We now describe this method in brief.

Grimme Correction Method for London Interactions

The dispersion corrected total energy is given as,

$$E_{DFT-D2} = E_{DFT} + E_{disp}, \tag{2.27}$$

where E_{DFT} is the total energy from DFT calculations for a chosen approximate exchange-correlation functional, and E_{disp} is the empirical dispersion correction which is given as,

$$E_{disp} = -s_6 \sum_{I=1}^{N_{at}-1} \sum_{J=I+1}^{N_{at}} \frac{C_6^{IJ}}{R_{IJ}^6} f_{damp}(R_{IJ}). \tag{2.28}$$

Here, N_{at} is the number of atoms in the system, C_6^{IJ} denotes the dispersion coefficient for a pair of atoms I and J, s_6 is a global scaling factor that depends only on the approximate functional used, and R_{IJ} is an interatomic distance between the atoms I and J. To avoid the singularity at small R_{IJ}, a damping function is used, given as,

$$f_{damp} = \frac{1}{1 + e^{\beta[(R_{IJ}/R_{IJ}^0)-1]}}. \tag{2.29}$$

Here, R_{IJ}^0 is the sum of atomic van der Waals radii of the atom pair $\{I, J\}$, and $\beta = -20$ is a parameter which provides larger corrections at intermediate distances (but still negligible dispersion correction for typical covalent bonding situations).

The dispersion coefficient C_6^{IJ} for a pair of atoms I and J, is written as a geometric mean of the individual coefficients for each atom, given as $C_6^{IJ} = \sqrt{C_6^I C_6^J}$. The values of the dispersion coefficients and atomic van der Waals radii have been accurately parametrized for many atoms of the periodic table [93]. The dispersion coefficients are calculated for an atom species x using the relation, $C_6^x = 0.05 N_s I_P^x \alpha^x$, where N_s has values 2, 10, 18, 36, and 54 for atoms from rows $1-5$ of the periodic table, respectively. Here I_P and α are the atomic ionization potential and the static dipole polarizabilities, respectively, which are determined using results based on accurate DFT/PBE0 calculations [97].

2.2 Density Functional Perturbation Theory

In Chapter 3, we have calculated the dielectric properties [the high frequency dielectric constant or the electronic part of the dielectric constant (ϵ_∞) and the static dielectric constant (ϵ_0)] of various systems, using density functional perturbation theory [98, 99]. Density functional perturbation theory (DFPT) is a method that has been developed to calculate the linear response of the system to an external perturbative field, in combination with standard DFT. Here, we describe briefly the formalism of DFPT and its application to the problem of calculating the dielectric constant as the linear response of the system to an external electric field. To calculate the ionic contribution to the dielectric constant, the calculation of zone center phonon modes is necessary. We therefore briefly describe the theory of lattice vibrations using DFPT.

2.2.1 Formalism of DFPT

As described in detail in Section 2.1, the material properties can be obtained by a self-consistent solution of the Kohn-Sham equations, given below:

$$n(\mathbf{r}) = 2\sum_{\alpha=1}^{N/2} \psi_\alpha^*(\mathbf{r})\psi_\alpha(\mathbf{r}), \tag{2.30}$$

$$\left\{ -\frac{\hbar^2}{2m_e}\nabla^2 + V_{\mathrm{KS}}(\mathbf{r}) \right\}\psi_\alpha(\mathbf{r}) = \epsilon_\alpha \psi_\alpha(\mathbf{r}), \tag{2.31}$$

$$V_{\mathrm{KS}}(\mathbf{r}) = V_{ext}(\mathbf{r}) + e^2 \int \frac{n(\mathbf{r}')}{|\mathbf{r}-\mathbf{r}'|} d\mathbf{r}' + V_{xc}(\mathbf{r}). \tag{2.32}$$

In general, the external perturbing potential is a differentiable function of a set of parameters $\lambda \equiv (\lambda_i)$. The parameters $\lambda \equiv (\lambda_i)$ can, for example, be the set of ionic positions in the case of the lattice vibration problem. To evaluate the appropriate response functions to the external perturbation, we calculate the first and second derivatives of the ground-state energy. According to the Hellmann-Feynman theorem, these are given as,

$$\frac{\partial E}{\partial \lambda_i} = \int \frac{\partial V_\lambda(\mathbf{r})}{\partial \lambda_i} n_\lambda(\mathbf{r}) d\mathbf{r}, \tag{2.33}$$

$$\frac{\partial^2 E}{\partial \lambda_i \partial \lambda_j} = \int \frac{\partial^2 V_\lambda(\mathbf{r})}{\partial \lambda_i \partial \lambda_j} n_\lambda(\mathbf{r}) d\mathbf{r} + \int \frac{\partial n_\lambda(\mathbf{r})}{\partial \lambda_i} \frac{\partial V_\lambda(\mathbf{r})}{\partial \lambda_j} d\mathbf{r} + \frac{\partial E_n(\mathbf{R})}{\partial \lambda_i \partial \lambda_j}. \tag{2.34}$$

Thus we need to calculate the response of the electron density, $\partial n_\lambda(\mathbf{r})/\partial\lambda_i$. In general, we can define the finite difference operator Δ^λ as:

$$\Delta^\lambda F = \sum_i \frac{\partial F_\lambda}{\partial\lambda_i}\Delta\lambda_i. \tag{2.35}$$

Thus for the electronic density (dropping the index λ),

$$\Delta n(\mathbf{r}) \;=\; 4\sum_{\alpha=1}^{N/2}\psi_\alpha^*(\mathbf{r})\Delta\psi_\alpha(\mathbf{r}). \tag{2.36}$$

The variation of the Kohn-Sham orbitals, $\Delta\psi_n(\mathbf{r})$, can be obtained by standard first-order perturbation theory and is given by the Sternheimer equation [100]:

$$(H_{\mathrm{KS}} - \epsilon_\alpha)\,|\Delta\psi_\alpha\rangle = -\,(\Delta V_{\mathrm{KS}} - \Delta\epsilon_\alpha)\,|\psi_\alpha\rangle, \tag{2.37}$$

where H_{KS} is the unperturbed Kohn-Sham Hamiltonian. Here,

$$\Delta V_{\mathrm{KS}}(\mathbf{r}) = \Delta V_{ext}(\mathbf{r}) + e^2\int\frac{\Delta n(\mathbf{r}')}{|\mathbf{r}-\mathbf{r}'|}d\mathbf{r}' + \left.\frac{d\,V_{xc}(n)}{dn}\right|_{n=n(\mathbf{r})}\Delta n(\mathbf{r}), \tag{2.38}$$

is the first-order correction to the self-consistent potential, and $\Delta\epsilon_\alpha = \langle\psi_\alpha\,|\Delta V_{\mathrm{KS}}|\,\psi_\alpha\rangle$ is the first-order variation of the Kohn-Sham eigenvalue ϵ_α. Equations (2.36),(2.37) and (2.38) form a set of self-consistent equations for the perturbed system, completely analogous to the Kohn-Sham equations in the unperturbed case. $\Delta V_{\mathrm{KS}}(\mathbf{r})$ requires the knowledge of $\Delta n(\mathbf{r})$, which in turn depends on the $\Delta\psi$'s, which can be solved for from the Sternheimer equation. This self-consistent loop is a set of N coupled linear equations.

The first-order correction to a particular eigenfunction of the Schrödinger equation given by Eq. (2.37) can be expressed as a superposition of the eigenfunctions of the unperturbed Hamiltonian, given as:

$$\Delta\psi_\alpha(\mathbf{r}) = \sum_{\beta\neq\alpha}\psi_\beta(\mathbf{r})\frac{\langle\psi_\beta\,|\Delta V_{\mathrm{KS}}|\,\psi_\alpha\rangle}{\epsilon_\alpha - \epsilon_\beta}. \tag{2.39}$$

Here β runs over all the occupied as well as empty states of the system, except the states for which the denominator vanishes. Substituting for $\Delta\psi_\alpha(\mathbf{r})$ in Eq. (2.36), the electron density can be written as:

$$\Delta n(\mathbf{r}) = 4\sum_{\alpha=1}^{N/2}\sum_{\beta\neq\alpha} \psi_\alpha^*(\mathbf{r})\psi_\beta(\mathbf{r})\frac{\langle\psi_\beta\,|\Delta V_{\mathrm{KS}}|\,\psi_\alpha\rangle}{\epsilon_\alpha-\epsilon_\beta} \tag{2.40}$$

$$= 4\sum_{\beta=N/2+1}^{\infty}\sum_{\alpha=1}^{N/2} \psi_\alpha^*(\mathbf{r})\psi_\beta(\mathbf{r})\frac{\langle\psi_\beta\,|\Delta V_{\mathrm{KS}}|\,\psi_\alpha\rangle}{\epsilon_\alpha-\epsilon_\beta}. \tag{2.41}$$

Equation (2.41) shows that the contributions to the electron-density response arising from products of occupied states cancel each other, and the β index now runs over the empty states only. This means that the electron density is unaffected by any perturbation which couples only the occupied states among each other and responds to only those components of the perturbation that couple the occupied and empty states. Consequently, equation (2.37) can be written as

$$(H_{\mathrm{KS}}-\epsilon_\alpha)\,|\Delta\psi_\alpha\rangle = -\hat{P}_c\Delta V_{\mathrm{KS}}|\psi_\alpha\rangle, \tag{2.42}$$

where $\hat{P}_c = \sum_{\beta=N/2+1}^{\infty}|\psi_\beta\rangle\langle\psi_\beta|$ is the projection operator onto the empty states.

2.2.2 Homogeneous electric fields

An applied electric field ($\mathbf{E_0}$) results in a screened electric field ($\mathbf{E}$) in the material, which then leads to a perturbative potential $V_{\mathbf{E}}(\mathbf{r}) = e\mathbf{E}\cdot\mathbf{r} = e\sum_\mu E_\mu r_\mu$, where μ runs over the three cartesian co-ordinates. Many electrostatic properties of a truly infinite solid are ill defined in the presence of such a potential because the position operator $\hat{\mathbf{r}}$ is ill defined in a periodic system, and hence its matrix elements between wavefunctions satisfying periodic boundary conditions are ill-defined.

In the linear response regime, these problems can be treated efficiently. The response of the wavefunction to the perturbative potential, requires only the off-diagonal matrix elements of the perturbing potential between the eigenfunctions of the unperturbed Hamiltonian as shown in Eq. (2.39). These terms are well defined:

$$\langle \psi_\beta \left| r_\mu \right| \psi_\alpha \rangle = \frac{\langle \psi_\beta \left| [H_{\mathrm{KS}}, r_\mu] \right| \psi_\alpha \rangle}{\epsilon_\alpha - \epsilon_\beta}, \qquad \forall m \neq n. \tag{2.43}$$

The commutator is directly related to the momentum p_μ,

$$[H_{\mathrm{KS}}, r_\mu] = -\frac{\hbar^2}{2m}\frac{\partial}{\partial r_\mu} = i\frac{\hbar}{m_e}p_\mu. \tag{2.44}$$

If an external electric field $\mathbf{E_0}$ is applied to a crystal, the field due to a macroscopic screened field ($\mathbf{E}$) is given as [101],

$$\mathbf{E} = \mathbf{E_0} - 4\pi\mathbf{P} \tag{2.45}$$

where $\mathbf{P}$ is the electronic polarization induced by the screened field $\mathbf{E}$. The perturbative potential arising from this screened electric field is given as $V^{macro}(\mathbf{r})$,

$$\Delta V^{macro}(\mathbf{r}) = e\mathbf{E}\cdot\mathbf{r} = e\sum_\mu E_\mu r_\mu \tag{2.46}$$

The response of the electronic density to the net screened field in the solid, $\mathbf{E}$, is given by $\Delta^{\mathbf{E}} n(\mathbf{r})$, which can be written as:

$$\Delta^{\mathbf{E}} n(\mathbf{r}) = 4\sum_{\alpha=1}^{N/2} \psi_\alpha^*(\mathbf{r})\Delta^{\mathbf{E}}\psi_\alpha(\mathbf{r}), \tag{2.47}$$

where $\Delta^{\mathbf{E}}\psi_\alpha(\mathbf{r})$ is the response of the wavefunction to the electric field, and is given as,

$$\begin{aligned} \Delta^{\mathbf{E}}\psi_\alpha(\mathbf{r}) &= \sum_{\beta\neq\alpha} \psi_\beta(\mathbf{r}) \frac{\langle \psi_\beta \left| V_{\mathbf{E}}(\mathbf{r}) \right| \psi_\alpha \rangle}{\epsilon_\alpha - \epsilon_\beta} \qquad (2.48) \\ &= e\sum_\mu E_\mu \sum_{\beta\neq\alpha} \psi_\beta(\mathbf{r}) \frac{\langle \psi_\beta \left| r_\mu \right| \psi_\alpha \rangle}{\epsilon_\alpha - \epsilon_\beta}. \qquad (2.49) \end{aligned}$$

This change in the electronic charge density in turn leads to local electric fields, the effect of which needs to be taken into account in the self-consistent solution procedure. The change in the potential energy due to these local fields is given by $V^{micro}(\mathbf{r})$:

$$\Delta V^{micro}(\mathbf{r}) = e^2 \int \frac{\Delta n^{\mathbf{E}}(\mathbf{r}')}{|\mathbf{r}-\mathbf{r}'|} d\mathbf{r}' + \left.\frac{dv_{xc}(n)}{dn}\right|_{n=n(\mathbf{r})} \Delta n^{\mathbf{E}}(\mathbf{r}), \tag{2.50}$$

The net perturbative potential is thus given as,

$$\Delta V^{\mathbf{E}}_{\mathrm{KS}}(\mathbf{r}) = \Delta V^{macro}(\mathbf{r}) + \Delta V^{micro}(\mathbf{r}) \tag{2.51}$$

$$= e\sum_{\mu} E_\mu r_\mu + e^2 \int \frac{\Delta n^{\mathbf{E}}(\mathbf{r}')}{|\mathbf{r}-\mathbf{r}'|} d\mathbf{r}' + \left.\frac{dV_{xc}(n)}{dn}\right|_{n=n(\mathbf{r})} \Delta n^{\mathbf{E}}(\mathbf{r}). \tag{2.52}$$

Thus the Sternheimer equation is given as:

$$(H_{\mathrm{KS}} - \epsilon_\alpha)\,|\Delta\psi^{\mathbf{E}}_\alpha\rangle = -e\sum_{\mu} E_\mu r_\mu |\bar{\psi}^{\mu}_\alpha\rangle - \hat{P}_c \Delta V^{micro}|\psi_\alpha\rangle, \tag{2.53}$$

where we have introduced $|\bar{\psi}^{\mu}_\alpha\rangle = \hat{P}_c r_\mu |\psi_\alpha\rangle$.

Now the macroscopic polarization can be calculated,

$$P_\mu = -\frac{e}{\Omega}\int r_\mu \Delta^{\mathbf{E}} n(\mathbf{r}) d\mathbf{r} \tag{2.54}$$

$$= -\frac{4e}{\Omega}\sum_{\alpha=1}^{N/2} \langle \bar{\psi}^{\mu}_\alpha | \Delta^{\mathbf{E}} \psi_\alpha \rangle, \tag{2.55}$$

where Ω is the volume of the system.

The set of equations (2.45), (2.47), (2.55), (2.50) and (2.53) form a self consistent set of equations that have to be solved for a given electric field $\mathbf{E_0}$. However it is computationally simpler to keep the value of the screened electric field $\mathbf{E}$ fixed and let only the microscopic components vary via Eqs. (2.47), (2.50), and (2.53). The macroscopic polarization is then calculated at the end once self consistency is achieved, using Eq. (2.55). Physically, this is equivalent to calculating the polarization response to a given screened electric field $\mathbf{E}$, instead of $\mathbf{E_0}$.

2.2.3 Phonon modes in crystalline solids

In perfect crystalline solids, the position of the I^{th} atom can be written as:

$$\mathbf{R}_I = \mathbf{R}_l + \boldsymbol{\tau}_s, \tag{2.56}$$

where $\mathbf{R}_l$ is the lattice vector of the l^{th} unit cell in the Bravais lattice and $\boldsymbol{\tau}_s$ is the equilibrium position of the s^{th} atom in the unit cell.

Crystal vibrations cause the atoms to deviate from their equilibrium positions. The displacement of the s^{th} atom in the l^{th} unit cell is $\mathbf{u}_s(l)$ and hence the position is:

$$\mathbf{R}_I = \mathbf{R}_l + \boldsymbol{\tau}_s + \mathbf{u}_s(l). \tag{2.57}$$

Normal modes of such vibrations in crystals are called phonons, and are classified by a wave-vector $\mathbf{q}$ and a mode index ν.

The Interatomic Force Constant (IFC) tensor is defined as:

$$C_{st}^{\alpha\beta}(l,m) \equiv \frac{\partial^2 E}{\partial u_s^\alpha(l)\partial u_t^\beta(m)} = C_{st}^{\alpha\beta}(\mathbf{R}_l - \mathbf{R}_m). \tag{2.58}$$

Because of translational invariance, the real-space IFCs depend on l and m only through the difference $\mathbf{R}_l - \mathbf{R}_m$. The derivatives are evaluated at $\mathbf{u}_s(l) = 0$ for all the atoms. The dynamical matrix, $\tilde{C}_{st}^{\alpha\beta}(\mathbf{q})$, is the Fourier transform of the real-space IFCs:

$$\tilde{C}_{st}^{\alpha\beta}(\mathbf{q}) = \sum_l e^{-i\mathbf{q}\cdot\mathbf{R}_l} C_{st}^{\alpha\beta}(\mathbf{R}_l) \tag{2.59}$$

$$= \frac{1}{N_c}\frac{\partial^2 E}{\partial u_s^{*\alpha}(\mathbf{q})\partial u_t^\beta(\mathbf{q})}, \tag{2.60}$$

where N_c is the number of unit cells in the crystal.

The phonon frequencies, $\omega(\mathbf{q})$, are the solutions of the secular equation:

$$\sum_{t,\beta}\left(\tilde{C}_{st}^{\alpha\beta}(\mathbf{q}) - M_s\omega^2(\mathbf{q})\delta_{st}\delta_{\alpha\beta}\right) u_t^\beta(\mathbf{q}) = 0, \tag{2.61}$$

where M_s is the atomic mass of the s^{th} atomic species.

The dynamical matrix can be decomposed into an electronic and an ionic contribution:

$$\tilde{C}_{st}^{\alpha\beta}(\mathbf{q}) = {}^{el}\tilde{C}_{st}^{\alpha\beta}(\mathbf{q}) + {}^{ion}\tilde{C}_{st}^{\alpha\beta}(\mathbf{q}), \tag{2.62}$$

where the electronic contribution is given as:

$$\begin{aligned} {}^{el}\tilde{C}_{st}^{\alpha\beta}(\mathbf{q}) &= \frac{1}{N_c}\Big[\int \left(\frac{\partial n(\mathbf{r})}{\partial u_s^{\alpha}(\mathbf{q})}\right)^* \frac{\partial V_{ion}(\mathbf{r})}{\partial u_t^{\beta}(\mathbf{q})} d\mathbf{r} \\ &+ \int n(\mathbf{r}) \frac{\partial^2 V_{ion}(\mathbf{r})}{\partial u_s^{*\alpha}(\mathbf{q}) \partial u_t^{\beta}(\mathbf{q})} d\mathbf{r}\Big]. \end{aligned} \tag{2.63}$$

The ionic contribution ${}^{ion}\tilde{C}_{st}^{\alpha\beta}(\mathbf{q})$ arises from the ion-ion interaction energy [the last term of Eq. (2.34)] and does not depend on the electronic structure. Its calculation involves taking the second order derivative of the Ewald term [35].

Now, the Born effective charge tensor of the s^{th} atomic species is the partial derivative of the macroscopic polarization with respect to a periodic displacement of all the atoms of s species at zero electric field [99]:

$$eZ^*_{s,\mu\nu} = \Omega \frac{\partial P_\mu}{\partial u_s^{\nu}(\mathbf{q}=0)}\bigg|_{E=0}. \tag{2.64}$$

2.2.4 Dielectric Constants

When an external electric field ($\mathbf{E}_0$) is applied, the electrons as well as the ions respond to it and result in a change in the polarization of the material. The screened electric field ($\mathbf{E}$) is a combined effect of this electronic as well as ionic screening. The dielectric constant of a material quantifies the change in the screened electric field in a material due to the application of an external electric field.

The dielectric constant of a material depends on the frequency of the external field. In the high frequency limit (frequency $\sim 10^{15}$ Hz), only the electrons can respond to the external field. Thus the high frequency dielectric constant (ϵ_∞) is basically the electronic contribution to the total dielectric constant. In the static case, the dielectric constant has contributions from both the electronic and ionic parts. This is known as the static dielectric constant (ϵ_0).

The electronic contribution to the dielectric constant tensor is defined as,

$$E_{0\mu} = (E_\mu + 4\pi P_\mu) = \sum_\nu \epsilon_\infty^{\mu\nu} E_\nu. \tag{2.65}$$

Using Eq. (2.55), we finally obtain the high frequency dielectric constant as [98],

$$\epsilon_\infty^{\mu\nu} \quad = \quad \delta_{\mu\nu} - \frac{16\pi e}{\Omega E_\nu} \sum_{\alpha=1}^{N/2} \langle \bar{\psi}_\alpha^\mu | \Delta^{\mathbf{E}_\nu} \psi_\alpha \rangle. \tag{2.66}$$

The static dielectric constant (ϵ_0) is the combined response of the electronic as well as the ionic part of the system to the applied electric field, and is given by [99]:

$$\epsilon_0^{\mu\nu} = \epsilon_\infty^{\mu\nu} + \frac{4\pi}{\Omega} \sum_m \frac{S_{m,\mu\nu}}{\omega_m^2}, \tag{2.67}$$

where

$$S_{m,\mu\nu} = \left(\sum_{s,\mu'} Z^*_{s,\mu\mu'} \frac{u^{\mu'}_{s,m}}{\sqrt{M_s}} \right) \left(\sum_{t,\nu'} Z^*_{t,\nu\nu'} \frac{u^{\nu'}_{t,m}}{\sqrt{M_t}} \right). \tag{2.68}$$

where $S_{m,\mu\nu}$ is the mode oscillator strength tensor, and is defined in terms of the Born effective charges Z^*, the atomic masses M_s and the normalized eigenvectors $u^\mu_{s,m}$ of the s^{th} atom or ion along a given direction μ for a particular mode m. ω_m is the phonon mode frequency at the zone center and Ω is the unit cell volume. μ, ν, μ' and ν', run over the three spatial directions. For the computation of ϵ_0, the knowledge of all the phonon frequencies at the zone center is required.

2.3 Electronic Transport

The flow of electrons that constitutes a current in a many-particle system is a result of an imbalance in the chemical potential of the electrons, that has been created either by an applied bias voltage or due to some other reason. In most macroscopic systems, the current-voltage characteristics follow the very well known Ohm's law. The resistance to the current arises from the microscopic mechanism of scattering of electrons due to phonons and random scatterers (impurities, defects, or grain boundaries) in these systems [102]. In nanosystems, the size of the system itself can be smaller than the mean free path between two scattering processes. As a result, Ohm's law is no longer expected to be valid. Many other factors can govern the flow of electrons in these nanosystems, like electronic structure and quantum confinement effects due to the small size of these nanosystems [103].

To understand the transport properties of electrons in such systems, one needs to solve the many-body problem in a non-equilibrium scenario. This is done by the Non Equilibrium Greens Function (NEGF) theory [104, 105]. In this section, we would like to describe very briefly the formalism of NEGF, with the point of view of its application to a two-terminal setup. The formalism of NEGF theory as developed by Keldysh is very rigorous [104] and has vast scope for application, ranging from transient flow [106, 107] to steady state flow, coherent as well as non-coherent regimes. However here, we will restrict ourselves to the description of steady state coherent transport.

2.3.1 Non Equilibrium Greens Function Technique (NEGF)

A typical two terminal transport consists a scattering center (SC) connected to two semi-infinite metallic leads on the left (L) and right (R) (see Fig. 2.2). The scattering center (SC) contains the molecule or the nanosystem across which the the electronic current of electrons is allowed to flow. For effective screening of the electrostatic potential between the nanosystem and the leads, a few layers of the metallic lead on either side can be included in the SC [83].

Let $\hat{H}_L$ and $\hat{H}_R$ be the Hamiltonians describing the semi-infinite leads L and R, respectively. The retarded Green's functions associated with these Hamiltonians are given by $\hat{G}_L^+(E)$ and $\hat{G}_R^+(E)$, respectively, and are defined as:

$$\hat{G}_L^+(E) = \left\{\epsilon^+ \hat{S}_L - \hat{H}_L\right\}^{-1}, \tag{2.69}$$

and

$$\hat{G}_R^+(E) = \left\{\epsilon^+ \hat{S}_R - \hat{H}_R\right\}^{-1}, \tag{2.70}$$

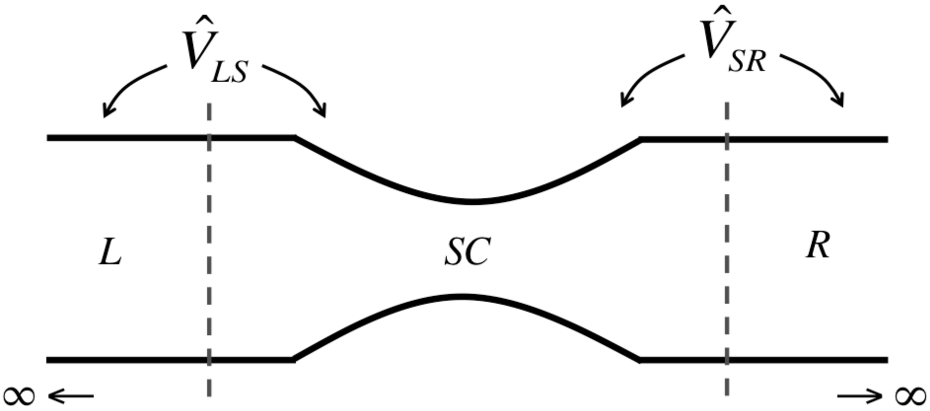

Figure 2.2: *A typical two terminal transport setup.*

where $\hat{S}$ is the overlap matrix, and $\epsilon^+ = E + \eta$, $\eta \to 0^+$. These Green's functions for the leads L and R, can be found by doing separate calculations for the left and right leads. The isolated SC is described by the Hamiltonian $\hat{H}_S$. We now want to determine $\hat{G}^+(E)$, the Green's function for the entire setup.

We can assume that the leads, L and R couple with the SC by some potentials $(\hat{V}_{LS} + \hat{V}_{LS}^\dagger)$ and $(\hat{V}_{SR} + \hat{V}_{SR}^\dagger)$, respectively. Schrödinger equations for the total system can be written as:

$$\begin{bmatrix} \epsilon^+\hat{S}_L - \hat{H}_L & \hat{V}_{LS} & 0 \\ \hat{V}_{LS}^\dagger & \epsilon^+\hat{S}_S - \hat{H}_S & \hat{V}_{SR}^\dagger \\ 0 & \hat{V}_{SR} & \epsilon^+\hat{S}_R - \hat{H}_R \end{bmatrix} \begin{bmatrix} |\phi_L\rangle \\ |\phi_S\rangle \\ |\phi_R\rangle \end{bmatrix} = 0, \tag{2.71}$$

where $|\phi_L\rangle$, $|\phi_S\rangle$, $|\phi_R\rangle$ are the wavefunctions associated with the three regions described above. We can now define the self-energy operators:

$$\hat{\Sigma}_L^+(E) \equiv \hat{V}_{LS}^\dagger \hat{G}_L^+(E) \hat{V}_{LS}, \tag{2.72}$$

and

$$\hat{\Sigma}_R^+(E) \equiv \hat{V}_{SR}^\dagger \hat{G}_R^+(E) \hat{V}_{SR}. \tag{2.73}$$

In terms of these self energy operators, we get,

$$\left[\epsilon^+ \hat{S}_S - \hat{H}_S - \hat{\Sigma}^+_L(E) - \hat{\Sigma}^+_R(E)\right] |\phi_S\rangle = 0. \tag{2.74}$$

Thus $\hat{G}^+(E)$, the Green's function for the entire setup, is given as:

$$\hat{G}^+(E) = \left\{\epsilon^+ \hat{S}_S - \hat{H}_S - \hat{\Sigma}^+_L(E) - \hat{\Sigma}^+_R(E)\right\}^{-1}. \tag{2.75}$$

In the absence of any coupling with the leads, the energy eigenvalues of the isolated SC are the poles of Eq. (2.75) without the self energy terms. Note that the self energy operators are non-Hermitian. We can then define the quantities called the Broadening matrices,

$$\hat{\Gamma}_{L,R}(E) = -2 \text{ Im}\left\{\hat{\Sigma}^+_{L,R}(E)\right\} = i\left[\hat{\Sigma}^+_{L,R}(E) - \hat{\Sigma}^+_{L,R}(E)^\dagger\right]. \tag{2.76}$$

The Green's function $\hat{G}^+(E)$ thus becomes:

$$\hat{G}^+(E) = \left\{\epsilon^+ \hat{S}_S - \hat{H}_S - \text{Re}\left[\hat{\Sigma}^+_L(E) + \hat{\Sigma}^+_R(E)\right] - i\left[\hat{\Gamma}_L(E) + \hat{\Gamma}_R(E)\right]\right\}^{-1}. \tag{2.77}$$

The effect of the coupling with the leads is to "renormalize" (shift in energy) the discrete energy levels of the isolated SC, as well as broaden them. The shift is given by $\text{Re}\left[\hat{\Sigma}^+_L(E) + \hat{\Sigma}^+_R(E)\right]$ and the broadening is given by $\left(\hat{\Gamma}_L(E) + \hat{\Gamma}_R(E)\right)$. The broadening of these states gives a finite lifetime to these states, $\tau = 2\hbar/\left(\hat{\Gamma}_L(E) + \hat{\Gamma}_R(E)\right)$.

The equilibrium density of states is given by $\hat{D}(E) = \frac{i}{2\pi} \lim_{\eta \to 0^+} \left[\hat{G}^+(E) - \hat{G}^+(E)^\dagger\right]$. Thus the total equilibrium density is given by,

$$n_{eq} = \int dE\ \hat{D}(E) f(E-\mu) = -\frac{1}{\pi}\int dE\ \text{Im}\{\hat{G}^+(E)\} f(E-\mu), \tag{2.78}$$

where $f(E-\mu)$ is the Fermi-Dirac distribution function, defined as

$$f(E-\mu) = \frac{1}{1 + e^{(E-\mu)/k_B T}},$$

where k_B is the Boltzmann constant, $\mu_L = \mu_R = \mu$, is the chemical potential of the leads

L and R, and T is the temperature. At $T = 0$, the Fermi-Dirac distribution is simply,

$$\begin{aligned} f(E-\mu) &= 1 \qquad\qquad E < \mu & (2.79) \\ &= 0 \qquad\qquad E > \mu. & (2.80) \end{aligned}$$

Application of an external bias voltage

The leads L and R are treated as reservoirs of electrons, each with a chemical potential μ_L and μ_R, respectively. The effect of an applied bias voltage V is to change the chemical potential of one of the leads with respect to the other, i.e., to produce a rigid shift in the energy spectra of the leads. In the presence of this external bias, the electronic density of the SC changes, which in turn changes the potential in the SC. Thus the effect of the bias needs to be taken into account self-consistently. The Hamiltonian of the SC depends on the non-equilibrium density $\hat{H}_S = \hat{H}_S[n]$. The Hamiltonian of the total system then takes the form,

$$H = \begin{bmatrix} \hat{H}_L + \hat{S}_L eV/2 & \hat{V}_{LS} + \hat{S}_{LS} eV/2 & 0 \\ \hat{V}_{LS}^\dagger + \hat{S}_{LS}^\dagger eV/2 & \hat{H}_S & \hat{V}_{SR}^\dagger - \hat{S}_{LS}^\dagger eV/2 \\ 0 & \hat{V}_{SR} - \hat{S}_{SR} eV/2 & \hat{H}_R - \hat{S}_R eV/2 \end{bmatrix}. \tag{2.81}$$

In the presence of the bias, the non-equilibrium charge density is given by,

$$n = \frac{1}{2\pi} \int dE \; \hat{G}^+(E) \Big\{ \hat{\Gamma}_L f(E-\mu_L) + \hat{\Gamma}_R f(E-\mu_R) \Big\} \hat{G}^+(E)^\dagger, \tag{2.82}$$

where $\mu_{L,R} = \mu \pm eV/2$ and $\hat{\Gamma}_{L,R} = \hat{\Gamma}_{L,R}(E \mp eV/2)$. $\hat{G}^+(E)$ is given by Eq. (2.75), where we have put $\hat{\Sigma}^+_{L,R} = \hat{\Sigma}^+_{L,R}(E \mp eV/2)$.

Note that this integration in Eqn 2.82 is difficult, as the integral is unbounded from below. However, the equation can be simplified drastically if we write, $n = n_{eq} + n_V$:

$$n_{eq} = -\frac{1}{\pi} \int dE \; \mathrm{Im}\{\hat{G}^+(E)\} f(E-\mu_L), \tag{2.83}$$

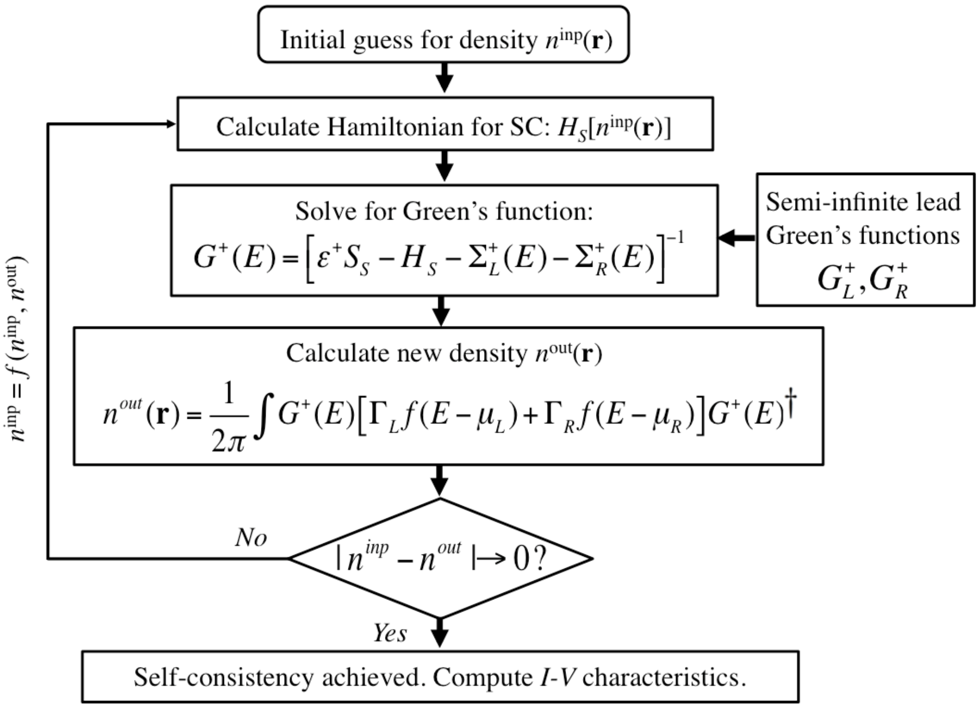

Figure 2.3: *Flow chart showing the self-consistency loop for the iterative solution of the NEGF formalism.*

and

$$n_V = \frac{1}{2\pi}\int dE\ \hat{G}^+(E)\hat{\Gamma}_R\hat{G}^+(E)^\dagger\Big[f(E-\mu_R) - f(E-\mu_L)\Big]. \tag{2.84}$$

n_{eq} can be thought of as the equilibrium density, with both the reservoirs at the same chemical potential μ_L, whereas n_V is the density arising due to the non-equilibrium conditions. It is computationally easy to evaluate n_V, as it is bounded on both sides by the two Fermi-Dirac functions. Though n_{eq} is unbounded, it is possible to evaluate it using a contour integral technique because of the analytical behavior of $\hat{G}^+(E)$.

The self-consistent procedure is demonstrated by a flowchart in Fig. 2.3. First a trial density n^{inp} is used to compute H. Then using Eqns. (2.76) and (2.75), the broadening matrices $\hat{\Gamma}_L$, $\hat{\Gamma}_R$ and $\hat{G}^+(E)$ are obtained. These quantities are then used to evaluate a new estimate for n using Eq. (2.82). This process is iterated until the difference between the density of two consecutive steps is less than a pre-defined tolerance value, and self-consistency is achieved.

Once self-consistency is achieved, one can calculate the current I, given as:

$$I = \frac{e}{h} \int dE \; T(E,V) \Big[f(E-\mu_R) - f(E-\mu_L) \Big], \tag{2.85}$$

where $T(E,V)$ is the transmission coefficient, which can be calculated using the Green's functions, given by the relation:

$$T(E,V) = \mathrm{Tr}\{\hat{\Gamma}_L \hat{G}^+(E)^\dagger \hat{\Gamma}_R \hat{G}^+(E)\}. \tag{2.86}$$

This is known as the Landauer formula for the current [108]. Note here that the current is given for each spin channel. In case of a non-spin polarized calculation, a factor of two is to be multiplied.

2.4 Codes Used

In this thesis, most of the calculations are done using the PWscf package of the Quantum-ESPRESSO distribution [78]. For electronic transport calculations, we have used the SMEAGOL code [30, 83], that interfaces the non-equilibrium Green's function scheme with the DFT implementation in the SIESTA code [82].

Chapter 3

Dielectric properties of crystalline SiGeN and SiCN materials

Now, we want to apply the theoretical techniques described in the previous chapter to various nanomaterials, with the aim of understanding and then favorably tuning the properties which are best suited for applications. To start with, we look at how the electronic and dielectric properties of silicon nitride can be changed by the progressive substitution of silicon atoms with either germanium or carbon atoms. This chapter is an example of how varying the chemical composition can be used to tune the dielectric properties of these materials.

Some of the results presented in this chapter have been published in Ref. [109].

3.1 Introduction

The remarkable mechanical strength, thermal stability and electronic properties of silicon nitride have resulted in its widespread application in a wide variety of fields, such as microelectronics, cutting tools [38], optoelectronic devices [39, 40], and microelectromechanical systems (MEMS) [41]. Ternary silicon nitride-based materials possess some attractive properties for such applications, and the advantage in such materials is that these properties can be tuned through variations in the chemical composition. For instance, the mechanical (e.g., bulk modulus) and electronic properties (e.g., band gap, leakage behavior) of silicon carbon nitride (SiCN) materials are dependent on the chemical composition of the film [110, 111] and the band gap of silicon germanium nitride (SiGeN) is dependent on the Si:Ge ratio [17]. This ability to tune physical properties through changes in chemical composition widens the scope of application of these materials. Hence, a systematic study of the variation of dielectric properties with chemical composition becomes important from a technological point of view [112].

Here we investigate the structural and dielectric properties of crystalline SiGeN and SiCN with different Si:Ge and Si:C ratios, respectively, using first principles density functional theory (DFT) calculations. Silicon nitride, SiCN, and SiGeN are used in a broad range of applications in the microelectronics industry, due to their insulating dielectric properties: silicon nitride is used as a gate dielectric and spacer material [113], SiCN as a low-k etch stop layer [114] and Cu diffusion barrier [115] in the back end of the line technology, and crystalline germanium nitride (Ge_3N_4) is a promising candidate for a passivation layer and gate dielectric for Ge-channel field effect transistor devices [116,117]. As a first step towards designing SiGeN and SiCN materials with desired dielectric properties, we wish to gain a deeper understanding of the relation between dielectric properties and chemical composition.

In general, these nitrides find applications in both crystalline and amorphous phases. However, the dielectric properties of an amorphous materials can be influenced by other factors, such as bonding structure and mass density/porosity, in addition to chemical composition. A comprehensive study of the dielectric properties of amorphous systems accounting for all these factors is computationally rather expensive. Thus, as a first step, we focus on the dielectric properties of bulk crystalline SiGeN and SiCN materials. Our aim here is to get a systematic understanding of the impact of chemical composition on the structural and dielectric properties of SiCN and SiGeN materials. There have been previous first principles studies on the dielectric properties of Si_3N_4: crystalline, amorphous as well as thin films [118, 119], but we are not aware of any *ab initio* study on the impact of germanium (carbon) concentration on the dielectric properties of crystalline

SiGeN (SiCN) materials.

3.2 Computational Details

The DFT calculations presented in this chapter were carried out using the PWscf package of the Quantum-ESPRESSO distribution [78], which uses a plane-wave basis set. The interaction between the ion cores and the valence electrons was treated using ultrasoft pseudopotentials. A plane-wave cutoff of 40 Ry for the wavefunctions, and 400 Ry for the charge densities, was found to be sufficient for the convergence of total energy, stress and forces. In this chapter, we have used the variable-cell optimization method to relax the cell parameters and atomic positions, until the forces on each atom are less than 0.5 mRy/bohr, and the pressure on the supercell is less than 0.05 GPa. We have used the local density approximation (LDA) for the exchange-correlation functional.

In our study, we consider (1) a $1\times1\times2$ supercell of the β-phase and (2) a primitive unit cell of the α-phase, for both SiGeN and SiCN materials, at each concentration ξ. Both these unit cells contain 28 atoms and are of similar dimensions. For this unit cell size, a $4\times4\times6$ **k**-point grid was found to be sufficient for accurate calculation of structural and dielectric properties.

We have used the density functional perturbation theory (DFPT) approach to determine the dielectric constant tensors as a linear response to the perturbative electric field [98,99]. As described in detail in the previous chapter, the response of the electronic charge density to the perturbative electric field is used to determine the electronic contribution to the dielectric tensor, the high-frequency dielectric constant tensor ($\epsilon_\infty^{\mu\nu}$), as given by Eq. 2.66. The static dielectric constant tensor ($\epsilon_0^{\mu\nu}$) is the total response of the electronic as well as the ionic part of the system to the applied electric field, and is given by:

$$\epsilon_0^{\mu\nu} = \epsilon_\infty^{\mu\nu} + \frac{4\pi}{\Omega}\sum_m \frac{S_{m,\mu\nu}}{\omega_m^2}, \tag{3.1}$$

where

$$S_{m,\mu\nu} = \left(\sum_{i,\mu'} Z^*_{i,\mu\mu'}\frac{u_{i,m\mu'}}{\sqrt{M_i}}\right)\left(\sum_{j,\nu'} Z^*_{j,\nu\nu'}\frac{u_{j,m\nu'}}{\sqrt{M_j}}\right). \tag{3.2}$$

Here $S_{m,\mu\nu}$ is the mode oscillator strength tensor [99] and is defined in terms of the Born effective charges Z^*, the atomic masses M_i and the normalized eigenvectors $u_{i,m\mu}$ of the i^{th} ion along a given direction μ for a particular mode m. ω_m is the phonon mode frequency at the zone center and Ω is the unit cell volume. μ, ν, μ' and ν', run over the three spatial directions. Thus for the computation of ϵ_0, the knowledge of all the phonon frequencies at the zone center is required, which then requires the solution of the dynamical matrix at the zone center. In our calculations, the phonon frequencies and the normalized eigenmodes were determined using DFPT calculations. The methodology for the calculation of phonon modes has described in the previous chapter in Section 2.2.4.

3.3 Results and Discussion

In this section we focus on our results for the dielectric properties of SiGeN and SiCN materials. We first look at the structural and electronic properties of pure Si_3N_4, Ge_3N_4, and C_3N_4. We then try to understand the effect of systematic substitution of Si atoms by Ge on the dielectric constant as one goes from Si_3N_4 to Ge_3N_4. We discuss the trends observed in the dielectric properties of SiGeN materials with Ge incorporation in Sub-section 3.3.2. Similarly, we look at the effect of systematic substitution of Si atoms by C atoms on the dielectric constant as one goes from Si_3N_4 to C_3N_4, in Sub-section 3.3.3.

3.3.1 Pure Phases: Si_3N_4, Ge_3N_4, and C_3N_4.

Silicon nitride exists in three crystalline phases: α, β and γ, of which the β-phase is the most stable one at room temperature [120, 121]. Germanium nitride exists in at least five different phases: α, β, γ, pseudo-cubic and graphitic, of which, again the β-phase is the most stable one [117, 122]. The prototypical β-structure has a hexagonal unit cell of 14 atoms, i.e., two formula units of Si_3N_4/Ge_3N_4 stacked in an ABAB… fashion. The α-phase, which is a metastable phase, has a hexagonal unit cell with 28 atoms, i.e., four formula units of Si_3N_4/Ge_3N_4 stacked in an ABCDABCD… fashion. For our study, we consider (1) a 1 × 1 × 2 supercell of the β-phase and (2) a primitive unit cell of the α-phase, both of which contain 28 atoms and are of similar dimensions. Our results for

α-phase

Systems	Unit cell parameters				Volume	Band
	a (Å)	b (Å)	c (Å)	γ	Ω (Å^3)	Gap (eV)
Si_3N_4	7.719	7.719	5.594	120.0°	288.64	4.57
Ref. [110]	7.716	7.716	5.581	120.0°		
Ge_3N_4	8.183	8.183	5.915	120.0°	342.96	2.44
Ref. [130]	8.20	8.20	5.94	120.0°		
C_3N_4	6.433	6.433	4.684	120.0°	167.85	3.72
Ref. [110]	6.487	6.487	4.719	120.0°		
Ref. [123]	6.467	6.467	4.710	120.0°		

β-phase

Systems	Unit cell parameters				Volume	Band
	a (Å)	b (Å)	c (Å)	γ	Ω (Å^3)	Gap (eV)
Si_3N_4	7.572	7.572	5.781	120.0°	287.07	4.22
Ref. [124]	7.570	7.570	5.784	120.0°		
Ref. [127]	7.557	7.557	5.770	120.0°		
Ref. [128]	7.65	7.65	5.68	120.0°		
Ref. [129]	7.607	7.607	5.822	120.0°		
Ge_3N_4	8.008	8.008	6.130	120.0°	340.42	2.34
Ref. [131]	8.03	8.03	6.16	120.0°		
C_3N_4	6.373	6.373	4.785	120.0°	168.33	3.10
Ref. [123]	6.402	6.402	4.808	120.0°		
Ref. [128]	6.43	6.43	4.78	120.0°		
Ref. [134]	6.44	6.44				

Table 3.1: *Optimized structural parameters and band gap (eV) at zero pressure for α- and β-phases of Si_3N_4, Ge_3N_4 and C_3N_4. Our results are compared with those from the literature, where available.*

the structural properties of the pure silicon and germanium nitride crystals (shown in Table 3.1) compare well with results from earlier first principles calculations [117, 122–125, 127, 128] and experiments [129–131]. The computed band gaps, 4.22 eV for β-Si_3N_4, and 4.57 for α-Si_3N_4, compare fairly well with experimental values, $4.6 - 5.5$ eV for β-Si_3N_4, and 5.0 eV for the α-Si_3N_4 phase [132]. For germanium nitride, the band gaps of 2.34 eV for β-Ge_3N_4, and 2.44 for α-Ge_3N_4, are considerably underestimated. The difference between computed and experimental values is expected due to the well-known band gap underestimation issue in DFT.

The crystal structure of C_3N_4 has been the focus of many articles [42, 134], owing to the reported super-hard properties of C_3N_4 materials that arise due to the strong covalent

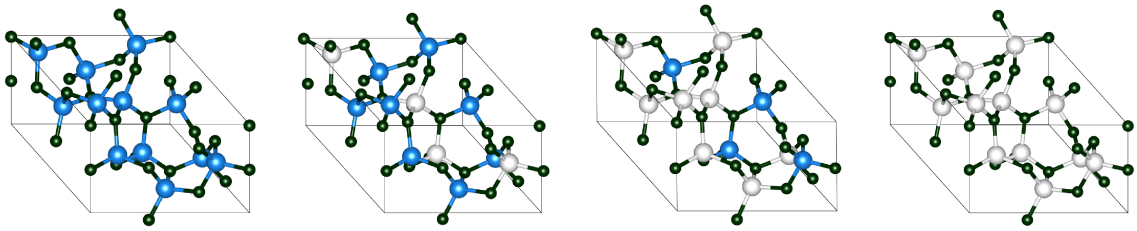

(a) α-Si_3N_4 (b) α-Si_2GeN_4 (c) α-$SiGe_2N_4$ (d) α-Ge_3N_4

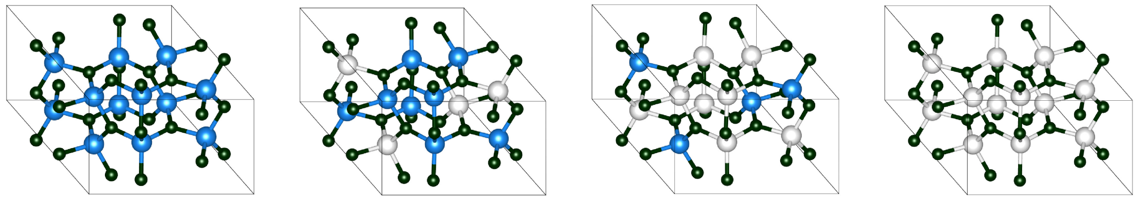

(e) β-Si_3N_4 (f) β-Si_2GeN_4 (g) β-$SiGe_2N_4$ (h) β-Ge_3N_4

Figure 3.1: *Optimized structures of* α-$Si_{3-\xi}Ge_{\xi}N_4$ *(top row) and* β-$Si_{3-\xi}Ge_{\xi}N_4$ *(bottom row) for different values of* ξ*. The* 28*-atom unit cell shown here correspond to the lowest energy configuration at each value of* ξ*. Silicon atoms are shown as large blue spheres, germanium as large white spheres and nitrogen as small green spheres. This figure has been published in Ref. [109].*

C-N bonds. The β-C_3N_4 structure has been reported earlier [42, 134] by DFT studies, as a possible super-hard material with a bulk modulus larger than that of diamond. Here we have considered both α- and β-phases for the C_3N_4 structures, similar to silicon and germanium nitride phases. We find that the α-phase is energetically the more stable phase. Similar to earlier studies, the β-C_3N_4 we get from our calculations has a structure very similar to that of β-Si_3N_4, with an average C-N bond-distance of 1.45 Å. There are, however, no experimental reports of crystalline C_3N_4 structures.

In Table 3.2 and Table 3.3, we have compared our results for phonon mode frequencies of β-Si_3N_4 and β-Ge_3N_4, with the experimental and theoretical results available in the literature. Our results are in good agreement with earlier results.

3.3.2 SiGeN Materials

We model $Si_{3-\xi}Ge_{\xi}N_4$ by substituting Si atoms in the Si_3N_4 matrix with Ge atoms. The valence shells of silicon and germanium are similar, and therefore this substitution is chemically justified. In both α- and β-phases for $Si_{3-\xi}Ge_{\xi}N_4$, we consider structures with four different germanium concentrations ($\xi = 0, 1, 2, 3$). The configurations in which all silicon

β-Ge_3N_4

	Theory	
Mode	Ref. [125]	Our Results
Raman		
A_g	108	107
E_{2g}	106	111
E_{1g}	129	128
E_{2g}	275	278
A_g	309	317
E_{2g}	373	376
A_g	443	437
E_{1g}	721	748
A_g	781	803
E_{2g}	791	815
E_{2g}	878	897
Infrared		
A_u	247	223
E_{1u}	271	271
E_{1u}	339	335
A_u	703	730
E_{1u}	739	765
E_{1u}	878	900
Other		
B_u	137, 306, 365, 896	147, 311, 375, 912
B_g	172, 254, 753	167, 231, 777
E_{2u}	169, 735	167, 761

Table 3.3: *Computed phonon frequencies (cm^{-1}) compared with previous calculations for β-Ge_3N_4.*

β-Si_3N_4

	Experiment		Theory	
Mode	Ref. [126]	Ref. [127]	Ref. [124]	Our Results
Raman				
E_{2g}	186	181	176	177
A_g	210	200	196	198
E_{1g}	229	225	218	220
E_{2g}	451	444	435	440
A_g	–	456	453	454
E_{2g}	619	610	608	612
A_g	732	725	717	723
E_{1g}	865	859	854	867
E_{2g}	928	921 917	928	
A_g	939	930 926	938	
E_{2g}	1047	1067	1030	1037
Infrared				
A_u	380	378	354	360
E_{1u}	447	424	414	419
E_{1u}	580	562	554	560
A_u	910	848	843	857
E_{1u}	985	886	882	896
E_{1u}	1040	1021	1017	1025
Other				
B_u				243, 548, 647, 1056
B_g	-	-	-	263, 398, 886
E_{2u}				298, 871

Table 3.2: *Computed phonon frequencies (cm^{-1}) compared with experimental results and previous calculations for β-Si_3N_4.*

atoms are substituted by germanium atoms correspond to the structure of Ge_3N_4. Many structural configurations for intermediate concentrations corresponding to Si_2GeN_4 and $SiGe_2N_4$ are possible; we have considered a few symmetrically non-equivalent configurations for dielectric constant calculations. Fig. 3.1 shows the lowest energy configurations for each germanium concentration. The structural properties for SiGeN materials at various germanium concentrations are given in Table 3.4. Due to the larger size of germanium compared to that of silicon, we find that the lattice constants for $Si_{3-\xi}Ge_{\xi}N_4$ increase linearly with increasing germanium concentration. This is in accordance with Vegard's law [135]. The structure deviates only marginally from its hexagonal symmetry for intermediate Ge concentrations ($\xi = 1, 2$). For all intermediate Ge concentrations, the β-phase is more stable than the α-phase. This is not an unexpected result, as in the pure phase, the β-phase is favored over the α-phase for both Si_3N_4 and Ge_3N_4. The β phase is lower in energy than the corresponding α phase by 32.8 meV per formula unit, 29.7 meV per formula unit and 2 meV per formula unit, for ξ= 1, 2, and 3, respectively. For ξ=1, the spread in the total energy between different configurations is 53 meV per formula unit for the α phase, and 16 meV per formula unit for the β phase. For ξ=2, the spread in the total energy is 2.7 meV per formula unit for the α phase, and 13 meV per formula unit for the β phase.

The dielectric constants of α- and β-$Si_{3-\xi}Ge_{\xi}N_4$ from our calculations are listed in Table 3.5. For each configuration, ϵ_∞ and ϵ_0 are calculated by averaging over the three diagonal components of the respective dielectric tensors. For a particular concentration ξ in a particular phase, the dielectric constants are calculated by a Boltzmann weighted average (corresponding to room temperature) over all considered configurations. The high-frequency dielectric constant (ϵ_∞) for β-Si_3N_4 is found to be 4.25, in good agreement with earlier DFPT studies [124,127,136] and experiments [137]. For calculating the static dielectric constant ϵ_0, we need to compute all the phonon frequencies at the zone center. As a benchmark, we have compared the zone center phonon modes for β-Si_3N_4 with experiments and earlier studies (See Table 3.2), and find that our results for the zone center phonon frequencies are in good agreement with both experiments [126], as well as

Systems: α-$Si_{3-\xi}Ge_{\xi}N_4$

System (ξ)	Unit cell parameters				Volume	Band
	a (Å)	b (Å)	c (Å)	γ	Ω (Å^3)	Gap (eV)
Si_3N_4 (0)	7.719	7.719	5.594	120.0°	288.64	4.57
Si_2GeN_4 (1)	7.880	7.880	5.690	120.1°	305.70	3.95
$SiGe_2N_4$ (2)	8.029	8.024	5.807	120.1°	323.66	3.20
Ge_3N_4 (3)	8.183	8.183	5.915	120.0°	342.96	2.44

Systems: β-$Si_{3-\xi}Ge_{\xi}N_4$

System (ξ)	Unit cell parameters				Volume	Band
	a (Å)	b (Å)	c (Å)	γ	Ω (Å^3)	Gap (eV)
Si_3N_4 (0)	7.572	7.572	5.781	120.0°	287.07	4.22
Si_2GeN_4 (1)	7.726	7.708	5.892	120.03°	303.78	3.76
$SiGe_2N_4$ (2)	7.833	7.882	6.008	119.95°	321.46	3.13
Ge_3N_4 (3)	8.008	8.008	6.130	120.0°	340.42	2.34

Table 3.4: *Optimized structural parameters and band gap (eV) at zero pressure for* α-$Si_{3-\xi}Ge_{\xi}N_4$ *and* β-$Si_{3-\xi}Ge_{\xi}N_4$. *For simplicity, results are presented for only the lowest energy configurations at each value of* ξ. *Our results are compared with those from the literature, where available.*

theoretical results [124, 127]. The static dielectric constant ϵ_0 for β-Si_3N_4 is found to be 7.70.

Our zone center phonon frequencies for β-Ge_3N_4 (shown in Table 3.3), also compare well with earlier studies [125]. We find ϵ_∞ and ϵ_0 for β-Ge_3N_4 to be 5.05 and 9.72, and for α-Ge_3N_4 to be 5.05 and 9.76, respectively. These values are in excellent agreement with previously reported experimental values of $9.5-9.7$ for Ge_3N_4 [138–140]. No imaginary phonon frequencies are found for any of the considered configurations. The static dielectric constants (ϵ_0) presented in our study here include the vibrational contribution. Our results are therefore in better agreement with the experimental results than previously reported first principles results [117].

Our results for the variation of dielectric constants ϵ_∞ and ϵ_0 with germanium concentration are shown in Fig. 3.2. As the Ge concentration increases, the high-frequency dielectric constant ϵ_∞ increases almost linearly: ϵ_∞ of Ge_3N_4 is $18-19\%$ higher than the corresponding value for Si_3N_4. This monotonic increase in the high-frequency dielectric constant correlates well with the decrease in the band gap of the systems on Ge incorporation. The static dielectric constant also increases fairly linearly with Ge concentration:

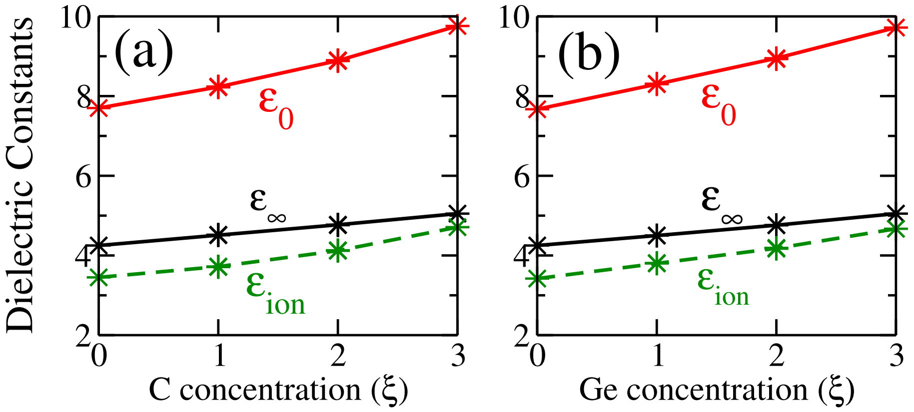

Figure 3.2: *Variation of static and high-frequency dielectric constants with germanium concentration for (a) α-$Si_{3-\xi}Ge_\xi N_4$ and (b) β-$Si_{3-\xi}Ge_\xi N_4$. Asterisk symbols show the dielectric constants for the various configurations considered at a particular germanium concentration ξ. Note that the values of dielectric constants for various configurations considered at a particular ξ are very close, and hence overlap in the plot. The ionic contribution to the dielectric constant is also shown. This figure has been published in Ref. [109].*

ϵ_0 of Ge_3N_4 is 26 – 27% higher than the corresponding value for Si_3N_4. The reason behind this increase in static dielectric constant is discussed in the following paragraphs.

The static dielectric constant contains contributions from both the electronic part ϵ_∞ and the ionic part ϵ_{ion}, given as $\epsilon_0 = \epsilon_\infty + \epsilon_{\text{ion}} = \epsilon_\infty + \frac{4\pi}{\Omega}\sum_m \frac{S_m}{\omega_m^2}$. Both ϵ_∞ and ϵ_{ion} increase monotonically, resulting in the increase in ϵ_0. As mentioned earlier, the ionic part of the dielectric constant ϵ_{ion} (see the fourth column of Table 3.5) is proportional to the Born effective charge (Z^*), and inversely proportional to the square of the phonon mode frequency ω^2 and the unit cell volume Ω. Thus it is essential to look at the Born effective charges and phonon modes of Si_3N_4 and Ge_3N_4 materials to identify the reason behind the observed increase in ϵ_{ion} values.

In β-Si_3N_4, the average values of Z^* over the silicon atoms are (3.33, 3.28, 3.38) in the (x, y, z) directions, respectively. The tetrahedral environment of Si results in this nearly isotropic behavior of Z^*. Each nitrogen atom finds itself at the center of a triangle formed by silicon atoms, which is clearly not an isotropic environment. The nitrogen atoms can be classified as N^{6h} (occupying the 6h Wyckoff site) and N^{2c} (2c Wyckoff site) species. The Z^* values for N^{6h} are (−1.61, −3.12, −2.78) and for N^{2c} are (−2.91, −2.91, −1.76) along the (x, y, z) directions respectively. In the case of β-Ge_3N_4, again the tetrahedrally co-ordinated germanium atoms have an average value of Z^* (3.37, 3.37, 3.36), whereas the

Systems: α-$Si_{3-\xi}Ge_{\xi}N_4$

System (ξ)	ϵ_0	ϵ_∞	ϵ_{ion}	ω_i (cm^{-1})
Si_3N_4 (0)	7.70	4.25	3.45	895.7(13%), 849.7^2(11%) 852.9^2(5%)
Si_2GeN_4 (1)	8.23	4.51	3.72	-
$SiGe_2N_4$ (2)	8.89	4.77	4.12	-
Ge_3N_4 (3)	9.76	5.05	4.71	730.6^2(10%), 738.7(10%) 305.5^2(6%), 290.1^2(4%)

Systems: β-$Si_{3-\xi}Ge_{\xi}N_4$

System (ξ)	ϵ_0	ϵ_∞	ϵ_{ion}	ω_i (cm^{-1})
Si_3N_4 (0)	7.67	4.25	3.42	856.7(25%), 895.7^2(19%) 418.9^2(9%)
Si_2GeN_4 (1)	8.30	4.50	3.80	-
$SiGe_2N_4$ (2)	8.95	4.76	4.18	-
Ge_3N_4 (3)	9.72	5.05	4.67	730.5(16%), 765.5^2(13%) 334.5^2(12%), 269.9^2(11%) 219.8(10%)

Table 3.5: *Static (ϵ_0) and high-frequency (ϵ_∞) dielectric constants of α- and β-$Si_{3-\xi}Ge_{\xi}N_4$ materials. ϵ_{ion} denotes the ionic contribution to ϵ_0. At each given value of ξ, these quantities are averaged over all the configurations considered in our study, as described in the text. The last column for Si_3N_4 and Ge_3N_4, shows a few phonon modes which contribute maximally to ϵ_{ion}. The percentage contributions are shown in parentheses and the superscript "2" denotes a doubly degenerate phonon mode.*

Z^* values for the trigonally coordinated nitrogen atoms N^{6h} and N^{2c} are (−1.54, −3.25, −2.84) and (−2.88, −2.89, −1.85), respectively. There is very little difference in the Born effective charges in the cases of Si_3N_4 and Ge_3N_4. Thus the covalency of the Si-N and Ge-N bonds, in the respective Si_3N_4 and Ge_3N_4 materials, seems to play a weak role in the increase of ϵ_{ion}. Thus we can conclude that the observed increase in ϵ_{ion} must arise predominantly from the difference in the phonon mode frequencies of the two materials.

The lowest three optical phonon modes frequencies for β-Si_3N_4 are 177 cm^{-1}, 177 cm^{-1} and 198 cm^{-1}, respectively, and the highest two frequencies are 1037 cm^{-1} and 1056 cm^{-1}. These values compare well with earlier reported values [127]. The lowest three optical phonon mode frequencies for β-Ge_3N_4 are 107 cm^{-1}, 111 cm^{-1} and 111 cm^{-1}, and the highest two frequencies are 900 cm^{-1} and 912 cm^{-1}, which are in good agreement with earlier vibrational studies [125]. An overall reduction in the phonon mode frequencies is observed as one goes from Si_3N_4 to Ge_3N_4. This reduction can be attributed to the larger mass of the germanium atoms. Next, we compute the individual contributions of the various phonon modes to the ionic part of the dielectric constant (see Fig. 3.3). The ionic part of the dielectric constant derives maximum contribution ($\geq$99.5%) from the infra-red (IR) active phonon modes. For β-Si_3N_4, the IR active modes are at 360 cm^{-1}, 419 cm^{-1}, 560 cm^{-1}, 857 cm^{-1}, 896 cm^{-1}, 1025 cm^{-1}, in agreement with earlier results [124, 127]. The IR active modes for β-Ge_3N_4, are at 220 cm^{-1}, 270 cm^{-1}, 334 cm^{-1}, 731 cm^{-1}, 766 cm^{-1}, 900 cm^{-1}, which compare well with earlier results [125]. The lower IR-active phonon mode frequencies of β-Ge_3N_4, compared to β-Si_3N_4, result in a higher ϵ_{ion} value for β-Ge_3N_4, despite a larger unit-cell volume.

In Fig. 3.3, we have shown the contribution of various phonon modes to the ionic part ϵ_{ion} for the cases of intermediate germanium concentrations, Si_2GeN_4 and $SiGe_2N_4$. The plots in Fig. 3.3 indicate that for a fixed value of ξ, the contributing phonon modes are quite close in energy for the various considered configurations. The following trend emerges from our results: the contributing phonon modes shift towards lower frequencies as the germanium concentration increases, for both α- and β-phases, resulting in the monotonic increase in ϵ_{ion} as one goes from Si_3N_4 to Ge_3N_4.

To summarize, the systematic reduction in the frequencies of the most contributing phonon modes, results in the monotonic increase in the ionic contribution to the dielectric constant (ϵ_{ion}) of SiGeN materials with increasing Ge concentration. The Born effective charges for silicon and germanium are nearly unchanged, and thus the covalency of Si-N and Ge-N bonds plays a rather weak role in the observed increase in ϵ_{ion}. The reduction in the phonon frequencies can be attributed to the larger atomic mass of germanium. The increase in ϵ_{ion} combined with the monotonic increase in ϵ_∞ leads to the observed trend in static dielectric constant of SiGeN materials. These results show that the dielectric properties of bulk crystalline SiGeN materials are strongly dependent on their chemical composition (Si:Ge ratio) and can hence be tuned through changes in chemical composition. With this result in mind, that ϵ_0 increases monotonically with germanium concentration from 7.69 for Si_3N_4 to 9.67 Si_3N_4, we next look at SiCN materials in which

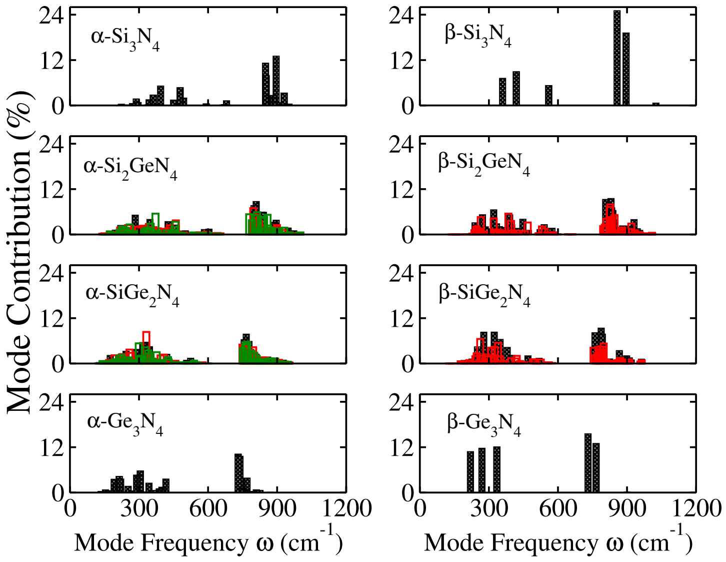

Figure 3.3: *Contribution of various phonon modes to the ionic part of the dielectric constant* (ϵ_{ion}) *of* α*-*$Si_{3-\xi}Ge_{\xi}N_4$ *and* β*-*$Si_{3-\xi}Ge_{\xi}N_4$*. For intermediate germanium concentrations,* Si_2GeN_4 *and* $SiGe_2N_4$*, the phonon mode contributions for the various considered configurations are shown in different colors. At a particular germanium concentration, the phonon mode contributions are very similar for the various configurations considered in our study. This figure has been published in Ref. [109].*

Si atoms are substituted with C atoms, to see whether ϵ_0 undergoes a monotonic reduction as one goes from Si_3N_4 ($\epsilon_0 = 7.70$) to C_3N_4 ($\epsilon_0 = 7.13$).

3.3.3 SiCN Materials

We now model $Si_{3-\xi}C_{\xi}N_4$ by substituting Si atoms in the Si_3N_4 matrix by C atoms. In addition to the similar valence shell configurations of Si and C, this model is supported by the experimental observation that the occurrence of Si-C bonds is very rare compared to Si-N and C-N bonds in SiCN materials [141,142]. As for $Si_{3-\xi}Ge_{\xi}N_4$, we consider $Si_{3-\xi}C_{\xi}N_4$ structures with four different carbon concentrations ($\xi = 0, 1, 2, 3$), in both α- and β-phases. The configurations in which all silicon atoms are substituted by carbon correspond to the theoretically reported (though not yet experimentally confirmed) structures of C_3N_4. Fig. 3.4 shows the lowest energy configurations for each C concentration. Table 3.6 shows the variation of structural properties with carbon concentration.

In general, the $Si_{3-\xi}C_{\xi}N_4$ lattice constant reduces with increasing carbon concentration, due to the smaller size of carbon compared to that of silicon. The structure also

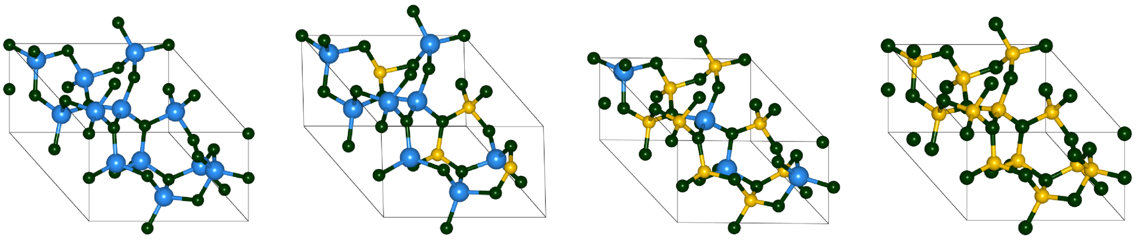

(a) α-Si_3N_4 (b) α-Si_2CN_4 (c) α-SiC_2N_4 (d) α-C_3N_4

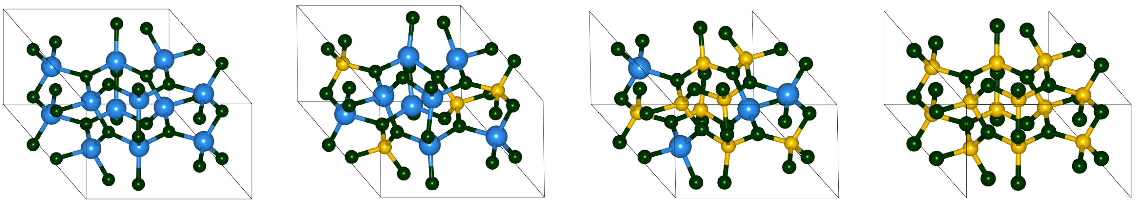

(e) β-Si_3N_4 (f) β-Si_2CN_4 (g) β-SiC_2N_4 (h) β-C_3N_4

Figure 3.4: *Optimized α-$Si_{3-\xi}C_\xi N_4$ (top row) and β-$Si_{3-\xi}C_\xi N_4$ (bottom row) structures for different values of ξ. The 28-atom unit cell shown here correspond to the lowest energy configuration at each value of ξ. Silicon atoms are shown as large blue spheres, carbon as small light yellow spheres and nitrogen as small green spheres. This figure has been published in Ref. [109].*

shows slight deviations from its hexagonal symmetry for intermediate C concentrations ($\xi = 1, 2$). We find that pristine β-Si_3N_4 is lower in energy than α-Si_3N_4 by 18.2 meV per formula unit of Si_3N_4, which compares well with earlier reported values [120]. However, as we introduce C in the structure, we find that the α-phase becomes progressively more stable than the β-phase. This observation is in accordance with earlier DFT studies [143] as well as with the experimental observation that the structure of SiCN crystalline thin films is better matched with the α-phase [142]. The energy of α-$Si_{3-\xi}C_\xi N_4$ is lower than the corresponding β-$Si_{3-\xi}C_\xi N_4$ by 48.7 meV per formula unit, 73.2 meV per formula unit and 236.1 meV per formula unit, for ξ= 1, 2, and 3, respectively. For ξ=1, the spread in the total energy is 128 meV per formula unit for the α phase, and 43 meV per formula unit for the β phase. For ξ=2, the spread in the total energy is 223 meV per formula unit for the α phase, and 179 meV per formula unit for the β phase.

The average dielectric constants of $Si_{3-\xi}C_\xi N_4$ from our calculations are listed in Table 3.7. We have shown our results for the variation of dielectric constants ϵ_∞ and ϵ_0 with carbon concentration in Fig. 3.5. We find that ϵ_∞ monotonically increases with carbon concentration: ϵ_∞ of C_3N_4 is 17-18% higher than the corresponding value for Si_3N_4. On

Systems: α-$Si_{3-\xi}C_{\xi}N_4$

System (ξ)	Unit cell parameters a (Å)	 b (Å)	 c (Å)	 γ	Volume Ω (Å^3)	Band Gap (eV)
Si_3N_4 (0)	7.719	7.719	5.594	120.0°	288.64	4.57
Si_2CN_4 (1)	7.328	7.214	5.336	119.9°	244.33	3.47
SiC_2N_4 (2)	6.949	6.949	4.965	121.1°	205.35	3.45
C_3N_4 (3)	6.433	6.433	4.684	120.0°	167.85	3.72

Systems: β-$Si_{3-\xi}C_{\xi}N_4$

System (ξ)	Unit cell parameters a (Å)	 b (Å)	 c (Å)	 γ	Volume Ω (Å^3)	Band Gap (eV)
Si_3N_4 (0)	7.572	7.572	5.781	120.0°	287.07	4.22
Si_2CN_4 (1)	7.035	7.217	5.502	119.6°	242.81	2.62
SiC_2N_4 (2)	6.745	6.842	5.175	120.8°	205.07	2.82
C_3N_4 (3)	6.373	6.373	4.785	120.0°	168.33	3.10

Table 3.6: *Optimized structural parameters and band gap (eV) at zero pressure for α-$Si_{3-\xi}C_{\xi}N_4$ and β-$Si_{3-\xi}C_{\xi}N_4$ materials. For simplicity, results are presented for only the lowest energy configurations at each value of ξ. Our results are compared with those from the literature, where available.*

the other hand, the static dielectric constant increases with carbon concentration up to $\xi = 2$, and then decreases markedly for C_3N_4 ($\xi = 3$). This non-monotonic behavior of ϵ_0 between the two end points Si_3N_4 and C_3N_4 is interesting, and, at first sight, rather surprising. We focus on the ionic contribution ϵ_{ion}, to understand this trend. The ionic part of the dielectric constant (see the fourth column of Table 3.7) is proportional to the Born effective charge (Z^*), and inversely proportional to the square of the phonon mode frequency ω^2 and the unit cell volume Ω (See Eqns. 3.1 and 3.2). We can define a cumulative oscillator strength tensor $\Delta^{\mu\nu}$, as: $\Delta^{\mu\nu} = \sum_m S_{m,\mu\nu}/\omega^2$, which contains the combined contributions of the Born effective charges and the phonon mode frequencies. The average oscillator strength, Δ, (column 5 of Table 3.7) can be calculated as one-third of the trace of $\Delta^{\mu\nu}$, for a particular configuration. Eq.(3.1) can be rewritten as

$$\epsilon_0 = \epsilon_\infty + \epsilon_{\text{ion}} = \epsilon_\infty + \frac{4\pi\Delta}{\Omega}. \tag{3.3}$$

For a particular ξ, the Δ and Ω values for the considered (symmetry non-equivalent) configurations are very close to each other. The individual values of Δ and Ω differ from

Systems: α-$Si_{3-\xi}C_{\xi}N_4$

System (ξ)	ϵ_0	ϵ_∞	$\epsilon_{\rm ion}$	Δ (Å^3)	Ω (Å^3)
Si_3N_4 (0)	7.70	4.25	3.45	79.24	288.64
Si_2CN_4 (1)	8.35	4.73	3.62	75.34	248.65
SiC_2N_4 (2)	9.29	5.01	4.28	68.33	205.96
C_3N_4 (3)	7.05	5.03	2.02	27.11	167.85

Systems: β-$Si_{3-\xi}C_{\xi}N_4$

System (ξ)	ϵ_0	ϵ_∞	$\epsilon_{\rm ion}$	Δ (Å^3)	Ω (Å^3)
Si_3N_4 (0)	7.67	4.25	3.42	78.13	287.07
Si_2CN_4 (1)	8.50	4.77	3.73	72.17	242.80
SiC_2N_4 (2)	8.56	4.98	3.58	59.86	205.36
C_3N_4 (3)	7.21	4.97	2.24	30.01	168.33

Table 3.7: *Static (ϵ_0) and high-frequency (ϵ_∞) dielectric constants of α- and β-$Si_{3-\xi}C_{\xi}N_4$ materials. $\epsilon_{\rm ion}$ denotes the ionic contribution to ϵ_0, Δ is the average oscillator strength. The last column shows the unit-cell volume Ω. For each value of ξ, the quantities are averaged over all the configurations considered in the study, as described in the text.*

the average by a maximum of 10 % and 3 %, respectively. It is easy to explain the observed trend using Eq.(3.3) and the Δ and Ω values in Table 3.7. In α-$Si_{3-\xi}C_{\xi}N_4$ structures, as one goes from Si_3N_4 to Si_2CN_4 (SiC_2N_4), the average oscillator strength reduces by only 6% (14%) whereas the unit-cell volume reduces by 14% (29%), thus leading to higher ϵ_{ion} values. This, combined with the increase in ϵ_∞ values with increasing ξ, leads to a higher static dielectric constant for the intermediate configurations, Si_2CN_4 and SiC_2N_4, compared to Si_3N_4. However, in the case of C_3N_4, there is a pronounced reduction in Δ: compared to Si_3N_4, Δ is lower by about 66%, but the unit-cell volume is smaller by only 42%, resulting in the smallest $\epsilon_{\rm ion}$ value among the four cases, and an ϵ_0 value lower than that of Si_3N_4. Similar reasoning explains the trend observed in β-$Si_{3-\xi}C_{\xi}N_4$ structures as well. We discuss the reason behind such a marked reduction in Δ in C_3N_4 further below.

In β-C_3N_4, the average values of Z^* are (2.41, 2.41, 1.99) for the carbon atoms, (−1.16, −2.18, −1.62) for N^{6h} and (−2.18, −2.18, −1.08) for N^{2c} along the (x, y, z) directions, respectively. These Born effective charges are considerably reduced as compared to those observed in the case of Si_3N_4. This might result from the very strong covalent character of the C-N bond, in carbon nitride. The phonon frequencies in the case of β-C_3N_4 are also hardened as compared to β-Si$_3$N$_4$: 194 cm^{-1}, 303 cm^{-1} and 303 cm^{-1}. This hardening of the phonon modes in combination with the decrease in the Born effective charges results in a big reduction of about 62% in Δ for β-C$_3$N$_4$. Similar factors result in the marked reduction of Δ by about 66% for α-C$_3$N$_4$.

Analyzing the results in this chapter, we can now comment on the general behavior of the dielectric constant of SiCN materials. Experimental studies have shown that amorphous SiCN films have a dielectric constant approximately 25% lower than silicon nitride [114]. However, there have not been any earlier studies on the reason behind this observed reduction. The dielectric constant of amorphous SiCN films may depend on many factors like: (i) chemical composition of the constituent elements, i.e., silicon, carbon, and nitrogen, (as seen in our study), (ii) degree of amorphization and specific structural details [119], (iii) density of the sample and (iv) strain as well as defects present in the experimental sample. A detailed analysis accounting for all these factors is therefore necessary for a better understanding of the dielectric behavior in amorphous SiCN films. Our results show that in bulk crystalline SiCN materials, even though the oscillator strength decreases with higher carbon concentration, the accompanied reduction in unit-cell volume leads to higher ϵ_0 for intermediate carbon concentrations, and hence results in a non-monotonic trend in ϵ_0, on going from Si$_3$N$_4$ to C$_3$N$_4$.

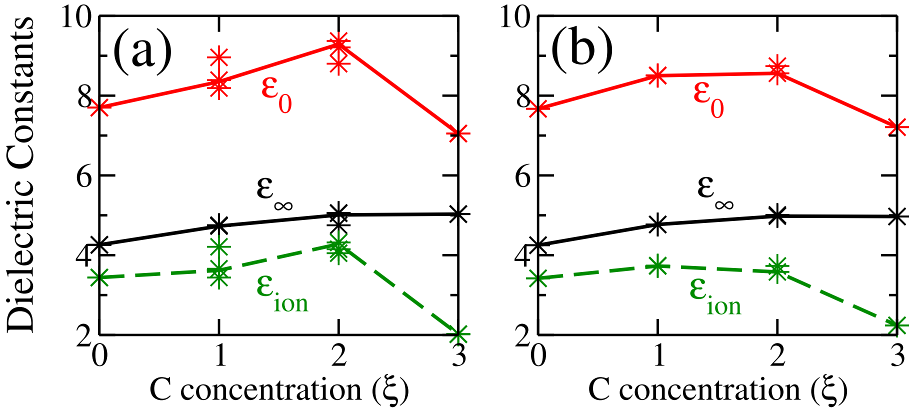

Figure 3.5: *Variation of static and high-frequency dielectric constants with carbon concentration for (a) α-Si$_{3-\xi}$C$_\xi$N$_4$ and (b) β-Si$_{3-\xi}$C$_\xi$N$_4$. Asterisk symbols show the dielectric constants for the various configurations considered at a particular carbon concentration ξ. The ionic contribution to the dielectric constant is also shown. This figure has been published in Ref. [109].*

3.4 Summary and Conclusions

To summarize our results, we have studied the effect of both germanium and carbon concentration on the high-frequency and static dielectric constants of the α- and β-phases of crystalline $Si_{3-\xi}Ge_{\xi}N_4$ and $Si_{3-\xi}C_{\xi}N_4$ materials, respectively. We find that both the high-frequency dielectric constant (ϵ_{∞}) and the static dielectric constant (ϵ_0) display a monotonic increase with germanium concentration, in $Si_{3-\xi}Ge_{\xi}N_4$ materials. The increase in the ionic part of the dielectric constant is due to the systematic lowering of the contributing phonon mode frequencies. We find chemical composition (Si:Ge ratio) has a strong effect on the dielectric properties of $Si_{3-\xi}Ge_{\xi}N_4$ materials, and hence $Si_{3-\xi}Ge_{\xi}N_4$ materials with desired dielectric constant values can be fabricated through appropriate changes in chemical composition. In $Si_{3-\xi}C_{\xi}N_4$ materials, the incorporation of carbon results in an energetic preference for the α-phase over the β-phase, which is in agreement with earlier studies. Regarding the dielectric constant, the high-frequency dielectric constant (ϵ_{∞}) displays a monotonic increase with carbon concentration. The static dielectric constant shows a rather complex trend: compared to Si_3N_4, ϵ_0 increases by $15 - 20$ % for intermediate carbon concentrations ($\xi = 1, 2$) but shows a marked reduction for C_3N_4. This trend is explained in terms of the relative changes in average oscillator strength (Δ) and unit-cell volume (Ω) with carbon concentration.

Chapter 4

Point Defects in Twisted Bilayer Graphene

In the previous chapter, we explored the possibility of tuning the dielectric properties of bulk materials by progressively changing the chemical composition. In this chapter, we try to either remove atoms, or alter their positions and bonding topology, in systems like Twisted Bilayer Graphene (TBLG) to create defects, and see how the electronic and magnetic properties are affected. It is important to note that now we have moved to a two dimensional system (which is nanoscopic along the z-direction), and this introduces certain changes in the computational modeling procedure. Some of the results presented in this chapter have been published in Ref. [144].

4.1 Introduction

Graphene is an attractive candidate for use in the electronics industry owing to its mechanical and electronic properties, and indeed it has even been speculated that one day graphene could replace silicon as the primary material for electronics [18, 145]. Graphene also exhibits several exotic properties, such as a room temperature quantum Hall effect [145], and a possibility of observing the Casimir effect [21]. It is the interesting conical shaped band structure of graphene near the Fermi level E_F (as a result of which electrons behave like massless Dirac fermions [7]), that leads to many of its unusual electronic properties.

However, many of these properties like the Dirac cones go away when graphene layers are assembled together in the conventional Bernal stacking, also known as AB-stacking, where successive layers are displaced by both a vertical and a lateral shift, to get graphite or multilayer graphene. However, in recent years, there has been the appealing discovery that if instead a few layers of graphene are grown so that successive layers are aligned with a twist with respect to each other, there then appears to be an apparent electronic decoupling between layers, so that the Dirac cones are retained, at least for large angles of twist [146–148]. An additional parameter for tuning the properties of graphene, viz., the twist angle, is thus obtained. Varying the twist angle can be used to reduce the Fermi velocity (slope of the Dirac cones). At small twist angles, twisted bilayer graphene has also been shown to have many intriguing properties, such as localization of electrons, and van Hove singularities in the electronic density of states which lie very close to the Fermi level [43]. This in turn also raises the possibility of seeing other interesting phenomena such as superconductivity in twisted bilayer graphene. Other fascinating results on twisted bilayer graphene (TBLG) include the demonstration of Hofstadter's Butterfly in the energy spectrum in a magnetic field [149], and neutrino-like oscillations as a result of coupling of the Dirac cones of the two rotated layers [150]. Graphene layers with a twist can now be grown by a variety of methods, which allow one to access a range of twist angles [151–153]. However, the nature and extent of the interlayer coupling, and the consequences thereof, continue to be debated [154].

The questions we want to ask are: in what way are these properties altered upon the introduction of defects in TBLG? And can we deliberately introduce defects in a particular manner so as to tune various properties of TBLG? There has always been a lot of interest in defects in graphene and other low-dimensional carbon materials [155]. Much of this interest stems from concerns about how the presence of such defects will affect the functioning of these materials in applications. Defects such as monovacancies, divacancies, interstitials and Stone-Wales defects [156] are known to affect the mechanical, electronic and magnetic properties of carbon materials. There have, for example, been several studies to check to what extent the presence of defects affects electrical conductance

[157–159]. However, it has also been appreciated that it might be possible to purposely design defective structures with a view toward creating certain functionalities [158, 160]. Among the possible advantages that the presence of defects in graphene can confer, it has been shown that they can induce magnetic moments [45–50], and improve gas sensing properties [51]. It has also been suggested that the introduction of defects can be used for band-gap engineering [44, 52, 158]. Defects can be deliberately created by, e.g., irradiation with electrons [161–164] or ions [165–168], oxidation [169] hydrogenation [170–173], or fluorination [174, 175].

In this theoretical study we perform first principles density functional theory (DFT) calculations to study the properties of two kinds of point defects: Stone-Wales (SW) defects and monovacancies in twisted bilayer graphene. We are particularly interested in the question of how the electronic band structure in the neighborhood of E_F (i.e., the Dirac cones) is affected by the presence of defects.

4.2 Computational Details

We have performed spin-polarized DFT calculations using the PWscf package of the Quantum ESPRESSO distribution [78]. We use ultrasoft pseudopotentials [89] to describe the interactions between the ion cores and valence electrons. A plane wave basis set with kinetic energy cut-offs of 40 Ry and 480 Ry for the wavefunctions and charge densities, respectively, was found to be sufficient to get converged values of the total energy and forces. The geometry of all the structures was optimized using Hellmann-Feynman forces [90] until the force on each atom was less than 0.001 Ry/bohr along all three directions. Convergence was aided by making use of the Marzari-Vanderbilt smearing scheme [178], with a small smearing width of 0.001 Ry. Simulated scanning tunneling microscopy (STM) images were obtained using the Tersoff-Hamann theory [179], as incorporated in the “pp.x” post-processing tool supplied with Quantum-ESPRESSO.

In this chapter, we have considered two different levels of approximation for the exchange-correlation interactions: (i) the local density approximation (LDA) in the Perdew-Zunger form [71], and (ii) the generalized gradient approximation (GGA) in the Perdew-Burke-Ernzerhof (PBE) form [77]. The LDA has been a common choice in many previous DFT studies on TBLG. However, given that the (weak) coupling between the two graphene layers is important in TBLG, and that there has been much debate about its nature and extent, we feel that it is desirable to have an accurate treatment of these interlayer interactions, where van der Waals interactions (which are absent in conventional DFT calculations) may be expected to play a crucial role. For this reason, along with the PBE exchange-correlation, we also incorporate the van der Waals interactions as a semi-empirical correction, using the "DFT-D2" treatment suggested by Grimme [93, 177]. Of these three kinds of theoretical treatments (LDA, PBE and DFT-D2), the results using DFT-D2 should be regarded as being the most reliable, and most of our results have been obtained using this approach. However, we also present some results with the other two treatments for purposes of comparison; we believe that this is of interest since several authors still continue to use these other functionals, especially the LDA, in order to treat such systems, and it is therefore worth examining their reliability.

In our calculations, we use periodic boundary conditions and the unit cell is repeated along all three directions. Thus to model a two-dimensional system like TBLG, we need to consider a large vacuum region along the direction normal to the graphene layers (the z direction), so that there is no interaction between two periodic images along that direction. This introduces additional computational cost as one has to deal with a larger system. For our calculations, a vacuum spacing of about 13 Å was found sufficient, to make the interaction between periodic images along z direction negligible. For sampling the Brillouin zone, we use a Monkhorst-Pack mesh of $(21 \times 21 \times 1)$ k-points for the primitive unit cell of graphene [176], and proportionately equivalent meshes for larger supercells of graphene systems, for the self-consistent-field calculations. However, for the post-processing calculations, an extremely accurate k-point sampling was needed in order to obtain a precise computation of the Fermi energy, and therefore much finer grids were used. The k-point grid spacing was further reduced in regions of the Brillouin zone (near the Dirac points)

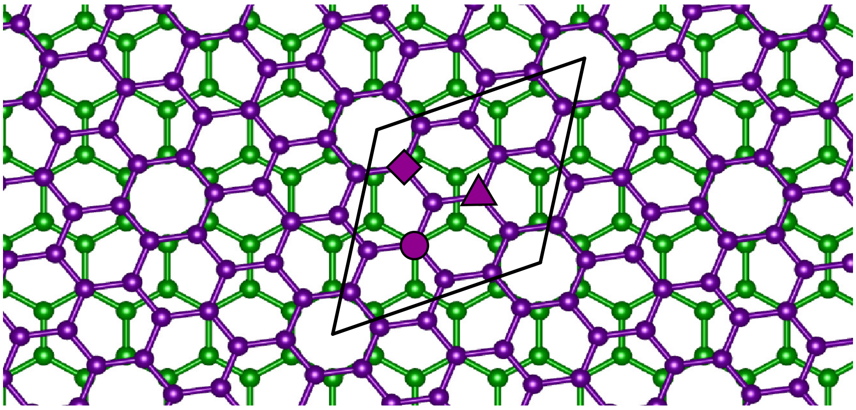

Figure 4.1: *A bilayer of graphene with rotational stacking fault (TBLG) with a rotation angle of 38.213°. The upper layer is shown in violet and lower layer in green, the 28-atom primitive unit cell (S_1) is also shown by the black rhombus. Examples of three symmetry-inequivalent types of sites in the upper layer are shown with different shapes: α-site (circle), β-site (triangle) and γ-site (square). This figure has appeared in Ref. [144].*

where it was deemed necessary to have a particularly dense sampling; the weights assigned to k-points were appropriately adjusted.

The details of this non-uniform, weighted k-point mesh and tests of its accuracy have been described in detail in the Appendix A of this thesis.

4.3 Twisted Bilayer Graphene

Twisted Bilayer Graphene is a system of two graphene layers stacked in such a way that one layer is rotated at an angle with respect to the other. Modeling TBLG requires the construction of a commensurate supercell, with the necessary finiteness required for practical computation. A number of such commensurate supercells are possible depending on the twist angle between the two graphene layers [180]. We describe below the commensuration condition and the construction of a commensurate unit cell of TBLG for an arbitrary set of twist angles. We also describe in detail the Brillouin zone of TBLG, especially the **K** points, in order to make clear the notation used in this chapter, and to enable the reader to follow the analysis of results that is presented later in Section 4.4.1.

4.3.1 Geometric Properties

A TBLG system is created by placing two layers of graphene on top of each other, one of which is "unrotated" (U), and the other "rotated" (R).

If $\mathbf{a}_1^{\mathrm{U}}$ and $\mathbf{a}_2^{\mathrm{U}}$ are the primitive lattice vectors of the (unrotated) graphene honeycomb lattice, then a supercell for the unrotated layer can be constructed by the supercell lattice vectors: $\mathbf{A}_1^{\mathrm{U}} = m_1\mathbf{a}_1^{\mathrm{U}} + m_2\mathbf{a}_2^{\mathrm{U}}$ and $\mathbf{A}_2^{\mathrm{U}} = -m_2\mathbf{a}_1^{\mathrm{U}} + (m_1 + m_2)\mathbf{a}_2^{\mathrm{U}}$, where m_1 and m_2 are integers. The second graphene layer is rotated by an angle θ; its primitive lattice vectors are given by: $\mathbf{a}_1^{\mathrm{R}} = R(\theta)\mathbf{a}_1^{\mathrm{U}}$ and $\mathbf{a}_2^{\mathrm{R}} = R(\theta)\mathbf{a}_2^{\mathrm{U}}$, where $R(\theta)$ is the rotation matrix. For such a rotated lattice, a supercell can be constructed by the supercell lattice vectors: $\mathbf{A}_1^{\mathrm{R}} = n_1\mathbf{a}_1^{\mathrm{R}} + n_2\mathbf{a}_2^{\mathrm{R}}$ and $\mathbf{A}_2^{\mathrm{R}} = -n_2\mathbf{a}_1^{\mathrm{R}} + (n_1 + n_2)\mathbf{a}_2^{\mathrm{R}}$, where n_1 and n_2 are integers.

The condition for commensuration is given by:

$$n_1\mathbf{a}_1^{\mathrm{R}} + n_2\mathbf{a}_2^{\mathrm{R}} = m_1\mathbf{a}_1^{\mathrm{U}} + m_2\mathbf{a}_2^{\mathrm{U}}. \tag{4.1}$$

We use a common choice for graphene primitive lattice vectors: $\mathbf{a}_1^{\mathrm{U}} = a(1, 0)$ and $\mathbf{a}_2^{\mathrm{U}} = a(1/2, \sqrt{3}/2)$, where a is the lattice constant of graphene. For this choice of primitive lattice vectors, the above commensuration relation becomes:

$$\begin{pmatrix} n_1 \\ n_2 \end{pmatrix} = \begin{pmatrix} \cos\theta + \frac{1}{\sqrt{3}}\sin\theta & +\frac{2}{\sqrt{3}}\sin\theta \\ -\frac{2}{\sqrt{3}}\sin\theta & \cos\theta - \frac{1}{\sqrt{3}}\sin\theta \end{pmatrix} \begin{pmatrix} m_1 \\ m_2 \end{pmatrix}. \tag{4.2}$$

This equation maps one integer pair (n_1, n_2) onto another (m_1, m_2), with the constraint that $m_1^2 + m_2^2 + m_1 m_2 = n_1^2 + n_2^2 + n_1 n_2$. As pointed out in Ref. [180], this is a Diophantine problem, which has to be solved to find out integer pairs (n_1, n_2) and (m_1, m_2) that satisfy Eq. (4.2). The authors of Ref. [180] solve this problem analytically; we instead solve this using a simple numerical code to get a set of integer values for (n_1, n_2) and (m_1, m_2) for different angles of twist θ. For integer pairs satisfying the above commensuration condition, the twist angle θ is given by:

$$\theta = \cos^{-1}\left(\frac{2m_1n_1 + m_1n_2 + m_2n_1 + 2m_2n_2}{2(m_1^2 + m_2^2 + m_1m_2)}\right). \tag{4.3}$$

A few of the commensurate twist angles and the corresponding integer pairs are given in Table 4.1, which we have obtained using our code. Note that $\theta = 0°$ and $\theta = 60°$ denote the trivial cases of AA-stacked BLG and AB-stacked BLG, respectively. For each commensurate angle, there is another angle which gives another commensurate supercell with the same lattice constant, such that the difference of these two angles is 60° or a multiple of 60°. This is exemplified in cases 2(i) & 2(ii) and 3(i) & 3(ii) of Table 4.1.

No.	Twist angle θ	Integer pairs (n_1, n_2) & (m_1, m_2)	Comments
1	0°	(1,0) & (1,0)	AA-stacked BLG
2(i)	38.213°	(2,1) & (3,-1)	$(\sqrt{7} \times \sqrt{7})$
2(ii)	-21.787°	(2,1) & (1,2)	$(\sqrt{7} \times \sqrt{7})$
3(i)	27.796°	(3,1) & (4,-1)	$(\sqrt{13} \times \sqrt{13})$
3(ii)	-32.204°	(3,1) & (1,3)	$(\sqrt{13} \times \sqrt{13})$
4	60°	(1,0) & (1,0)	AB-stacked BLG

Table 4.1: *A list of a few integer pairs and twist angles that yield commensurate unit cells for TBLG. The cases of $\theta = 0°$ and $\theta = 60°$ denote the trivial cases of AA-stacked BLG and AB-stacked BLG, respectively. The last column also denotes how large the supercell of TBLG is with respect to the primitive cell of graphene.*

The primitive lattice vectors of the twisted bilayer, $\mathbf{A}_1^{\mathrm{B}}$ and $\mathbf{A}_2^{\mathrm{B}}$, are related to the unrotated primitive lattice vectors of the single layer, $\mathbf{a}_1^{\mathrm{U}}$ and $\mathbf{a}_2^{\mathrm{U}}$, by:

$$\mathbf{A}_1^{\mathrm{B}} = m_1\mathbf{a}_1^{\mathrm{U}} + m_2\mathbf{a}_2^{\mathrm{U}}, \tag{4.4}$$

and

$$\mathbf{A}_2^{\mathrm{B}} = -m_2\mathbf{a}_1^{\mathrm{U}} + (m_1 + m_2)\mathbf{a}_2^{\mathrm{U}}. \tag{4.5}$$

The smallest possible non-trivial unit cell corresponds to $m_1 = 2$, $m_2 = 1$; by Eqs. (4.2) and (4.3), this gives $n_1 = 3$, $n_2 = -1$, and $\theta = 38.213°$. This is the angle of twist used for the TBLG considered in our study, its primitive unit cell contains 14 atoms in each layer. The unit cell vectors for this primitive unit cell S_1 are $\mathbf{A}_1^{\mathrm{B}} = 2\mathbf{a}_1^{\mathrm{U}} + \mathbf{a}_2^{\mathrm{U}}$ and $\mathbf{A}_2^{\mathrm{B}} = -\mathbf{a}_1^{\mathrm{U}} + 3\mathbf{a}_2^{\mathrm{U}}$. In Fig. 4.1 we have shown the structure of TBLG with this twist angle, with the primitive unit cell S_1 of the twisted bilayer indicated by the black rhombus. Note that for this choice of twist angle, the upper (rotated) layer contains three symmetry-inequivalent types of carbon atoms, which we label α, β and γ (see Fig. 4.1). Note that the α-site atom of the upper layer falls exactly atop a carbon atom of the lower layer, and γ-site atoms form a hexagon of atoms which lies over a similar but rotated hexagon of atoms of the lower layer.

However, most of our calculations on defects have been performed using a larger unit cell S_2, which has lattice vectors that are twice as long: $\mathbf{A}_1^{\mathrm{B}} = 4\mathbf{a}_1^{\mathrm{U}} + 2\mathbf{a}_2^{\mathrm{U}}$ and $\mathbf{A}_2^{\mathrm{B}} = -2\mathbf{a}_1^{\mathrm{U}} + 6\mathbf{a}_2^{\mathrm{U}}$. This unit cell contains 56 atoms in each layer, i.e., 112 atoms in the bilayer unit cell; this corresponds to the choice $m_1 = 4$, $m_2 = 2$.

In addition to the lattice vectors, the specification of the atomic position vectors (atomic basis) is also necessary, for constructing TBLG. A primitive unit cell of graphene contains two atoms, the atomic basis vectors of which can be commonly specified as: $\mathbf{b}_1 = 0\ \mathbf{a}_1^{\mathrm{U}} + 0\ \mathbf{a}_2^{\mathrm{U}}$ and $\mathbf{b}_2 = \frac{1}{3}\ \mathbf{a}_1^{\mathrm{U}} + \frac{1}{3}\ \mathbf{a}_2^{\mathrm{U}}$. A supercell of TBLG, which is indexed by integer pairs (m_1, m_2) and (n_1, n_2), has $2(m_1^2 + m_2^2 + m_1 m_2)$ carbon atoms in each layer. For the unrotated layer, the atomic basis vectors can be calculated as:

$$\mathbf{b}_1^{\mathrm{U}} = p\ \mathbf{a}_1^{\mathrm{U}} + q\ \mathbf{a}_2^{\mathrm{U}} \qquad \text{and} \qquad \mathbf{b}_2^{\mathrm{U}} = \Big(p + \frac{1}{3}\Big)\mathbf{a}_1^{\mathrm{U}} + \Big(q + \frac{1}{3}\Big)\mathbf{a}_2^{\mathrm{U}}, \tag{4.6}$$

where p and q are integers, such that $p \in \{p^{\min}, p^{\min}+1, \ldots, p^{\max}\}$ and $q \in \{q^{\min}, q^{\min}+1, \ldots, q^{\max}\}$. The limits $p^{\min}$, $p^{\max}$, $q^{\min}$, and $q^{\max}$, depend on the integer pairs (m_1, m_2). They are defined as: $p^{\min} = \min\ [\ 0, -m_2, m_1, m_1 - m_2]$, $p^{\max} = \max\ [\ 0, -m_2, m_1, m_1 - m_2]$, $q^{\min} = \min\ [\ 0, m_2, m_1 + m_2, m_1 + 2m_2]$, and $q^{\max} = \max\ [\ 0, m_2, m_1 + m_2, m_1 + 2m_2]$. In addition, one should apply the constraints that these atomic position vectors lie inside the area of the supercell of TBLG. This is given by the set of conditions:

$$\begin{aligned} & m_2 p - m_1 q \leq 0, \\ \text{and}\quad & (m_1 + m_2)p + m_2 q \geq 0, \\ \text{and}\quad & m_2 p - m_1 q > -({m_1}^2 + {m_2}^2 + m_1 m_2), \\ \text{and}\quad & (m_1 + m_2)p + m_2 q < ({m_1}^2 + {m_2}^2 + m_1 m_2). \end{aligned} \tag{4.7}$$

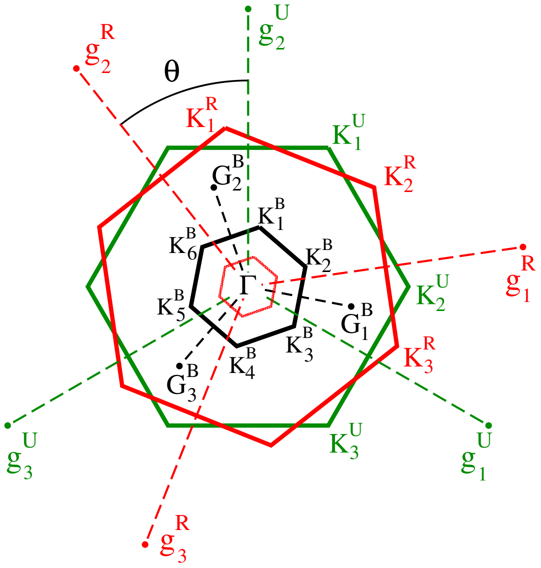

Figure 4.2: *The first Brillouin zone (FBZ) corresponding to the unrotated graphene layer (green), the rotated graphene layer (red) and TBLG (for S_1 in black and S_2 in blue). The Dirac points $\mathbf{K}_1$, $\mathbf{K}_2$, and $\mathbf{K}_3$ for the unrotated (superscript U), rotated (superscript R) and TBLG-S_1 (superscript B) are also shown. This figure has appeared in Ref. [144].*

Similar conditions arise for the rotated layer in terms of (n_1, n_2).

4.3.2 Brillouin Zone

The knowledge of the structure of the reciprocal space and the Brillouin zone is very essential in order to gain an understanding of the electronic properties of TBLG. If $\mathbf{g}_1^{\mathrm{U}}$ and $\mathbf{g}_2^{\mathrm{U}}$ are the primitive reciprocal lattice vectors corresponding to the unrotated layer, and $\mathbf{g}_1^{\mathrm{R}}$ and $\mathbf{g}_2^{\mathrm{R}}$ are the primitive reciprocal lattice vectors corresponding to the rotated layer, the reciprocal lattice vectors of the TBLG are given by:

$$\mathbf{G}_1^{\mathrm{B}} = \left\{\frac{m_1 + m_2}{m_1^2 + m_2^2 + m_1 m_2}\right\}\mathbf{g}_1^{\mathrm{U}} + \left\{\frac{m_2}{m_1^2 + m_2^2 + m_1 m_2}\right\}\mathbf{g}_2^{\mathrm{U}} \tag{4.8}$$

$$\mathbf{G}_1^{\mathrm{B}} = \begin{cases} \frac{3}{7}\mathbf{g}_1^{\mathrm{U}} + \frac{1}{7}\mathbf{g}_2^{\mathrm{U}}, & \text{for } S_1 \qquad (4.8\mathrm{A}) \\[2em] \frac{3}{14}\mathbf{g}_1^{\mathrm{U}} + \frac{1}{14}\mathbf{g}_2^{\mathrm{U}}, & \text{for } S_2 \qquad (4.8\mathrm{B}) \end{cases}$$

and

$$\mathbf{G}_2^{\mathrm{B}} = -\left\{\frac{m_2}{m_1^2 + m_2^2 + m_1 m_2}\right\}\mathbf{g}_1^{\mathrm{U}} + \left\{\frac{m_1}{m_1^2 + m_2^2 + m_1 m_2}\right\}\mathbf{g}_2^{\mathrm{U}} \tag{4.9}$$

$$\mathbf{G}_2^{\mathrm{B}} = \begin{cases} -\frac{1}{7}\mathbf{g}_1^{\mathrm{U}} + \frac{2}{7}\mathbf{g}_2^{\mathrm{U}}, & \text{for } S_1 \qquad \text{(4.9A)} \\ \\ -\frac{1}{14}\mathbf{g}_1^{\mathrm{U}} + \frac{2}{14}\mathbf{g}_2^{\mathrm{U}}, & \text{for } S_2 \qquad \text{(4.9B)} \end{cases}$$

Inversely, we can write the primitive reciprocal lattice vectors corresponding to the unrotated layer in terms of the reciprocal lattice vectors of the TBLG.

$$\mathbf{g}_1^{\mathrm{U}} = m_1\mathbf{G}_1^{\mathrm{B}} - m_2\mathbf{G}_2^{\mathrm{B}} \tag{4.10}$$

$$\mathbf{g}_1^{\mathrm{U}} = \begin{cases} 2\mathbf{G}_1^{\mathrm{B}} - \mathbf{G}_2^{\mathrm{B}}, & \text{for } S_1 \qquad \text{(4.10A)} \\ \\ 4\mathbf{G}_1^{\mathrm{B}} - 2\mathbf{G}_2^{\mathrm{B}}, & \text{for } S_2 \qquad \text{(4.10B)} \end{cases}$$

and

$$\mathbf{g}_2^{\mathrm{U}} = m_2\mathbf{G}_1^{\mathrm{B}} + (m_1 + m_2)\mathbf{G}_2^{\mathrm{B}} \tag{4.11}$$

$$\mathbf{g}_2^{\mathrm{U}} = \begin{cases} \mathbf{G}_1^{\mathrm{B}} + 3\mathbf{G}_2^{\mathrm{B}}, & \text{for } S_1 \qquad \text{(4.11A)} \\ \\ 2\mathbf{G}_1^{\mathrm{B}} + 6\mathbf{G}_2^{\mathrm{B}}, & \text{for } S_2 \qquad \text{(4.11B)} \end{cases}$$

Similar relations for the rotated layer can be found by just replacing m_1 and m_2 by n_1 and n_2, respectively.

The reciprocal lattice and the first Brillouin zone for the unrotated and rotated graphene layers, and the twisted bilayer graphene, are shown in Fig. 4.2. The first Brillouin zone for the TBLG (shown by the black hexagon in Fig. 4.2) corresponds to a twist angle of 38.213°, for the smallest commensurate supercell S_1. A similar figure can be obtained when S_2 is used, shown by the blue hexagon. Note that by the translational symmetry of the lattice, $\mathbf{K}_1^{\mathrm{B}}$, $\mathbf{K}_3^{\mathrm{B}}$ and $\mathbf{K}_5^{\mathrm{B}}$ are identical; similarly, $\mathbf{K}_2^{\mathrm{B}}$, $\mathbf{K}_4^{\mathrm{B}}$ and $\mathbf{K}_6^{\mathrm{B}}$ are identical. If, in addition, one has inversion symmetry or time-reversal symmetry, then all six $\mathbf{K}$ points are identical. However, these symmetries are valid at the corners of the Brillouin zone only, and need not necessarily hold in the interior of the Brillouin zone, i.e., one need not have three-fold or six-fold symmetry always present. In particular, the introduction of defects may lower the symmetry. The $\mathbf{K}_1^{\mathrm{U}}$ and $\mathbf{K}_2^{\mathrm{U}}$ points in the Brillouin zone of the unrotated layer can be folded onto points in the first Brillouin zone of the TBLG lattice:

$$\mathbf{K}_1^{\mathrm{U}} = (m_1 - m_2)\mathbf{K}_1^{\mathrm{B}} + m_2(\mathbf{G}_1^{\mathrm{B}} + \mathbf{G}_2^{\mathrm{B}}) \tag{4.12}$$

$$\mathbf{K}_1^{\mathrm{U}} = \begin{cases} \mathbf{K}_1^{\mathrm{B}} + (\mathbf{G}_1^{\mathrm{B}} + \mathbf{G}_2^{\mathrm{B}}), & \text{for } S_1 \qquad \text{(4.12A)} \\ \\ \mathbf{K}_2^{\mathrm{B}} + (2\mathbf{G}_1^{\mathrm{B}} + 3\mathbf{G}_2^{\mathrm{B}}), & \text{for } S_2 \qquad \text{(4.12B)} \end{cases}$$

and

$$\mathbf{K}_2^{\mathrm{U}} = (m_1 - m_2)\mathbf{K}_2^{\mathrm{B}} + m_2\mathbf{G}_1^{\mathrm{B}} \tag{4.13}$$

$$\mathbf{K}_2^{\mathrm{U}} = \begin{cases} \mathbf{K}_2^{\mathrm{B}} + \mathbf{G}_1^{\mathrm{B}}, & \text{for } S_1 \qquad \text{(4.13A)} \\ \\ \mathbf{K}_1^{\mathrm{B}} + 3\mathbf{G}_1^{\mathrm{B}}, & \text{for } S_2 \qquad \text{(4.13B)} \end{cases}$$

Similarly for the rotated layer,

$$\mathbf{K}_1^{\mathrm{R}} = (n_1 - n_2)\mathbf{K}_1^{\mathrm{B}} + n_2(\mathbf{G}_1^{\mathrm{B}} + \mathbf{G}_2^{\mathrm{B}}) \tag{4.14}$$

$$\mathbf{K}_1^{\mathrm{R}} = \begin{cases} \mathbf{K}_1^{\mathrm{B}} + \mathbf{G}_2^{\mathrm{B}}, & \text{for } S_1 \qquad \text{(4.14A)} \\ \\ \mathbf{K}_2^{\mathrm{B}} + 3\mathbf{G}_2^{\mathrm{B}}, & \text{for } S_2 \qquad \text{(4.14B)} \end{cases}$$

and

$$\mathbf{K}_2^{\mathrm{R}} = (n_1 - n_2)\mathbf{K}_2^{\mathrm{B}} + n_2\mathbf{G}_1^{\mathrm{B}} \tag{4.15}$$

$$\mathbf{K}_2^{\mathrm{R}} = \begin{cases} \mathbf{K}_2^{\mathrm{B}} + (\mathbf{G}_1^{\mathrm{B}} + \mathbf{G}_2^{\mathrm{B}}), & \text{for } S_1 \qquad \text{(4.15A)} \\ \\ \mathbf{K}_1^{\mathrm{B}} + (3\mathbf{G}_1^{\mathrm{B}} + 2\mathbf{G}_2^{\mathrm{B}}), & \text{for } S_2 \qquad \text{(4.15B)} \end{cases}$$

Thus, $\mathbf{K}_1^{\mathrm{U}}$ folds onto Γ or $\mathbf{K}_1^{\mathrm{B}}$ or $\mathbf{K}_2^{\mathrm{B}}$, depending on whether $(m_1 - m_2)$ is $3n$ or $3n+1$ or $3n+2$, respectively, where n is an integer. Similarly, for the rotated layer, $\mathbf{K}_1^{\mathrm{R}}$ folds onto Γ or $\mathbf{K}_1^{\mathrm{B}}$ or $\mathbf{K}_2^{\mathrm{B}}$, depending on whether $(n_1 - n_2)$ is $3n$ or $3n+1$ or $3n+2$, respectively, where n is an integer. For TBLG with the supercell S_1, we therefore have the following mappings: $\mathbf{K}_1^{\mathrm{U}} \to \mathbf{K}_1^{\mathrm{B}}$ and $\mathbf{K}_2^{\mathrm{U}} \to \mathbf{K}_2^{\mathrm{B}}$. Similarly, when performing calculations with the supercell S_2, we have: $\mathbf{K}_1^{\mathrm{U}} \rightarrow \mathbf{K}_2^{\mathrm{B}}$ and $\mathbf{K}_2^{\mathrm{U}} \rightarrow \mathbf{K}_1^{\mathrm{B}}$.

Thus when we use S_1 or S_2 to analyze the band-structure of the TBLG, the Dirac cones will continue to appear at the **K** points of the Brillouin zone of the supercell. Thus, these are the points whose vicinity we will focus on, to see whether the introduction of defects opens up a band gap and/or alters the linear dispersion relation.

4.3.3 Properties of pristine TBLG

First, to benchmark our calculations with earlier results, we perform calculations on defect-free bilayer graphene, with both Bernal stacking and twisted stacking. Our results for the energetics and geometry, for AB-BLG and TBLG, with both LDA and DFT-D2 approaches, as well as with the PBE alone, are shown in Table 4.2. While both LDA and DFT-D2 give values of the interlayer distance d that are in reasonably good agreement with experiment, use of the PBE alone leads to a value that is far too large. However, the DFT-D2 leads to a result for the exfoliation energy E_{exf}, i.e., the energy required for exfoliating a graphene layer from the bilayer system, that is closer to experimental estimates than the LDA result; once again the PBE result is completely erroneous. All of these results are in agreement with previous theoretical work [151, 185, 186]. Also note that both LDA and DFT-D2 show that AB-BLG is lower in total energy than TBLG by about 2 meV/atom, however PBE alone leads to TBLG being more stable by the very small amount of 0.04 meV/atom. On going from AB-BLG to TBLG, there is a very slight increase in d, which causes a small decrease in E_{exf}; however, these changes are very small.

Figs. 4.3 (a)–(c) show simulated STM images of SLG, AB-BLG and TBLG; the input local densities of states for these calculations were obtained from DFT-D2 calculations. For a single layer of graphene, the STM image clearly shows the honeycomb like arrangement of carbon atoms. In the case of AB-stacked bilayer graphene, the image reflects the three-fold symmetry of Bernal stacking. These images are in excellent agreement with earlier reported experimental STM images [187]. In the case of TBLG, at first glance, the STM image might appear rather similar to that of the single layer of graphene, however closer examination of the STM image brings out the effect of the twisted lower layer. The

AB stacked BLG

Method (XC)	in-plane C-C bond length a_0 (Å)	Interlayer distance d (Å)	Exfoliation Energy E_{exf} (meV/atom)
LDA	1.41	3.34	12.4
PBE	1.42	4.15	0.8
DFT-D2	1.42	3.20	26.1
Expt.	1.42	3.35 [181]	43 [182] 35±10 [183] 31±2 [184]

Twisted BLG

Method (XC)	in-plane C-C bond length a_0 (Å)	Interlayer distance d (Å)	Exfoliation Energy E_{exf} (meV/atom)
LDA	1.41	3.40	10.8
PBE	1.42	4.35	0.8
DFT-D2	1.42	3.30	24.0

Table 4.2: *Results for structure and energetics of AB-stacked bilayer graphene and TBLG, as obtained with different approaches.* a_0 *is the in-plane nearest neighbor C-C bond length,* d *is the interlayer distance, and* E_{exf} *is the exfoliation energy. Note that the experimental values are for graphite, not for bilayer graphene.*

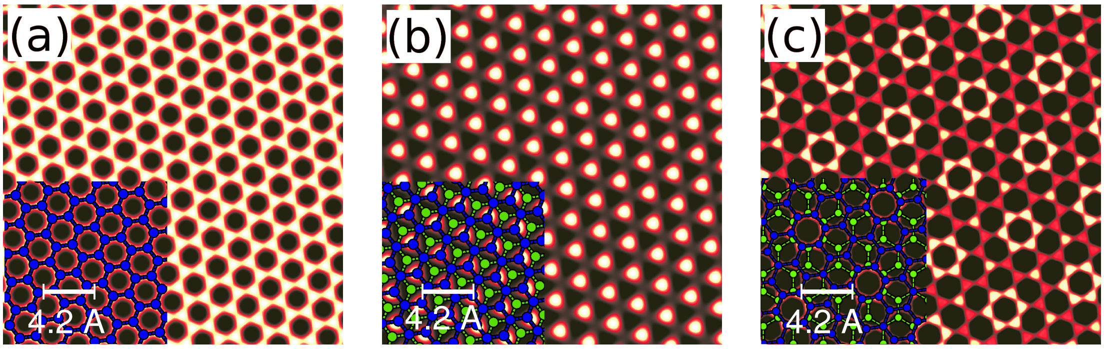

Figure 4.3: *Simulated STM images for (a) Single layer of graphene (SLG), (b) AB-stacked BLG, and (c) Twisted-BLG. The insets show an overlay of the atomic positions of the system. The blue circles are the carbon atoms of the upper layer of graphene, and the green circles are the carbon atoms of the lower layer. This figure has appeared in Ref. [144].*

relatively brighter spots in this image correspond to the positions where the atoms of both layers lie directly on top of each other, thus enhancing the STM signal.

In Fig. 4.4, we plot the electronic band structure along the path Γ–M_1^B–K_1^B–Γ as obtained using DFT-D2 for pristine (defect-free) twisted bilayer graphene, using the S_2 supercell. We first compare the results for TBLG with those obtained for SLG. Panels (a) and (b) show the regions of the band structure near the Fermi energy ($E_F = 0$ eV) for SLG and TBLG, respectively. Panels (d) and (e) show the band structure in the energy range E_F - 19.8 eV to E_F - 17.4 eV. At first glance, the band structure for TBLG resembles very closely that of SLG near E_F [compare panels (a) and (b) of Fig. 4.4], and it might seem that there is no interaction between the layers of TBLG. However, if we look at the low lying energy states for TBLG, we can clearly see that these states have split in energy. This is a clear manifestation of the interlayer chemical interactions in TBLG. The two band structures are quite different in the intermediate energy ranges (not shown), however in the vicinity of the Fermi energy the Dirac bands become almost degenerate. If we zoom in, into the vicinity of the $\mathbf{K}_1^\mathrm{B}$ point, we obtain a conical dispersion with the

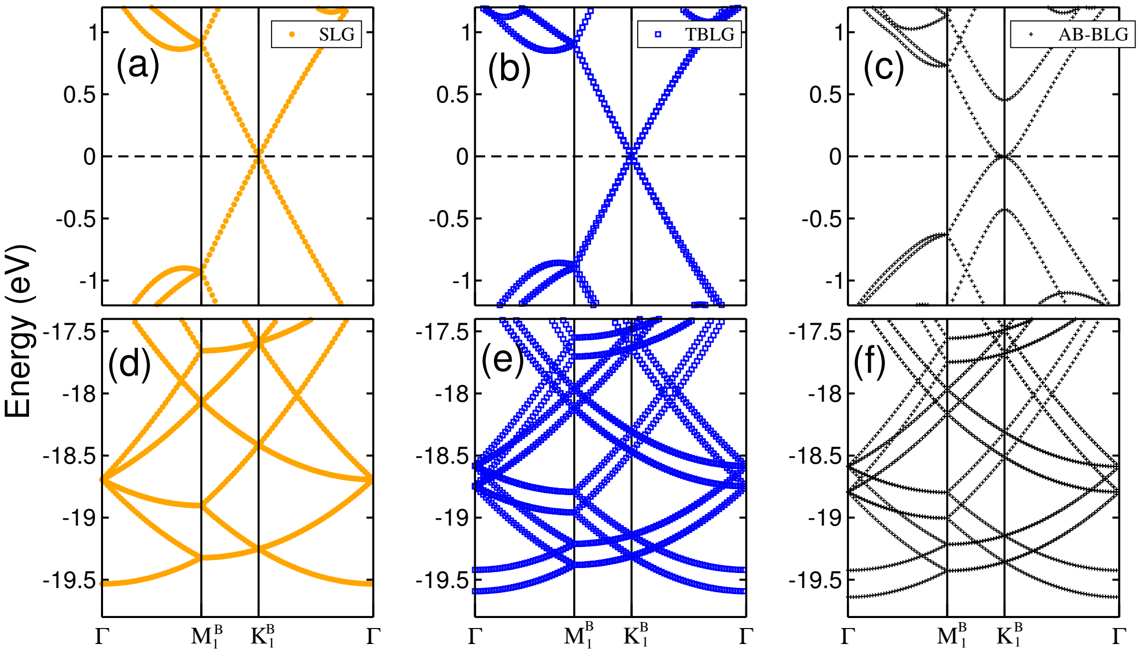

Figure 4.4: *Comparison of band structure of SLG, pristine TBLG, and AB stacked BLG, shown for states near the Fermi energy E_F (a), (b), and (c), respectively, and for low-lying states (d), (e), and (f), respectively. The Fermi energy E_F is at 0.*

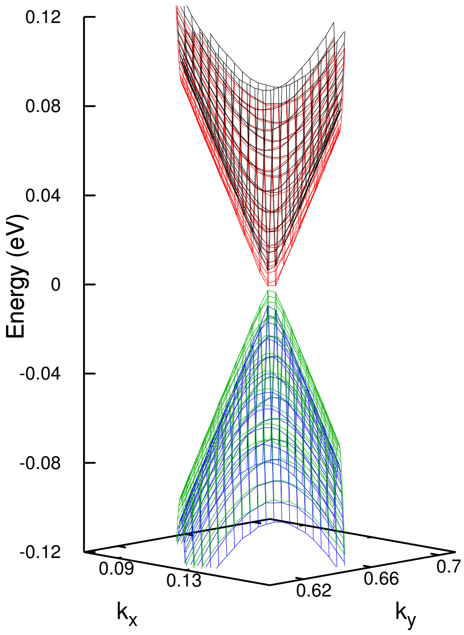

Figure 4.5: *Calculated Band structure of pristine TBLG in the vicinity of* $\boldsymbol{K}_1^{\mathrm{B}}$. *Four bands are shown: two valence bands (blue and green), and two conduction bands (red and black). The Fermi energy* E_F *is at 0. This figure has appeared in Ref. [144].*

Dirac point lying exactly at $\mathbf{K}_1^{\mathrm{B}}$, and the Dirac crossing energy E_D=E_F. This is in good agreement with previous authors [180]. In Fig. 4.5, we have plotted the energy surfaces of the two topmost valence bands, which we call VB2 (blue in Fig. 4.5) and VB1 (green), and the two lowest-lying conduction bands, CB1 (red) and CB2 (black). Note that VB1 and VB2 are almost, but not quite, degenerate, being shifted in energy by ∼9 meV; similarly CB1 and CB2 are displaced in energy by ∼9 meV. Note also that there is no band gap between VB1 and CB1. These results are similar to those obtained by previous authors who have performed calculations on TBLG [180]. Fig. 4.5 is useful in that it serves as a baseline to compare our other results to further below, when we will see how its features are modified upon the introduction of defects.

The band structure for AB stacked BLG is also show in Figs. 4.4(c) and 4.4(f), for comparison with that of SLG and TBLG. The low lying states have again split in energy for this case, the splitting is slightly larger (∼50 meV) than that observed for TBLG. The states near E_F, however, show parabolic bands, which is a well known signature of Bernal stacking.

To understand the interlayer interactions in TBLG in more detail, we plot a charge redistribution map, which shows the difference in the charge density of TBLG compared to the sum of the individual charge densities of the two isolated layers forming TBLG. We have plotted this charge redistribution map for TBLG in Fig. 4.6(a) and we compare it with a similar map plotted for AB stacked BLG [Fig. 4.6(b)]. The red lobes denote an increase, whereas the green lobes denote a depletion, of electronic density of the system. We see a clear difference in the reorganization of the charge density for TBLG and AB-BLG. In the case of AB-BLG, there is a depletion in charge density over those atoms which lie exactly atop the atoms of the other layer, possibly due to the repulsion of the π-electron cloud. Those atoms which fall at the hollow site show an increase in charge density. In the case of TBLG, the interactions are complex and give rise to a symmetric pattern in the charge redistribution. Once again, we find a charge density depletion in the vicinity of those atoms which lie nearly atop the atoms of the other layer. For example, the α-site atoms of TBLG, which lie atop atoms of the lower layer, show a depletion in electron density. Also the hexagon formed by the γ-site atoms, that nearly matches with a similar hexagon of the lower layer, shows a depletion in the electronic density. Elsewhere, where there is no direct overlap of atoms of the two layers, we find that the electronic density increases. The charge redistribution in both these cases clearly reflects the symmetry of the lattice, and gives a clear indication of the presence of interlayer interactions.

4.4 Defects in Twisted Bilayer Graphene

We consider two types of point defects in TBLG, viz., the Stone-Wales defect and the monovacancy. For defects we work with a larger supercell S_2 which is 2×2 times as large as the supercell S_1. We perform calculations considering all possible inequivalent sites of one defect in the S_2 supercell, for both the Stone-Wales defect and the monovacancy. This supercell corresponds to one defect in 56 carbon atoms per layer, i.e., a defect density of 1.8%. For the monovacancy, we have in addition considered defect densities of 7.2% (corresponding to one vacancy in the S_1 supercell with 14 carbon atoms in each layer) and 0.8% (corresponding to one defect in supercell S_3, which is 3×3 times as large as S_1, and

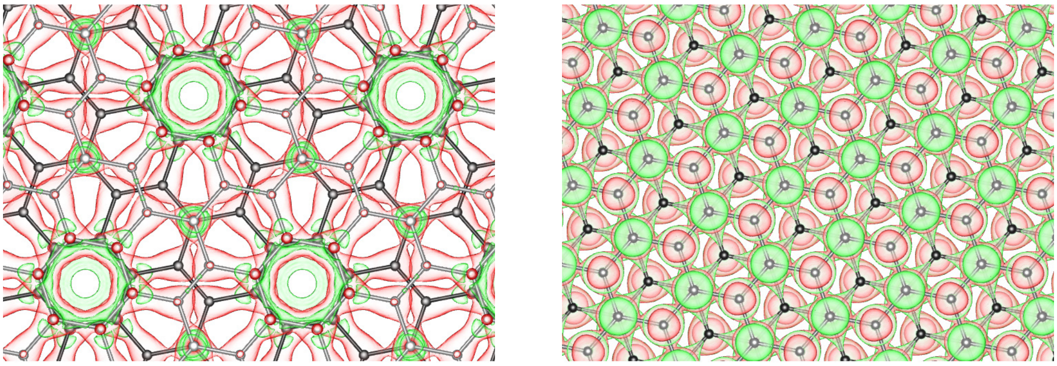

(a) TBLG (b) AB stacked BLG

Figure 4.6: *Charge density redistribution for pristine TBLG and AB stacked BLG, due to the presence of interlayer coupling. The red lobes correspond to an increase, and the green lobes denote a depletion, in the electron density due to the presence of the other layer. The isosurfaces shown correspond to a density value of* $\pm 9.5 \times 10^{-5}$ *e/bohr*^{3} *for both cases. The atoms of the upper graphene layer are shown in gray, and the lower layer in black.*

contains 126 carbon atoms in each layer).

For comparison of various properties of the above-mentioned defects in TBLG, we also consider the same defects in a single layer of graphene (SLG), as well as in an AB-stacked bilayer graphene (we refer to this as AB-BLG). To facilitate comparison, i.e., maintain the same defect density and system symmetry, we use a similar S_2 supercell also for our calculations on SLG and AB-BLG.

4.4.1 Stone-Wales Defect

A Stone-Wales (SW) defect is formed by rotating a single carbon-carbon bond in the graphene sheet by 90°, resulting in a structure with a pair each of seven-membered and five-membered rings. This is known to be one of the most common defects in graphene-related systems and carbon nanotubes [156]. It has been reported from calculations on SLG [188] that an out-of-plane distortion of the carbon atoms in the vicinity of the SW defect further stabilizes this defect. In our study of SW defects in TBLG, we explicitly check if permitting such distortions stabilizes the SW defect.

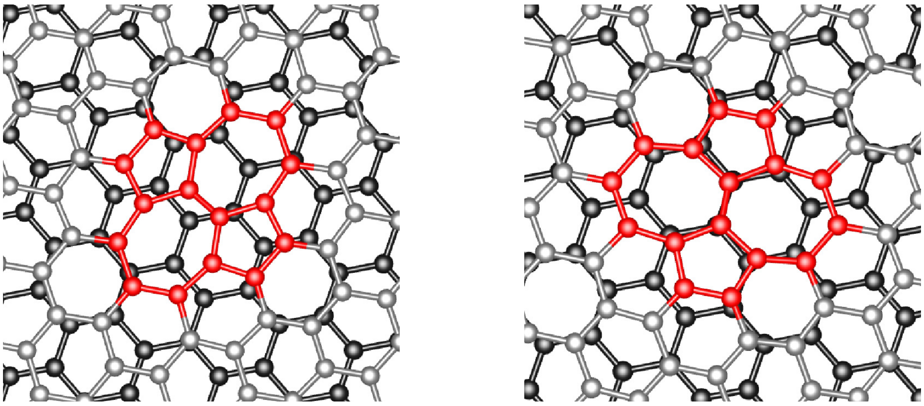

(a) $\alpha\beta$-SW (b) $\beta\beta$-SW

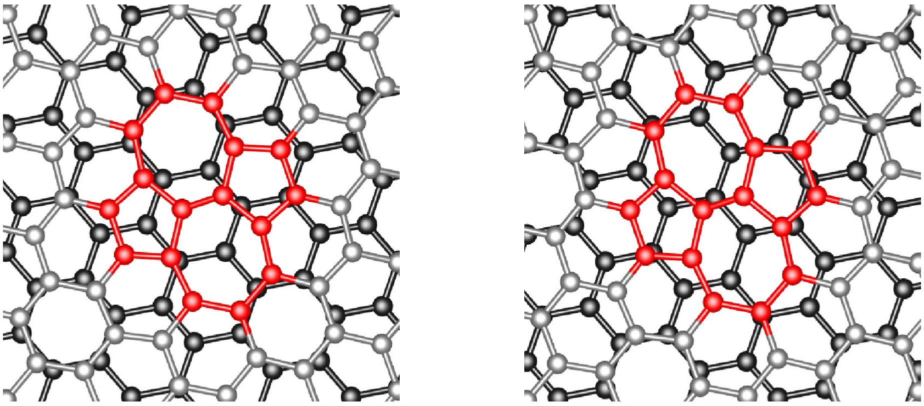

(c) $\beta\gamma$-SW (d) $\gamma\gamma$-SW

Figure 4.7: *Relaxed geometries for (a) $\alpha\beta$-SW, (b) $\beta\beta$-SW, (c) $\beta\gamma$-SW, and (d)$\gamma\gamma$-SW defects in TBLG. Lower layer atoms are black, and the upper defective layer atoms are light gray. The C atoms near the SW defect are colored red for visual ease. This figure has appeared in Ref. [144].*

Structural properties

We create the SW defect in one of the layers of the TBLG, and look at the change in the structural and electronic properties due to the defect. We compare our results with those of SW defects in SLG and AB-BLG. Unlike SLG or AB-BLG, where only one type of site for a SW defect is possible, in TBLG, there can be many inequivalent defect-sites, with the number depending on the angle of twist between the two layers. For the case of TBLG chosen by us, where the two layers are rotated by a relative angle of 38.213°, there can be four inequivalent geometries (see Fig. 4.7), corresponding to four different choices of the rotated bond; we name these $\alpha\beta$-SW, $\beta\gamma$-SW, $\beta\beta$-SW, and $\gamma\gamma$-SW, with the labeling convention denoting which pair of adjacent atoms is connected by the rotated bond (see Fig. 4.1).

For SLG, we find that a sinusoidal distortion pattern about the defect center results in the most stable geometry of the SW defect [see Figs. 4.8(a) and 4.8(b)], in agreement with earlier reports [188]. The amplitude of distortion, Z, which is the difference between the largest upward displacement and the largest downward displacement, is as large as 1.2 Å [see Fig. 4.8(c)] for a SW defect in SLG within a supercell of size S_2, which is in good agreement with earlier values of about 1 Å for supercells of similar size. In the case of the bilayers, we find that SW defects in both AB-BLG and TBLG are stabilized by a similar sinusoidal distortion pattern; however the amplitude of the distortion in the defective layer is reduced to about 0.7 Å, the presence of the second layer inhibits the distortion. In our study, we have also allowed the undefective layer to relax, it exhibits a smaller distortion amplitude of ∼0.2 Å. Fig. 4.8(c) shows the comparison of the net distortion of the graphene layers for the cases of single layer, AB-stacked bilayer, and twisted bilayer of graphene. Both the twisted and the AB-stacked bilayers show a very similar extent of distortion.

The energy of formation of the SW defect, as obtained with the various approaches, is given in Table 4.3. When no out-of-plane distortion is permitted, the formation energies are larger, these values listed in parentheses in Table 4.3. First for SLG, we find that the sinusoidal distortion leads to a stabilization of about 220 meV/defect; this is in good agreement with earlier results [188]. This can be seen clearly by comparing the results

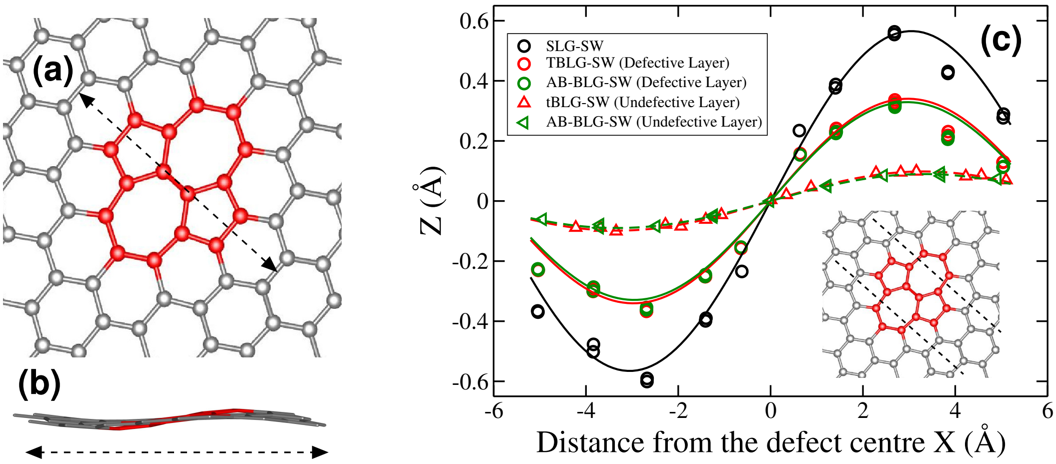

Figure 4.8: *Structure for SW defect in SLG, (a) the top-view and (b) the side-view showing the distortion of the defective graphene sheet. The side view in (b) is taken by viewing perpendicular to the dashed line in (a). (c) The distortion pattern for the SW defects in SLG, TBLG and AB-BLG. The zero of the distortion amplitude is taken at the center of the SW defect. The dashed line in the inset encloses the atoms over which the deviations from* Z=0 *are measured. This figure has appeared in Ref. [144].*

when this distortion is permitted with those when it is suppressed.

In the case of the bilayers, the distortion leads to a stabilization of the SW defect, as compared to the undistorted case. This stabilization energy is about 40 meV in AB-BLG, and about 60 meV in TBLG. For TBLG, we find that the defect formation energy depends only very slightly on the position of the defect. This is because the interaction between the layers is small. Similarly, the energy to form a SW defect in TBLG is very similar to that in AB-stacked BLG. The small differences in defect formation energy (of the order of tens of meV) between the different kinds of Stone-Wales defects in TBLG are due to the differences in interlayer coupling when the SW defect is situated at different positions in the graphene sheet. Note that when the calculations are performed with the PBE alone, these differences disappear. In this case the interlayer coupling is described very poorly and becomes negligible. From the DFT-D2 calculation, we see that it costs an additional 140–180 meV to create a SW defect in TBLG compared with SLG. Most of this increase in energy is because the energy-lowering due to distortion along the z-direction is hindered by the presence of the second layer. The same effect is seen in our LDA results; once again, it is absent in the PBE results.

Band Structure

The band structure of AB-stacked bilayer graphene is characterized by parabolic bands that touch near the **K** points in the Brillouin zone, at the Fermi level E_F [see Fig. 4.4(c)]. In contrast, for twisted bilayer graphene, there are Dirac cones, i.e., linear bands that touch at the **K** points, at E_F (recall Fig. 4.5 above). Given the large interest in linear dispersion, as well as the potential importance of the band-gap engineering of graphene, we wish to know whether, upon the introduction of defects such as Stone-Wales defects and monovacancies, (i) the Dirac cones are maintained (ii) if not, in what way are they altered, i.e., are they shifted in energy, and (iii) whether gaps open up, and if so, at what energies. As we will show below, clear signatures of the importance of interlayer coupling emerge when looking at the band structure, as opposed to the energetics of defect formation.

We examine the electronic band structure of SLG, AB-BLG and TBLG, containing a single SW-defect in the S_2 supercell. No perceptible spin-polarization was found in any of the cases, and we therefore present non-spin-polarized results. In the presence of the SW defect, our structures break the reflection symmetry about the two axes passing through the SW defect. Consequently, the irreducible Brillouin zone (IBZ) is half of the first Brillouin zone [shown by the shaded region in the TBLG Brillouin zone in Fig. 4.9(a)]. Let us consider first the high-symmetry points that lie in this IBZ. As mentioned in Section III above, by the translational symmetry of the lattice, $\mathbf{K}_1^{\mathrm{B}}$ is identical to $\mathbf{K}_3^{\mathrm{B}}$; further, by

Stone-Wales defect: Formation energies (eV)						
Method/XC	SLG	AB-BLG			TBLG	
		$\alpha\beta$-SW	$\alpha\beta$-SW	$\beta\beta$-SW	$\beta\gamma$-SW	$\gamma\gamma$-SW
LDA	5.25	5.39	5.36	5.38	5.35	5.36
	(5.47)	(5.47)	(5.45)	(5.47)	(5.45)	(5.46)
PBE	5.14	5.15	5.16	5.16	5.15	5.16
	(5.35)	(5.38)	(5.35)	(5.35)	(5.35)	(5.35)
DFT-D2	5.09	5.27	5.24	5.27	5.23	5.24
	(5.32)	(5.31)	(5.30)	(5.33)	(5.29)	(5.31)
Expt.	6.02 [189]					

Table 4.3: *Stone Wales defect formation energies for SLG, AB-BLG, and TBLG, with sine-like distortions in the defective layer. The values in parentheses are the formation energies when there is no distortion along z of the defective layer.*

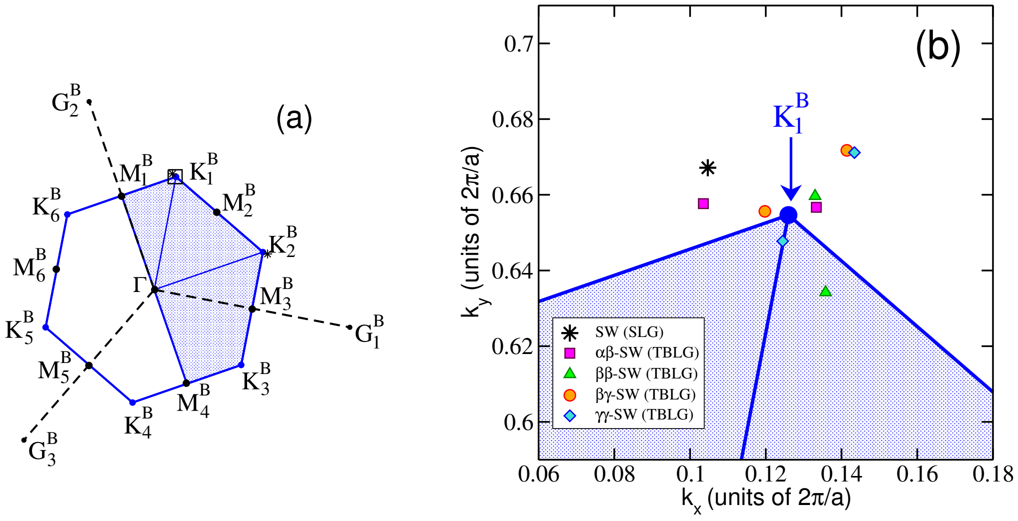

Figure 4.9: *(a) The First Brillouin Zone for the S_2 supercell of TBLG, and (b) the zoomed view of the region marked by the square in (a) showing the position of the Dirac point E_D for SLG with SW defect (asterisk) and Dirac points E_D^1 and E_D^2 for the four types of SW defect in TBLG. This figure has appeared in Ref. [144].*

using time-reversal symmetry, these are also identical to $\mathbf{K}_2^{\mathrm{B}}$. Thus, electronic eigenvalues should be identical at these three **K** points. However, no symmetries relate the three points $\mathbf{M}_1^{\mathrm{B}}$, $\mathbf{M}_2^{\mathrm{B}}$, and $\mathbf{M}_3^{\mathrm{B}}$.

Generally in the case of graphene, one tends to plot the band structure along a path connecting the high symmetry points of the Brillouin zone Γ, **K** and **M**. However, as we will see below, it is not particularly useful, and perhaps even misleading, to plot the band structure for our systems along these high-symmetry directions. Instead, we plot the surfaces of energy dispersion $E(k_x, k_y)$, in the vicinity of the point $\mathbf{K}_1^{\mathrm{B}}$, which is the region of especial interest. These results, for SW defects in SLG and AB-BLG, and the four distinct types of SW defects in TBLG, are plotted in Fig. 4.10.

Before we proceed to the band structure of TBLG, it is of interest to first consider the band structure of SLG with a SW defect, as it will help us to interpret our results for TBLG with SW defects. The band-structure of SW defects in SLG has been studied extensively in the literature. However it has been a subject of debate, whether or not the presence of the SW defect opens up a gap [44, 190]. This phenomenon of the presence or absence of the gap, has been shown to depend on the size of the supercell chosen to study the defect [191]. For supercell sizes that are $3n$ (n is an integer) times the graphene

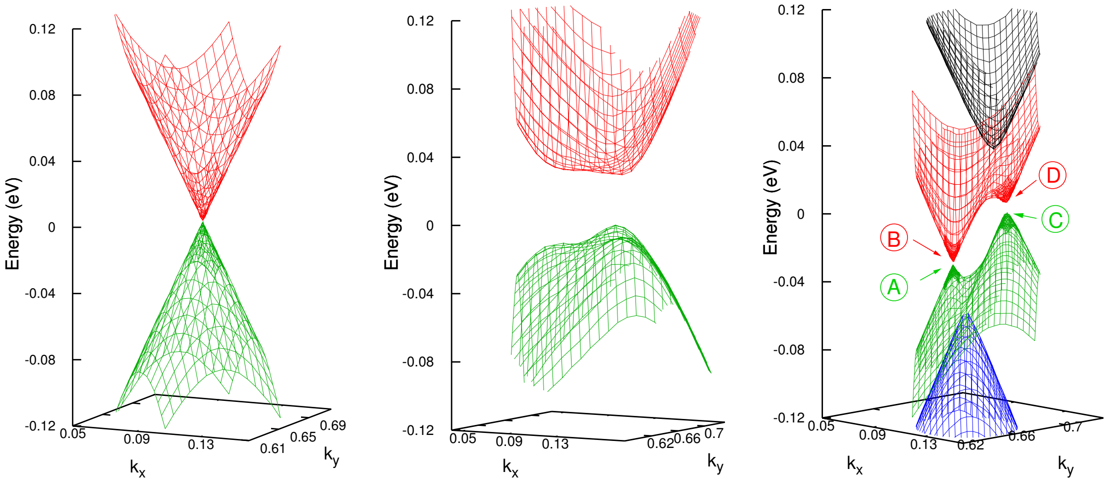

(a) SW (SLG) (b) SW (AB-stacked BLG) (c) $\gamma\gamma$-SW (TBLG)

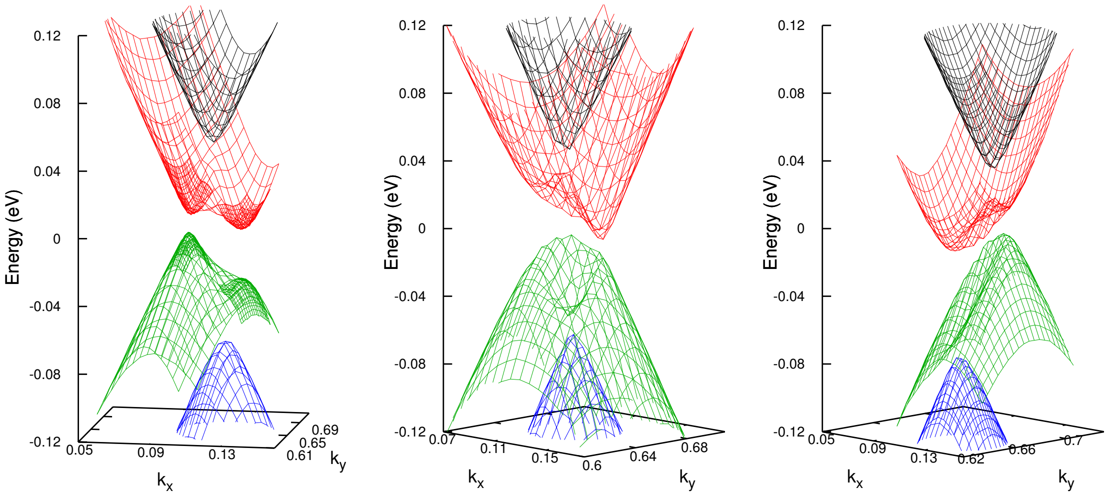

(d) $\alpha\beta$-SW (TBLG) (e) $\beta\beta$-SW (TBLG) (f) $\beta\gamma$-SW (TBLG)

Figure 4.10: *(a) Band structure in the vicinity of the Dirac point for the SW defect in* S_2 *supercell of SLG, and (b) band structure in the vicinity of* $\boldsymbol{K}_1^{\mathrm{B}}$ *for the SW defect in the* S_2 *supercell of AB-stacked BLG. Panels (c), (d), (e), and (f) show the band structure for* $\gamma\gamma$*-SW,* $\alpha\beta$*-SW,* $\beta\gamma$*-SW, and* $\beta\beta$*-SW, respectively in the vicinity of* $\boldsymbol{K}_1^{\mathrm{B}}$*. The degenerate Dirac bands for the TBLG split into a complex band-structure in addition to the shift from* $\boldsymbol{K}_1^{\mathrm{B}}$*. The valence band maxima (VBM) and the conduction band minima (CBM) are shown in panel (b) of Fig. 4.9, for all the cases of the SW defect in TBLG. This figure has appeared in Ref. [144].*

primitive unit cell, where the **K** point folds onto Γ, the presence of the SW defect opens up a gap. However for other supercell sizes, where this **K** to Γ folding is absent, the Dirac cone is preserved, and no gap arises due to the SW defect. In addition, there is a shift of the Dirac point away from the **K** point. The cause of these shifts in the Dirac point has been attributed to electron-phonon coupling [192]; note that the 90° bond rotation involved in the formation of SW defects can be viewed as a linear combination of Γ-point phonon modes [191]. In Fig. 4.10(a) we see that the Dirac cone is preserved even after introducing the SW defect, but the Dirac point has been shifted in k-space [see also Fig. 4.9(b), where the position of the shifted Dirac point is indicated by the asterisk]. Note however that the Dirac crossing energy E_D remains at the Fermi energy E_F.

Next, we consider the band structure of a SW defect in AB-BLG [see Fig. 4.10(b)]. The higher valence band VB1, and the lower conduction band CB1, have been plotted; VB2/CB2 lie considerably lower/higher in energy and are therefore not seen in this figure. A band gap of ∼34 meV has opened up in this case. The bands are very flat in the vicinity of $\mathbf{K}_1^{\mathrm{B}}$, and we therefore do not define a Dirac point.

Finally, we consider the band structure of the four kinds of SW defects in TBLG, in the vicinity of $\mathbf{K}_1^{\mathrm{B}}$. We show these results in Figs. 4.10(c)–4.10(f). It is interesting to compare these figures with Fig. 4.5, which shows the band structure of TBLG in the absence of the SW defect. We see that the introduction of the SW defect has had a significant impact on the band structure of TBLG. Moreover, the four figures 4.10(c)–4.10(f) show perceptible differences. This is because, as can be seen in Fig. 4.7, the registry between the atoms of the two layers is quite different for the four types of SW defects, as a result of which the interlayer coupling is quite different in the four cases.

Let us first consider Fig. 4.10(c), which is the easiest of the four to understand in terms of how it arises from two twisted bilayers, one of which contains a SW defect. The Dirac points of the two layers are shifted from each other in k-space, *even when we consider the "small" Brillouin zone that is commensurate with both layers* [See the blue hexagon in Fig. 4.2, also shown in Fig. 4.9]. We wish to emphasize that this is different from the usual case of pristine TBLG with, e.g., the S_2 supercell, where the Dirac points corresponding to the upper and lower layers are shifted in extended k-space, but fold back to the same $\mathbf{K}_1^{\mathrm{B}}$ point when considering the "small" Brillouin zone corresponding to the commensurate supercell. For conceptual purposes, it is easy to think of each of these two Dirac points as arising from the Dirac points of the two individual layers, one unrotated and pristine, and the other rotated and containing a SW defect (note, however, that this picture is oversimplified, and needs to be further qualified). For TBLG with a $\gamma\gamma$ SW defect, the Dirac point that arises primarily from the unrotated and undefective layer lies very close to the $\mathbf{K}_1^{\mathrm{B}}$ point [see the position of the blue diamond that lies within the first BZ in Fig. 4.9(b)]. The second Dirac point, which arises primarily from the rotated defective layer, is shifted further away from $\mathbf{K}_1^{\mathrm{B}}$ [see the position of the second blue diamond in Fig. 4.9(b)], as a result of the SW defect, as was seen, e.g., in Fig. 4.10(a). Very small minigaps open up at the two Dirac points due to interactions between the two layers. The two Dirac crossing energies E_D^1 and E_D^2 are slightly shifted with respect to each other, with one lying slightly below the Fermi energy E_F, and the other lying slightly above it. At energies further away from E_F, the two Dirac cones intersect, and the resulting avoided crossings result in the opening up of band gaps. As a result of this, the band VB1 has a skewed "M" shape, the band CB1 has a skewed "W" shape, and the bands VB2 and CB2 directly below and above these have conical shapes. The saddle points in VB1 and CB1 that form where the two cones fuse will give rise to van Hove singularities in the electronic density of states.

The same kind of interpretation applies to the other three types of SW defects ($\alpha\beta$, $\beta\beta$ and $\beta\gamma$) shown in Figs. 4.10(d)–4.10(f), although in these cases the underlying double cone structure is more distorted since the gaps that open up are larger (though the system remains semi-metallic), because of a greater effect of interlayer coupling. We point out that one effect of the introduction of the SW defects is an increase in the density of states at the Fermi energy, since the Dirac points E_D^1 and E_D^2 have now been shifted slightly below and above E_F.

As already noted, in Fig. 4.9(b) we have marked the positions in k-space of the Dirac points for the four kinds of SW defects in our TBLG. The Dirac points have been defined

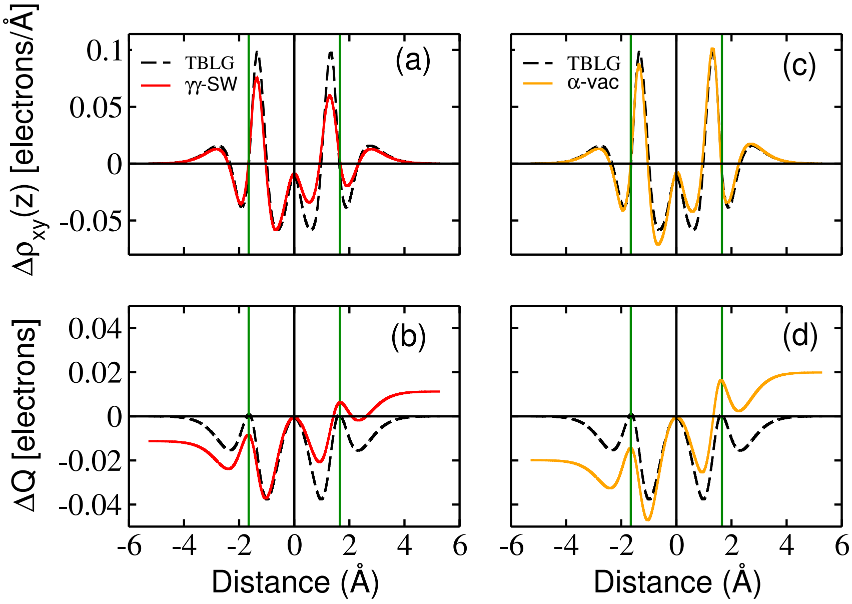

Figure 4.11: *Planar integral of the change in electronic charge density difference* $\Delta\rho_{xy}(z)$ *for (a) the SW defect (solid red line) and (c) monovacancy (solid orange line) in TBLG. The black dashed line in (a) and (b) shows the value of* $\Delta\rho_{xy}(z)$ *for pristine TBLG. The zero of the abscissa marks the midpoint between the two layers of TBLG. The net electronic charge lost or gained by the individual layers,* ΔQ*, is found by integrating* $\Delta\rho_{xy}$ *outwards from the midpoint of the layers. The cumulative value of* $\Delta Q(z)$ *for (c) the SW defect and (d) monovacancy in TBLG is shown. The black dashed line in (c) and (d) shows the value of* ΔQ *for pristine TBLG. This figure has appeared in Ref. [144].*

as the points in k-space corresponding to the maximum of VB1 and the minimum of CB1. Of these, one (arising primarily from the pristine layer) lies close to $\mathbf{K}_1^{\mathrm{B}}$, and one (arising primarily from the layer with the Stone-Wales defect) lies farther away. It is important to note that the direction of the shift of the second Dirac point (corresponding to the minimum of CB1) in k-space depends on the orientation of the SW defect in real space. For example, note that the points corresponding to the minimum of CB1 of $\beta\gamma$-SW and $\gamma\gamma$-SW case [shown by the round orange and blue diamond symbols in Fig. 4.9(b)] lie very close to each other; this is due to the fact that the orientation of $\beta\gamma$-SW and $\gamma\gamma$-SW defects are very similar [see Fig. 4.7(c) and Fig. 4.7(d)].

The skewed shape of the band structure arising from double Dirac cones [see Fig. 4.10], where VB1 looks like a tilted "M", and CB1 like a tilted "W", is reminiscent of the effects of a transverse electric field on the band structure of twisted bilayer graphene [43,146]. Note that even quite small electric fields (arising, e.g., due to a very minute charge transfer) can be expected to have a big effect on the positioning of the Dirac points with respect to E_F, because of the very low electronic density of states in this region. We next check what the nature of the charge transfer (between the two graphene layers) and charge redistribution (in the vicinity of each graphene layer) is when two graphene sheets are brought together to form our TBLG systems. In Fig. 4.11 (a) we have plotted our results for $\Delta\rho_{xy}(z)$, the planar integral of the change in electronic charge density of TBLG with a $\gamma\gamma$ SW defect, referenced to the sum of the charge densities of an isolated pristine graphene layer and an isolated graphene layer with a SW defect. Note that the charge densities of the latter two systems are computed making use of their geometries in the combined system. For comparison, we also plot the same results for TBLG without a SW defect. One can clearly see that while the curve for pristine TBLG (black dashed line) is symmetric about the midpoint, that for TBLG with a SW defect (red solid line) is asymmetric. By integrating $\Delta\rho_{xy}(z)$ outward from the midpoint, i.e., $z = 0$, we get the results shown in Fig. 4.11 (b). This shows clearly that upon bringing the two layers together, there is a depletion of electronic charge from the pristine layer, and an accumulation of charge in the defective layer; the net charge transferred is 0.0106 electrons. It is therefore quite tempting to apply a model in which there is a uniform positive charge (depletion of electrons) on the pristine layer and uniform negative charge (accumulation of electrons) on the defective layer, and approximate its effects as those of an electric field due to a parallel plate capacitor. This would yield an electric field of strength 1.3×10^8 NC^{-1}. We see from Fig. 4.10(c) that in our case, E_D shifts by $\sim$0.02 eV with respect to E_F. These results appear to be consistent with those of a previous study of undefective TBLG in an electric field, where the authors found that an electric field of 8.95×10^8 NC^{-1} resulted in the Dirac points getting shifted with respect to E_F by $\sim$0.1 eV [146]. However, while these results might seem initially encouraging, the actual situation is not so simple, since in our case, the shift in energy of the two Dirac points is opposite in sign to that predicted by this simple model of charge transfer, whether interpreted in terms of the direction of the electric field, or (equivalently) in terms of how E_F and E_D should shift with respect to one another when electrons are removed or added.

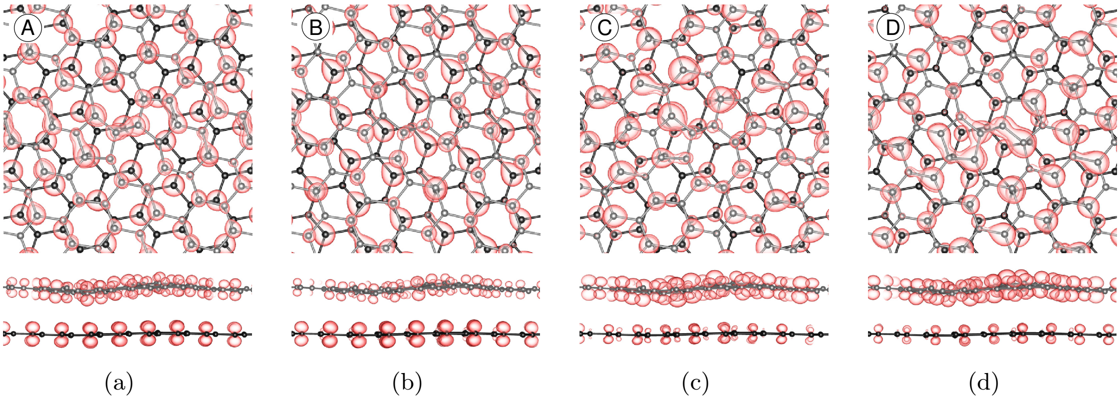

(a) (b) (c) (d)

Figure 4.12: *The distribution of charge density corresponding to the four states that lie just above and below the Dirac points for the case of $\gamma\gamma$-SW defect in TBLG (corresponding to the labels (A), (B), (C), and (D) shown in Fig. 4.10(c)), shown by the red lobes, for an isosurface of 7×10^{-4} e/bohr^3. The top panel shows the top view, where the upper layer is shown in gray and the lower layer in black. The bottom panels show the side view. This figure has appeared in Ref. [144].*

A similar situation, in which the relative shift between E_F and E_D is, in some cases, in the direction opposite to that expected from a naive model of charge transfer, has been observed by previous authors who studied the electronic structure of graphene on metals [193–196]. The authors of those previous studies attributed this to the presence of chemical interactions between the graphene and metal surface, which cannot be accounted for by the simple picture of charge transfer. For our systems, we find unmistakable signatures of the interaction between the two layers; it is clear that a scenario in which one Dirac cone is seen as arising entirely from the pristine layer, and the other as arising entirely from the defective layer, is not correct. As evidence of this, in Fig. 4.12, we have plotted the charge densities of four states very near the Dirac points, one each just above and below E_D^1, and one each just above and below E_D^2, for the case of the $\gamma\gamma$ Stone-Wales defect in TBLG. In all four cases, it is obvious that the states have significant charge density on both graphene layers, even though the two states near E_D^1 have a greater charge density on the pristine (lower) layer, and those near E_D^2 have a greater charge density on the defective (upper) layer.

We have also computed the band-structure of the $\gamma\gamma$ SW defect in TBLG using the LDA. Upon comparing with the results obtained using DFT-D2, (see Fig. 4.10) we find almost no change in the vicinity of E_F, although there are some slight differences at energies away from E_F.

4.4.2 Monovacancy Defect

A monovacancy defect can be created in a graphene sheet by removing one of the carbon atoms. In our example of TBLG, there are three inequivalent choices for the site at which this can be done; we term the resulting monovacancies as being of type α, β and γ (see Fig. 4.1). We introduce one defect per S_2 supercell for all these three types of monovacancies. This corresponds to a defect density of 1.8% For the case of the α-monovacancy, we have also considered defect densities of 7.2% and 0.8%, these correspond to defect calculation in different supercells S_1 and S_3, respectively. This allows us to examine the role of defect-defect interactions and strain relaxation in the defective systems.

The energy needed to create these vacancies is known as the monovacancy formation energy. The formation energy of a monovacancy [197] is defined as:

$$\Delta E_{\text{vac}} = E^{\text{vac}}_{S_i} - \left(\frac{N-1}{N} \right) E^{\text{novac}}_{S_i} \tag{4.16}$$

where $E^{\text{novac}}_{S_i}$ is the total energy of the pristine system containing N atoms in the supercell S_i, and $E^{\text{vac}}_{S_i}$ is the total energy of the supercell S_i that contains a single monovacancy and is comprised of $N-1$ atoms. Note that the system with the monovacancy is found to possess a magnetic moment, and all these total energies are therefore obtained from spin-polarized DFT calculations.

Our results for the monovacancy formation energy for various single-layer and bilayer graphene systems are shown in Table 4.4. As in the case of the SW defect, we see that the different atomic arrangements in the different types of monovacancies are not significantly reflected in the energetics of defect formation: the values of ΔE_{vac} for the three types of monovacancy for TBLG are very close to one another, and also to the values for SLG and AB-BLG.

Structural Properties

In all the three types of monovacancies considered for TBLG, both layers remain almost planar. The nearest-neighbor atoms of the vacancy site are displaced noticeably from their positions in the undefective structure. The removal of a carbon atom results in the under-coordination of its three nearest neighbor carbon atoms, resulting in the creation of unpaired electrons over each carbon atom. The three-fold symmetry about the vacancy site is broken by a Jahn-Teller type distortion, resulting in an effective bonding between any two of the three nearest neighbor carbon atoms. We find that two of the atoms are attracted toward each other and the distance between these atoms is reduced significantly, showing a signature of bonding. A similar phenomenon has earlier been reported for a monovacancy in a single layer of graphene [46] and for an AB-stacked bilayer of graphene [198]. We observe such a phenomenon in all the three vacancy positions: α, β and γ-vacancy [see Figs. 4.13(a), 4.13(b) and 4.13(c)]. For the choice of defective supercell S_2, this bond distance is found to be 2.05 Å, 2.03 Å, and 2.04 Å, for α, β and γ-vacancies, respectively. For the case of the α-vacancy, we have also considered different supercells S_1 and S_3, corresponding to a defect density of 7.2% and 0.8%, respectively. In these cases, this shorter bond distance is found to be 2.29 Å and 1.86 Å, respectively.

Note that as the size of the supercell used for studying the defect increases (i.e., the defect density goes down), the Jahn-Teller distortion is much more prominently observed. In a larger supercell, the strain induced by the presence of the monovacancy can relax more effectively, via a progressive displacement of the atoms from their original positions. This displacement of carbon atoms goes down as one moves away from the defect. The size of the supercell introduces a constraint on this relaxation. Thus, the larger the supercell, the better is the strain relaxation, and the more prominent is the effect of Jahn-Teller distortion. For our calculations of defects in the supercells, S_1, S_2, and S_3, the average in-plane stress was found to be -0.142, -0.071, and -0.043 eV/Å^2, respectively. The negative sign denotes that this is a tensile stress. This clearly shows that the maximum strain relaxation is observed in the largest supercell.

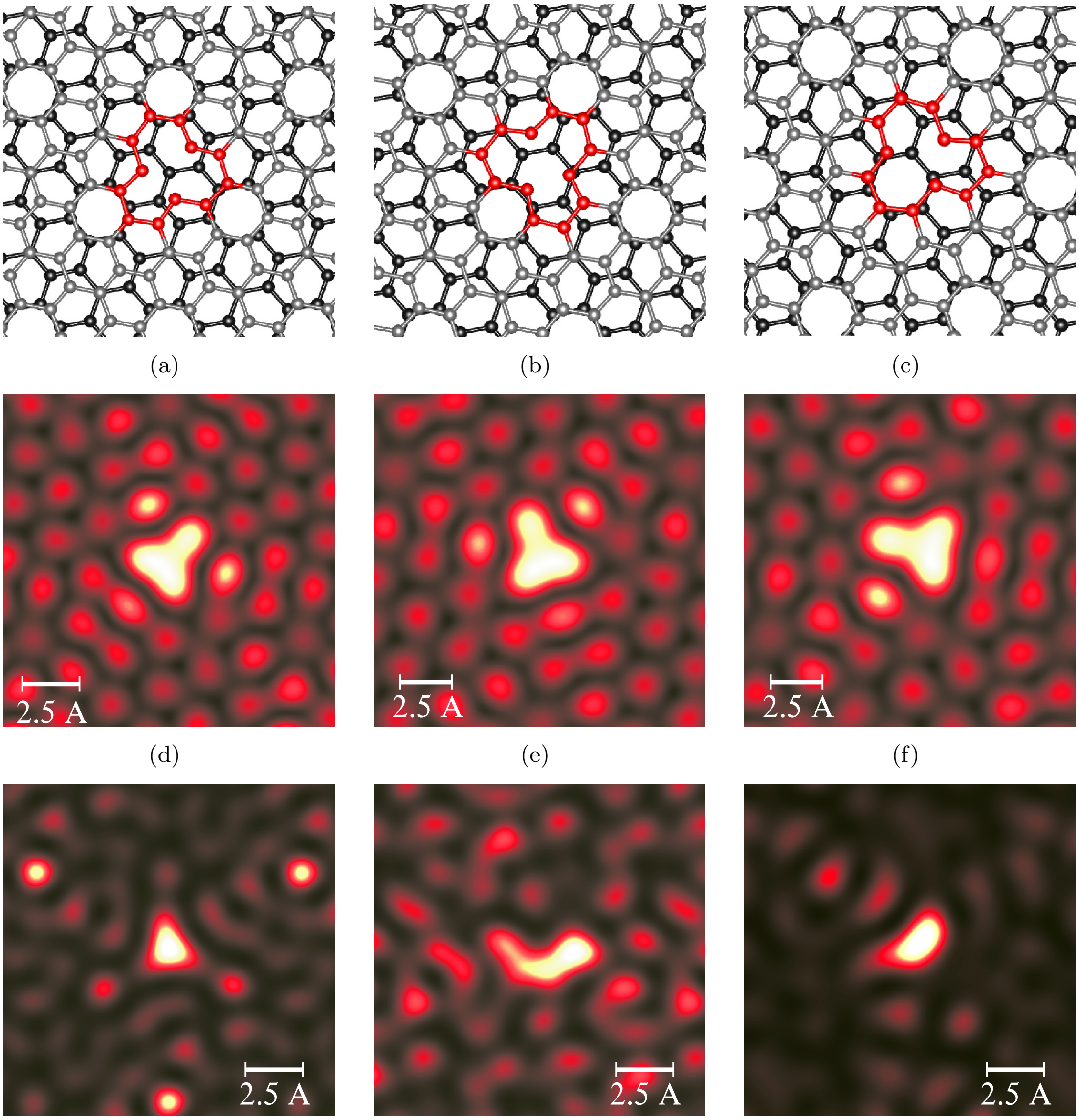

(a) (b) (c)

(d) (e) (f)

(g) (h) (i)

Figure 4.13: *Atomic structures for (a) α-vacancy, (b) β-vacancy, and (c) γ-vacancy. Lower layer atoms are black, and the upper defective layer atoms are light gray. The C atoms near the vacancy-defect are colored red for visual ease. Simulated STM images "taken" from the defective side for α-, β-, and γ vacancies are shown in Figs. (d), (e), and (f), respectively and those "taken" from the undefective side are shown in Figs. (g), (h), and (i), respectively. The images from the defective side are essentially indistinguishable, but the STM images from the undefective side show the effects of the relative orientation with respect to the other layer. This figure has appeared in Ref. [144].*

Simulated STM images

Next, we compute simulated STM images of the monovacancy defects in TBLG (see Fig. 4.13), making use of a bias voltage of 0.4 eV. The STM images of the three types of monovacancies (α, β and γ) are basically indistinguishable, if the STM image is taken from the defective side of the bilayer. Interestingly, however, if the STM image is taken from the *undefective* side of the bilayer, one can distinguish between the three types of monovacancies, as their STM images show markedly different signatures; see the three lowest panels in Fig. 4.13.

Electronic Structure and Magnetic Properties

Creating a monovacancy in TBLG results in the appearance of a magnetic moment; its origin is similar to that in single layer graphene [48, 50]. In a pristine graphene layer, each carbon atom is bonded to three of its neighbors by three sp^2 hybridized σ-bonds and one π-bond, each bond sharing two electrons. When one carbon atom is removed to create a monovacancy, the carbon atom that is removed takes away its share of four electrons, and there are three unsatisfied sp^2 σ-electrons (one electron localized on each of the three nearest neighbor carbon atoms) and one π-electron, near the monovacancy. These unpaired electrons in each of these states will try to maximize the spin, giving rise to a net magnetic moment of 4 μ_B. As noted above, two of the three C atoms surrounding the vacancy rebond, lowering the energy via a Jahn-Teller type distortion. The spins of the σ-electrons involved in this bonding pair up, due to Pauli's exclusion principle. Thus the monovacancy is expected to have a net magnetic moment of 2 μ_B, arising from one σ state and one π state. This is why creating a monovacancy in a graphene sheet results in the appearance of a magnetic moment. However, as the π-electrons have a somewhat itinerant character, and their bands cross the Fermi level, there is fractional occupation of this state, so that the magnetic moment becomes less than 2 μ_B. In our case of a monovacacy in TBLG, in supercells of different sizes S_1, S_2 and S_3, we find a net magnetic moment of 1.81 μ_B, 1.25 μ_B and 1.85 μ_B per defect, respectively. These values are in good agreement with earlier reported values for monovacancy defects in SLG (magnetic moments of ranging from 1 μ_B to 2 μ_B depending on the defect concentration [46, 50]) and in AB-BLG (magnetic moment of 1.3 μ_B [198]). In Table 4.4, we have reported the values for the net magnetic moment per defect, defined as $M_{net} = \int d^3r(\rho^{\uparrow}(\mathbf{r}) - \rho^{\downarrow}(\mathbf{r}))$

Monovacancy defect: Formation energies ΔE_{vac}(eV)

Method (XC)	SLG	AB-BLG		TBLG		
		α-Vac	β-Vac	α-Vac	β-Vac	γ-Vac
LDA	8.09	8.06	8.03	8.07	8.08	8.07
PBE	7.72	7.71	7.71	7.72	7.72	7.72
DFT-D2	7.77	7.76	7.72	7.77	7.79	7.77
Expt.	7.0±0.5 [199]					

Monovacancy defect: Magnetic Moments (μ_{B})

Method (XC)	SLG	AB-BLG		TBLG		
		α-Vac	β-Vac	α-Vac	β-Vac	γ-Vac
LDA	1.25	1.25	1.25	1.25	1.25	1.25
	(1.46)	(1.46)	(1.47)	(1.46)	(1.46)	(1.46)
PBE	1.25	1.25	1.25	1.25	1.25	1.25
	(1.63)	(1.63)	(1.64)	(1.63)	(1.63)	(1.64)
DFT-D2	1.25	1.25	1.25	1.25	1.25	1.25
	(1.63)	(1.64)	(1.65)	(1.64)	(1.63)	(1.63)

Table 4.4: *Calculated values of monovacancy formation energy and net magnetic moments (M_{net}), for SLG, AB-BLG, and TBLG. The values in parentheses denote the absolute magnetization per defect (M_{abs}).*

and the absolute magnetic moment per defect, defined as $M_{abs} = \int d^3r|(\rho^{\uparrow}(\mathbf{r}) - \rho^{\downarrow}(\mathbf{r}))|$, for each of the cases considered by us in the supercell S_2. Here $\rho^{\uparrow}(\mathbf{r})$ and $\rho^{\downarrow}(\mathbf{r})$ are the up-spin and down-spin charge densities, respectively, and the integration is carried out over the supercell S_2. All three exchange-correlation functionals give $M_{net} = 1.25\ \mu_B$ for all systems. Interestingly however, the values obtained for M_{abs} vary with the functionals used, being $\sim 1.46\ \mu_B$ for LDA and $\sim 1.63\ \mu_B$ for PBE and DFT-D2. No significant changes in magnetic moments are seen on going from SLG to AB-BLG or TBLG.

We examine the band structure of twisted bilayer graphene to see the effect of the twist; these results are shown in Fig. 4.14. Due to the presence of the vacancy in the twisted supercell, the IBZ becomes half of the entire BZ, similar to that in the case of the SW defect. In the case of SW defects, we had observed a shift of the Dirac cone from the **K** point, and hence had plotted the three-dimensional band structure to ensure the correct visualization of the energy bands. In the case of monovacancies in TBLG, there is no shift in the position of the Dirac point in k-space. Therefore, it is sufficient to plot

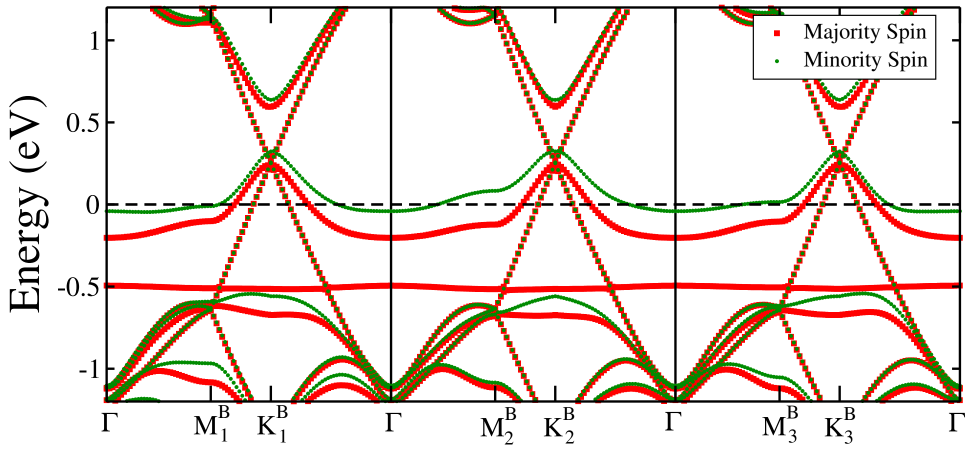

(a) α-vac TBLG

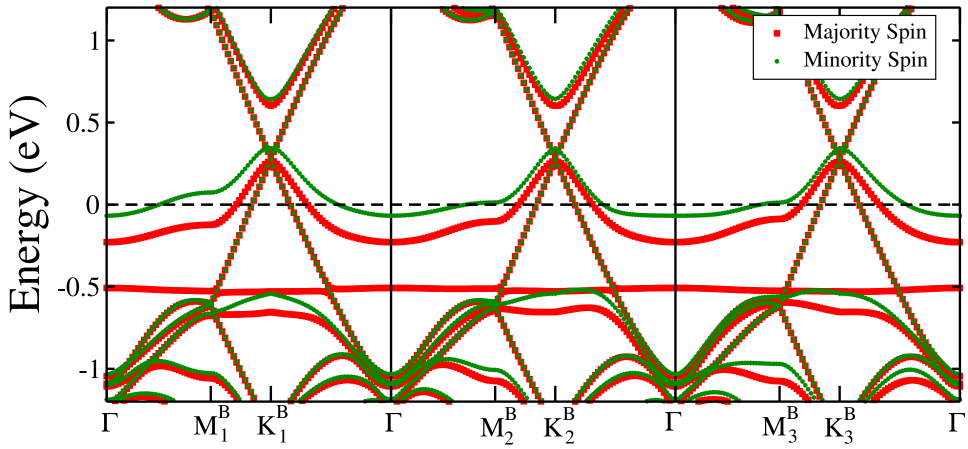

(b) β-vac TBLG

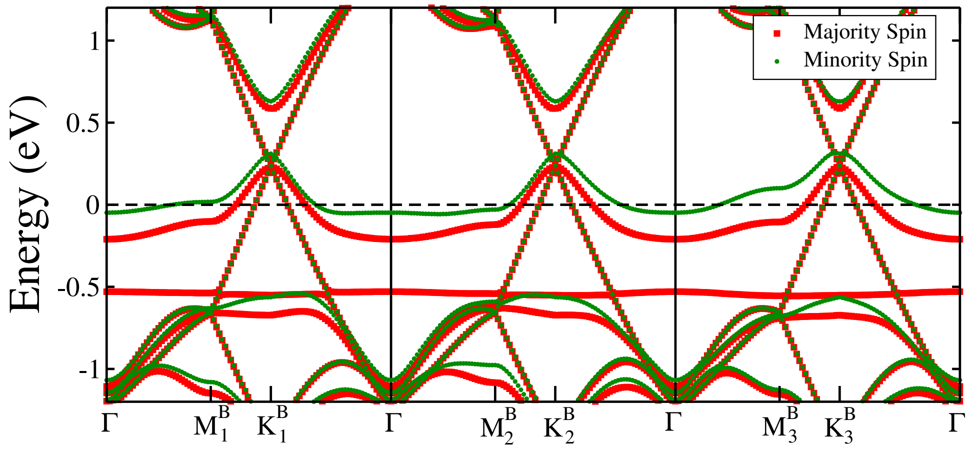

(c) γ-vac TBLG

Figure 4.14: *Electronic band structure for (a) α-, (b) β-, and (c) γ- monovacancies in TBLG, plotted along high-symmetry directions in the Brillouin zone shown in Fig. 4.9(a). The majority spin channel is shown in red and the minority in green. The dashed line denotes the position of the Fermi energy E_F. This figure has appeared in Ref. [144].*

the band structure along the conventionally used paths in the BZ; we show the plotted band structure in Fig. 4.14. We first compare the results obtained in the three types of monovacancy defects in TBLG. We see that for a particular type of monovacancy, the features of the four bands (two up-spin and two down-spin) that cross the Fermi level are quite similar in each third of the IBZ. Moreover, these four bands are also quite similar for the three different types of monovacancies (differences in the band structure become more apparent as one moves further away from the Fermi level). Therefore, for simplicity, when discussing the features of the band structure, and comparing it with the band structure of a monovacancy in SLG and pristine SLG, we will restrict ourselves to considering the band structure of the α-monovacancy in TBLG, in one-third of its IBZ.

We carry out this comparison in Fig. 4.15. It is interesting to note that the band structure of TBLG with a monovacancy [Figs. 4.15(c) and 4.15(g)] is clearly derived from the superposition of the band structures of a pristine SLG layer [Figs. 4.15(a) and 4.15(e)] and SLG with a monovacancy [Figs. 4.15(b) and 4.15(f)] with some important modifications. The bands derived from those of pristine SLG are shifted up in energy quite significantly, so that the Dirac crossing point E_D now occurs $\sim$ 0.25 eV above E_F. In contrast, the bands arising from the layer with the monovacancy defect are shifted very slightly down in energy, there is also a slight change in their shape, which has a significant impact on the density of states because of the flat dispersion.

The shifting up/down of bands can be caused due to three reasons: (i) the layer with the monovacancy has one atom removed, and hence has four valence electrons less than the pristine layer, (ii) there is a charge transfer between the layers, similar to that observed in the case of the Stone-Wales defect, and (iii) there is a chemical interaction between the layers. The effect of (i) alone can be artificially examined by separating the two layers by a very large distance of 6.5 Å. The band structure for this artificial case is shown in Figs. 4.15(d) and (h). In this case, we find that the Dirac crossing energy E_D arising from the pristine layer lies 0.32 eV above E_F; this shift can be attributed entirely to the requirement of equilibration of the Fermi energies of the two layers. However, when the spacing between the two layers is reduced to its equilibrium value of 3.3 Å, this upward shift is partially canceled by a downward shift that arises due to the combined effect of (ii) and (iii), resulting in the final upward shift of 0.25 eV observed.

The initial shift of 0.32 eV can also be understood from computations of the work function W. The work function is defined as the difference in energy between the vacuum level and the Fermi energy E_F. For SLG, we find that $W = 4.24$ eV, whereas for SLG with a monovacancy, $W = 4.56$ eV; both of these values are computed making use of the same S_2 unit cell that is used for calculations of TBLG. When the two layers are brought together, with an interlayer separation of 6.5Å, we again obtain $W = 4.56$ eV; this is because of the flat dispersion of the monovacancy states near E_F and the resulting high value of the density of states, so that the states arising from the layer with the monovacancy do not shift perceptibly in energy, whereas the states arising from the pristine layer are shifted in energy by $4.56 - 4.24 = 0.32$ eV.

The interlayer interaction becomes more clear when we compare the low-lying states shown in the bottom panels [(e), (f), (g), and (h)] of Fig. 4.15. When a pristine SLG, and a SLG with a monovacancy are brought together, in the absence of any interlayer coupling, the lowest energy states shown in Fig. 4.15(h) are clearly a superposition of the states in Fig. 4.15(e) and 4.15(f). However in the presence of interlayer interactions, the lowest lying states split in energy. These splittings are a clear signature of the interlayer coupling between the two layers.

The interlayer charge transfer described above can be computed, as in the case of the Stone-Wales defect, by integrating the planar average of the charge redistribution. The planar average is plotted as a function of the z coordinate in Fig. 4.11(c) and is seen to be asymmetric. On integrating outward from the midpoint of the two graphene layers, we find that the pristine layer has lost 0.02 electrons, and the layer with the monovacancy has gained 0.02 electrons [see Fig. 4.11(d)]. These values are in good agreement with the values obtained from a Bader charge analysis, which yields a net charge on the pristine layer of 223.983 electrons, and on the defective layer of 220.016 electrons, i.e., 0.016 electrons have been transferred from the former to the latter.

In Fig. 4.16, we plot a charge density difference map which shows the redistribution in

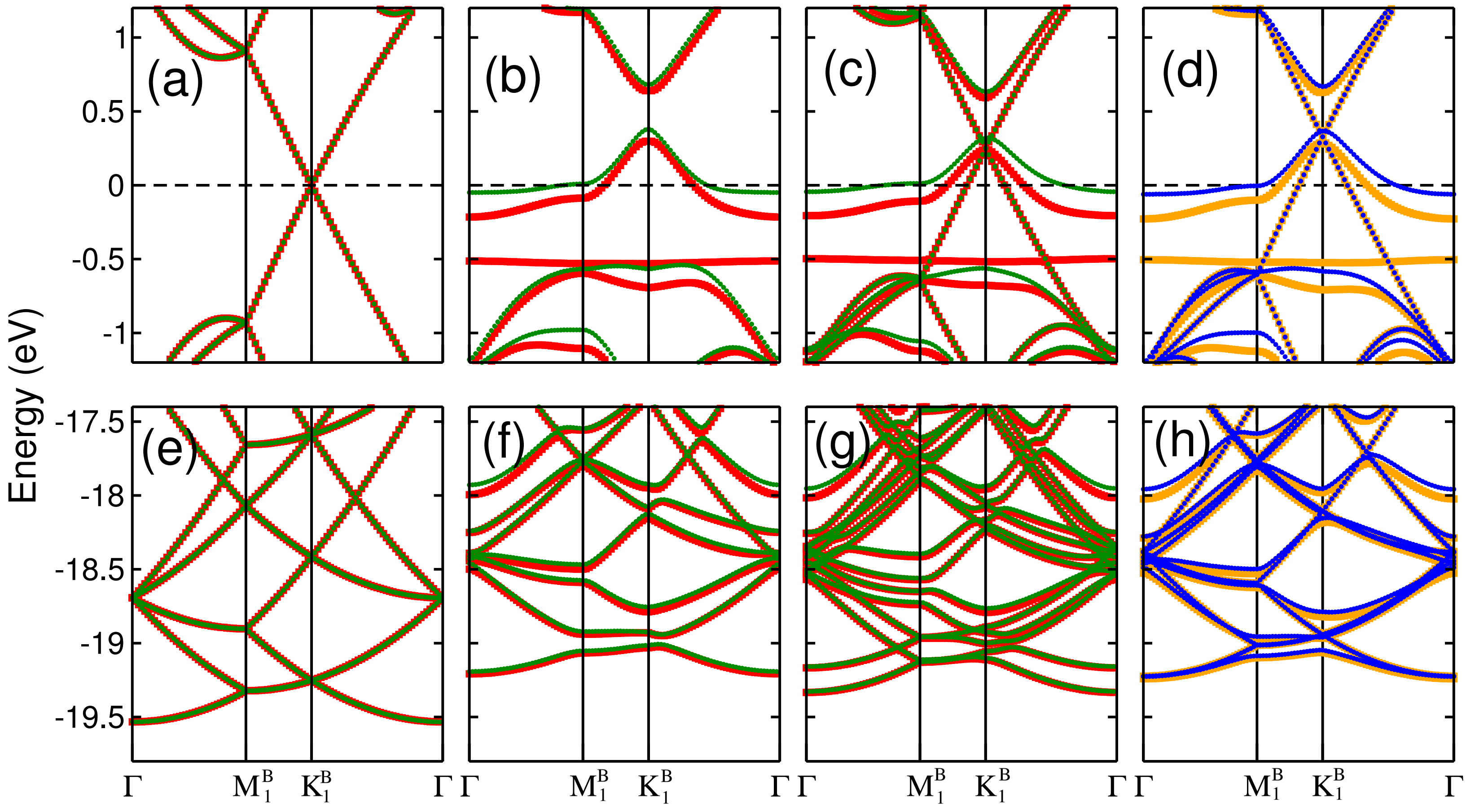

Figure 4.15: *Electronic band structure for SLG (a) and (e), monovacancy in a SLG (b) and (f), α-monovacancy in TBLG (c) and (g), plotted along high-symmetry directions in the Brillouin zone shown in Fig. 4.9(a). We have also plotted the band structure for the case of α-monovacancy in an artificial case of TBLG with interlayer distance of 6.5 Å shown in panels (d) and (h). The top panels (a), (b), (c) and (d) show the band structure in the vicinity of* E_F. *The bottom panels (e), (f), (g), (h), show the low lying states. The dashed line denotes the position of the Fermi energy* E_F. *Red and green symbols indicate values for the majority and minority spins, respectively. In panels (d) and (h), we have used orange and blue symbols for majority and minority spins, respectively, to show the bands for the artificial case of TBLG with interlayer distance of 6.5 Å.*

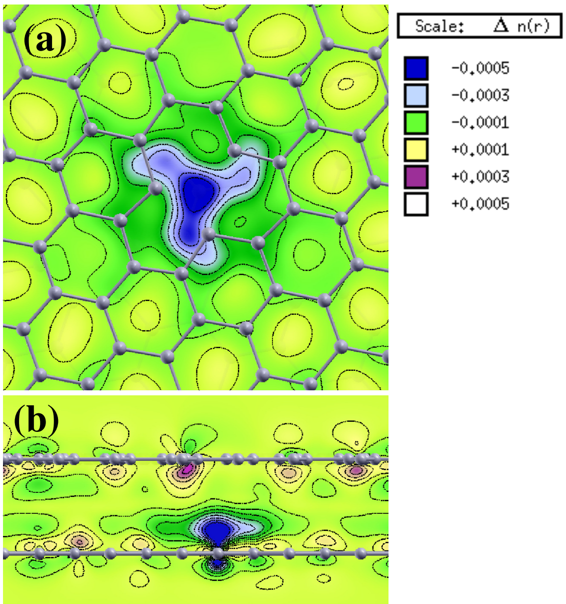

Figure 4.16: *Charge density redistribution in the vicinity of the undefective lower layer of TBLG due to the presence of an* α*-monovacancy in the upper layer. Part (a) shows the contours of the depleted charge density in a plane about 0.8 Å above the undefective layer. The atoms of the upper layer are shown as a reference. Part (b) shows a cross-sectional view of the redistributed charge in a plane perpendicular to the layers. The units of the charge density redistribution are e/bohr*^{3}*. This figure has appeared in Ref. [144].*

charge upon bringing the two twisted layers (one pristine, and one with a monovacancy) together. To obtain this map, we subtract the individual charge densities of the defective SLG and the pristine SLG (maintaining their geometry as that in the combined system), from the charge density of the defective bilayer. A region of charge depletion is developed below the vacancy site, slightly above the undefective layer. We have plotted this for the α monovacancy; similar plots are obtained for the β and γ monovacancies. The charge redistribution in the presence of a monovacancy is again a manifestation of the interlayer coupling in twisted bilayer graphene.

Once again, as seen in the case of TBLG with a Stone-Wales defect, merely considering a simple model of the net electronic charge transfer from the undefective to the defective layer, would lead one to expect that E_D will shift up further upon reducing the separation from 6.5 Å to 3.3 Å. The fact that, in contrast, it shifted downward, is a manifestation of the chemical interaction between the layers, as already discussed in the case of the SW defect.

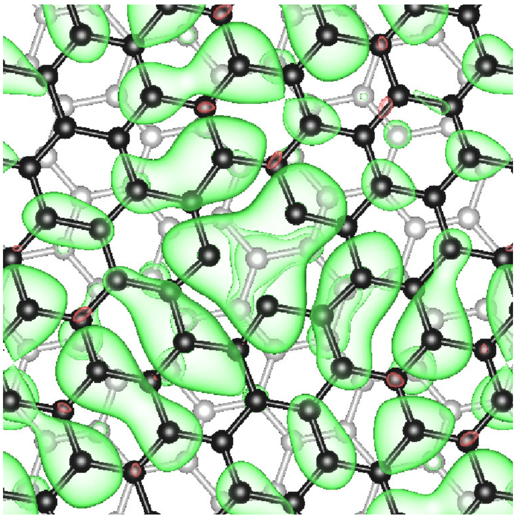

Figure 4.17: *Spatial extent of the spin polarized charge density* ρ_{SP} *corresponding to the states in an energy window* $\{E_F - 0.05\text{eV}, E_F\}$ *for the case of monovacancy in TBLG. The isosurfaces shown correspond to a density value of* $\pm 2 \times 10^{-5}$ *e/bohr*^{3}*. Green lobes denote negative values, and red lobes (barely perceptible) denote positive values. This figure has appeared in Ref. [144].*

The magnetic defect state that arises due to the creation of the vacancy in a single layer of graphene (SLG) can be seen in the band structure as a spin-polarized flat band about 0.5 eV below the Fermi energy E_F, and it can also be identified as a sharp peak in the density of states [see Figs. 4.15(b) and 4.15(c)]. This corresponds to the unpaired σ-electron on one of the atoms near the vacancy. Further, the Dirac-like π-electrons are scattered by the monovacancy, resulting in the breakdown of the Dirac cone in the defective sheet, and instead opening up of a gap. The Fermi energy is lowered due to the removal of a carbon atom, and hence the Fermi level falls in the bands below this opened gap. The π-band is also spin polarized, as can be seen in the energy range -0.25 eV to 0.4 eV. The high density of states near the Fermi energy for one of the spin channels leads to a high spin polarization of π-electrons below E_F.

The spin-polarized charge density ρ_{SP} is defined as the difference between the majority and minority spin charge densities. In Fig. 4.17, we have plotted ρ_{SP} in an energy window of width 0.05 eV below E_F, for an α monovacancy in TBLG. It is clearly evident that the spin polarization is not restricted to the immediate neighborhood of the monovacancy, but is widespread in spatial extent. This may lead to a high degree of spin polarization of a current that is passed through such a system. However, the net spin-polarization of the charge density, in a situation of randomly oriented monovacancy defects, may depend on the sublattice details of a particular distribution of the defects, similar to that seen in the case of SLG [48].

4.5 Summary and Conclusions

In this chapter, we have studied two types of point defects, viz., Stone-Wales defects and monovacancy defects, that can arise or can be induced in twisted bilayer graphene. We have focused on how these defects alter the structural, electronic and magnetic properties of twisted bilayer graphene. We have compared these results with the same defects in single layer graphene and AB-stacked bilayer graphene.

The formation energy of these defects is very similar to those of the corresponding defects in single layer graphene and in AB-stacked graphene; this is to be expected because the coupling between the two layers in twisted bilayer graphene is weak. The effect of the presence of the second layer on the defect energetics is not particularly prominent. Also inducing the defect on various symmetry-inequivalent sites on TBLG does not appreciably affect the defect formation energy.

However the presence of the weak interlayer coupling manifests itself more appreciably when we examine the band structure of TBLG with defects. When we consider TBLG with a SW defect in one of the layers, the band structure near E_F can be interpreted as arising from a combination of two Dirac cones, that are shifted slightly in energy and momentum. The shift in energy of the two Dirac cones is due to the combined effect of a transfer of electrons from the pristine to the defective layer, and a chemical interaction between the two layers; this mimics the effect of placing the system in an electric field. The site at which the SW defect is created also affects the band structure – at some sites, the underlying double cone structure near the K points is distorted by the opening up of mini gaps. However, actual experimental control on the defect formation site might be difficult.

We note here that the use of periodic boundary conditions in our plane wave calculations means that we actually have a periodic array of SW defects. Recent work has shown that it is possible to create multiple Dirac cones by artificially engineering a lateral periodic potential by creating a superlattice [200].

The creation of a monovacancy in one layer of TBLG causes the Dirac cone of the other layer to shift up in energy by ~ 0.25 eV. This is a combined effect of the requirement of the equilibration of the Fermi energies, charge transfer and chemical interaction between the sheets. Both SW defects and monovacancies increase the density of states at E_F; this should be of relevance to transport properties. Similar to what is observed in the case of the monovacancy defect in SLG and AB-BLG, the monovacancy defect in TBLG results in a magnetic moment. A sharp magnetic defect state arises from the unpaired σ-electron on one of the nearest-neighbor atoms of the vacant site. The defect has a magnetic moment of $\sim 1.2 - 1.8\ \mu_{\mathrm{B}}$, depending on the defect density. Spatially extended, spin polarized π-states are also observed near the Fermi energy, both in the case of SLG and TBLG. This raises a possibility of a large spin-polarization of the current in the defective layer.

By comparing results obtained with the LDA, GGA (PBE) and DFT-D2 methods, we find that the PBE alone (i.e., without van der Waals interactions incorporated) generally leads to an inadequate description of the properties bilayer graphene in general, and TBLG in particular. In general, both LDA and DFT-D2 give very similar results, with a few notable exceptions: the exfoliation energy predicted by DFT-D2 is in closer agreement with experiment. Also note that even though both these methods give similar results for the net magnetic moment M_{net}, they give different values for the absolute magnetic moment M_{abs} for TBLG with a monovacancy.

In summary, we have studied the effect of creating point defects in TBLG, either by removing atoms or altering their positions. We have seen that the creation of these defects alters the electronic and magnetic properties of twisted bilayer graphene.

Chapter 5

Physical Origins of Weak H_2 Binding on Carbon Nanostructures

In the last two chapters, we had focused on tuning those properties of nanostructured materials which are relevant for applications in electronics. Now we try to enhance the adsorptive properties of carbon nanostructures, which would be helpful for designing better on-board gas storage materials for vehicular applications. We do this by adding new chemical functional groups to these nanostructures, which would act as binding sites for gas molecules. In this study we limit ourselves to H_2 adsorption. As a substrate for adsorption, we choose zigzag graphene nanoribbons, and vary the chemical functionalization of the edges of these nanoribbons, in an attempt to enhance the binding of H_2.

We have now moved to one dimensional systems (zigzag graphene nanoribbons), as we want to model the adsorption properties at chemically functionalized edges of carbon nanostructures. In our calculations, which use periodic boundary conditions, we now need to incorporate vacuum spacing along two directions of our system, one normal to the graphene layer, and the other perpendicular to the zigzag edge. This will further increase the computational expense of our calculations.

Some of the results presented in this chapter have been published in Ref. [201].

5.1 Introduction

Due to many reasons, like increasing costs and depleting resources, finding alternatives to fossil fuels has become essential. For on-board vehicular applications, hydrogen is an ideal candidate as a fuel. It is the most abundant element in the universe, and is an extremely clean burning fuel, producing only water vapor when combusted or used in a fuel cell. Being the lightest element, it also has excellent gravimetric energy density, next only to nuclear power. However, it is not viable to store hydrogen in gaseous or liquid form for vehicular applications, and it is necessary to find new ways of storing hydrogen. On-board storage as a compressed gas or liquid requires heavy, large, and cumbersome tanks under potentially cryogenic conditions, and raises safety concerns due to the highly explosive nature of gaseous hydrogen. A possible solution to this problem is to store hydrogen in the solid state [53], i.e, to adsorb hydrogen molecules on the surface or in interior voids of a solid. This solution is still a tricky one, as only an optimum adsorption energy range is ideal for gas storage. From a thermodynamic perspective, the ideal gas binding strength is intermediate between physisorption and chemisorption. This means the gas should not bind so strongly to the substrate that its release is inhibited; at the same time, it should not bind so weakly that a significant amount cannot be stored at ambient temperature and readily achievable pressures [202].

Carbon-based materials are one class of materials that have been considered for the adsorptive storage of H_2 and other small gas molecules [53, 202]. Several micro- and mesoporous systems, including activated carbon, as well as recently synthesized carbon nanostructures such as fullerenes, carbon nanotubes and graphene, have high theoretical capacities due to their large surface area [54, 55]. However, the binding of molecular hydrogen to these materials is generally too weak. There have been a number of suggestions for increasing the binding strength of hydrogen on carbon nanostructure. These include doping the carbon substrate with alkali or transition metals, as well as applying mechanical strain on the substrate, or changing the curvature [203, 204]. However, none of these approaches on their own, has been proven to be sufficiently successful. One could try to combine many strategies in order to enhance adsorption in carbon-based systems, so that these materials can achieve room-temperature storage targets.

Another solution for enhancing the adsorption on carbon based materials would be to create reactive edges, as well as proper chemical functionalization of these edges, so that these serve as binding sites for the hydrogen molecules. There are many theoretical and experimental studies that have shown that the presence of edges significantly affects the properties of graphene [205, 206]. The changes in coordination and electronic configuration near the edges result in significant changes in the chemical reactivity of graphene [207,208]. In particular, zigzag edges were shown to exhibit high reactivity [209]. It has also been shown that some small chemical functional groups such as carboxyl [210] and hydroxyl [209], as well as some large molecules such as peptides [211], tend to bind preferentially to the edges of graphene sheets. The presence of these functional groups affects the stability and electronic and magnetic properties of the system [212–215].

Chemical functionalization of the edges also represents a promising avenue for tuning the hydrogen uptake of activated carbons. Activated carbon materials are cheap, and can be produced from agricultural waste via pyrolysis, followed by treatment with a base or acid. The precise structure of activated carbons is not known, but model structures generally consist of fragments of sp^2 bonded graphitic sheets, with a large proportion of exposed edges [216]. Activated carbons feature functional groups such as phenolic (OH), amine (NH_2), phosphonic (H_2PO_3), peroxide (OOH), pyran (-O-), and carboxyl (COOH); it is believed that these groups occur mostly at graphitic edges [218].

In this chapter, we study what is the effect of chemical functionalization of the zigzag edges on the adsorption of hydrogen molecules. We wish to find out which functional groups are best, and why they are so. We try to gain fundamental insights into the key physical contributions that give rise to weak binding of gas molecules on sp^2 carbon substrates, and which of these might best be leveraged for further increasing absorptive capacity. The relevance of this study can be viewed in two ways: it can be seen as a study of the adsorption properties of graphene and graphene nanoribbons themselves. At the same time, it can be viewed as having implications for the use of activated carbons and related materials as hydrogen storage media.

5.2 Computational Details

We have performed spin-polarized density functional theory (DFT) calculations using the PWscf code, which is part of the Quantum-ESPRESSO distribution [78]. We used a plane wave basis set to expand the Kohn-Sham wave functions of the system. We also used ultrasoft pseudopotentials [89] to deal with the interactions between ionic cores and valence electrons. A plane-wave cutoff of 40 Ry for the wavefunctions and 480 Ry for the charge densities was used. The Perdew-Burke-Ernzerhof (PBE) [77] form of the generalized gradient approximation was utilized to approximate the exchange-correlation interactions. We have used a (4×4) unit cell of graphene to perform adsorption calculations on an extended graphene sheet, for which a Brillouin zone sampling of $(3 \times 3 \times 1)$ k-points in a Monkhorst-Pack grid was found to be sufficient. Calculations of adsorption on zigzag graphene nanoribbons (ZGNRs) were performed using a ribbon that was six carbon atoms wide, with a unit cell that was eight carbon atoms long; for these calculations, a $(3 \times 4 \times 1)$ k-point grid was used. To improve convergence we have used Marzari-Vanderbilt cold smearing [178] with a width of 0.007 Ry. In order to aid comparison with earlier results on adsorption of methane and carbon dioxide on edge-functionalized ZGNRs [219], we have used system sizes and calculation parameters that generally match with this study.

The binding of hydrogen to the systems considered in our study is expected to be weak and governed by van der Waals interactions. Three kinds of interaction terms are included in the van der Waals interactions, (i) the Keesom term, which is the interaction between permanent dipoles in the system, (ii) the Debye term, which is the interaction between permanent dipoles and induced dipoles in the system, (iii) the London dispersion term, which is the the interaction between instantaneously induced dipoles in the system. The London dispersion term is generally not correctly included in traditional DFT calculations. However, several methods have been developed in recent years to include these dispersive interactions in DFT calculations [93–95]. The inclusion of the London term is vital to get a correct description of weak binding of gases, and therefore one should use one of these methods. We have chosen to use the "DFT-D2" treatment of Grimme, which gives a fairly accurate treatment of London dispersion interactions at relatively low computational cost [93].

In our calculations, we consider three different regimes of chemical functionalization of the edges of ZGNRs: (1) the dilute functionalization regime, where one functional group is adsorbed on one of the zigzag edges of the unit cell considered [see Fig. 5.1(a)], (2) the strong functionalization regime, where two functional groups (of the same type) are adsorbed on the same edge, using the same unit cell [see Fig. 5.1(b)], and (3) the mixed functionalization regime, where two different functional groups are adsorbed on the same edge, using the same unit cell [see Fig. 5.1(c)]. In the strong and mixed functionalization regimes, the two functional groups in the unit cell are allowed to orient differently with respect to each other. In these cases, different starting orientations of the functional groups were allowed and the most energetically favorable configurations thus found, were used for H_2 adsorption. As an example of this allowed freedom of orientation, we have shown in Fig. 5.1(b) the OH groups oriented opposite to each other. In this case however, the most favored configuration was one in which the OH groups orient in the same direction, and this configuration was used for studying hydrogen binding.

The geometry of the functionalized zigzag graphene nanoribbon (FZGNR) system is first optimized, and the total energy of the system, E_{FZGNR} is computed. Next, a hydrogen molecule is adsorbed on this FZGNR system, the geometry is again optimized, and the total energy of the combined system, $E_{\mathrm{FZGNR+H_2}}$ is computed. The force tolerance for geometry optimization is 10^{-3} Ry/bohr.

The adsorption energy is defined as:

$$E_{\mathrm{ads}} = -(E_{\mathrm{FZGNR+H_2}} - E_{\mathrm{H_2}} - E_{\mathrm{FZGNR}}), \tag{5.1}$$

where $E_{\mathrm{H_2}}$ is the energy of an isolated hydrogen molecule in the gas phase. Note that with this convention, a positive value of adsorption energy means that binding is favored.

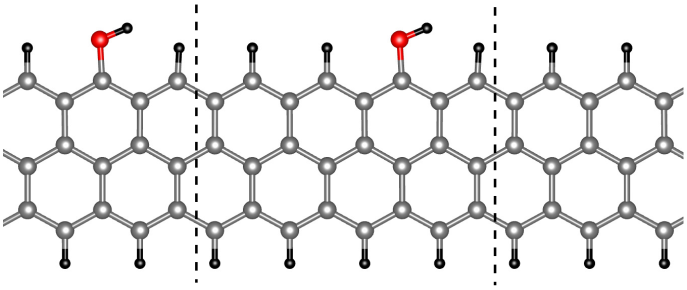

(a) Dilute FZGNR

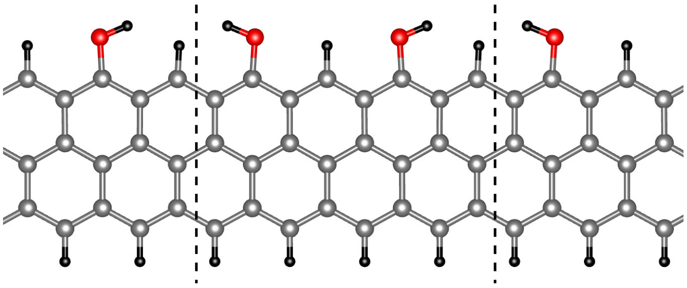

(b) Strong FZGNR

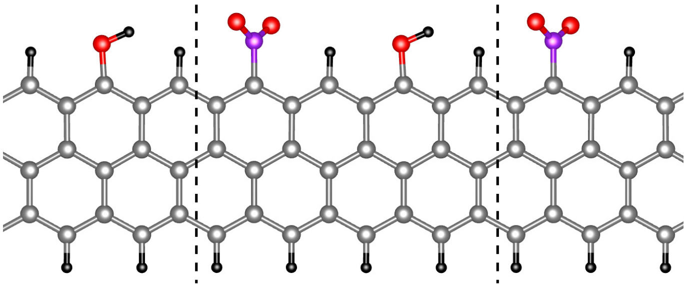

(c) Mixed FZGNR

Figure 5.1: *The functionalized ZGNR used in the calculations. As an example, the geometry for OH functionalization is shown, for both dilute and strong functionalization. For the mixed functionalization, we show the geometry for the case of NO_2–OH functionalization. The black dashed lines demarcate the boundaries of the unit cell. Color scheme for atomic spheres: H (black), C (gray), O (red), N (violet). This figure has been published in Ref. [201].*

5.3 H_2 Adsorption on Graphene

First, we want to look at the adsorption of hydrogen on a bare graphene sheet and an unfunctionalized edge of a Zigzag Graphene Nanoribbon, which would serve as benchmarks for our results on adsorption of chemically functionalized ZGNRs. We also want to compare our results for the bare graphene sheet and unfunctionalized ZGNRs, with those already available in the literature.

For hydrogen adsorption on a barge graphene sheet, we consider different adsorption

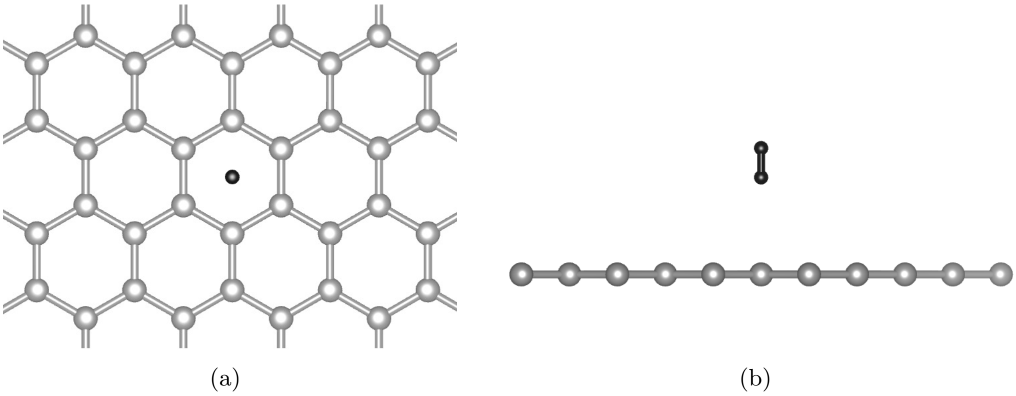
(a) (b)

Figure 5.2: *Optimized adsorption geometry for hydrogen adsorption on pristine graphene, top view shown in (a) and side view in (b). The center of mass of the H_2 molecule sits at a distance of 2.87 Å above the graphene sheet. Color scheme for atomic spheres: H (black), C (gray).*

sites, as well as different orientations of the H_2 molecule. We find that the hydrogen molecule prefers to bind on the hollow site of the graphene sheet, with its molecular axis oriented perpendicular ($\perp$) to the plane of the graphene sheet; the center of mass of the H_2 molecule sits at a distance of 2.87 Å above the graphene sheet (see Fig. 5.2). In this case, we find that the hydrogen molecule binds with an adsorption energy E_{ads} of 52 meV. We find that the hydrogen adsorption in the parallel ($\|$) geometry (where the H_2 molecular axis is oriented parallel to the plane of the graphene sheet), is slightly less favorable, with a binding strength of 50 meV, and a molecule-graphene basal plane distance of 2.84 Å. Our values are in good agreement with experimental values of 43 meV and 2.87 Å for H_2 adsorption on graphite [221]. Many of the previous theoretical investigations on this system did not incorporate van der Waals interactions. rendering a comparison of our results with theirs unsuitable; in fact it has been reported that use of the GGA alone (without London dispersion interactions) leads to the absence of a stable adsorption site for hydrogen on graphene [222]. In some cases however, calculations including van der Waals interactions have been reported to give values for the adsorption energies E_{ads} for hydrogen molecules on graphene that are broadly ranged from 50 – 70 meV. The separation of the hydrogen molecule from the graphene in these cases was found to lie between 2.7 and 3.2 Å and both $\|$ and $\perp$ geometries were reported as preferred [223–225].

To highlight the importance of London dispersion interactions, we separate out E_L, the contribution of the London interactions to the adsorption energy. By examining these contributions, we find that the contribution E_L from these interactions to the binding of H_2 on graphene is 64 meV, i.e., at this geometry, in the absence of London interactions, the net interaction between graphene and the hydrogen molecule would be repulsive.

5.4 H_2 Adsorption on Edge Functionalized Zigzag Graphene Nanoribbons

When we go from graphene to a graphene nanoribbon, the formation of edges leads to several changes in the electronic as well as magnetic properties, due to the change in the chemical environment at the edges. Generally the edges of zigzag nanoribbons are passivated by hydrogen atoms, to satisfy the dangling bonds. When we try to adsorb an H_2 molecule near the unpassivated edge of a ZGNR, we find that the H_2 molecule is dissociated into H atoms, which then individually passivate two carbon atoms at the edge. We therefore choose H-passivated ZGNRs (both the edges are passivated by hydrogen atoms) to study molecular hydrogen adsorption, and to benchmark our results on edge functionalized ZGNRs.

For chemical functionalization of the edges of ZGNRs, we consider five functional groups: OH, NH_2, COOH, NO_2, and H_2PO_3. Importantly, note that the first two groups are considered to be electron-donating groups, while the latter three are considered to be electron-withdrawing groups. The dangling bonds at the ribbon edges were all passivated with H atoms.

For adsorption at or near the edges of the ZGNRs, in order to span the space of possible geometries, several kinds of initial geometries were considered. Our initial and final geometries can be divided into two broad categories, “outer edge” (OE) and “inner edge” (IE). In the former, we place the hydrogen molecule outside the edge of the ribbon, whereas in the latter, we place it directly above the ribbon, but near the functionalized edge. For the OE configurations, we have tried different starting positions for aligning the H_2 molecule with respect to the ZGNR; these can be divided into two categories: “out of plane” (OP) and “in plane” (IP) configurations. In the IP configurations, the center of mass of the hydrogen molecule lies initially in the plane of the graphene nanoribbon,

		Outer edge adsorption			Inner edge adsorption	
Group	μ_1 (D)	E_{ads} (meV)	μ_2 (D)	R (Å)	E_{ads} (meV)	R (Å)
Graphene	-	-	-	-	$\boxed{52}$	2.87
Bare(H)	0.0	35	0.011	2.89	$\boxed{55}$	2.97
NO_2	4.22	39	0.065	3.19	$\boxed{60}$	3.06
NH_2	1.13	46	0.041	2.55	$\boxed{66}$	2.94
OH	1.224	$\boxed{61}$	0.076	2.34	57	2.94
COOH	1.78	$\boxed{76}$	0.107	2.42	61	2.96
H_2PO_3	2.76	$\boxed{87}$	0.118	2.34	57	2.93

Table 5.1: *Adsorption energies E_{ads}, for H_2 adsorbed on dilute FZGNRs. μ_1 and μ_2 are estimates of the dipole moments on the FZGNR and H_2, respectively. For OE adsorption, R is the distance between these dipoles. For IE adsorption, R is the perpendicular distance of the H_2 molecule from the FZGNR. The highest adsorption energies for each functional group have been boxed.*

whereas in the OP configurations, it lies above this plane. For each of these configurations, the H_2 molecular axis can be oriented either parallel or perpendicular to the edge of the FZGNR. For IE adsorption, one can only have “out of plane” OP geometries; however one can still start with the H_2 molecular axis either parallel or perpendicular to the edge of the FZGNR. Further, one can position the H_2 molecule at different sites near the edge, e.g., at atop or hollow sites. By starting from such a large variety of initial geometries, we have obtained a number of stable geometries for H_2 on the FZGNRs.

5.4.1 Dilute Functionalization

We first consider the case of dilute functionalization [cf Fig. 5.1(a)], where we have attached one functional group at one of the edges of the ZGNR in the unit cell considered. It is of interest to consider separately our results for the outer edge and inner edge configurations, since the binding mechanisms are different in the two cases. In Table 5.1, we have tabulated our results for the adsorption energy E_{ads}, for the lowest-energy geometry of the OE as well as IE types, for the H-passivated ZGNR and the five functionalized ZGNRs. The boxed number indicates which of the two, OE or IE, constitutes the most stable adsorption geometry.

One notable finding from our results shown in Table 5.1 is that the adsorption of a hydrogen molecule is more favorable near the edges of the nanoribbon than binding over the center of the graphene sheet. Notice that all the edges show a larger adsorption energy than that on graphene. We find that for the H-passivated edge, as well as the ZGNRs functionalized with NH_2 and NO_2, the hydrogen molecule prefers to bind on the inner edge, where it can interact with both the π manifold of the graphene sheet and the atoms of the functional group. The binding at this site is stronger than binding to the outer edge or to an extended graphene sheet. On the other hand, for the other three functional groups that contain OH moieties, viz., OH, COOH and H_2PO_3, the hydrogen molecule likes to bind at the outer edge where it can interact primarily with the functional group. In this case, the binding is again stronger than than that observed for an extended graphene sheet or for the H-passivated edge. This suggests that the presence of functionalized edges in graphitic substrates will increase the binding of hydrogen. These edge-induced enhancements should also be expected for other similarly weakly adsorbed gas species on graphene, since the key binding mechanisms are likely analogous.

We now wish to understand the origin of the enhanced binding of hydrogen in the presence of functionalized edges. It is important to note that the chemical functional groups which we have used for functionalization will impart a permanent dipole moment to the FZGNR. This permanent dipole moment can induce a dipole on the H_2 molecule. To see this we carry out a charge redistribution analysis (similar to that shown in Chapter 4) where we examine how the electronic charge density of the system reorganizes itself upon adsorption of hydrogen. To do this, we subtract the individual charge densities of the substrate FZGNR and the H_2 molecule, from the charge density of the adsorbed system FZGNR+H_2. This is given as:

$$\Delta\rho = \rho(\mathrm{FZGNR} + \mathrm{H_2}) - \rho(\mathrm{FZGNR}) - \rho(\mathrm{H_2}). \tag{5.2}$$

Note that the charge densities of the individual systems are evaluated at geometries corresponding to those in the combined system.

We have plotted the charge redistribution maps (isosurfaces of the charge difference

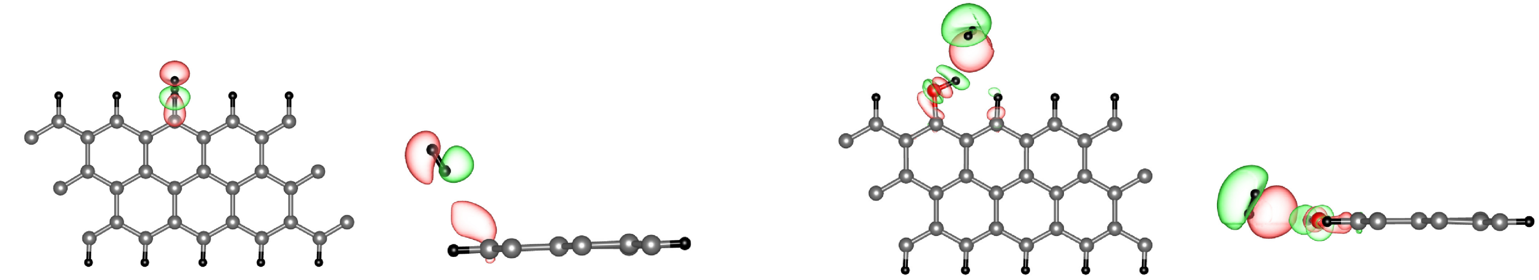

(a) Bare H Top view (b) Bare H Side view (c) OH Top view (d) OH Side view

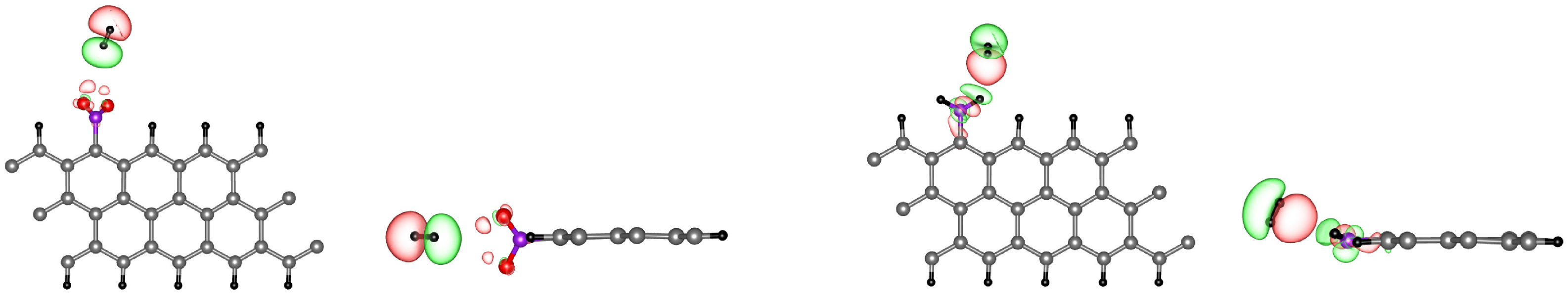

(e) NO_2 Top view (f) NO_2 Side view (g) NH_2 Top view (h) NH_2 Side view

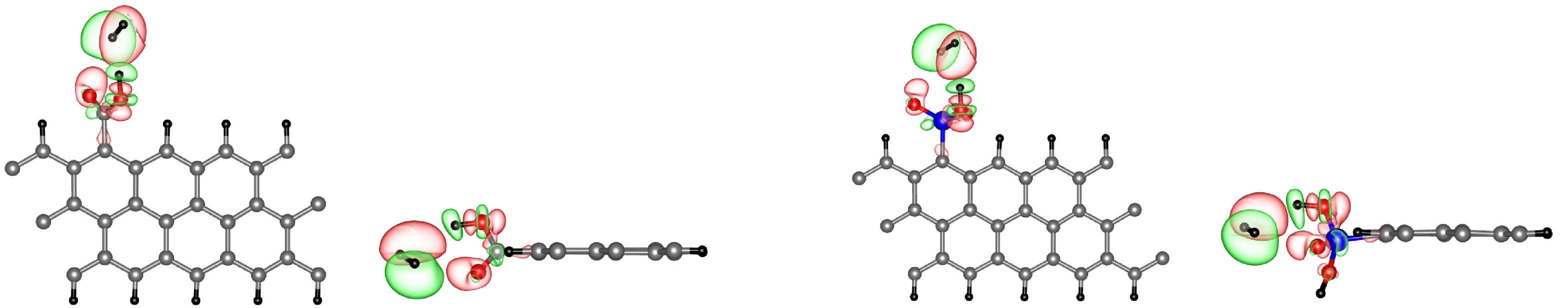

(i) COOH Top view (j) COOH Side view (k) H_2PO_3 Top view (l) H_2PO_3 Side view

Figure 5.3: *Optimal adsorption geometries, and redistribution of electronic charge upon adsorption of hydrogen on the outer edge of the various dilute FZGNRs. Red and green lobes correspond to a gain and depletion of electronic charge, respectively. The isosurfaces corresponding to* $\Delta\rho = \pm 2 \times 10^{-4}$ *electrons/bohr*^{3} *are plotted for all the cases. Color scheme for atomic spheres: H (black), C (gray), O (red), P (blue), N (violet). This figure has been published in Ref. [201].*

$\Delta\rho$) for the most favored adsorption geometries for the OE cases, in Fig. 5.3. Here the red lobes depict an accumulation and the green lobes show a depletion of the electronic charge. We can clearly see that, in every case, there is a dipole induced on the hydrogen molecule when it is placed in the vicinity of the functionalized substrate. It is the permanent dipole on the functionalized substrate that induces this dipole moment on the H_2 molecule. Interestingly, we find that the dipolar axis need not coincide with the molecular axis.

We can make certain interesting observations just by looking at the induced dipoles and their orientations. Firstly for the FZGNRs functionalized by electron-donating groups OH and NH_2, we find that the orientation of the induced dipoles are very similar [see Figs. 5.3(c), 5.3(d), 5.3(g) and 5.3(h)]. In both cases, the red lobe (electron accumulation) of the induced dipole points toward the functional group, whereas the molecular axis is oriented perpendicular to the dipole axis. In addition, the molecule is positioned slightly above the plane of the FZGNR. In the case of dilute functionalization with electron-withdrawing groups COOH or H_2PO_3 [see Figs. 5.3(i), 5.3(j), 5.3(k) and 5.3(l)], we again notice this orientational similarity. In both cases, the OH bond and a remaining O atom are approximately coplanar with the induced dipole on the H_2 molecule. This dipole points with the red lobe (electron accumulation) toward the OH of the functional group, in rough alignment with the H_2 molecular axis. However, functionalization with NO_2 (which is known to be a strong electron withdrawing group) is qualitatively different from the other cases: the H_2 molecule lies in the plane of the FZGNR, with the green lobe (electron depletion) pointing toward the edge, and the molecular axis (as well as the dipolar axis) oriented perpendicular to the edge [see Figs. 5.3(e) and 5.3(f)].

A significant contribution to the electrostatic interaction energy may be expected from the appearance of induced dipoles on H_2; we now wish to quantify this contribution. As a first step, we try to evaluate the interaction energy between the permanent dipole moment on the FZGNR and the induced dipole on the H_2 molecule, i.e., the Debye interaction. To do this we need to estimate the permanent dipole on the FZGNR, and the dipole induced on the H_2 molecule. The permanent dipole on the functionalized nanoribbon is difficult to evaluate because of issues related to the problems in computing the dipole moments of an extended system [226]. However, we can obtain an estimate of this quantity by considering instead a benzene molecule functionalized with the same functional group. We therefore consider the dipole moments of nitrobenzene, aniline, phenol, benzoic acid and phenylphosphonic acid. Experimental values for the dipole moments of the first four of these compounds are available, and are listed as the dipole moments μ_1 in Table 5.1. For phenylphosphonic acid, no experimental data appears to be available, and we therefore use a theoretically computed value [227]. To estimate the magnitude of the induced dipole on the H_2 molecules, we can again look at the charge redistribution plots. One can notice that the induced lobes of the charge density, in the vicinity of the H_2 molecule are clearly separated from the charge density of the FZGNR. Therefore, one can integrate the charge inside the red or the green lobes of the dipole, bound by an isosurface of a certain threshold value; this value was chosen to be 2×10^{-4} e/bohr^3. (An optimum value of this threshold parameter should be used, this value should be small enough that the error thus introduced in estimating the charge is small, and should be large enough, so that the red and green lobes near the H_2 molecule are sufficiently separated out from the rest of the charge distribution.) The product of this charge, multiplied by the distance between the weighted centers of the two lobes, gives the dipole moment. This quantity is tabulated as μ_2 in Table 5.1. Finally, we also list in Table 5.1, the value of R, our estimate of the distance between the centers of the dipoles μ_1 and μ_2.

We can now estimate the Debye contribution to the adsorption energy, i.e., the electrostatic interaction energy between the permanent dipole on the FZGNR and the induced dipole on the hydrogen molecule, as $E_D = \mu_1\mu_2/R^3$, ignoring the angular dependence. This is shown by the green triangles in Fig. 5.4, where we show our results for E_D, plotted as a function of the adsorption energy E_{ads}.

We find that, in general, the Debye term E_D follows a similar trend to that observed for the adsorption energy. The largest values for the Debye energy are obtained for the COOH and H_2PO_3 groups, which have both the OH groups and a lone pair present. It has been pointed out in earlier studies [219] that there is a charge transfer from the lone pair of the doubly bonded O atom to the other O-H bond within the functional group,

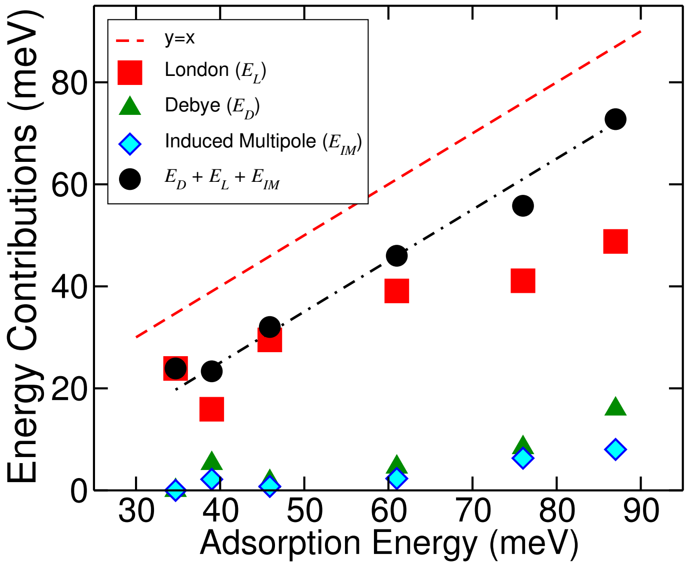

Figure 5.4: *Energy contributions from the London interaction (E_L), shown by red squares, the Debye interaction (E_D), shown by green triangles, and the induced multipolar interactions (E_{IM}), shown by cyan diamonds, for the outer edge adsorption of dilute functionalized ZGNRs. The sum of these contribution is shown by black dots. The black dashed-dotted line is a guide to the eye. The red dashed line is the $y = x$ line, i.e. the line at which the net contributions from the different interactions should add up to the adsorption energy E_{ads}. Note that the energy range of the x-axis does not start from zero. This figure has been published in Ref. [201].*

resulting in further polarization of the O-H bond. This results in a greater electrostatic interaction between the functionalized substrate and the induced dipole of the adsorbed molecule. The lone pairs tend to deplete electron density nearby, i.e., create the green lobe of the induced dipole, due to Coulombic repulsion. Accordingly, it can be noted that in the case of OH-containing functional groups, the larger the number of lone pairs (basically the number of oxygen atoms), the larger is the adsorption energy: H_2PO_3 > COOH > OH.

From Fig. 5.4, we see that the magnitudes of E_D are considerably smaller than those of E_{ads}. We have of course made many approximations in calculating E_D, e.g., approximating the permanent dipole moment of the FZGNR by that of functionalized benzene, the assumption of point dipoles, ignoring directional dependence, and the neglect of induced moments on the FZGNR; nevertheless, these are unlikely to account for the large discrepancy between E_D and E_{ads}.

Therefore, we next try to estimate the London dispersion interactions between the hydrogen molecule and the FZGNR, and to see whether these supply the missing contribution to E_{ads}. We obtain this contribution E_L as follows:

$$E_L = -(E^{disp}_{\mathrm{FZGNR+H_2}} - E^{disp}_{\mathrm{H_2}} - E^{disp}_{\mathrm{FZGNR}}), \tag{5.3}$$

where the three terms on the right-hand-side are the contributions from dispersion interactions to the total energy of the corresponding systems; note that $E^{disp}_{\mathrm{H_2}}$ is negligible. We have plotted the results for E_L as the red squares in Fig. 5.4. Note that our results for E_L for various functional groups follow the trends observed for E_{ads}, with the lowest enhancement for NO_2, and the highest for H_2PO_3.

For evaluating the Debye interaction term, we have estimated the permanent dipole moment of the FZGNR in the absence of H_2. However in the presence of the hydrogen molecule, there is also a redistribution of the charge density on the FZGNR. We can clearly see from the charge density redistribution plots, that there are moments induced on the functional group due to the presence of H_2. There are also higher-order multipolar electrostatic interactions between this assembly of charges, which will contribute to the adsorption energy. We refer to this contribution to the adsorption energy as E_{IM}. This can be evaluated; we do so by integrating the charge within each red and green charge density lobe, and then calculating the Coulomb energy of the resulting equivalent assembly of point charges. In this term, we include the dipole formation energy, which is the Coulomb interaction energy between the two opposite charges on the H_2 dipole.

Finally, we compute the sum of all these contributions, $E_D + E_L + E_{IM}$ (black dots in Fig. 5.4) and compare it with our values of E_{ads}. The two quantities follow one another with very good agreement, this means that the change in adsorption energy over all the functional groups, has been well accounted for. Our results in Fig. 5.4, show that in all the cases of OE adsorption for dilute functionalization, the majority of the binding is due to the London dispersion interactions, a small fraction (varying between 6% and 18%) comes from Debye interactions, and a smaller fraction (varying between 2% and 9%) comes from the induced multipole interactions.

We point out that the calculated E_{ads} in Fig. 5.4 is consistently greater in magnitude than the sum of the predicted electrostatic and dispersion contributions. As we will see below, it turns out that we observe a similar offset (15–20 meV) between the calculated and predicted values across all of our dilute and strong functionalized ribbons. It is possible that this offset is due to the many approximations made in evaluating all the contributions, alternatively, this energy mismatch may be due to the reorganization energy of the electronic charge within the π cloud.

Next, we consider the case of inner edge (IE) adsorption, again in the dilute functionalization regime. We have shown the lowest-energy geometries, together with the charge redistribution, for the IE geometries, in Fig. 5.5. We find that, only in the case of NO_2 functionalization, the atop site closest to the functional group is most favored for H_2 adsorption. In this particular case, we find an induced dipole moment on the H_2 molecule, $\mu_2 = 0.026$ D, which leads to a Debye interaction energy $E_D = 2$ meV. However, for all remaining cases, the hydrogen molecule prefers to bind at the hollow site closest to the functional group, with the H_2 molecular axis oriented approximately perpendicular to the plane of the FZGNR. In these cases, the Debye interaction as well as the other electrostatic terms are extremely small. Almost all of the binding comes from London dispersion interactions. In fact, if we turn off the London interactions, the adsorption can be disfavored in many of these cases.

It is worth mentioning, however, that one does notice a reorganization of electronic charge in the vicinity of the hydrogen molecule, indicated by the red and green lobes in Fig. 5.5. Moreover, unlike in the case of OE adsorption, the net charge contained within these two lobes for IE adsorption is no longer equal; instead, in this case we find that the magnitude of charge contained within the red lobe is larger than that within the green lobe. This indicates the possibility of net electronic charge transfer from the FZGNR to the H_2 molecule. Note that the red and green lobes in Fig. 5.5, which shows IE adsorption, are drawn for a lower isosurface value than in Fig. 5.3, which shows OE adsorption.

Another important feature which can be seen in all the IE cases where the H_2 adsorption is at a hollow site, is that there is a significant redistribution of the charge in the π cloud of the graphene sheet. This is manifested in the red lobe directly below the H_2 molecule in Fig. 5.5. There is a reorganization of electronic charge, so that charge

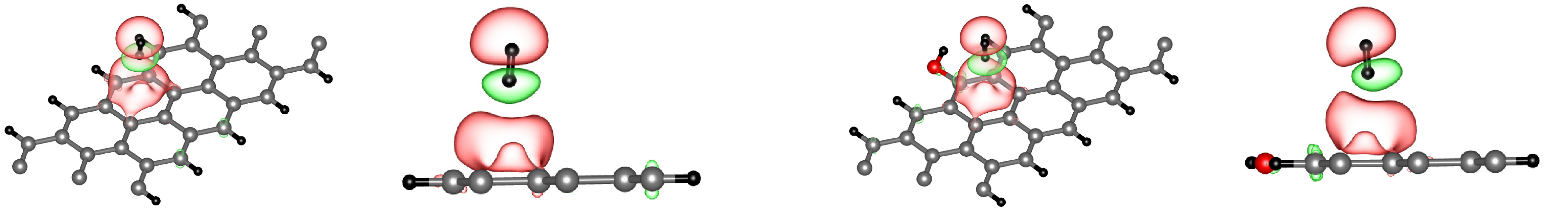

(a) Bare H Top view (b) Bare H Side view (c) OH Top view (d) OH Side view

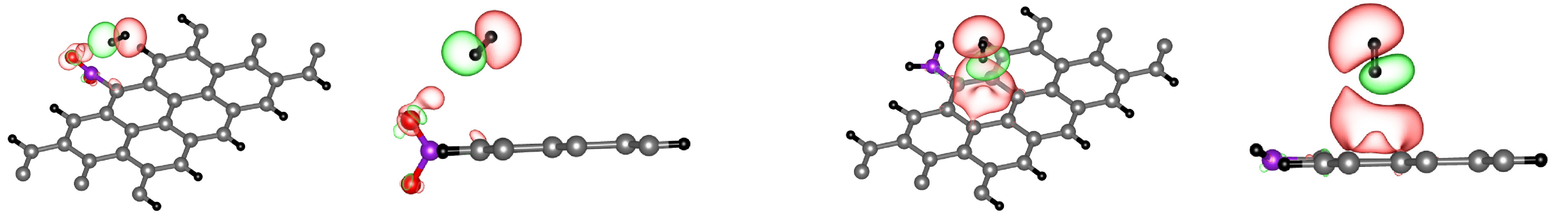

(e) NO_2 Top view (f) NO_2 Side view (g) NH_2 Top view (h) NH_2 Side view

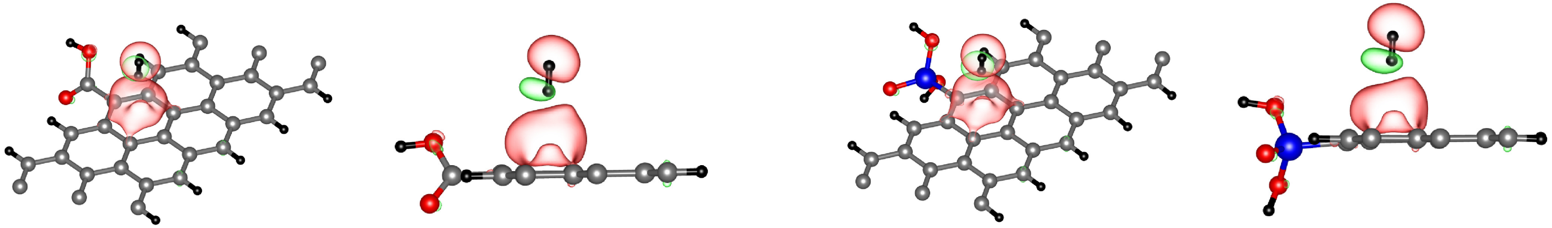

(i) COOH Top view (j) COOH Side view (k) H_2PO_3 Top view (l) H_2PO_3 Side view

Figure 5.5: *Optimal adsorption geometries, and redistribution of electronic charge upon adsorption of hydrogen, on the inner edge of the various dilute FZGNRs. Red and green lobes correspond to a gain and depletion of electronic charge, respectively. The interaction with the* π*-cloud of FZGNR is clearly seen here for all cases, except the case of functionalization by* NO_2*, where the* H_2 *sits at an atop site. The isosurfaces corresponding to* $\Delta\rho = \pm 8\times10^{-5}$ *electrons/bohr*^{3} *are plotted for all the cases, except (e) and (f), where the isosurfaces corresponding to* $\Delta\rho = \pm 2\times10^{-4}$ *electrons/bohr*^{3} *are shown. Color scheme for atomic spheres: H (black), C (gray), O (red), P (blue), N (violet). This figure has been published in Ref. [201].*

is removed from the π orbitals of carbon atoms further away from the adsorption site, which then accumulates at the adsorption site. In the presence of the functional group, this accumulated charge lobe near the adsorption site is further modified (see Fig. 5.5). When the functional group attached is electron donating in nature, the electronic charge in the π cloud is slightly enhanced in the region near the functional group, whereas if the functional group is electron withdrawing, there is a depletion of charge from the π cloud in the region near the functional group. This results in the lopsided nature of the bottommost red lobes in Fig. 5.5, and reflects the electron donating or withdrawing nature of the functional group.

The electron donating or withdrawing capacity of the functional group can be quantified using the Hammett parameter σ [229], which is well known in the organic chemistry literature. Positive/negative values of the Hammett parameter indicate the electron-withdrawing/electron-donating strength of the functional group. We can now draw correlations between the magnitude or the orientation of the charge redistribution, and the electron withdrawing or donating character of a functional group, as estimated by the Hammett parameter. For this we define Q_r and Q_g as the charges contained in the red and green lobes, respectively, in the vicinity of the H_2 molecule, bound by an isosurface of a threshold value of $\pm 8 \times 10^{-5}$ electrons/bohr^3. We also find the weighted centers of these two lobes. The line joining these two centers is analogous to a dipole axis. This line need not coincide with the molecular axis, and is tilted at an angle θ to the normal of the plane, as is clearly visible from the side views in Fig. 5.5. In Fig. 5.6, we have plotted our results for the charges Q_r and Q_g, as well as the tilt angle θ, for the different functional groups, for IE adsorption, as a function of the Hammett parameter. We see that all three quantities correlate well with the Hammett parameter σ, i.e., with the electron donating or withdrawing nature of the functional group. For the non-functionalized graphene nanoribbon, the line joining Q_r and Q_g is oriented vertically (perpendicular to the graphene nanoribbon); it progressively tilts toward or away from the functionalized edge, as the electron donating or withdrawing nature of the functional group is increased.

Collectively, the results in Fig. 5.6 strongly point to the role of the π electron cloud

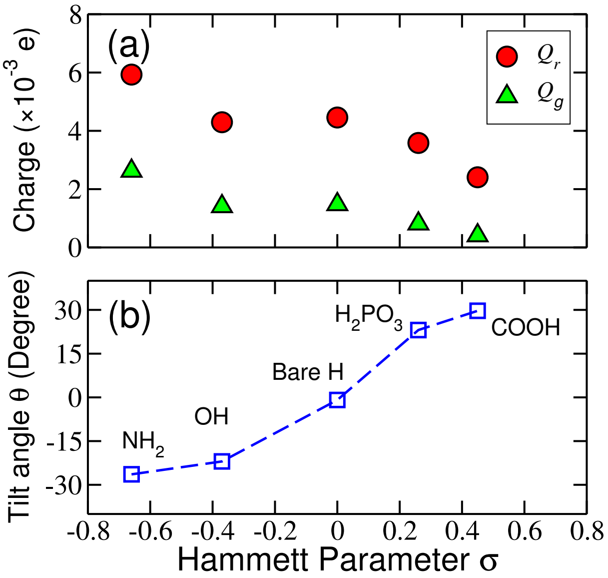

Figure 5.6: *Variation of (a) the charges Q_r and Q_g, and (b) the tilt angle of the line joining Q_r and Q_g with respect to the normal to the graphene plane, as a function of the Hammett parameter of the functional group attached for IE adsorption of H_2. Q_r and Q_g are the charges contained in the red and green lobes, respectively, in the vicinity of the H_2 molecule, within an isosurface value of $\Delta\rho = \pm 8 \times 10^{-5}$ electrons/bohr^3. A tilt angle toward the functional group is taken to be negative, and a tilt away from the functional group is taken to be positive. This figure has been published in Ref. [201].*

in determining the dipole and charge on the adsorbed H_2 molecule, since the electron withdrawing or donating character of the attached functional group will directly affect the occupation of the π cloud. An electron withdrawing group depletes the electron density in the π-cloud, and hence the charge transfer from the sheet to the H_2 molecule is reduced. This results in reduced values of Q_r and Q_g for increasing values of the Hammett parameter σ, as can be seen from Fig. 5.6(a). Similar reasoning explains the increase in values of Q_r and Q_g for decreasing values of Hammett parameter σ, i.e, for electron-donating groups. Moreover, this group-induced depletion or accumulation is not entirely isotropic, and leads to the lopsided shapes of the π-cloud. We believe this is the cause of the tilting behavior in Fig. 5.6(b). In particular, for higher positive values of σ, the π density will be slightly withdrawn from the region near the functional group. In response to this asymmetric π accumulation, the dipole of the H_2 molecule reorients itself, so that the dipole axis tilts away from the functional group. This picture is reversed for an electron-donating group. As these charge redistribution values are small, the forces induced on the H_2 molecule are

		Outer edge				Inner edge
Group	μ_1 (D)	E_{ads} (meV)	μ_2 (D)	R (Å)	R' (Å)	E_{ads} (meV)
NO_2	4.22	$\boxed{61}$	0.019	3.25	3.22	57
NH_2	1.13	$\boxed{77}$	0.067	2.68	2.75	69
OH	1.224	$\boxed{78}$	0.083	2.71	2.97	60
COOH	1.78	$\boxed{98}$	0.129	2.39	2.83	58
H_2PO_3	2.76	$\boxed{115}$	0.140	2.29	2.93	62

Table 5.2: *Adsorption energies E_{ads}, for H_2 adsorbed on the outer edge of strongly functionalized ZGNRs. μ_1 and μ_2 are estimates of the dipole moments on the FZGNR and H_2, respectively. For OE adsorption, R and R' are the distances between the dipole μ_2 and the two functional groups. The highest adsorption energies for each functional group have been boxed.*

minor, so that they do not affect the molecular orientation.

5.4.2 Strong Functionalization

Next we consider the case of strongly functionalized zigzag graphene nanoribbons (SFZGNRs); cf. Fig. 5.1(b). In Table 5.2, we have tabulated our results showing the adsorption energy E_{ads}, for the most favorable geometry of the OE as well as IE type, for the five functionalized ZGNRs. The boxed number indicates which of the two, OE or IE, constitutes the most stable adsorption geometry.

We find that in case of the strongly functionalized ZGNRs, outer edge (OE) adsorption of hydrogen molecule is always favored over inner edge adsorption. Also strong functionalization results in a significant enhancement of the H_2 adsorption energies in the OE case compared to dilute functionalization. This can be seen by comparing the values in Table 5.2 with those in Table 5.1. The highest value of adsorption energy of 115 meV is obtained in the case of strong functionalization by H_2PO_3. An overall enhancement in the adsorption energy by 30%–60% is observed for OE adsorption, compared to dilute functionalization. However, the IE adsorption energies are very similar to those obtained in the dilute functionalized case. This is consistent with the notion that IE adsorption is dominated by the dispersion interactions with the π cloud, which are less affected by the presence of the additional edge functional groups.

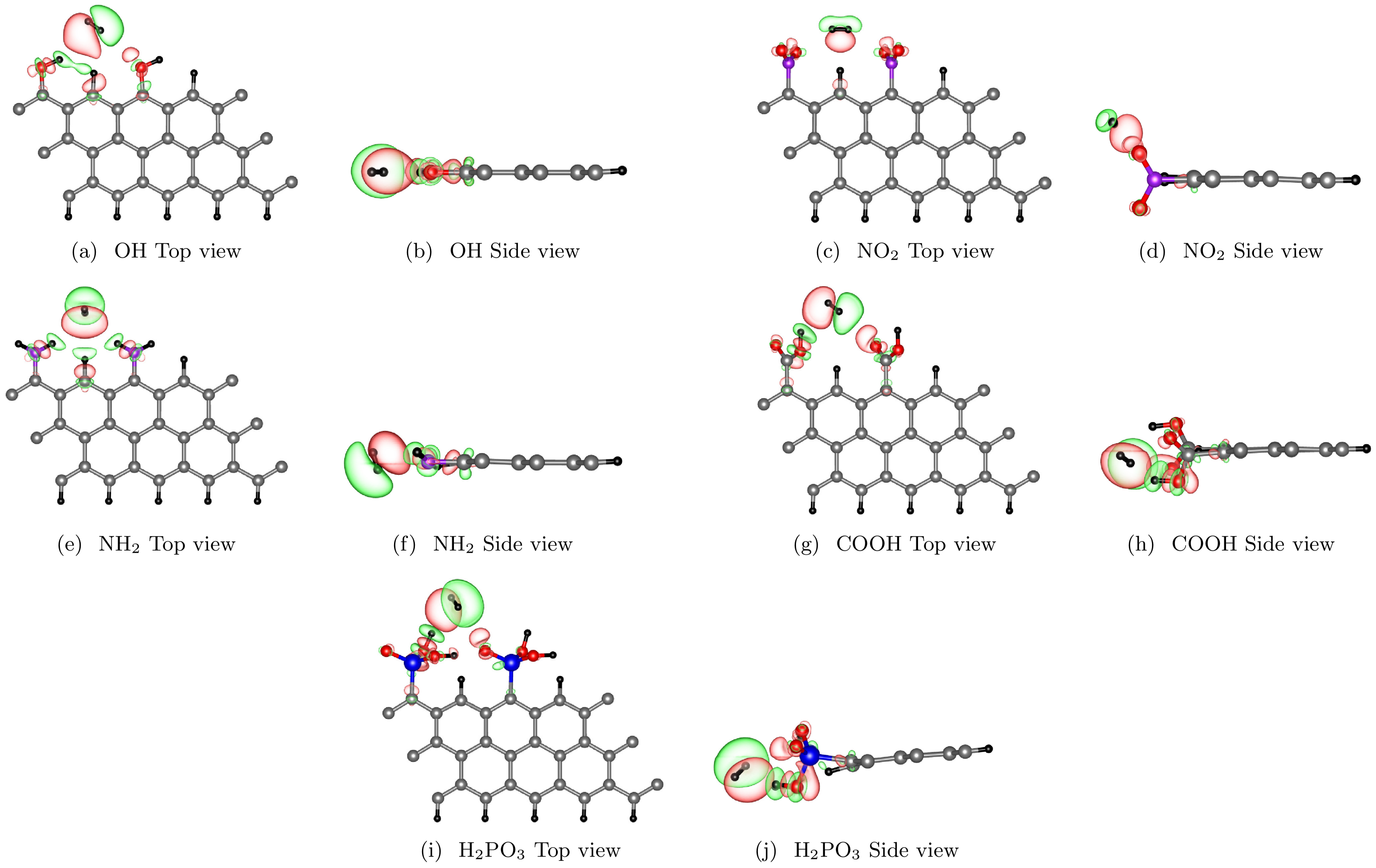

(a) OH Top view (b) OH Side view (c) NO_2 Top view (d) NO_2 Side view

(e) NH_2 Top view (f) NH_2 Side view (g) COOH Top view (h) COOH Side view

(i) H_2PO_3 Top view (j) H_2PO_3 Side view

Figure 5.7: *Optimal adsorption geometries, and redistribution of electronic charge upon adsorption of hydrogen, on the outer edge of the various strong FZGNRs. Red and green lobes correspond to a gain and depletion of electronic charge, respectively. The isosurfaces corresponding to* $\Delta\rho = \pm 2 \times 10^{-4}$ *electrons/bohr*^{3} *are plotted for all the cases. Color scheme for atomic spheres: H (black), C (gray), O (red), P (blue), N (violet). This figure has been published in Ref. [201].*

In Fig. 5.7, we have plotted the isosurfaces of the charge redistribution $\Delta\rho$, for the most favored adsorption geometry for the OE adsorption, for the strongly functionalized ZGNR. As before, the red lobes show an accumulation of electrons, and green lobes show a depletion of electrons. An induced dipole on the hydrogen molecule is clearly seen in every case. One can notice that the dipole on the H_2 molecule in the three cases OH-SFZGNR, COOH-SFZGNR, and H_2PO_3-SFZGNR, orients between the OH part of one group and the lone pair of the adjacent group. In the case of OH, this lone pair is on the oxygen atom of the OH group, while in the case of COOH and H_2PO_3, it is on the doubly bonded O atom. The doubly bonded O of the functional group has a lone pair of electrons which leads to the depletion of electronic density, leading to the green lobe of the induced dipole on H_2. The binding mechanism seems to be quite similar to that observed in the case of dilute functionalization by COOH and H_2PO_3; there too the dipole moment of the H_2 preferred to align between an OH and a lone pair. However the difference between the two is that in the case of dilute functionalization, the dipole aligned between an OH and a doubly bonded O of the same functional group, whereas in the case of strong functionalization, the double bonded O and OH between which it aligns belong to two adjacent functional groups. As a result, the steric repulsion in the strongly functionalized case is smaller than in the dilute case, allowing the induced dipole on the H_2 to approach closer to the functional groups, thereby increasing the electrostatic attraction between them, as well as London dispersion interactions.

Interestingly, the relationship between the binding energy and the number of available lone pairs on the oxygens of nearby OH, COOH, and H_2PO_3 functional groups is linear. This result is consistent for both dilute and strong functionalized ZGNRs (see Fig. 5.8). The linearity suggests that all oxygen lone pairs in all functional groups participate to some degree in charge reorganization. For dilute functionalization, the charge reorganization remains local to a single functional group, whereas for strong functionalization, both neighboring groups participate. This fact is also confirmed upon careful examination of the relevant panels in Figs. 5.3 and 5.7. We conclude that functional groups with high oxygen content are likely to be effective for enhanced gas binding.

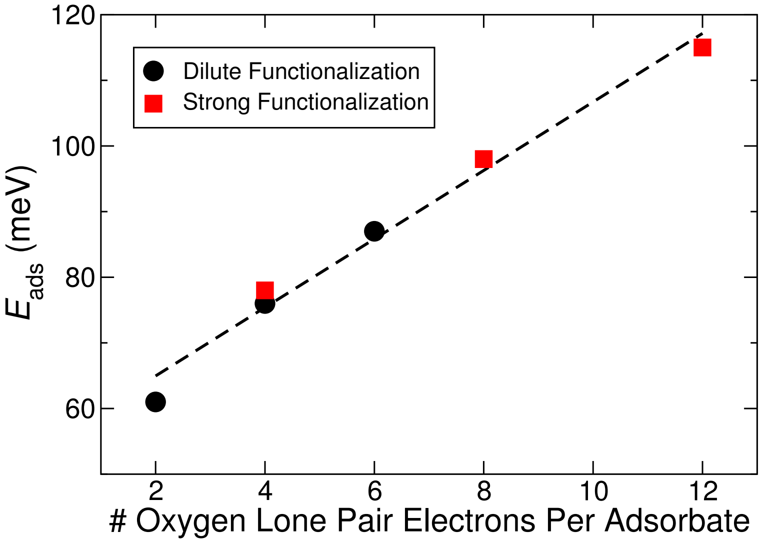

Figure 5.8: *Adsorption energy E_{ads} of H_2 adsorbed on ZGNRs functionalized with groups (OH, COOH or H_2PO_3) containing the OH moiety, as a function of the number of oxygen lone pairs per adsorbate. Note the very clearly linear relationship. This figure has been published in Ref. [201].*

As before, we estimate the various contributions to E_{ads}, for the case of strong functionalization (see Fig. 5.9). The London dispersion interactions are the major contribution to the adsorption energy, contributing ∼50% to 75% of the total value. The Debye contribution has been estimated by carrying out a charge redistribution analysis similar to that described in Section 5.4.1. Here too, when we consider the Debye contribution E_D, we find that the ordering of the various functional groups follows the same ordering as the total adsorption energy E_{ads}, being smallest for NO_2-FZGNR and the largest for H_2PO_3-FZGNR. The contributions range from 5% to 26%. In addition, we also calculate the contribution E_{IM} from the interactions between the assemblage of induced multipoles on the functional groups due to the presence of the H_2 molecule. This interaction contributes about 3% to 10% of the total contribution to E_{ads}.

It is important to note that the reason for the increased binding in the case of strong functionalization is not the same for all the functional groups. For the three functional groups that contain OH moieties, viz., OH, COOH and H_2PO_3, this increased binding arises from an enhancement in both London dispersion as well as electrostatic (Debye and multipolar) interactions, whereas for NO_2 and NH_2, most of it is due to an increased contribution from London interactions.

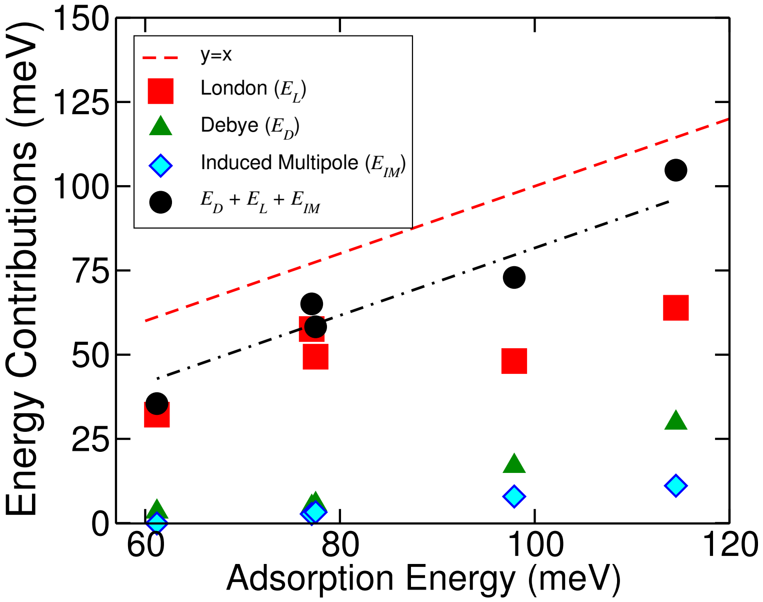

Figure 5.9: *Energy contributions from the London interaction (E_L), shown by red squares, the Debye interaction (E_D), shown by green triangles, and the induced multipolar interactions (E_{IM}), shown by cyan diamonds, for the outer edge adsorption of strongly functionalized ZGNRs. The sum of these three contributions is shown by black dots. The black dashed-dotted line is a guide to the eye. The red dashed line is the $y = x$ line, i.e., the line at which the net contribution from the different interactions should add up to the adsorption energy E_{ads}. Note that the energy range of the x-axis does not start from zero.*

5.4.3 Mixed Functionalization

Next we consider cases where the ZGNR is "strongly functionalized" with two different functional groups (Mixed-FZGNR), cf. Fig. 5.1(c). With the five functional groups considered in this study, we have the possibility of ten combinations. However, it is possible that some functional groups might not like to mix, and it may not be energetically favorable to have configurations in which one finds two different functional groups side by side. To estimate whether two groups like mixing, we compare the energy of the mixed situation with that in which the two kinds of functional groups are phase segregated. We compute the mixing energy of two functional groups A and B:

$$\Delta E_{\text{mix}} = E_{\text{A+B}} - \frac{1}{2}(E_{\text{A}} + E_{\text{B}}), \tag{5.4}$$

where $E_{\text{A+B}}$ is the total energy of the 50-50 mixed system A+B, and E_{A} and E_{B} are the total energies of the phase-segregated A and B systems, respectively. If ΔE_{mix} is negative,

Groups (A – B)	ΔE_{mix} (meV)	Outer edge adsorption E_{ads} (meV)	μ_1^A (D)	μ_1^B (D)	μ_2 (D)	R_A (Å)	R_B (Å)
NO_2–NH_2	-195	$\boxed{88}$	4.22	1.13	0.123	3.03	2.59
NO_2–OH	-72	$\boxed{110}$	4.22	1.224	0.148	3.12	2.42
NO_2–COOH	-26	$\boxed{74}$	4.22	1.78	0.052	3.20	2.73
NO_2–H_2PO_3	355	–	–	–	–	–	–
NH_2–OH	8	$\boxed{83}$	1.13	1.224	0.071	2.82	2.64
NH_2–COOH	-105	$\boxed{89}$	1.13	1.78	0.118	2.51	3.24
NH_2–H_2PO_3	204	–	–	–	–	–	–
OH–COOH	-30	$\boxed{106}$	1.224	1.78	0.128	2.38	3.06
OH–H_2PO_3	293	–	–	–	–	–	–
COOH–H_2PO_3	368	–	–	–	–	–	–

Table 5.3: *Results from ab initio calculations for mixed functionalization. Mixing energies ΔE_{mix}, and adsorption energies of molecular hydrogen E_{ads}, for different combinations of functional groups for mixed FZGNRs. μ_1^A, μ_1^B, denote the permanent dipole moments on the functionalized substrate due to A and B, respectively (see Table 5.1) and μ_2 is the induced dipole moment on the hydrogen molecule. R_A and R_B denote the distance from the centre of the dipole on the hydrogen molecule to the functional groups A and B, respectively. The adsorption energies for each case have been boxed, in order to facilitate comparison with the previous tables.*

then mixing is favorable, whereas if it is positive, phase segregation is preferred. The values obtained for ΔE_{mix} for the ten different combinations of the functional groups considered by us are listed in Table 5.3. We find that only five out of the ten possible combinations like to mix: viz., NO_2–NH_2, NO_2–OH, NO_2–COOH, NH_2–COOH, and OH–COOH, and we therefore restrict ourselves to these five combinations when studying H_2 adsorption on the outer-edge of the Mixed-FZGNR. In addition, we also consider the NH_2–OH case, because in this case, ΔE_{mix}, though positive, is very small. We also restrict ourselves to considering only outer edge adsorption, as inner edge adsorption does not lead to a significant binding of H_2 in the strong functionalized case.

In Fig. 5.10, we have plotted the most favored adsorption geometry for the OE adsorption for the Mixed-FZGNRs, along with isosurfaces indicating the charge redistribution $\Delta\rho$. Once again, red lobes correspond to an accumulation of electrons, and green lobes correspond to a depletion of electrons. One can clearly see the induced dipole on the

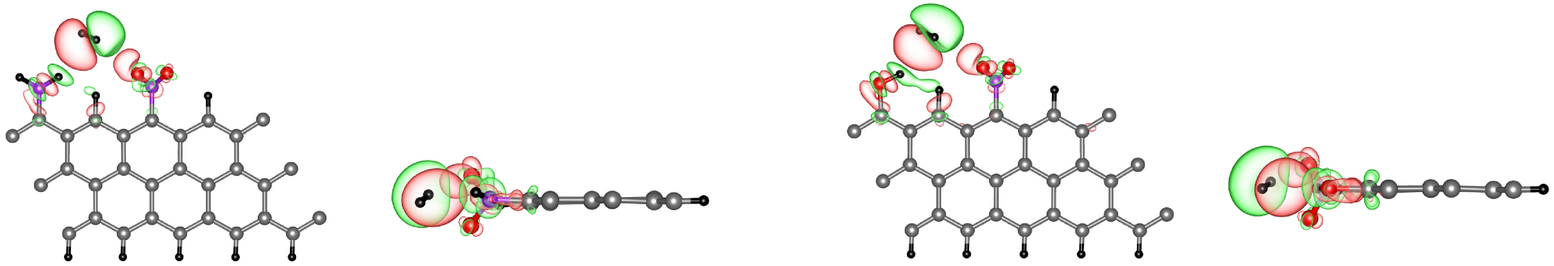

(a) NO_2–NH_2 Top view (b) NO_2–NH_2 Side view (c) NO_2–OH Top view (d) NO_2–OH Side view

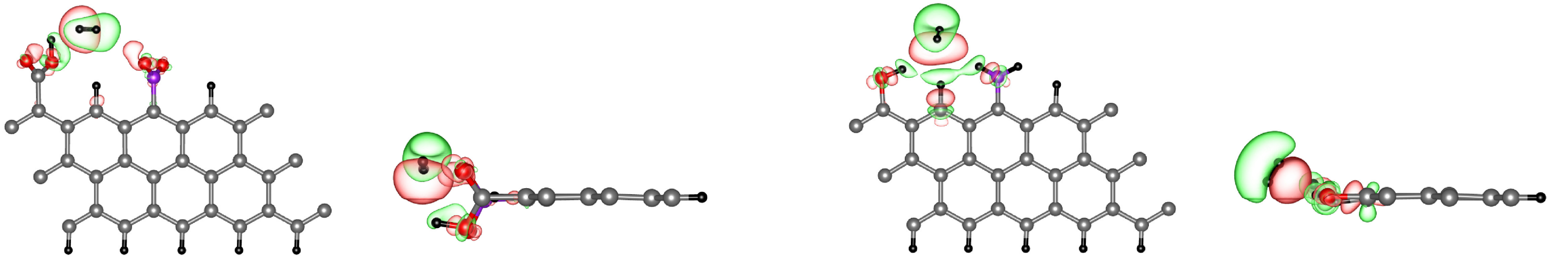

(e) NO_2–COOH Top view (f) NO_2–COOH Side view (g) NH_2–OH Top view (h) NH_2–OH Side view

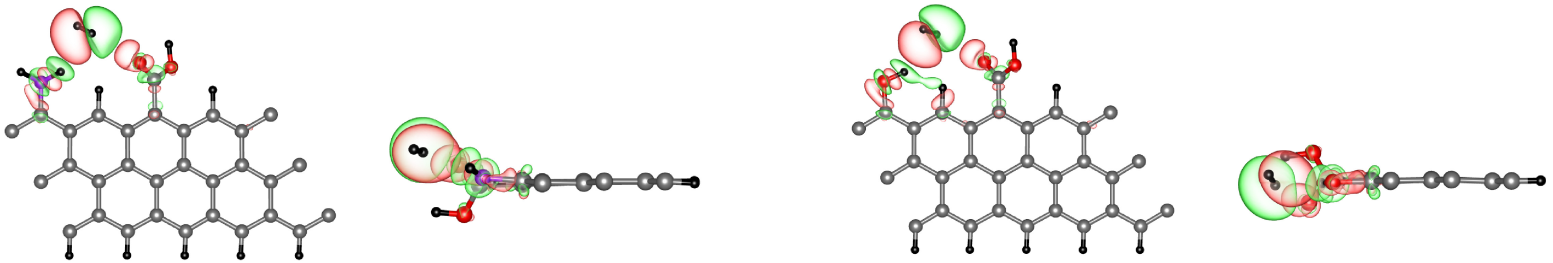

(i) NH_2–COOH Top view (j) NH_2–COOH Side view (k) OH–COOH Top view (l) OH–COOH Side view

Figure 5.10: *Optimal adsorption geometries, and redistribution of electronic charge upon adsorption of hydrogen, on the outer edge of the mixed functionalized ZGNRs. Red and green lobes correspond to a gain and depletion of electronic charge, respectively. The isosurfaces corresponding to* $\Delta\rho = \pm 2 \times 10^{-4}$ *electrons/bohr*^{3} *are plotted for all the cases. Color scheme for atomic spheres: H (black), C (gray), O (red), N (violet). This figure has been published in Ref. [201].*

hydrogen molecule in every case. Interestingly, the dipole on the H_2 prefers to orient itself in between an OH or NH group of one functional group and a lone pair on the doubly bonded O atom on the adjacent functional group. This is easily noticeable in the cases of NO_2–OH, NO_2–NH_2, NH_2–COOH, and OH–COOH. In these cases, the dipole moments induced on the H_2 are parallel to the edge of the ZGNR, and quite large. In the two remaining cases, viz., NO_2–COOH and NH_2–OH, the dipole moments are perpendicular to the edge, and much smaller.

In some cases, one notices a remarkable synergy for mixed functionalization, with the combination of two functional groups giving rise to much higher binding than can be obtained with functionalization by either functional group alone. This is most marked for the combination NO_2-OH, which leads to a binding of 110 meV, whereas strong functionalization by NO_2 or OH alone led to binding strengths of 61 and 78 meV respectively. The mechanism behind this synergy is easy to understand, with the induced dipole on the H_2 again aligning between the OH on one side, and the lone pair on the NO_2 on the other side; such a favorable electrostatic alignment is not possible with either functional group when present alone.

We note also that in order to achieve the proper synergy for mixed functionalization, it appears to be favorable to pick one functional group that is electron-withdrawing in nature, and another that is electron-donating. Note that for mixed functionalization, the relative binding energy in the presence of oxygen-containing functional groups does not follow the linear trend, as was observed as a function of the number of oxygen lone pairs for dilute and strong functionalization with a single functional group (cf. Fig 5.8). This is likely an artifact of the very different mechanism of charge reorganization between the two functional groups.

Once again, we estimate the various contributions to E_{ads}, for the case of mixed functionalization (see Fig. 5.11). Note that for all six systems considered here, the contribution from London dispersion interactions, E_L, is more or less the same. Thus, the range of values for E_{ads} obtained arises entirely from the different values of the electrostatic interactions (E_D and E_{IM}) in the different systems. This demonstrates that electrostatic

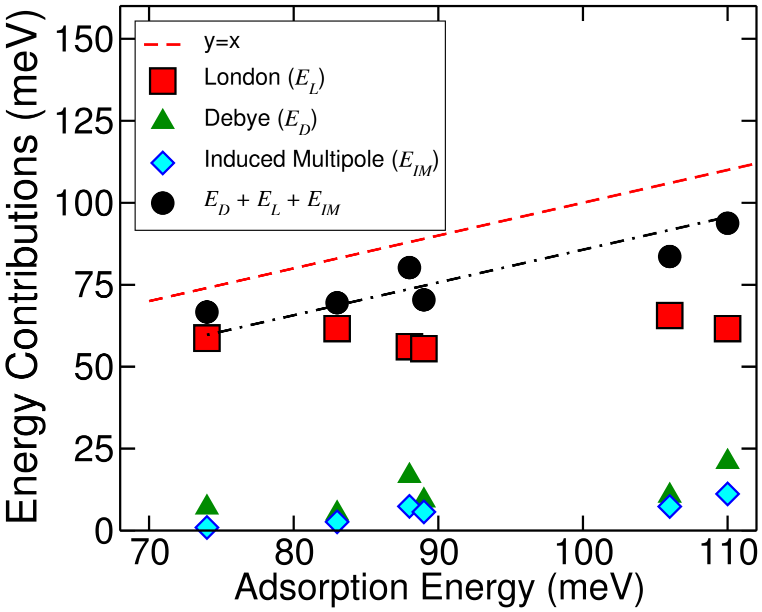

Figure 5.11: *Energy contributions from the London interaction (E_L), shown by red squares, the Debye interaction (E_D), shown by green triangles, and the induced multipolar interactions (E_{IM}), shown by cyan diamonds, for the outer edge adsorption of mixed functionalized ZGNRs. The sum of these three contributions is shown by black dots. The black dashed-dotted line is a guide to the eye. The red dashed line is the $y = x$ line, i.e., the line at which the net contribution from the different interactions should add up to the adsorption energy $E_{\rm ads}$. Note that the energy range of the x-axis does not start from zero. This figure has been published in Ref. [201].*

interactions (and not just the London interactions) can be effectively tuned to obtain increases in binding strength.

5.5 Summary and Conclusions

In this chapter, we have used first principles density functional theory based calculations to enhance the adsorption of hydrogen molecules on carbon nanostructures, by chemically functionalization. We have used graphene nanoribbons for this study, whose edges are modified by chemical functional groups. We have taken care to incorporate the London dispersion interactions which are essential for an accurate treatment of such a scenario of weak binding. These are incorporated in our calculations within the semi-empirical DFT-D2 treatment.

Our study establishes that hydrogen always prefers to bind to the edge of the nanoribbons rather than to the interior of a graphene sheet. We find that chemical functionalization helps enhance the strength of the hydrogen binding to these graphene nanoribbons. We have considered different regimes of functionalization, dilute, strong, as well as mixed functionalization, and we find that by properly choosing the functional groups, the binding can be enhanced by about ∼120% with respect to the pristine graphene sheet or H-passivated ZGNR. Of the various functional groups considered by us, the largest enhancement in binding is found in the cases of “strong functionalization” with H_2PO_3, and “mixed functionalization” with NO_2 and OH, or OH and COOH. For those functional groups that contain the OH moiety, the adsorption energy is linearly proportional to the number of lone pairs on oxygen atoms. In each of these cases, the oxygen lone pairs play a key role in stabilizing the binding by facilitating local charge redistribution. We also observe an interesting synergy between several functional groups in the case of mixed functionalization, where a significantly larger binding is obtained when a combination of functional groups is used, than would be obtained with either functional group present alone. Our results suggest that this synergy is best leveraged in the simultaneous presence of neighboring electron-withdrawing and electron-donating functional groups.

We have also separated out the contributions of different interactions. We find that most of the binding comes from the London dispersion interactions. However, for all binding configurations, we also find a significant redistribution of electronic charge induced on the hydrogen molecule. It is important to note that the axis of this induced “dipole” [1] need not coincide with the molecular axis. For adsorption outside the edge of the graphene nanoribbon (“outer edge” adsorption), the electronic redistribution contributes significantly to the binding energy as Debye and higher-order multipole interactions. For adsorption over the ribbon edge (“inner edge” adsorption), this contribution to the binding energy is somewhat smaller in magnitude; nevertheless, one also notices a distortion of the π electron cloud of graphene just below the molecule. In this case, both the orientation and the magnitude of the charge redistribution on the H_2 molecule clearly

---

[1] For OE, the induced positive and negative charges are equal (constituting a dipole), whereas for IE, they are unequal due to partial charge transfer.

reflect the electron donating or withdrawing capacity of the functional group (quantified by the Hammett parameter), and its effect on the local occupation of the π manifold of the nanoribbon.

Our results allow us to obtain valuable insight into the origins of the weak binding of molecules such as hydrogen to graphene and functionalized graphene nanostructures. Even though the London dispersion interactions provide a major component of the binding, and their inclusion is extremely crucial in any realistic theoretical treatment of such systems, we note that other electrostatic interactions provide a considerable fraction of the total binding strength. We also note that these electrostatic contributions can be effectively tuned by edge functionalization with appropriate chemical modification, thereby resulting in further increases in gas uptake.

While this enhancement in binding at the edge can be used to tailor graphene and/or activated carbon materials so as to increase the uptake of hydrogen, this value of adsorption energy needs to be further enhanced by $\sim$40 meV before it reaches the optimum value of $\sim$150 meV that is desirable for on-board vehicular applications [231]. Nevertheless, we suggest that edge functionalization could be useful when used in combination with other strategies, in order to achieve the required room-temperature storage capacity. In addition, we believe we can translate many of our qualitative conclusions to other weakly adsorbed gases on sp^2 carbon substrates, where the underlying binding mechanisms are similar.

Chapter 6

Spin Transport Properties and Molecular Magnetoresistance of Dithienylethene Molecule attached to Magnetic Nickel Leads

Now we come to the final study of this thesis. Following the same line of study as seen in the earlier chapters, we use first principles calculations to study the spin transport and magnetoresistance properties of an organic molecule called dithienylethene, connected to magnetic nickel leads. We want to tune the spin-polarized transport in this nonmagnetic molecule and to enhance its magnetoresistance properties; we attempt to do this by changing the shape and geometry of the magnetic Ni leads to which this molecule is attached. We have now moved from nanostructured materials to a single molecule, which can be thought of as the ultimate limit of miniaturization. Note that in studying transport properties, we are no longer in the equilibrium situation, and first principles calculations based on advanced non-equilibrium theories need to be incorporated. Here we use calculations based on the non-equilibrium Green's function technique, implemented in combination with DFT, to calculate the transport properties. This drastically increases the computational cost. Some of the results presented in this chapter were published in Refs. [232]

and [233].

6.1 Introduction

The field of molecular electronics has attracted considerable interest in recent years [26, 234–239]. Molecules have the advantage of being defect free, and easy to synthesize on a large scale by simple chemical methods. There have been reports of p-n junctions [26], rectifiers [234] and switches [235], all made with molecules. Realizing an electronic circuit where the electronic components consist of single molecules can be imagined as the ultimate limit of the miniaturization of electronics.

Another novel, rapidly growing field, hand in hand with the field of molecular electronics, is that of molecular spintronics, where the spin degree of freedom can be leveraged to accomplish new types of functionalities [29, 30]. Organic molecules are especially attractive candidates for molecular spintronics, as they offer high spin coherence and long spin lifetimes due to weak spin-orbit and hyperfine interactions. The typical system studied in molecular electronics consists of a molecule placed between metal leads; for spintronics applications, it is of interest to consider the case where the metal is ferromagnetic [240–242]. By studying such systems both experimentally and theoretically, it has been shown that, by a suitable choice of molecules and anchoring groups, it is possible to obtain a large bias-dependent magnetoresistance [30, 243]. Large values of magnetoresistance (MR) are desirable for applications such as information storage and recording.

Molecule-metal interfaces [244] and system geometry play a vital role in determining the properties of systems relevant to molecule electronics. Properties like charge transfer and the ionization potential of organic thin films can be tuned by varying the orientation of the organic molecules [245, 246]. It has also been shown that the symmetry of small molecules affects the accessible conformational fluctuations, and as a result the measured conductance [239]. An extreme example of the influence of molecular conformation on conductance is provided by photoswitching molecules such as dithienylethene and diarylethenes [247–255], where the breaking of a C-C bond switches the molecule reversibly between highly-conducting and highly-resistive conformations.

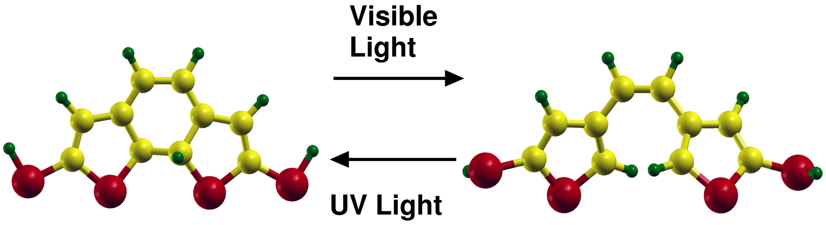

Figure 6.1: *The two geometrical conformations of the dithienylethene molecule, at the left is the 'closed' conformation and at the right is the 'open' conformation. Switching between the two conformations can be achieved by shining light. Color code: yellow balls C, large red balls S and small green balls H.*

In addition to varying molecular orientations and molecular conformations, another way of changing the system geometry is by varying the shape of the leads, or the way in which the molecule makes contact to the leads. Among the many open questions in the field of molecular spintronics, is that of how best to connect molecular components with the outside world. There have been a few previous theoretical studies of how the transport properties of molecular systems are affected by the molecule-lead contact [60–64]. In these studies, the authors found that the conductance depended on the contact geometry, by up to an order of magnitude. Break junction and Scanning Tunneling Microscopy (STM) experiments on molecular transport observed either conductance values distributed over a wide range, or peaked at a few values, which was attributed to the presence of a number of different molecule-lead atomic conformations when performing repeated experiments [64,236,256]. However, we are not aware of any such study that considered magnetic systems. In this chapter, we examine how the contact geometry affects the properties of spin molecular systems, in particular, the magnetoresistance. We show that this property is surprisingly easy to understand, and that the contact geometry plays a crucial role in determining the magnetoresistance. For our study, we consider a dithienylethene (DTE) molecule attached between nickel leads. DTE is a photoswitching molecule that can be reversibly switched between two stable conformations ('closed' and 'open') by shining ultraviolet or visible light (see Figure 6.1). In the closed conformation, the molecule is a good conductor via resonant transport, while in the open conformation it is a poor conductor via a tunneling mechanism. For our purpose, using DTE is of interest because this permits us to investigate and compare these two different conduction regimes, while retaining the same molecule-lead anchoring configuration. Ni is a so-called strong ferromagnet, i.e., one spin channel in the *d*-band is completely filled. Earlier theoretical and experimental studies have examined the conduction properties of DTE molecules between non-magnetic leads [257–260].

6.2 Computational Details

Our calculations for determining the electronic structure and equilibrium geometry of the molecule under consideration here were performed within the framework of *ab initio* density functional theory (DFT) [66]. In this study, we have used the DFT code SIESTA [82], which uses an efficient numerical atomic orbital basis set for the description of the valence electrons. Using a localized basis set has the advantage of reducing computational time, as the large matrices involved in the computations become mostly sparse in a representation of localized basis functions. A double ζ plus polarization orbital basis set was used for all the atoms in the molecule. In contrast, the atoms in the leads were treated at the level of single ζ orbitals for the d electrons and double ζ orbitals for the s electrons plus a p polarization orbital. The interactions between the core and the valence electrons were described using norm-conserving, non-local Troullier-Martins pseudopotentials [261]. The Perdew-Burke-Ernzerhof (PBE) [77] form of the generalized gradient approximation (GGA) for the exchange-correlation energy functional was used.

To perform the spin polarized transport calculations, we have used the SMEAGOL code [30, 83, 262], that interfaces the non-equilibrium Green's function (NEGF) scheme for electronic transport [263], with the DFT implementation in the SIESTA code. For our calculations, we consider a typical two terminal setup (as described earlier in Chapter 2), with the molecule or the scattering center (SC) connected between two semi-infinite metallic leads on the left (L) and right (R). The scattering center (SC) contains the molecule across which the the spin-polarized current of electrons is allowed to flow, as well as a few layers of the metallic lead on either side, so as to allow a smooth matching of the electrostatic potential in the molecule with that in the leads [83]. The leads (L and R) are treated as reservoirs of electrons, each with a chemical potential (μ_L and μ_R). The effect of an applied bias voltage is to change the chemical potential of one of the leads with respect to the other, i.e., to produce rigid shifts in the energy spectra of the leads. The non-equilibrium Green's function for the SC is given as,

$$G(E,V) = \left[E + i0^+ - H(V) - \Sigma_L(E,V) - \Sigma_R(E,V)\right]^{-1} , \tag{6.1}$$

where $H(V)$ is the Hamiltonian of the SC (which is a functional of the charge density), V is the applied potential (bias), E is the energy, and $\Sigma_{L,R}$ are the energy- and bias-dependent self-energies of the left, right leads. The self energies describe the interaction of the SC with the leads and are essential for establishing the appropriate open boundary conditions of the transport problem. The Green's functions are calculated via a self-consistent procedure, which accounts for the non trivial potential profile which develops in the SC as an effect of the external bias potential on the charge density of the scattering center. After the convergence of the self-consistent procedure, the transmission function $T(E,V)$ is calculated using the Landauer-Büttiker formula [108],

$$T(E,V) = \mathrm{Tr}\left[\Gamma_L(E,V)G(E,V)\Gamma_R(E,V)G^\dagger(E,V)\right] , \tag{6.2}$$

where $\Gamma_{L,R}(E,V) = i(\Sigma_{L,R} - \Sigma^\dagger_{L,R})$ is the broadening matrix for leads L, R. The transmission function is calculated for each spin channel, and thus is labeled by a spin index σ. The transmission function of Eq. (6.2) is integrated over the bias window ($E_F - eV/2$, $E_F + eV/2$) to yield the spin-dependent current:

$$I^\sigma(V) = \frac{e}{h}\int_{-\infty}^{\infty} T^\sigma(E,V)\left[f(E-\mu_L) - f(E-\mu_R)\right] dE \, . \tag{6.3}$$

6.3 The Dithienylethene molecule

The dithienylethene (DTE) molecule is a non-magnetic organic photoswitching molecule, that can reversibly switch between two stable conformations (“closed” and “open”) upon shining ultraviolet or visible light (see Fig. 6.1). The structure of the DTE molecule consists of three carbon rings: a central hexagonal ring, connected on either side to two

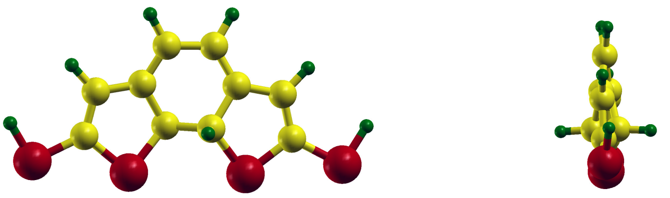

(a) Closed, front view (b) Closed, side view

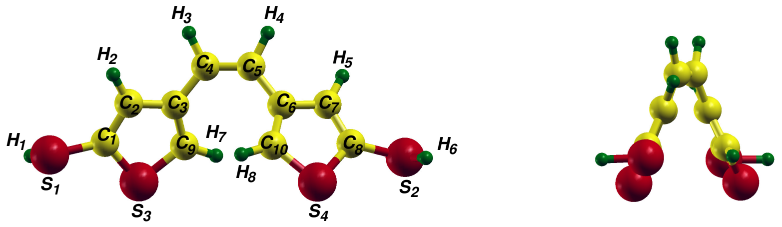

(c) Open, front view (d) Open, side view

Figure 6.2: *Front and side view of the geometry for the (a), (b) closed and (c), (d) open conformations of the DTE molecule, respectively. Color code: C – yellow, S – red, H – green.*

five-fold rings (four carbon atoms and a sulfur atom), with thiol groups on either side. It is one of the carbon-carbon bonds of the central hexagonal ring that breaks when the molecule is irradiated by visible light, thus changing the geometry from a "closed" conformation to an "open" conformation. The reverse transformation from "open" to "closed" can be caused by irradiation with ultraviolet light.

The differing geometries and resulting electronic structures of these two conformations give rise to very different conduction properties. The "closed" molecule shows much higher conductivity than that observed in the case of the "open" molecule. Experiments have shown that the "closed" conformation of a pyridine-terminated DTE molecule attached to gold leads has higher conductivity than the "open" molecule, by at least a factor of 30 [255]. The DTE molecule and its derivatives can find many applications, e.g., as opto-electronic switches. There have been many theoretical as well as experimental studies of DTE and related molecules attached to Au leads, with the aim of exploiting this particular virtue of the molecules. The sulfur atoms of the thiol groups are generally used to attach to the metal leads in these transport setups. Molecular crystals composed of molecules related to DTE have been experimentally reported to show large shape changes upon irradiation, and hence can find applications as photo-responsive actuators [264].

We want to understand the role of the molecule-metal contact in determining the spin dependent transport and magnetoresistance properties of molecules. The DTE molecule is a good candidate for such a study, as it has two advantages: (i) the 'photoswitching' aspect, where the effect of the molecule-metal contact on the relative conductance of the two conformations of the molecule can be understood, (ii) the "closed" and the "open" conformations of DTE can be considered as representative of the two different possible transport regimes; with the highly conducting "closed" conformation representing the resonant transport regime and the low conduction via the "open" conformation resulting in an example of the tunneling transport regime. Thus using the two conformations of the DTE molecule has the advantage of allowing us to investigate and compare the effect of the lead contact in both of these transport regimes, without significantly altering the molecule-lead anchoring configuration.

We first examine the structural properties of the two conformations of an isolated DTE molecule (See Fig. 6.2). The "closed" conformation of the DTE molecule is a rather planar molecule, with the central six-fold ring and the five-fold rings on either side as well as the thiol attachments on either side lying mostly in one plane. Only two sp^3 bonded carbon atoms of the central ring (atoms C_9 and C_{10}) and the hydrogen atoms attached to them (atoms H_7 and H_8) protrude out of the plane of the molecule on either side [see Fig 6.2(b)]. It is the bond between these two carbon atoms of the central ring that is involved in the photoswitching process, this C-C bond is broken as the molecule switches from its "closed" to "open" conformation. We optimized the geometry of an isolated DTE molecule in both the conformations in a large cubical box of dimension 30 Å, and found the length of this particular C-C bond length to be 1.51 Å for the "closed" conformation and 3.13 Å for the "open" conformation. In the "open" conformation, these two carbon atoms are no longer sp^3 bonded, but are instead sp^2 bonded, and hence like to be in the plane of the three atoms to which they are attached. The two pentagonal rings of the open molecule prefer to lie in different planes in the "open" conformation [see Fig 6.2(d)], where the planes in which these rings lie make an angle of $\sim 45^\circ$ with each other. We note that upon checking the results for the structure of the isolated DTE molecules using the plane wave pseudopotential code Quantum ESPRESSO, we obtain very similar results.

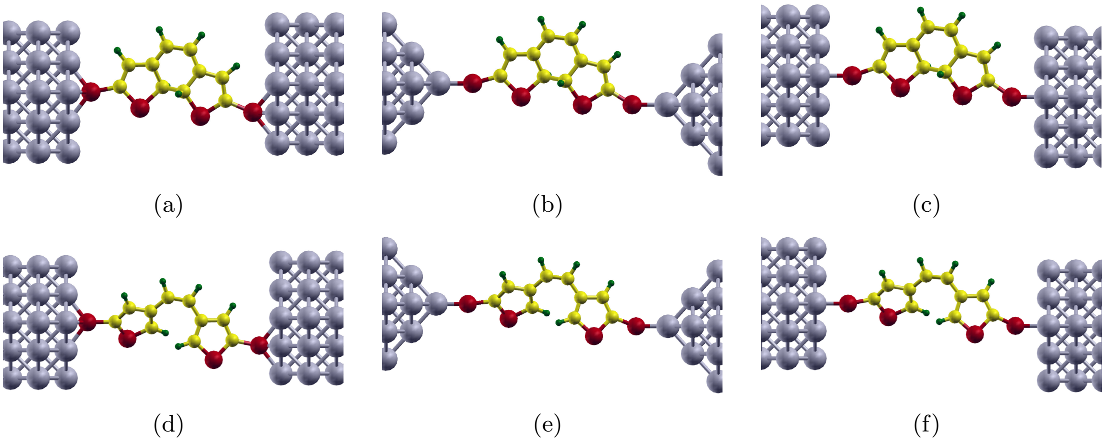
(a) (b) (c) (d) (e) (f)

Figure 6.3: *Geometries of systems studied (a) Closed and (d) Open conformation of the DTE molecule between flat Ni leads, attached to the hollow site, (b) Closed and (e) Open conformation of the DTE between sharp Ni leads, and (c) Closed and (f) Open conformation of the DTE between flat Ni leads, attached to the atop sites. Color code: C – yellow, S – red, H – green, Ni – gray.*

6.4 Systems studied

To understand the effect of lead geometry on the spin dependent transport properties and the magnetoresistance (MR), we consider two extreme cases of lead geometry: one (Case A) consisting of a flat Ni(100) surface [see Figs. 6.3(a) and 6.3(d)] and the other (Case B) consisting of a pointed one-atom-sharp tip [see Figs. 6.3(b) and 6.3(e)]. In Case A, the DTE molecule is connected to the leads in such a way that the end sulfur atoms of the molecule bind to the hollow site of the flat Ni(100) surface, this is the energetically most favorable binding site. In this calculation, the Ni(100) surface was modeled by a slab consisting of five layers of Ni, with 3 × 3 atoms per layer on each side of the molecule, with periodic boundary conditions in the perpendicular directions. In Case B, the sharp tip is constructed by placing a pyramidal Ni apex over a Ni(100) surface. In this case, the sulfur ends of the molecule bind to an atop site on the pointed tip. To understand whether the changes in the magnetoresistance that arise in these two extreme cases are a result of the change in the tip geometry or are an effect of the anchoring site, we consider a third, intermediate, situation where the DTE molecule is attached to the rather energetically unfavorable atop binding site of the flat Ni(100) surface [see Figs. 6.3(c) and 6.3(f)]. We perform calculations using both closed and open conformations of the molecule in all these three cases.

For calculating the MR, we need to consider two distinct relative spin orientations of the leads: (i) parallel (↑↑), and (ii) antiparallel (↑↓), to each other. Thus we have performed calculations on twelve different configurations in total, each of these calculations are carried out at bias voltages varying from 0 V to 0.8 V.

6.5 Results

We first try to highlight the differences in the transport properties of the two conformations of the DTE molecule, the “closed” and “open” conformations. As mentioned earlier, the closed molecule shows much higher conductance than the open molecule. The differences in the transport mechanisms of the two conformations can be clearly seen by looking at differences in their electronic structures.

6.5.1 “Closed” molecule v/s “Open” molecule

The electronic properties of the DTE molecule crucially depend on its geometry. The switching of the molecule from one conformation to the other results in a change in the electronic structure of the molecule. This can be seen by looking at the frontier molecular orbitals, i.e., the highest occupied molecular orbital (HOMO) and the lowest unoccupied molecular orbital (LUMO) for the closed and open conformations of the DTE molecule (See Fig. 6.4). It is easy to notice that in the closed case, the charge density corresponding to the HOMO and the LUMO is mainly located between alternating carbon atoms of the carbon backbone (atoms C_1–C_8) that connects the sulfur atoms (S_1 and S_2) of the end thiol attachments [see Fig. 6.4(a)]. On the other hand, the HOMO and LUMO of the open molecule have significant charge density between alternate carbon atoms of the central carbon ring [see Fig. 6.4(b)]. It is this difference in the spatial distribution of the frontier orbitals of the closed and the open conformations, that will result in the distinct conduction properties of the two conformations.

When the molecule is in contact with the leads, the sharp molecular states broaden as well as shift in energy. In Fig. 6.4 we have shown, as an example, the densities of states of both the closed and open conformations of DTE, when connected to the hollow site

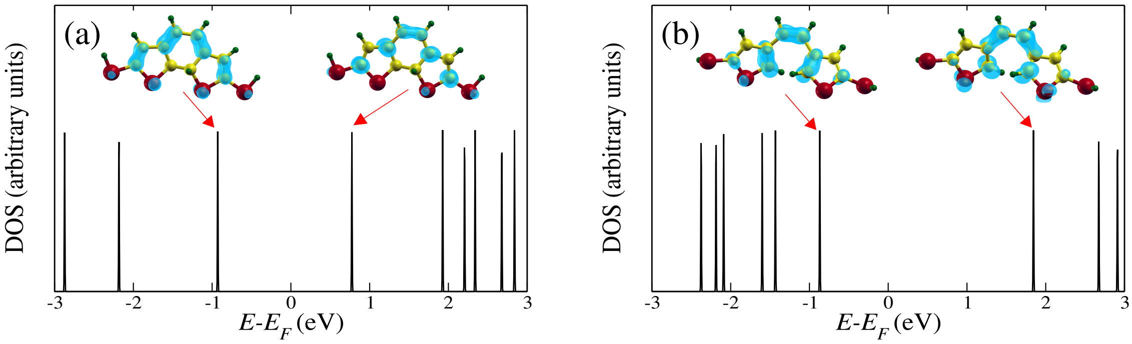

Figure 6.4: *Density of states and frontier Molecular Orbitals for the (a) closed and (b) open conformations of the DTE molecule, corresponding to the HOMO and the LUMO, respectively. The charge density corresponding to an isosurface value of 0.005 e/bohr*^{3} *is shown in blue. Color code: C – yellow, S – red, H – green.*

of the flat Ni leads, in ↑↑ (black curve) and ↑↓ (magenta curve) spin orientations of the leads. In the case of the closed conformation, the HOMO and the LUMO become broad peaks centered at about 0.5 eV below E_F and at about 1.1 eV above E_F, respectively. For the open conformation, the broadening of the HOMO and LUMO is smaller, resulting in the fairly sharp peak features at around 1.5 eV below E_F and at about 1.2 eV above E_F, respectively.

A number of previous studies have established that the closed conformation of the DTE molecule is a good conductor and conducts via a resonant transport mechanism, while the open conformation is a poor conductor and conducts via a tunneling mechanism, in the open conformation. We therefore examine the projected density of states (PDOS) on the different atoms in the system. As an example, we have plotted the PDOS over different atoms of the closed and the open molecule attached to the hollow site of flat leads in the ↑↑ spin orientation (see Fig. 6.5). It is clearly evident that for the closed conformation, the variation in the PDOS in the neighborhood of the Fermi energy is negligible as one traverses the C-backbone, resulting in resonant transport. On the other hand for the open conformation, the PDOS decays exponentially as one goes from the two ends to the middle of the C-backbone, which is a clear signature of tunneling transport. Note that the y-axis scales in Figs. 6.5 (a) and (b) are different.

Next, we will describe spin polarized transport via the DTE molecule, and attempt to understand the effect of varying the lead geometry on the spin-dependent conduction

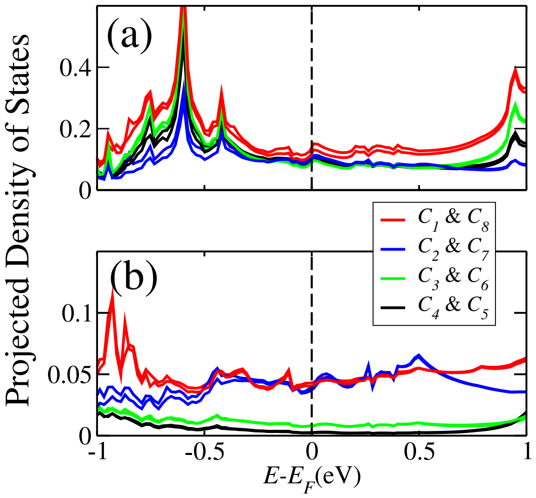

Figure 6.5: *Projected density of states over the different carbon atoms along the C-backbone for (a) closed conformation and (b) open conformation of the DTE molecule connected to the hollow site of the flat Ni leads at zero bias in the ↑↑ spin orientation. The PDOS is summed over both the spin channels. See Fig 6.2(c) for the convention used to label the C-atoms.*

properties and the magnetoresistance of the DTE molecule.

6.5.2 Spin Polarized Conduction

First we plot the I-V characteristics for the closed and the open conformations of the DTE molecule in the three geometries cases discussed earlier (see Fig. 6.6). It is clear from the I-V characteristics that the current in the closed conformations is about two orders of magnitude higher than in the corresponding open conformations, both in the ↑↑ and the ↑↓ situations. The contributions of the majority (I_{up}), and the minority spin (I_{down}) channels to the total current are also shown.

Some general trends can be obtained by looking at the I-V characteristics, which apply for both closed and open conformations, despite the fact that the electronic transport mechanism in these conformations is drastically different. (a) In the ↑↑ situation, in general, both the spin channels show more or less equal contribution over the entire voltage range considered. (b) In the ↑↓ situation, the contribution from the two spin channels is roughly equal at low bias, but becomes increasingly disparate at higher bias voltages; this gives rise to a pronounced spin polarization of the current through the molecule. In the insets in Fig. 6.6, we also plot the degree of spin-polarization of the current (SP), which is defined as $(I_{\rm up} - I_{\rm down})/(I_{\rm tot})$, where $I_{\rm up}$ and $I_{\rm down}$ are the currents via the majority and minority spin channels, and $I_{\rm tot} = I_{\rm up} + I_{\rm down}$, is the total current. In all the geometries considered here, the degree of spin-polarization of the current is seen to increase with increasing the bias voltage in the $\uparrow\downarrow$ situation, up to about 0.7 V.

Looking at the *I*-*V* curves for DTE, it is interesting to note that the impact of the lead geometry appears to be more prominent in the tunneling transport regime (the open conformation) than in the resonant regime (the closed conformation). The current via the open conformation increases dramatically (by about an order of magnitude) in the cases where contact of the molecule is made to the sharp tip geometry (Case B) and to the atop site of the flat lead (Case C). This observation is in agreement with earlier studies showing that the conductance via an organic molecule is significantly affected by the interface with the leads. For example, theoretical studies show that the zero bias conductance of alkanethiols (where it is quite well established that the conduction occurs primarily due to a non-resonant tunneling process) connected to gold leads, depends strongly on the atomic arrangement in the lead [61].

To further emphasize the effect of the leads, we also plot the ratio of the currents in both the conformations of the molecule, $I_{\rm closed}/I_{\rm open}$. A large value of this quantity is advantageous for the use of the DTE molecule as an optoelectronic switch. Our results for this ratio, in the various tip geometries and attachment sites, are plotted in Fig. 6.7. We find that in Case A, where the molecule is attached to the hollow site of the flat Ni surface, this ratio is quite large, between 80–90 for the $\uparrow\uparrow$ spin orientation, and $\sim$70 for the $\uparrow\downarrow$ spin orientation of the leads. For Case B where the molecule is attached to the sharp tip, this ratio drastically drops down to 20–50 for the $\uparrow\uparrow$ spin orientation and 10–20 for the $\uparrow\downarrow$ situation. Even for Case C, where the molecule is attached to the energetically unfavorable atop site, this ratio is small, $\sim$20. This reduction is mainly an effect of the atop attachment site, rather than the sharp lead geometry. As seen earlier, the current in those cases where the open molecule is attached to the atop site increases, and hence the ratio $I_{\rm closed}/I_{\rm open}$ goes down. These results underline the significance of the contact geometry with the leads in determining the conduction properties. To summarize, if one

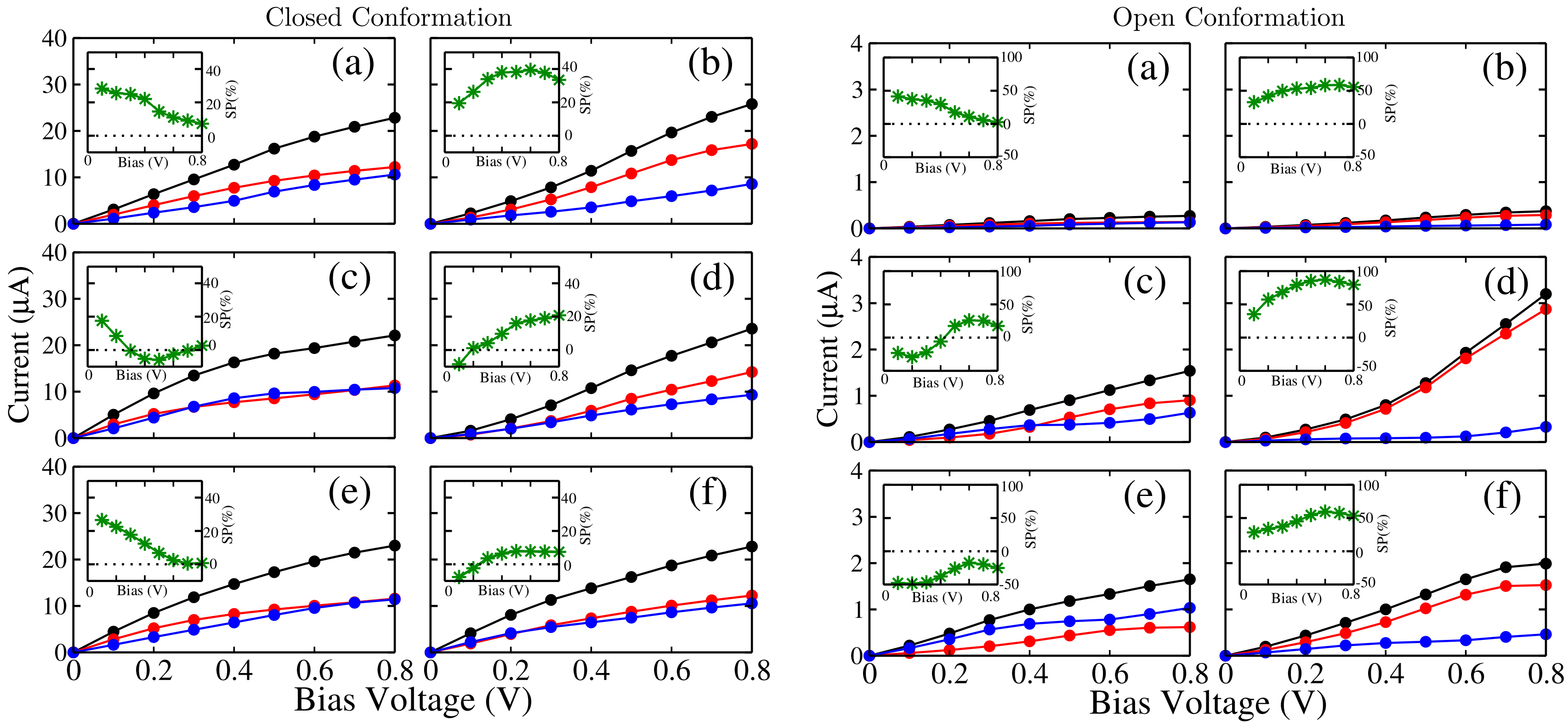

Figure 6.6: *The I-V characteristics for the closed conformation (left panels) and the open conformation (right panels) of DTE between Ni leads. (a) and (b) denote the ↑↑ and ↑↓ situations for Case A, (c) and (d) denote the ↑↑ and ↑↓ situations for Case B, and (e) and (f) denote the ↑↑ and ↑↓ situations for Case C, respectively. The red, blue and black dots indicate the up-spin, down-spin and total currents,* $I_{\rm up}$, $I_{\rm down}$ *and* $I_{\rm tot}$ *respectively. The insets show SP, the degree of spin polarization of the current, defined as* $(I_{\rm up} - I_{\rm down})/(I_{\rm tot})$. *These figures have been published in Ref. [233].*

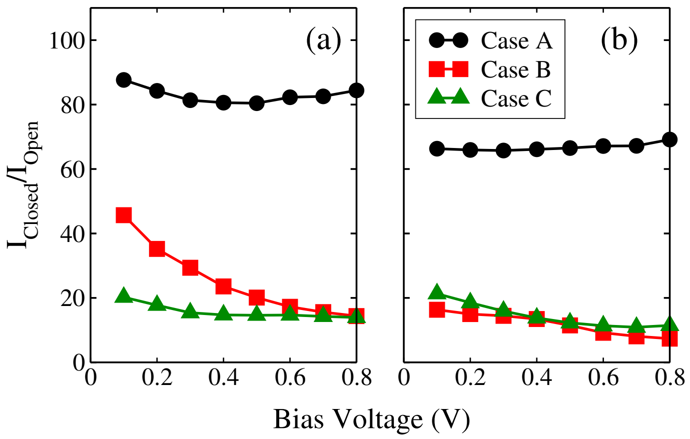

Figure 6.7: *The ratio of the current for the closed and the open molecule* $I_{\mathrm{closed}}/I_{\mathrm{open}}$ *for (a)* $\uparrow\uparrow$ *and (b)* $\uparrow\downarrow$ *situations, for Case A (black circles), Case B (red squares), and Case C (green triangles), respectively. This figure has appeared in Ref. [233].*

wants a high "on-off" current ratio via the molecule, it is would be best to make contact to the hollow sites of the flat leads.

To understand these results, we now look at the transmission coefficients, as a function of the bias voltage, for the different situations discussed above. The current through the DTE molecule is the integral of the bias dependent transmission coefficient over the relevant bias window, as described earlier in Eq. (6.3). If one compares the transmission coefficient in the closed and the open cases, on can clearly see that for the closed molecule there is a significant value of the transmission in the bias window, in contrast to the open molecule. This results in the low current in the open molecule.

Comparison with results for different lead materials

Before going to the detailed study of the magnetoresistance (MR), we wish to compare the effect of using different metals as leads on the conduction properties of the DTE molecule. We wish to compare our results for DTE connected to spin-polarized nickel leads, with those obtained by some of our earlier studies on the conductance of DTE using non-magnetic nickel, silver and gold leads [259, 260]. In this case, we compare only to the results obtained for the situation where DTE is attached to the flat nickel surface, in the case of parallel ($\uparrow\uparrow$) spin polarization of the leads. For better comparison, the distance

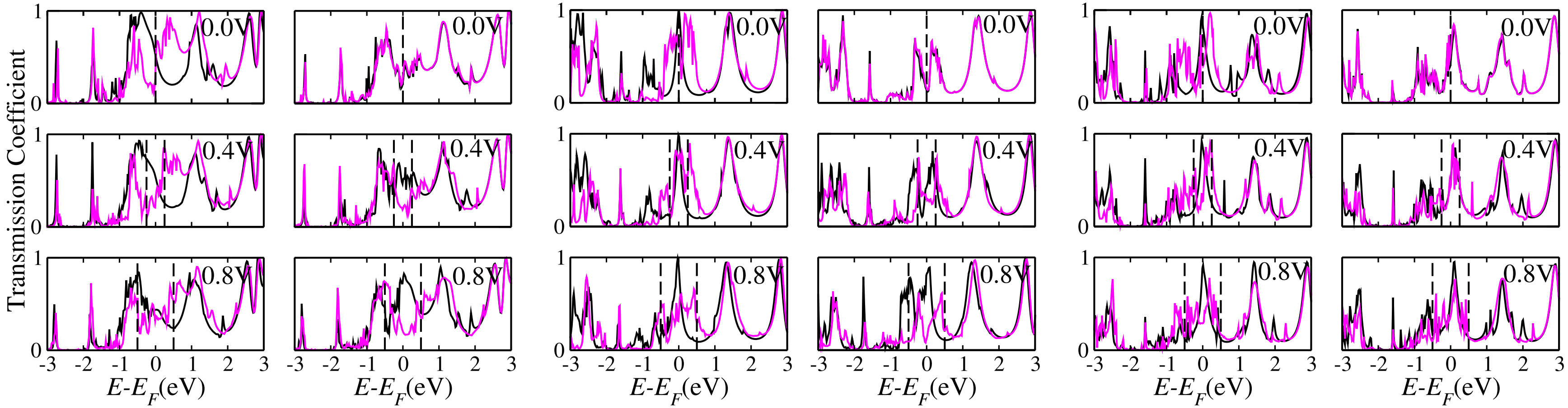

(a) (b) (c)

Figure 6.8: *Transmission Coefficient, as a function of energy E, for the closed conformation, at different bias voltages for (a) Case A: the DTE molecule between flat Ni leads, attached to hollow sites. (b) Case B: DTE between sharp Ni leads. (c) Case C: DTE between flat Ni leads, attached to atop sites. In (a), (b) and (c), the left-side panels are the results for parallel spin configuration of the leads, and the right-side panels for antiparallel spin configuration. The results for majority spin channel are denoted by black curves, and the results for minority channel by magenta curves.*

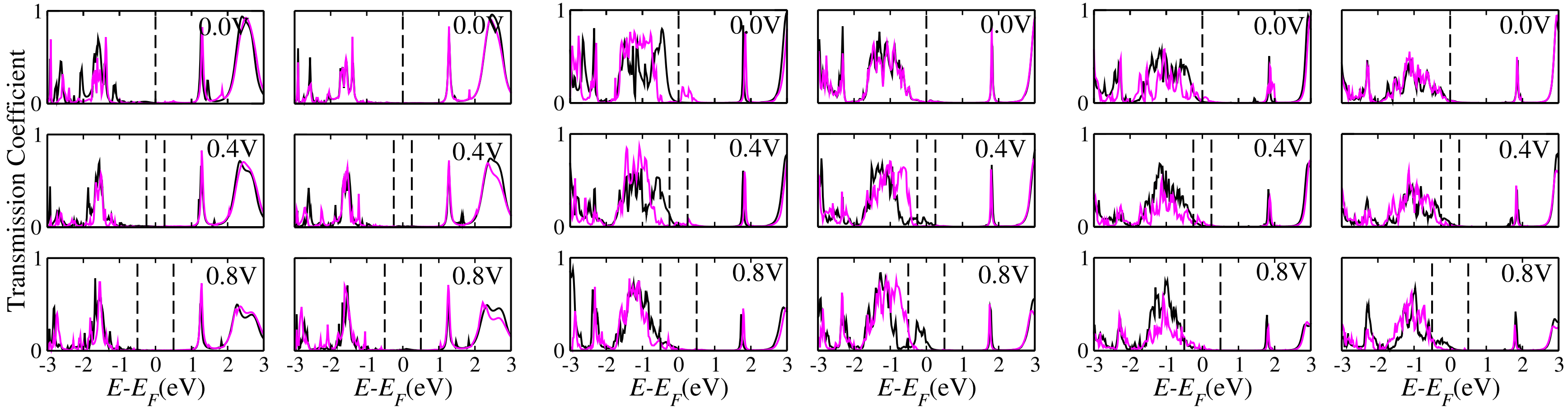

(a) (b) (c)

Figure 6.9: *Transmission Coefficient, as a function of energy E, for the open conformation, at different bias voltages for (a) Case A: the DTE molecule between flat Ni leads, attached to hollow sites. (b) Case B: DTE between sharp Ni leads. (c) Case C: DTE between flat Ni leads, attached to atop sites. In (a), (b) and (c), the left-side panels are the results for parallel spin configuration of the leads, and the right-side panels for antiparallel spin configuration. The results for majority spin channel are denoted by black curves, and the results for minority channel by magenta curves.*

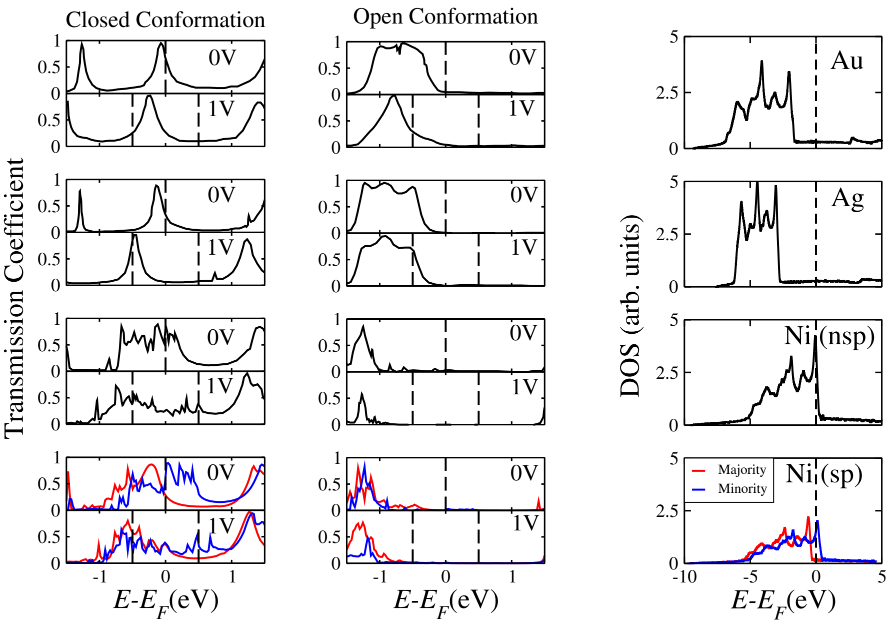

Figure 6.10: *Transmission coefficients as a function of energy, calculated for both closed and open conformations of the DTE molecule attached to four different lead materials: from top to bottom, Au, Ag, non-magnetic Ni, and spin-polarized Ni. For each material, the transmission functions calculated at zero bias and 1 V bias are shown. The red and blue curves denote the majority and minority spin transmission coefficients, respectively. The vertical dashed lines denote the bias window. The bulk DOS for each metal is also shown.*

between the metal and the sulfur atom of the DTE was fixed to be 1.9 Å, for all the metals. Though this was a stable geometry in the case of Au and Ag, this is an overestimation for the case of nickel (optimized distance for the case of nickel is about 1.45 Å for the closed conformation and 1.38 Å for the open conformation). However it was checked that the results are not qualitatively different than those for the optimized case.

In Fig. 6.10, we plot the transmission functions for the closed and the open molecule for different metal leads, for both closed and open conformations of the DTE molecule. The transmission function is plotted for zero bias as well as for a bias of 1 V. We have also plotted the bulk density of states (DOS) of the metals for comparison. One can see from the DOS that the d-states of Au and Ag are completely filled, and lie way below E_F. Thus the states contributing most to the transport properties are the s-states for these two metals. Ni is a strong ferromagnet, i.e., one spin channel in the d-band is completely filled. In the case of non-magnetic Ni, where spin-polarization is not allowed [denoted as Ni (nsp) in the figure], the d-states lie at E_F and show up as the sharp peaks in the DOS.

For spin-polarized Ni [denoted as Ni (sp) in the figure], the DOS is spin-split as shown, and is indicated by the majority (red) and minority (blue) curves. In this case, the *d*-states of the majority spin channel are filled and lie about 0.5 eV below E_F, whereas the minority spin channel shows the *d*-states at E_F.

The transmission functions also show some significant differences for the above listed metals. For Au and Ag the transmission function is quite similar, for both closed and open conformations of the DTE molecule. The transmission for the closed conformation shows a smooth Lorentzian-like structure for both these metals, which we point out is a signature of the *s*-like electrons contributing to it. As the bias is increased, these peaks move to lower energies, the magnitude of this shift is larger for Ag than for Au. For the open molecule, we see a broad feature in the transmission below E_F for both Ag and Au, which narrows down (prominently for Au) at higher bias. For the case of Ni (nsp) where it is not allowed to spin-polarize, we find that the transmission coefficient of the closed conformation shows a broad jagged feature centered around the Fermi energy. This is a distinct signature of the localized *d*-states. In the case of spin-polarized Ni, the minority spin channel again shows this distinct *d*-character in the transmission coefficient. The majority spin channel transmission resembles the transmission for the Au and Ag cases, with a clearly visible Lorentzian-like structure just below E_F. As the bias is increased, the majority spin channel gradually becomes jagged as the *d*-states increasingly start to contribute.

6.5.3 Magnetoresistance

Next, we compute the bias-dependent magnetoresistance (MR) for both the closed and the open conformations of the molecule, these results are plotted in Fig. 6.11. The magnetoresistance is given as

$$\mathrm{MR}(\%) = \left(\frac{\mathrm{I}_{\uparrow\uparrow} - \mathrm{I}_{\uparrow\downarrow}}{\mathrm{I}_{\uparrow\downarrow}} \right) \times 100 = \left(\frac{\mathrm{I}_{\uparrow\uparrow}}{\mathrm{I}_{\uparrow\downarrow}} - 1 \right) \times 100, \tag{6.4}$$

where $I_{\uparrow\uparrow}$ and $I_{\uparrow\downarrow}$ are the currents when the molecule is placed between leads that are spin-polarized parallel or anti-parallel relative to each other, respectively. The MR values

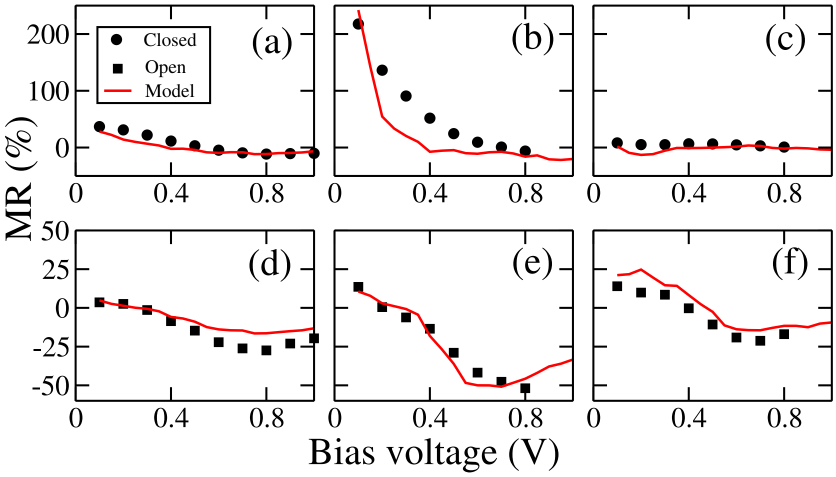

Figure 6.11: *Magnetoresistance calculated as a function of applied bias voltage. The symbols show the results from the ab initio calculations, while the lines show the results using the simple model described in detail ahead. Top panels (a), (b), and (c) show the MR results for Case A, Case B, and Case C, respectively, for the closed conformation, and bottom panels (d), (e), and (f) show the results for the open conformation. This figure has been published in Ref. [233].*

for the closed conformation are shown by dots, and those for the open conformation are shown by squares, for all the three cases of system geometries considered.

The MR shows a significant bias dependence for most of the cases considered. Most importantly, the magnetoresistance shows a large enhancement, in the case where the molecule is attached to the sharp tip geometry. More specifically, the slope of the MR vs V curve is much larger (and thus results in a much larger value of MR for most bias values) in Case B as compared to Case A. Interestingly, this is true for both closed and open conformations of the molecule, i.e., for both the resonant transport and tunneling transport regimes. For Case C, where the molecule is connected to an atop site of the flat Ni surface, the MR values are not significantly enhanced. Thus comparing the three cases, it is clear that the enhancement of MR is an effect of the sharp tip geometry rather than of the attachment site of the molecule lead contact.

Interestingly, we also see that in most of the cases, the MR becomes negative at higher bias voltages. Negative values of MR mean that the net current in the antiparallel ($\uparrow\downarrow$) spin configuration of the leads is higher than the current in the parallel ($\uparrow\uparrow$) spin case. Negative values of MR have been reported previously by Dalgleish *et al.*, who note that this may be expected to happen in general for molecules placed between ferromagnetic leads [265].

They observed that organic molecules connected between Fe leads show negative MR at higher bias, irrespective of whether the molecule conducts via resonant transport or via tunneling. They however speculated that this effect may be absent for Ni leads, due to the relatively small spin splitting in case of Ni in comparison with Fe; our results are contrary to this.

6.6 Discussion and Analysis

It is important to understand the origin of the above set of trends observed in the spin-polarized conduction and the bias dependent magnetoresistance properties of the DTE molecule. We believe that, the closed and the open conformations of the DTE molecule being representative of the resonant and tunneling transport regimes, an explanation of the above results should be applicable and extendable to most nonmagnetic molecules in general.

To gain some insight into our results, we first look at the projected density of states (PDOS) over various atoms of the the Ni/DTE/Ni system. We find that the most significant change in the PDOS, with the change in bias voltage applied, occurs for the two sulfur atoms that are used to anchor the DTE molecule to the Ni leads. This variation of anchoring sulfur atom PDOS is shown in Figs. 6.12 and 6.13 for the closed and open molecules, respectively, for all the cases considered by us. There are some common trends in how different features in these PDOS curves change with bias, e.g., one can observe that as the bias increases the PDOS curves become increasingly mismatched in energy for the $\uparrow\uparrow$ case, while the reverse happens in the $\uparrow\downarrow$ case. These trends are present in both closed and open molecules. This raises the possibility of the formulation of an explanation of the spin-dependent conduction and bias dependent MR properties of the entire molecule lead system, by focussing on the PDOS of the anchoring sulfur atoms alone. We now proceed to develop such an explanation.

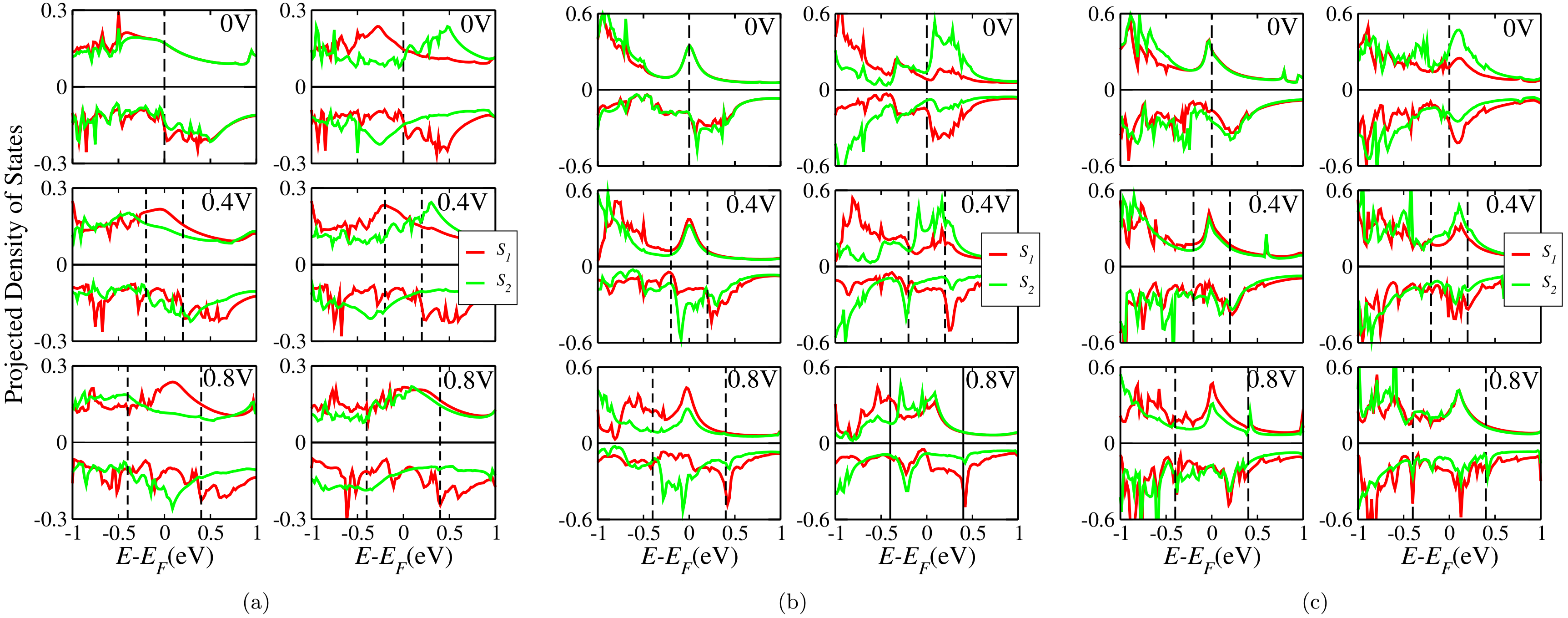

Figure 6.12: *Projected Density of States for the end sulfur atoms* S_1 *and* S_2 *for the closed conformation of the DTE molecule, for different lead geometries and different values of applied bias. (a) Case A: the DTE molecule between flat Ni leads, attached to hollow sites. (b) Case B: DTE between sharp Ni leads. (c) Case C: DTE between flat Ni leads, attached to atop sites. In (a), (b) and (c), the left-side panels are the results for parallel spin configuration of the leads, and the right-side panels for antiparallel spin configuration. Positive values denote the up (majority)-spin channel, and negative values denote the down (minority)-spin channel.*

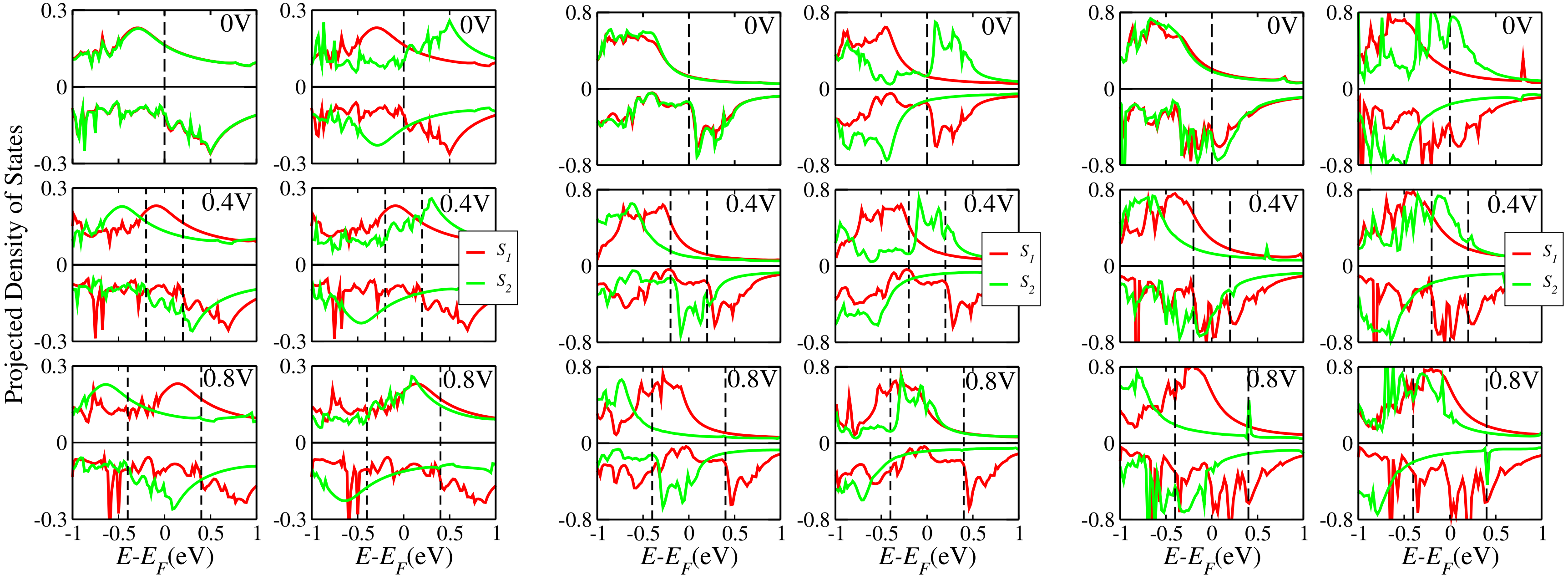

(a) (b) (c)

Figure 6.13: *Projected Density of States for the end sulfur atoms S_1 and S_2 for the open conformation of the DTE molecule, for different lead geometries and different values of applied bias. (a) Case A: the DTE molecule between flat Ni leads, attached to hollow sites. (b) Case B: DTE between sharp Ni leads. (c) Case C: DTE between flat Ni leads, attached to atop sites. In (a), (b) and (c), the left-side panels are the results for parallel spin configuration of the leads, and the right-side panels for antiparallel spin configuration. Positive values denote the up (majority)-spin channel, and negative values denote the down (minority)-spin channel.*

6.6.1 A Simple Model for Magnetoresistance

We have come up with a simple explanation for the origin of the MR properties of the Ni/DTE/Ni system, this is shown schematically in Fig. 6.14. We show in this figure, only the data of the PDOS for Case A, for simplicity of demonstration. Similar arguments hold for Case B and Case C. In Fig. 6.14, we basically compare the PDOS of the two end sulfur atoms, S_1 and S_2 (shown in red and green). The left hand panels of the figure are for the ↑↑ spin configuration, whereas the right hand panels show the results for ↑↓ spin configuration. The change in the PDOS of S_1 and S_2 as a function of the applied bias, for the closed conformation [panels (a) – (d)], and for the open conformation [panels (e) – (h)], is shown. A simple schematic model PDOS, with semi-circular density of states, is shown in the bottom panels [panels (i) – (l)], to facilitate easier conceptual understanding.

Consider the molecule attached to the Ni electrodes via sulfur atoms S_1 and S_2; the sulfur PDOS is spin-split due to the coupling with the magnetic Ni leads. At zero bias, in the ↑↑ spin configuration, the PDOS over S_1 and S_2 is identical, as shown schematically in Fig. 6.14(i) [also compare with Figs. 6.14(a) and 6.14(e)]. On the other hand, in the ↑↓ spin configuration, the sulfur PDOS is spin-reversed as shown in Fig. 6.14(j) [also see Figs. 6.14(b) and 6.14(f)].

A large PDOS over a sulfur end atom is favorable for transmission of electrons across the contact; thus for better conductance over the entire molecular junction, a large PDOS over both the end sulfur atoms is necessary. A mismatch in the PDOS over S_1 and S_2 will inhibit transport and thus reduce conductance. Thus, at low bias voltages, the conductance is larger in the ↑↑ spin configuration, than that in the ↑↓ case, resulting in positive MR for low bias voltages (see Fig. 6.11).

When the bias is applied, the PDOS for S_1 shifts to higher energies, while the PDOS for S_2 shifts lower in energy. This leads to an increasing mismatch between the PDOS of the left and the right sulfur atoms in the ↑↑ case, with increase in bias; this is shown schematically in Fig. 6.14(k) [and in Figs. 6.14(c) and 6.14(g) in the actual data]. On the other hand, in the ↑↓ situation, the increasing bias leads to a better matching between the PDOS of the two S atoms, in one of the spin channels, as can be seen in Fig. 6.14(l)

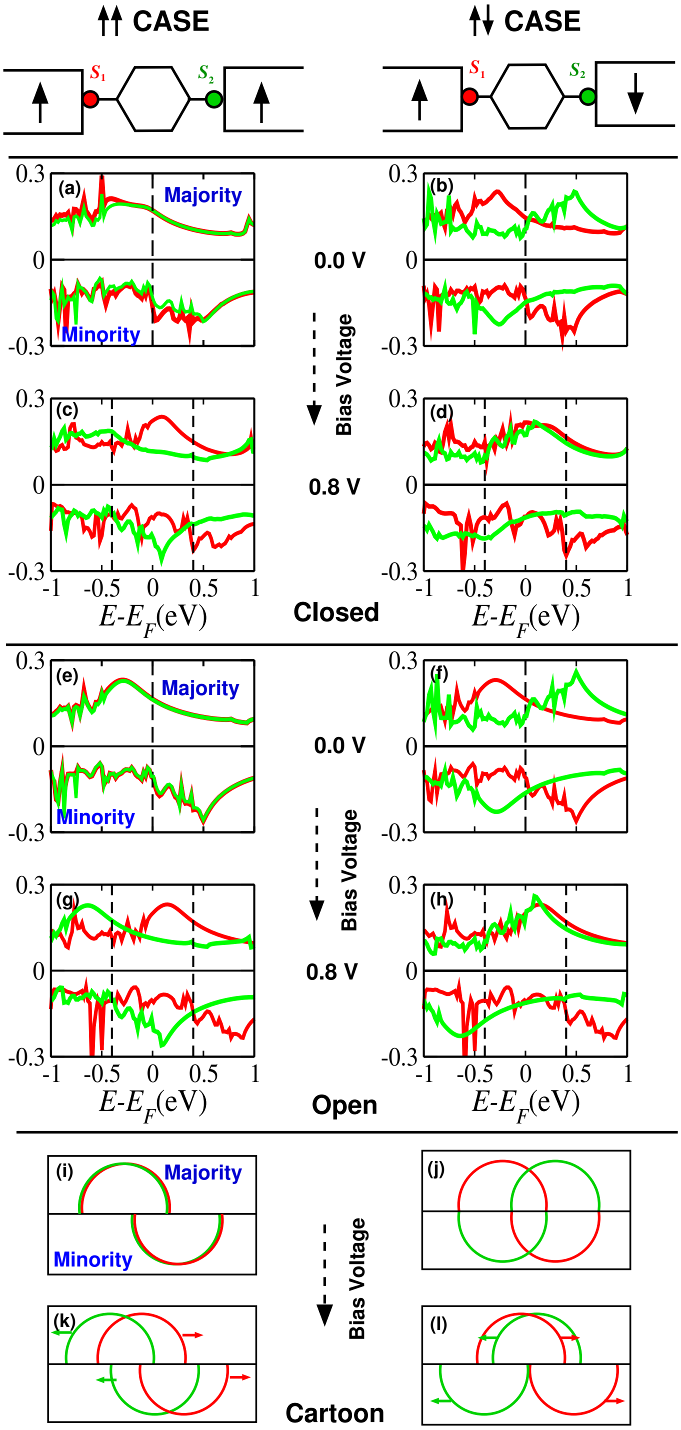

Figure 6.14: *Understanding the bias dependence of the magnetoresistance through the behavior of the PDOS on the anchoring atoms: a molecule (depicted as a hexagon) is anchored to spin-polarized leads through two sulfur atoms* S_1 *and* S_2 *(colored red and green). The panels on the left show the situation when the leads are spin-polarized parallel to each other (↑↑), and the three on the right when they are polarized anti-parallel (↑↓). (a) – (d) show the PDOS for the closed conformation, Case A, and (e) – (h) show the PDOS for the open conformation, Case A; and (i) – (l) are schematic depictions of a cartoon of the general behavior of the PDOS, to aid understanding. The red and green curves correspond to the PDOS on* S_1 *and* S_2 *respectively. The vertical dashed lines indicate the bias window. This figure has been published in Ref. [233].*

[and in Figs. 6.14(d) and 6.14(h) in the actual data]. This explains the increasing spin-polarization of the current at large bias in the ↑↓ case, as the conductance of the spin channel of which the PDOS starts matching, increases. As an example, if we compare Figs. 6.14(a) and 6.14(c) (the ↑↑ case), increasing the bias will cause the conductance to decrease, as one goes from a situation of almost complete overlap of the PDOS of S_1 and S_2 (red and green curves, respectively), to a drastically reduced overlap of the two. On the contrary, comparing Figs. 6.14(b) and 6.14(d) (the ↑↓ case), one goes from a situation of minimal overlap of the red and green curves, to a scenario of almost total overlap in the majority spin channel. This leads to a higher conductance, as well as a larger spin-polarization of the current. This also explains the negative MR at higher bias voltages, where $I_{\uparrow\uparrow}$ is larger than $I_{\uparrow\downarrow}$.

Now we proceed to put our simple model on a more quantitative footing. Let $\rho^{S_i}_{\sigma,\uparrow\uparrow}(E, V = 0)$ and $\rho^{S_i}_{\sigma,\uparrow\downarrow}(E, V = 0)$ be the PDOS on the anchoring sulfur atom S_i $(i = 1, 2)$, at $V = 0$ for the ↑↑ and ↑↓ spin orientation of the leads, respectively, that we have calculated from our DFT calculations. σ is the spin index that runs over "up" and "down" spin channels. Within our model, we assume that the effect of the applied bias voltage V is to cause a rigid shift in the PDOS: $\rho^{S_i}_{\sigma,\uparrow\uparrow}(E, V) \approx \tilde{\rho}^{S_i}_{\sigma,\uparrow\uparrow}(E, V) = \rho^{S_i}_{\sigma,\uparrow\uparrow}(E \pm V/2, 0)$ and $\rho^{S_i}_{\sigma,\uparrow\downarrow}(E, V) \approx \tilde{\rho}^{S_i}_{\sigma,\uparrow\downarrow}(E, V) = \rho^{S_i}_{\sigma,\uparrow\downarrow}(E \pm V/2, 0)$, where the + and − signs are for $i = 1$ and 2, respectively. Here $\tilde{\rho}^{S_i}_{\sigma}(E, V)$ is the approximation for the actual bias dependent PDOS calculated by adding a rigid shift due to the applied bias. As discussed earlier, the larger the PDOS, the larger is the probability that electron transport occurs across the contact. Thus the current flowing is proportional to the PDOS over both the anchoring sulfur atoms, in the relevant bias window, simultaneously. Thus, the total current flowing through the Ni/DTE/Ni system (adding up the contributions of both the spin channels), in the ↑↑ and the ↑↓ situation, respectively, is given as:

$$I_{\uparrow\uparrow} \propto \int\limits_{E_F-\frac{V}{2}}^{E_F+\frac{V}{2}} \Big(\tilde{\rho}^{S_1}_{up,\uparrow\uparrow}(E, V) \cdot \tilde{\rho}^{S_2}_{up,\uparrow\uparrow}(E, V) + \tilde{\rho}^{S_1}_{down,\uparrow\uparrow}(E, V) \cdot \tilde{\rho}^{S_2}_{down,\uparrow\uparrow}(E, V) \Big) dE, \qquad (6.5)$$

and

$$I_{\uparrow\downarrow} \propto \int\limits_{E_F-\frac{V}{2}}^{E_F+\frac{V}{2}} \Big(\tilde{\rho}^{S_1}_{up,\uparrow\downarrow}(E,V)\cdot\tilde{\rho}^{S_2}_{up,\uparrow\downarrow}(E,V)+\tilde{\rho}^{S_1}_{down,\uparrow\downarrow}(E,V)\cdot\tilde{\rho}^{S_2}_{down,\uparrow\downarrow}(E,V)\Big)dE. \qquad (6.6)$$

Thus the magnetoresistance is given as:

$$MR(\%) = \left\{ \frac{\int \left[\tilde{\rho}^{S_1}_{\mathrm{up},\uparrow\uparrow}(E,V)\cdot\tilde{\rho}^{S_2}_{\mathrm{up},\uparrow\uparrow}(E,V)+\tilde{\rho}^{S_1}_{\mathrm{down},\uparrow\uparrow}(E,V)\cdot\tilde{\rho}^{S_2}_{\mathrm{down},\uparrow\uparrow}(E,V)\right]dE}{\int \left[\tilde{\rho}^{S_1}_{\mathrm{up},\uparrow\downarrow}(E,V)\cdot\tilde{\rho}^{S_2}_{\mathrm{up},\uparrow\downarrow}(E,V)+\tilde{\rho}^{S_1}_{\mathrm{down},\uparrow\downarrow}(E,V)\cdot\tilde{\rho}^{S_2}_{\mathrm{down},\uparrow\downarrow}(E,V)\right]dE} - 1 \right\} \times 100, \qquad (6.7)$$

where the limits of integration are over the bias window, i.e., from $\{E_F - \frac{V}{2}\}$ to $\{E_F + \frac{V}{2}\}$. The approximate values of MR as estimated by Eq. (6.7), are shown by the red curves in Fig. 6.11. Our results obtained from such a simple model compare remarkably well with the more accurate results of the full self-consistent NEGF calculations. The model is very simple, however it succeeds in capturing the main features of our more exact results, i.e., (i) enhancement of MR for the sharp tip (Case B) compared to the flat surface (Case A), and (ii) the transition from positive to negative MR as the bias is increased. This suggests that the MR is mainly governed by the electronic structure of the contact sulfur atoms, as given by their zero bias projected density of states, given the spin polarization of the contact material. The electronic structure of the anchoring sulfur atoms is in turn very sensitive to the contact geometry.

6.7 Summary and Conclusions

To summarize our results, we have performed first principles DFT and NEGF transport calculations on a system consisting of a non-magnetic DTE molecule placed between spin-polarized Ni leads. We have shown that the understanding of the molecule-metal interface is very important in determining the properties of molecular spintronic systems. We have shown that the molecular magnetoresistance and the spin-polarized conductance can be tuned by changing the shape of the leads. We see a significant enhancement in the magnitude of the molecular magnetoresistance at most bias voltages, for the case where the molecule is anchored to a sharp metal tip rather than a flat metal surface. Our results show that precisely tailored transport properties will require atomic-scale precision in the contact geometry; however this is typically difficult to control experimentally. We also observe a transition from positive to negative magnetoresistance as the bias voltage is increased.

Our results are surprisingly simple to understand – our NEGF-level results for the behavior of magnetoresistance as a function of voltage can be reproduced not just qualitatively, but also to a large extent quantitatively, by a simple model which requires as its input only the projected density of states on the anchoring atoms of the molecule, calculated at zero bias. Estimates using this model can be obtained at significantly lower computational cost than that required when invoking the full machinery of the bias-dependent NEGF calculation. Importantly, our model is seen to hold for both the resonant transport and tunneling conducting regimes. We believe that this model can be quite helpful in obtaining predictive assessments of the bias dependent magnetoresistance properties of other molecules as well.

Chapter 7

Summary and Outlook

We now summarize the main findings of this thesis and present an outlook for possible directions of future research.

The broad aim of this thesis has been to design various materials properties of nanostructures which would be best suited to different technological applications, using first principles density functional theory based calculations. In this thesis, we have shown four different schemes, viz., compositional variation, deliberate creation of defects, chemical functionalization and morphological modification, can effectively tune properties for electronics, spintronics, and gas storage applications of nanostructured materials.

We started with tuning the dielectric properties of SiGeN and SiCN materials, by changing the relative composition of Si/Ge or Si/C. We observed almost linear monotonic increase in dielectric properties with composition for SiGeN, whereas a non-monotonic behavior was found to hold true for SiCN. Clearly SiGeN seems to be a good material for dielectric tuning, with a dielectric constant that can be tuned from ∼7.7 to ∼9.7.

Next, we created defects in a two-dimensional system of twisted bilayer graphene, either by removing atoms or changing their placement, and showed that many interesting feature in the electronic aspects arise. Notable among these properties are the creation of double Dirac cones, the appearance of magnetic moment, and an increase in the density of states at the Fermi level. This study of defects also provides us important insights into the extensively studied, and much debated aspect of weak interlayer coupling in bilayer graphene.

Then, we used chemical functionalizaton to enhance hydrogen adsorption in carbon nanostructures, by up to ∼120 % compared to that in pristine graphene. We identified the contributions from various interactions to the adsorption energies, and based on this understanding, provided guidance as to what interactions to tune for increasing the hydrogen adsorption. We also showed that there is an almost perfectly linear increase in the adsorption energy upon increasing the oxygen lone pair content. Though our study here was done for hydrogen adsorption, a similar line of analysis could be followed up for other weakly binding gases.

Finally we have enhanced the molecular magnetoresistance of a molecular spintronic setup of an organic dithienylethene molecule between magnetic nickel leads, by tuning the shape of the leads to which the molecule is attached. We have also developed a simple, computationally inexpensive yet predictive model to understand and quantify the full bias-dependent magnetoresistance. We believe that this model would work for other non-magnetic molecules as well as molecules connecting to leads via other connecting groups. Though the two stable geometries of the photoswitching dithienylethene molecule were used here as representative for resonant and tunneling transport, we also gain some knowledge about the effect of lead geometry on the photoswitching ON-OFF ratio. This would be of interest for opto-electronics applications.

Outlook

There are some open questions which can be addressed in the future. For example, as a follow up of our study to enhance the dielectric properties with composition shown in Chapter 3, one can tune the properties further by using simultaneous substitution of Si with Ge and C, to get materials like $Si_{3-\xi-\chi}Ge_{\xi}C_{\chi}N_4$. It would also be interesting to consider the role of defects and new dopants on the dielectric properties in such systems. The effect of amorphization on the dielectric properties would also be an interesting study. It would also be interesting to try new techniques like GW Approximation calculations to see an effect on the band gap and optical properties of these materials.

Following up on the results presented in Chapter 4, we would like to do transport calculations and see if indeed the presence of a monovacancy in TBLG leads to strongly spin-polarized transport.

For the issues concerning gas storage addressed in Chapter 5, we also want to explore other ideas for enhancing adsorption, as well as examine the coverage dependence of binding, in greater detail. We also wish to use the techniques developed in the study shown in this thesis, for understanding adsorptive storage of other gaseous fuels.

Based on the understanding developed in Chapter 6, we have a number of follow up studies in mind. The validation of the simple model for other molecules and other connecting groups, generalization of this model to explore full bias dependent magnetoresistance of magnetic molecules, are a few to mention. In this thesis work, we have been looking at photoswitching molecules that change shape and conductance properties on being exposed to light. However, we have studied them using ground state DFT; it would be interesting to return to some of these systems using time dependent density functional theory.

Appendix A

Brillouin zone integrations over a non-uniform k-point mesh.

In (pristine) graphene, the density of states (DOS) in the vicinity of the Fermi energy E_F is very low. This low DOS arises from the conical bands (Dirac cones) in the neighborhood of the **K** point. The Dirac cones cross exactly at the **K** point at E_F. Apart from the Dirac cones, there are no bands present in the rest of the Brillouin zone (BZ), in the energy window $\sim E_F - 2$ eV to $\sim E_F + 2$ eV. However, at other energies, there are bands which stretch all over the Brillouin zone.

As a result of such a band structure, the numerical BZ integrations in graphene are tricky. Some quantities, e.g., the Fermi energy E_F, can be very sensitive to the density of the k-point mesh used. Especially, progressively increasing the k-point sampling density does not guarantee a quick convergence of E_F. The problem lies in the fact that in the energy window $E_F - 2$ eV, the eigenvalues which contribute to the BZ integration come only from the neighborhood of the six corners of the BZ. Thus for the precise evaluation of E_F, one would like to have a high density of k-points near the six corners of the BZ. The correct evaluation of the Fermi energy also requires that the k-points at which the Dirac points lie, (i.e. the **K** points in the case of pristine graphene) must be included in the integration. This means that for graphene one must use an unshifted k-point mesh where n_k, the number of k-point divisions, is a multiple of three.

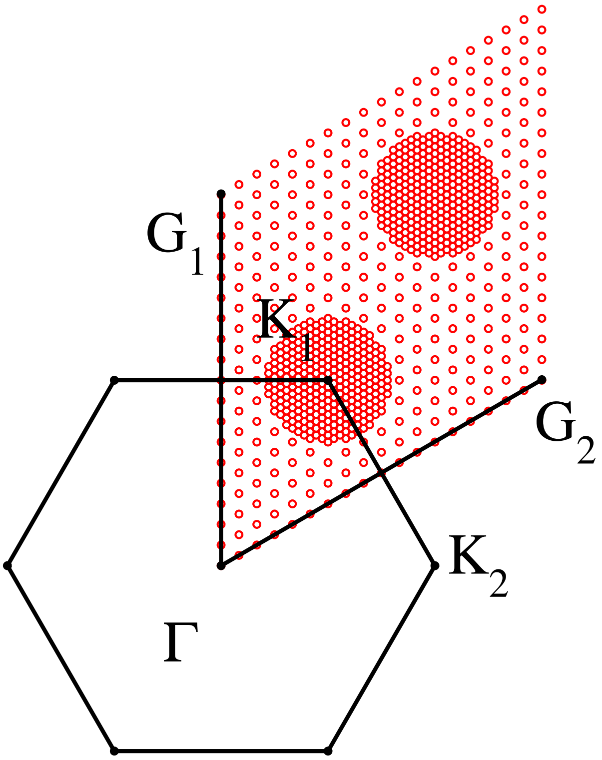

Figure A.1: *Non-uniform k-point sampling that is dense near the* **K** *point, but sparse in rest of the BZ. This mesh corresponds to* Δk_s*=18, and* Δk_d*=54.*

However in the case of Stone-Wales defects in graphene, the Dirac cone shifts slightly away from the **K** point. For getting a correct value of E_F, it is essential that the k-point at which the *shifted* Dirac point lies, is used in the integration. This can require a very dense k-mesh, if a uniform sampling is used. In such a scenario, a non-uniform k-point mesh (a k-point mesh which is very dense in the vicinity of the Dirac point, but relatively sparse in the rest of the BZ), would be better for carrying out the BZ integration. An example of such a non-uniform k-mesh is shown in Fig. A.1.

In this mesh, the BZ is divided into two regions with uniform k sampling: (1) a dense region in the vicinity of **K** point, with a k-point density $\rho_d = 1/\Delta {k_d}^2$ and (2) a sparse region in rest of the BZ, with a k-point density $\rho_s = 1/\Delta {k_s}^2$. Δk_d and Δk_d are the grid spacings of the dense and sparse k-meshes, respectively. The mesh shown in Fig. A.1,

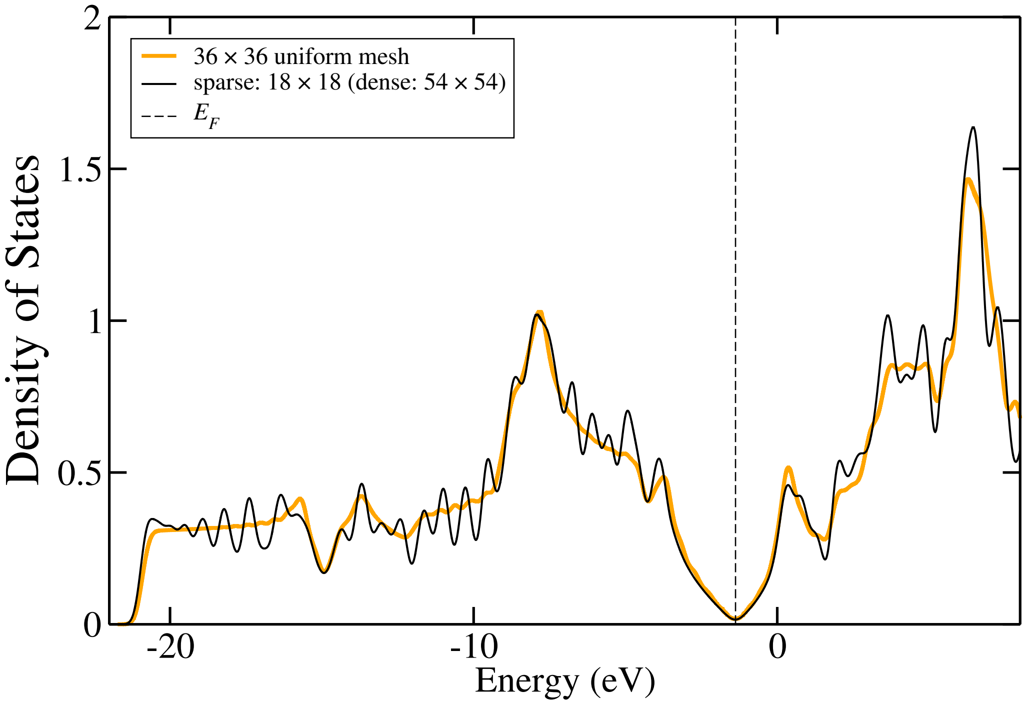

Figure A.2: *Comparison of DOS for a non-uniform k-mesh and a very dense uniform mesh for graphene. The non uniform mesh corresponds to* Δk_s=*18, and* Δk_d=*54, shown in Fig. A.1. The dense uniform mesh corresponds to a 36* × *36 Monkhorst-Pack mesh.*

corresponds to Δk_s=18, and Δk_d=54. For BZ integration, appropriate weights must be assigned to the k-points in each of the regions. These weights are simply proportional to the k-point density in the two regions, ρ_d and ρ_s.

Using such a non-uniform mesh we have calculated the DOS for graphene (see Fig. A.2). Our results compare quite well with the DOS calculated with a very fine k-point sampling.

Bibliography

[1] H. W. Kroto, J. R. Heath, S. C. O'Brien, R. F. Curl, and R. E. Smalley, Nature **318**, 162 (1985).

[2] W. A. de Heer, Rev. Mod. Phys. **65**, 611 (1993).

[3] S. Ijima, Nature **354**, 56 (1991).

[4] H. Ohnishi, Y. Kondo, and K. Takayanagi, Nature **395**, 780 (1998).

[5] X. Li, X. Wang, L. Zhang, S. Lee, and H. Dai, Science **319**, 1229 (2008).

[6] J. Cai, P. Ruffieux, R. Jaafar, M. Bieri, T. Braun, S. Blankenburg, M. Muoth, A. P. Seitsonen, M. Saleh, X. Feng, K. Müllen, and R. Fasel, Nature **466**, 470 (2010).

[7] K. S. Novoselov, A. K. Geim, S. V. Morozov, D. Jiang, M. I. Katsnelson, I. V. Grigorieva, S. V. Dubonos, and A. A. Firsov, Nature (London) **438**, 197 (2005).

[8] J. Tersoff, Phys. Rev. Lett. **74**, 434 (1995).

[9] E. P. Giannelis, Advanced Materials **8**, 29 (1996).

[10] Y. Nakae, Y. Seino, T. Teranishi, M. Miyake, S. Yamada, and H. Hori, Physica B: Condensed Matter **329**, 1183 (2003).

[11] K. S. Novoselov, V. I. Fal'ko, L. Colombo, P. R. Gellert, M. G. Schwab, and K. Kim, Nature **490**, 192 (2012).

[12] A. K. Geim and I. V. Grigorieva, Nature **499**, 419 (2013).

[13] R. P. Feynman (1959), http://www.its.caltech.edu/∼feynman/plenty.html

[14] M. Chander, Y. Z. Li, D. Rioux, and J. H. Weaver, Phys. Rev. Lett. **71**, 4154 (1993).

[15] Y. Cui and C. M. Lieber, Science **291**, 851 (2001).

[16] J. Chai, D. Wang, X. Fan, and J. M. Buriak, Nature Nanotechnology **2**, 500 (2007).

[17] J. N. Hart, N. L. Allan, and F. Claeyssens, Phys. Rev. B **84**, 245209 (2011).

[18] A. H. Castro Neto, F. Guinea, N. M. R. Peres, K. S. Novoselov, and A. K. Geim, Rev. Mod. Phys. **81**, 109 (2009).

[19] Y. Zhang, Y.-W. Tan, H. L. Stormer, and P. Kim, Nature **438**, 201 (2005).

[20] K. I. Bolotin, F. Ghahari, M. D. Shulman, H. L. Stormer, and P. Kim, Nature **462**, 196 (2009).

[21] I. V. Fialkovsky, V. N. Marachevsky, and D. V. Vassilevich, Phys. Rev. B **84**, 035446 (2011).

[22] S. Cahangirov, M. Topsakal, E. Aktürk, H. Sahin, and S. Ciraci, Phys. Rev. Lett. **102**, 236804 (2009).

[23] H. Liu,A. T. Neal, Z. Zhu, D. Tománek, and P. D. Ye, ACS Nano **8**, 4033 (2014).

[24] L. Li, Y. Yu, G. J. Ye, Q. Ge, X. Ou, H. Wu, D. Feng, X. H. Chen, and Y. Zhang, http://arxiv.org/ abs/1401.4117 (2014).

[25] L. Ci, L. Song, C. Jin, D. Jariwala, D. Wu, Y. Li, A. Srivastava, Z. F. Wang, K. Storr, L. Balicas, F. Liu, and P. M. Ajayan, Nature Materials **9**, 430 (2010).

[26] A. Aviram and M. Ratner, Chem. Phys. Lett. **29**, 277 (1974).

[27] C. Joachim, J. K. Gimzewski, and A. Aviram, Nature **408**, 541 (2000).

[28] E. Gazit, *Plenty of room for biology at the bottom: An introduction to bionanotechnology*, Imperial College Press, ISBN 978-1-86094-677-6 (2007).

[29] E. G. Emberley and G. Kirczenow, Chem. Phys. **281**, 311 (2002).

[30] A. R. Rocha, V. M. Garcia Suarez, S. W. Bailey, C. J. Lambert, J. Ferrer, and S. Sanvito, Nature Mater. **4**, 335 (2005).

[31] B. A. Joyce, Rep. Prog. Phys. **48** 1637 (1985).

[32] G. Binnig and H. Rohrer, US Patent 4343993 A.; G. Binnig, H. Rohrer, Rev. Mod. Phys. **59**, 615 (1987).

[33] G. Binnig, C. F. Quate, and Ch. Gerber, Phys. Rev. Lett. **56**, 930 (1986).

[34] M. F. Crommie, C. P. Lutz, and D. M. Eigler, Science **262**, 218 (1993).

[35] R. M. Martin, *Electronic Structure Basic Theory and Practical Methods*, Cambridge University Press, Cambridge (2004).

[36] M. Brandbyge, J.-L. Mozos, P. Ordejn, J. Taylor, and K. Stokbro, Phys. Rev. B **65**, 165401 (2002).

[37] E. Runge and E. K. U. Gross, Phys. Rev. Lett. **52**, 997 (1984).

[38] A. Zerr, G. Miehe, G. Serghiou, M. Schwarz, E. Kroke, R. Riedel, H. Fueß, P. Kroll, and R. Boehler, Nature **400**, 342 (1999).

[39] L. Dal Negro, J. H. Yi, J. Michel, L. C. Kimerling, S. Hamel, A. Williamson, and G. Galli, IEEE Journal of Selected Topics in Quantum Electronics **12**, 1628 (2006).

[40] L. Dal Negro, J. H. Yi, L. C. Kimerling, S. Hamel, A. Williamson, and G. Galli, Applied Physics Letters **88**, 183103 (2006).

[41] S. M. Spearing, Acta Materialia **48**, 179 (2000).

[42] A. Y. Liu and M. L. Cohen, Science **245**, 841 (1989).

[43] G. Li, A. Luican, J. M. B. Lopes dos Santos, A. H. Castro Neto, A. Reina, J. Kong, and E. Y. Andrei, Nature Physics **6**, 109 (2010).

[44] X. Y. Peng and R. Ahuja, Nano Lett. **8**, 4464 (2008).

[45] P. O. Lehtinen, A. S. Foster, A. Ayuela, A. Krasheninnikov, K. Nordlund, and R. M. Nieminen, Phys. Rev. Lett. **91**, 017202 (2003).

[46] P. O. Lehtinen, A. S. Foster, Y. Ma, A. V. Krasheninnikov, and R. M. Nieminen, Phys. Rev. Lett. **93**, 187202 (2004).

[47] O. V. Yazyev and L. Helm, Phys. Rev. B **75**, 125408 (2007).

[48] O. V. Yazyev, Rep. Prog. Phys. **73**, 056501 (2010).

[49] Y. Ma, P. O. Lehtinen, A. S. Foster, and R. M. Nieminen, New Journal of Physics **6**, 68 (2007).

[50] B. R. K. Nanda, M. Sherafati, Z. S. Popović, and S. Satpathy, New Journal of Physics **14**, 083004 (2012).

[51] Y. Zhang, Y. Chen, K. Zhou, C. Liu, J. Zeng, H. Zhang, and Y. Peng, Nanotechnology **20**, 185504 (2009).

[52] S. Y. Zhou, G. Gweon, A. V. Fedorov, P. N. First, W. A. De Heer, D. Lee, F Guinea, A. H. Castro Neto, and A. Lanzara, Nat. Mater. **6**, 770 (2007).

[53] J. Yang, A. Sudik, C. Wolverton, and D. J. Siegel, Chem. Soc. Rev. **39**, 656 (2010).

[54] A. C. Dillon and M. J. Heben, Appl. Phys. A **72**, 133 (2001).

[55] Y. Yürüm, A. Taralp, and T. N. Veziroglu, Int. J. Hydr. Energy **34**, 3784 (2009).

[56] M. N. Baibich, J. M. Broto, A. Fert, F. Nguyen Van Dau, F. Petroff, P. Etienne, G. Creuzet, A. Friederich, and J. Chazelas, Phys. Rev. Lett. **61**, 2472 (1988).

[57] G. Binasch, P. Grünberg, F. Saurenbach, and W. Zinn, Phys. Rev. B **39**, 4828 (1989).

[58] I. Zutic, J. Fabian, and S. Das Sarma, Rev. Mod. Phys. 76, 323 (2004).

[59] S. Sanvito, Chem. Soc. Rev. **40**, 3336 (2011).

[60] A. M. Bratkovsky and P. E. Kornilovitch, Phys. Rev. B **67**, 115307 (2003).

[61] K. H. Müller, Phys. Rev. B **73**, 045403 (2006).

[62] A. Grigoriev, J. Sköldberg, G. Wendin, and Z. Crljen, Phys. Rev. B **74**, 045401 (2006).

[63] H. Kondo, H. Kino, J. Nara, and T. Ohno, Phys. Rev. B **73**, 235323 (2006).

[64] C. Li, I. Pobelov, T. Wandlowski, A. Bagrets, A. Arnold, and F. Evers, J. Am. Chem. Soc. **130**, 318 (2008).

[65] M. Born and J. R. Oppenheimer, Ann. Physik **84**, 457 (1927).

[66] P. Hohenberg and W. Kohn, Phys. Rev. **136**, B864 (1964).

[67] W. Kohn and L. J. Sham, Phys. Rev. **140**, A1133 (1965).

[68] D. D. Johnson, Phys. Rev. B **38**, 12807 (1988).

[69] D. Vanderilt and S. G. Louie, Phys. Rev. B **30**, 6118 (1984).

[70] D. M. Ceperley and B. J. Alder, Phys. Rev. Lett. **45**, 566 (1980).

[71] J. P. Perdew and A. Zunger, Phys. Rev. B **23**, 5048 (1981).

[72] S. Vosko, L. Wilk, and M. Nussair, Can. J. Phys. **58**, 1200 (1983).

[73] R. O. Jones and O. Gunnarsson, Rev. Mod. Phys. **61**, 689 (1989).

[74] F. Herman, J. P. Van Dyke, and I. P. Ortenburger, Phys. Rev. Lett. **22**, 807 (1969)

[75] A. D. Becke, Phys. Rev. A **38**, 3098 (1988).

[76] J. P. Perdew and Y. Wang, Phys. Rev. B **45**, 13244 (1992).

[77] J. P. Perdew, K. Burke, and M. Ernzerhof, Phys. Rev. Lett. **77**, 3865 (1996).

[78] P. Giannozzi, S. Baroni, N. Bonini, M. Calandra, R. Car, C. Cavazzoni, D. Ceresoli, G.L Chiarotti, M. Cococcioni, I.Dabo, A. Dal Corso, S. de Gironcoli, S. Fabris, G. Fratesi, R. Gebauer, U. Gerstmann, C. Gougoussis, A. Kokalj, M. Lazzeri, L. Martin-Samos, N. Marzari, F. Mauri, R. Mazzarello, S. Paolini, A. Pasquarello, L. Paulatto, C. Sbraccia, S. Scandolo, G. Sclauzero, A. P Seitsonen, A. Smogunov, P. Umari, and R. M Wentzcovitch, J. Phys. Condens. Matter **21**, 395502 (2009).

[79] X. Gonze, J.-M. Beuken, R. Caracas, F. Detraux, M. Fuchs, G.-M. Rignanese, L. Sindic, M. Verstraete, G. Zerah, F. Jollet, M. Torrent, A. Roy, M. Mikami, Ph. Ghosez, J.-Y. Raty, and D. C. Allan. Computational Materials Science **25**, 478 (2002).

[80] J. A. Pople *et al.*, Gaussian Inc., Wallingford CT, 2004.

[81] O. K. Anderson *et al.*, *Electronic Structure and Physical Properties of Solids. The Uses of the LMTO Method*, edited by H. Dreysse, Springer Lecture Notes in Physics (Springer, New York, 2000).

[82] J. M. Soler, E. Artacho, J. D. Gale, A. García, J. Junquera, P. Ordejón, and D. Sánchez-Portal, J. Phys.: Condens. Matter **14**, 2745 (2002).

[83] A. R. Rocha, V. Garcia-Suarez, S. W. Bailey, C. J. Lambert, J. Ferrer, and S. Sanvito, Phys. Rev. B. **73**, 085414 (2006).

[84] O. F. Sankey and D. J. Niklewski, Phys. Rev. B 40, 3979 (1989).

[85] J. Junquera, O. Paz, D. Sánchez-Portal, and E. Artacho, Phys. Rev. B 64, 235111 (2001).

[86] J. C. Phillips and L. Kleinman, Phys. Rev. **116**, 287 (1959).

[87] W. E. Pickett, Computer Physics Reports **9**, 115 (1989).

[88] D. R. Hamann, M. Schlüter, and C. Chiang, Phys. Rev. Lett. **43**, 1494 (1979).

[89] D. Vanderbilt, Phys. Rev. B **41**, 7892 (1990).

[90] R. P. Feynman, Phys. Rev. **56** 340 (1939).

[91] D. C. Langreth, B. I. Lundqvist, S. D. Chakarova-Käck, V. R. Cooper, M. Dion, P Hyldgaard, A. Kelkkanen, J. Kleis, L. Kong, S. Li, P. G. Moses, E. Murray, A. Puzder, H. Rydberg, E. Schröder, and T. Thonhauser, J. Phys.: Condens. Matter **21**, 084203 (2009).

[92] I. E. Dzyaloshinskii, E. M. Lifshiftz, and L. P. Pitaevskii, Sov. Phys. Usp. **4**, 153 (1961).

[93] S. Grimme, J. Comp. Chem. **27**, 1787 (2006).

[94] A. Tkatchenko and M. Scheffler, Phys. Rev. Lett. **102**, 073005 (2009).

[95] M. Dion, H. Rydberg, E. Schröder, D.C. Langreth, and B.I. Lundqvist, Phys. Rev. Lett. **92**, 246401 (2004).

[96] O. A. Vydrov and T. Van Voorhis, Phys. Rev. Lett. **103**, 063004 (2009).

[97] C. Adamo and V. Barone, J Chem. Phys. **110**, 6158 (1999).

[98] S. Baroni, S. de Gironcoli, A. D. Corso, and P. Giannozzi, Rev. Mod. Phys. **73**, 515 (2001).

[99] X. Gonze, C. Lee, Phys. Rev. B **55**, 010355 (1997).

[100] R. M. Sternheimer, Phys. Rev. **96**, 951 (1954).

[101] D. Griffiths, *Introduction to Electrodynamics* (3rd Ed.).

[102] N. W. Ashcroft and N. D. Mermin, *Solid State Physics.*

[103] M. Di Ventra, *Electrical Transport in Nanoscale Systems*, Cambridge University Press.

[104] L. V. Keldysh, Zh. Eksp. Teor. Fiz. **47**, 1515 (1964) [Sov. Phys.-JETP **47**, 804 (1978)]

[105] L. P. Kadanoff and G. Baym, *Quantum Statistical Mechanics*, Benjamin, New York, (1962).

[106] A.-P. Jauho, Physica B **134**, 148 (1985).

[107] H. Haug and A.-P. Jauho, *Quantum Kinetics in Transport and Optics of Semiconductors*, Springer.

[108] M. Büttiker, Y. Imry, R. Landauer, and S. Pinhas, Phys. Rev. B. **31**, 6207 (1985).

[109] K. Ulman, R. Sathiyanarayanan, R. K. Pandey, K. V. R. M. Murali, and S. Narasimhan, Journal of Applied Physics **113**, 234102 (2013).

[110] C. W. Chen, M.-H. Lee, L. C. Chen, and K. H. Chen, Diamond and Related Materials **13**, 1158 (2004).

[111] C. W. Chen, T. C. Chang, P. T. Liu, T. M. Tsai, H. C. Huang, J. M. Chen, C. H. Tseng, C. C. Liu, and T. Y. Seng, Thin Solid Films **632**, 447 (2004).

[112] G. Pilania, C. C. Wang, K. Wu, N. Sukumar, C. Breneman, G. Sotzing, and R. Ramprasad, J. Chem. Inf. Model **53**, 879(2013).

[113] P. Kohli, A. Jain, H. Bu, S. Chakravarthi, C. Machala, S. T. Dunham, and S. K. Banerjee, Journal of Vacuum Science and Technology B **22**, 471 (2004).

[114] J. Martin, S. Filipiak, T. Stephens, F. Huang. M. Aminpur, J. Mueller, E. Demircan, L. Zhao, J.Werking, C. Goldberg, S. Park, and T. Parks, Proceedings of the IEEE International Inter connect Technology Conference, pp. 42-44 (2002).

[115] D. Edelstein, H. Rathore, C. Davis, L. Clevenger, A. Cowley, T. Nogami, B. Agarwala, S. Arai, A. Carbone, K. Chanda, F. Chen, S. Cohen, W. Cote, M. Cullinan, T. Dalton, S. Das, P. Davis, J. Demarest, D. Dunn, C. Dziobkowski, R. Filippi, J. Fitzsimmons, P. Flaitz, S. Gates, I. Gill, A. Grill, D. Hawken, K. Ida, D. Klaus, N. Klymko, M. Lane, S. Lane, I. Lee, W. Landers, W-K. Li, Y-H. Lin, E. Liniger, X-H. Liu, A. Madan, S. Malhotra, J. Martin, S. Molis, C. Muzzy, D. Nguyen, S. Nguyen, M. Ono, C. Parks, D. Questad, D. Restaino, A. Sakamoto, T. Shaw, Y. Shimooka, A. Simon, E. Simonyi, A. Swift, T. Van Kleeck, S. Vogt, Y-Y. Wang, W. Wille, J. Wright, C-C. Yang, M. Yoon, and T. lvers, IEEE 42^{nd} Annual International Reliability Physics Symposium, Pheonix, 2004.

[116] R. R. Lieten, S. Degroote, M. Kuijk, and G. Borghs, Appl. Phys. Lett. **91**, 222110 (2007).

[117] M. Yang, S. J. Wang, Y. P. Feng. G. W. Peng, and Y. Y. Sun, Journal of Applied Physics **102**, 013507 (2007).

[118] L. Giacomazzi and P. Umari, Phys. Rev. B **80**, 144201 (2009).

[119] T. A. Pham, T. Li, S. Shankar, F. Gygi, and G. Galli, Appl. Phys. Lett. **96**, 062902 (2010).

[120] A. Kuwabara, K. Matsunaga, and I. Tanaka, Phys. Rev. B **78**, 064104 (2008).

[121] W. Y. Ching, L. Ouyang, and J. D. Gale, Phys. Rev. B **61**, 8696 (2000).

[122] B. Molina and L. E. Sansores, Int. J. Quantum Chem, **80**, 249 (2000).

[123] D. M. Teter and R. J. Hemley, Science **271**, 53 (1996).

[124] T. A. Pham, T. Li, S. Shankar, F. Gygi, and G. Galli, Phys. Rev. B **84**, 045308 (2011).

[125] J. Dong, O. F. Sankey, S. K. Deb, G. Wolf, and P. F. McMillan, Phys. Rev. B **61**, 11979 (2000).

[126] N. Wada, S. A. Solin, J. Wong, and S. Prochazka, J. Non-Cryst. Solids **43**, 7 (1981).

[127] Y. Cai, L. Zhang, Q. Zeng, L. Cheng, and Y. Xu, Phys. Rev. B **74**, 174301 (2006).

[128] C. Z. Wang, E. G. Wang, and Q. Dai, Journal of Appl. Phys. **83**, 1975 (1998).

[129] O. Borgen and H. M. Seip, Acta Chem. Scand. (1947-1973) **15**, 1789 (1961).

[130] N. W. Wong, H. McMurdie, B. Paretzkin, C. Hubbard, and A. Dragoo, Powder Diffr. **3**, 50 (1987).

[131] S. N. Ruddelsden and P. Popper, Acta Crystallogr. **11**, 465 (1958).

[132] R. D. Carson and S. E. Schnatterly, Phys. Rev. B **33**, 2432 (1986).

[133] M. Y. Chen, D. Li, X. Lin, V. P. Dravid, Y. W. Chung, M. S. Wong, and W. D. Sproul, J. Vac. Sci. Technol. A **11**, 521 (1993).

[134] A. Y. Liu and M. L. Cohen, Phys. Rev. B **41**, 10727 (1990).

[135] L. Vegard, Z. Phys. **5**, 17 (1921).

[136] D. Fischer, A. Curioni, S. Billeter, and W. Andreoni, Phys. Rev. Lett. **92**, 236405 (2004).

[137] T. Goto and T. Hirai, Journal of Mater. Sci. **24**, 821 (1989).

[138] T. Maeda, T. Yasuda, M. Nishizawa, N. Miyata, Y. Morita, and S. Takagi, Applied Physics Letters **85**, 3181 (2004).

[139] G. A. Johnson and V. J. Kapoor, J. Appl. Phys. **69**, 3616 (1991).

[140] G. Okamoto, K. Kutsuki, T. Hosoi, T. Shimura, and H. Watanabe, Journal of Nanoscience and Nanotechnology Vol. **11**, 2856 (2011).

[141] C. W. Chen, C. C. Huang, Y. Y. Lin, L. C. Chen, and K. H. Chen, Diamond and Related Materials **14**, 1126 (2005).

[142] L. C. Chen, C. K. Chen, S. L. Wei, D. M. Bhusari, K. H. Chen, Y. F. Chen, Y. C. Jong, and Y. S. Huang, Appl. Phys. Lett. **72**, 2463 (1998).

[143] D. Hui-Jing, G. Li-Cong, L. Dong-Chun, Y. Dong-Li, and H. Ju-Long, Chin. Phys. Lett. **26**, 016403 (2009).

[144] K. Ulman and S. Narasimhan, Phys. Rev. B. **89**, 245429 (2014).

[145] A. K. Geim and K. S. Novoselov, Nature Materials **6**, 183 (2007).

[146] J. M. B. Lopes dos Santos, N. M. R. Peres, and A. H. Castro Neto, Phys. Rev. Lett. **99**, 256802 (2007).

[147] S. Shallcross, S. Sharma, and O. A. Pankratov, Phys. Rev. Lett. **101**, 056803 (2008).

[148] A. Luican, G. Li, A. Reina, J. Kong, R. R. Nair, K. S. Novoselov, A. K. Geim, and E. Y. Andrei, Phys. Rev. Lett. **106**, 126802 (2011).

[149] P. Moon and M. Koshino, Phys. Rev. B **85**, 195458 (2012).

[150] L. Xian, Z. F. Wang, and M. Y. Chou, Nano Lett. **13**, 5159 (2013).

[151] J. Hass, F. Varchon, J. E. Millán-Otoya, M. Sprinkle, N. Sharma, W. A. de Heer, C. Berger, P. N. First, L. Magaud, and E. H. Conrad, Phys. Rev. Lett. **100**, 125504 (2008).

[152] L. Meng, Z. Chu, Y. Zhang, J. Yang, R. Dou, J. Nie, and L. He, Phys. Rev. B **85**, 235453 (2012).

[153] Z. Y. Rong and P. Kuiper, Phys. Rev. B **48**, 17427 (1993).

[154] T. Ohta, J. T. Robinson, P. J. Feibelman, A. Bostwick, E. Rotenberg, and T. E. Beechem, Phys. Rev. Lett. **109**, 186807 (2012).

[155] A. Hashimoto, K. Suenaga, A. Gloter, K. Urita, and S. Iijima, Nature (London) **430**, 870 (2004).

[156] A. J. Stone and D. J. Wales, Chem. Phys. Lett. **128**, 501 (1986).

[157] F. Banhart, J. Kotakoski, and A. V. Krasheninnikov, ACS Nano **5**, 26 (2011).

[158] D. Zhan, J. Yan, L. Lai, Z. Ni, L. Liu, and Z. Shen, Adv. Mater. **24**, 4055 (2012).

[159] L. Pisani, B. Montanari and N. M. Harrison, New Journal of Physics **10**, 033002 (2008).

[160] J-H. Chen, W. G. Cullen, E. D. Williams, and M. S. Fuhrer, Nature Physics **7**, 535 (2011).

[161] Y. H. He, L. Wang , X. L. Chen, Z. F. Wu, W. Li, Y. Cai, and N. Wang, Appl. Phys. Lett. **99**, 033109 (2011).

[162] G. X. Liu, D. Teweldebrhan, and A. A. Balandin, IEEE Trans. Nanotechnol. **10**, 865 (2011).

[163] D. Teweldebrhan and A. A. Balandin, Appl. Phys. Lett. **94**, 013101 (2009).

[164] D. Teweldebrhan and A. A. Balandin, Appl. Phys. Lett. **95**, 246102 (2009).

[165] S. Mathew, T. K. Chan, D. Zhan, K. Gopinadhan, A. R. Barman, M. B. H. Breese, S. Dhar, Z. X. Shen, T. Venkatesan, and J. T. L. Thong, J. Appl. Phys. **110**, 084309 (2011).

[166] S. Mathew, T. K. Chan, D. Zhan, K. Gopinadhan, A. R. Barman, M. B. H. Breese, S. Dhar, Z. X. Shen, T. Venkatesan, and J. T. L. Thong, Carbon **49**, 1720 (2011).

[167] J. W. Bai, X. Zhong, S. Jiang, Y. Huang, and X. F. Duan, Nat. Nanotechnol. **5**, 190 (2010).

[168] M. M. Ugeda, I. Brihuega, F. Guinea, and J. M. Gomez-Rodriguez, Phys. Rev. Lett. **104**, 096804 (2010).

[169] S. Stankovich, D. A. Dikin, G. H. B. Dommett, K. M. Kohlhaas, E. J. Zimney, E. A. Stach, R. D. Piner, S. T. Nguyen, and R. S. Ruoff, Nature (London) **442**, 282 (2006).

[170] S. Ryu, M. Y. Han, J. Maultzsch, T. F. Heinz, P. Kim, M. L. Steigerwald, and L. E. Brus, Nano Lett. **8**, 4597 (2008).

[171] D. C. Elias, R. R. Nair, T. M. G. Mohiuddin, S. V. Morozov, P. Blake, M. P. Halsall, A. C. Ferrari, D. W. Boukhvalov, M. I. Katsnelson, A. K. Geim, and K. S. Novoselov, Science **323**, 610 (2009).

[172] Z. Q. Luo, J. Z. Shang, S. H. Lim, D. H. Li, Q. H. Xiong, Z. X. Shen, J. Y. Lin, and T. Yu, Appl. Phys. Lett. **97**, 233111 (2010).

[173] Z. H. Ni, L. A. Ponomarenko, R. R. Nair, R. Yang, S. Anissimova, I. V. Grigorieva, F. Schedin, P. Blake, Z. X. Shen, E. H. Hill, K. S. Novoselov, and A. K. Geim, Nano Lett. **10**, 3868 (2010).

[174] R. R. Nair, W. C. Ren, R. Jalil, I. Riaz, V. G. Kravets, L. Britnell, P. Blake, F. Schedin, A. S. Mayorov, S. J. Yuan, M. I. Katsnelson, H. M. Cheng, W. Strupinski, L. G. Bulusheva, A. V. Okotrub, I. V. Grigorieva, A. N. Grigorenko, K. S. Novoselov, and A. K. Geim, Small **6**, 2877 (2010).

[175] K. J. Jeon, Z. Lee, E. Pollak, L. Moreschini, A. Bostwick, C. M. Park, R. Mendelsberg, V. Radmilovic, R. Kostecki, T. J. Richardson, and E. Rotenberg, ACS Nano **5**, 1042 (2011).

[176] H. J. Monkhorst and J. D. Pack, Phys. Rev. B **13**, 5188 (1976).

[177] S. Grimme, J. Comput. Chem. **25**, 1463 (2004).

[178] N. Marzari, D. Vanderbilt, A. De Vita, and M. C. Payne, Phys. Rev. Lett. **82**, 3296 (1999).

[179] J. Tersoff and D. R. Hamann, Phys. Rev. Lett. **50**, 1998 (1983).

[180] S. Shallcross, S. Sharma, and O. A. Pankratov, Phys. Rev. B **81**, 165105 (2010).

[181] J. D. Bernal, Proc. R. Soc. London Ser. A **106**, 749 (1924).

[182] L. A. Girifalco and R. A. Ladd, J. Chem. Phys. **25**, 693 (1956).

[183] L. X. Benedict, N. G. Chopra, M. L. Cohen, A. Zettl, S. G. Louie, and V. H. Crespi, Chem. Phys. Lett. **286**, 490 (1998).

[184] Z. Liu, J. Z. Liu, Y. Cheng, Z. Li, L. Wang, and Q. Zheng, Phys. Rev. B **85**, 205418 (2012).

[185] S. Latil, V. Meunier, and L. Henrard, Phys. Rev. B **76**, 201402(R) (2007).

[186] Y. Mao and J. Zhong, Nanotechnology **19**, 205708 (2008).

[187] G. M. Rutter, S. Jung, N. N. Klimov, D. B. Newell, N. B. Zhitenev, and J. A. Stroscio, Nature Physics **7**, 649 (2011).

[188] J. Ma, D. Alfè, A. Michaelides, and E. Wang, Phys. Rev. B **80**, 033407 (2009).

[189] L. G. Zhou, and S. Shi, Appl. Phys. Lett. **83**, 1222 (2007).

[190] V. N. Popov, L. Henrard, and P. Lambin, Carbon **47**, 2448 (2009).

[191] S. N. Shirodkar and U. V. Waghmare, Phys. Rev. B **86**, 165401 (2012).

[192] S. Pisana, M. Lazzeri, C. Casiraghi, K. S. Novoselov, A. K. Geim, A. C. Ferrari, and F. Mauri, Nat. Mater. **6**, 198 (2007).

[193] G. Giovannetti, P. A. Khomyakov, G. Brocks, V. M. Karpan, J. van den Brink, and P. J. Kelly, Phys. Rev. Lett. **101**, 026803 (2008).

[194] P. A. Khomyakov, G. Giovannetti, P. C. Rusu, G. Brocks, J. van den Brink, and P. J. Kelly, Phys. Rev. B **79**, 195425 (2009).

[195] C. Gong, G. Lee, B. Shan, E. M. Vogel, R. M. Wallace, and K. Chao, J. Appl. Phys. **108**, 123711 (2010).

[196] K. Pi, K. M. McCreary, W. Bao, W. Han, Y. F. Chiang, Y. Li, S.-W. Tsai, C. N. Lau, and R. K. Kawakami, Phys. Rev. B **80**, 075406 (2009).

[197] R. Singh and P. Kroll, J. Phys.: Condens. Matter **21**, 196002 (2009).

[198] S. Choi, B. Jeong, S. Kim and G. Kim, J. Phys. Cond. Matt. **20**, 235220 (2008).

[199] P. A. Thrower and R. M. Mayer, Phys. Stat. Sol. A **47** 11 (1978).

[200] S. Dubey, V. Singh, A. K. Bhat, P. Parikh, S. Grover, R. Sensarma, V. Tripathi, K. Sengupta, and M. M. Deshmukh, Nano Lett. **13**, 3990 (2013).

[201] K. Ulman, D. Bhaumik, B. Wood, and S. Narasimhan, Journal of Chem. Phys. **140**, 174708 (2014).

[202] S. Satyapal, J. Petrovic, C. Read, G. Thomas, and G. Ordaz, Catal. Today **120**, 246 (2007).

[203] L. Wang and R. T. Yang, Catal. Rev. **52**, 411 (2010).

[204] V. Tozzini and V. Pellegrini, Phys. Chem. Chem. Phys. **15**, 80 (2013).

[205] O. Hod, J. E. Peralta, and G. E. Scuseria, Phys. Rev. B **76**, 233401 (2007).

[206] K. A. Ritter and J. W. Lyding, Nat. Mater. **8**, 235 (2009).

[207] S. Sharma, N. Nair, and M. Strano, J. Phys. Chem. C **113**, 14771 (2009).

[208] S. Sharma, J. H. Baik, C. J. Perera, and M. Strano, Nano Lett. **10**, 398 (2010).

[209] D. Jiang, B. G. Sumpter, and S. Dai, J. Chem. Phys. **126**, 134701 (2007).

[210] R. Yuge, M. Zhang, M. Tomonari, T. Yoshitake, S. Iijima, and M. Yudasaka, ACS Nano **2**, 1865 (2008).

[211] S. N. Kim, Z. Kuang, J. M. Slocik, S. E. Jones, Y. Cui, B. L. Farmer, M. C. McAlpine, and R. R. Naik, J. Am. Chem. Soc. **133**, 14480 (2011).

[212] O. Hod, V. Barone, J. E. Peralta, and G. E. Scuseria, Nano Lett. **7**, 2295 (2007).

[213] E. Kan, Z. Li, J. Yang, andJ. G. Hou, J. Am. Chem. Soc. **130**, 4224 (2008).

[214] R. G. A. Veiga, R. H. Miwa, and G. P. Srivastava, J. Chem. Phys. **128**, 201101 (2008).

[215] F. Cervantes-Sodi, G. Csányi, S. Piscanec, and A. C. Ferrari, Phys. Rev. B **77**, 165427 (2008).

[216] K. T. Thomson and K. E. Gubbins, Langmuir **16**, 5761 (2000).

[217] P. J. F. Harris, Z. Liu, and K. Suenaga, J. Phys. Condens. Matt. **20**, 362201 (2008).

[218] J. K. Brennan, T.J. Bandosz, K.T. Thomson and K. E. Gubbins, Colloid. Surf. A **539**, 187 (2001).

[219] B. C. Wood, S. Y. Bhide, D. Dutta, V. S. Kandagal, A. D. Pathak, S. N. Punnathanam, K. G. Ayappa, and S. Narasimhan, J. Chem. Phys. **137**, 054702 (2012).

[220] S. Ehrlich, J. Moellmann, and S. Grimme, Acc. Chem. Res. **46**, 916 (2013).

[221] G. Vidali, G. Ihm, H. Y. Kim, and M. W. Cole, Surf. Sci. Rep. **12**, 133 (1991).

[222] K. Tada, S. Furuya, and K. Watanabe, Phys. Rev. B **63**, 155405 (2001).

[223] A. J. Du and S. C. Smith, Nanotechnology **16**, 2118 (2005).

[224] Y. Ihm, V. R. Cooper, L. Peng, and J. R. Morris, J. Phys. Condens. Matt. **24**, 424205 (2012).

[225] F. Costanzo, P. L. Silvestrelli, and F. Ancilotto, J. Chem. Theory Comp. **8**, 1288 (2012).

[226] R. Resta, Rev. Mod. Phys. **66**, 899 (1994).

[227] D. Dutta, M.S.Engg. Thesis, Indian Institute of Science, Bangalore (2009).

[228] E. J. G. Santos and E. Kaxiras, Nano Lett. **13**, 898 (2013)

[229] L. P. Hammett, J. Am. Chem. Soc. **59**, 96 (1937).

[230] For OE, the induced positive and negative charges are equal (constituting a dipole), whereas for IE, they are unequal due to partial charge transfer.

[231] S. K. Bhatia and A. L. Myers, Langmuir **22**, 1688 (2006).

[232] K. Ulman, M. Imam, S. Narasimhan, A. Odell, and A. Delin, Nano Hybrids Vol. **4**, 1-20 (2013).

[233] K. Ulman, S. Narasimhan, and A. Delin, J. Chem. Phys. **140**, 044716 (2014).

[234] Z. Yao, H. W. C. Postma, L. Balents, and C. Dekker, Nature **402**, 273 (1999).

[235] J. Chen, M. A. Reed, A. M. Rawlett, and J. M. Tour, Science **286**, 1550 (1999).

[236] X. Xiao, B. Xu, and N. J. Tao, Nano Lett. **4**, 267 (2004).

[237] T. Rakshit, G.-C. Liang, A. W. Ghosh, and S. Datta, Nano Lett. **4**, 1803 (2004).

[238] L. Venkataraman, J. E. Klare, I. W. Tam, C. Nuckolls, M. S. Hybertsen, and M. L. Steigerwald, Nano Lett. **6**, 458 (2006).

[239] E. J. Dell, B. Capozzi, K. H. DuBay, T. C. Berkelbach, J. R. Moreno, D. R. Reichman, L. Venkataraman, and L. M. Campos, J. Am. Chem. Soc. **135**, 11724 (2013).

[240] K. Tsukagoshi, B. W. Alphenaar, and H. Ago, Nature **401**, 572 (1999).

[241] J. R. Petta, S. K. Slater, and D. C. Ralph, Phys. Rev. Lett. **93**, 136601 (2004).

[242] S. Sen and S. Chakrabarti, J. Am. Chem. Soc. **132**, 15334 (2010).

[243] S. Schmaus, A. Bagrets, Y. Nahas, T. K. Yamada, A. Bork, M. Bowen, E. Beaurepaire, F. Evers, and W. Wulfhekel, Nature Nanotechnology **6**, 185 (2011).

[244] N. Koch, N. Ueno, and A. T. S. Wee, The Molecule-Metal Interface (Wiley, 2013).

[245] L. Wang, L. Liu, W. Chen, Y. Feng, and A. T. S. Wee, J. Am. Chem. Soc. **128**, 8003 (2006).

[246] W. Chen, H. Huang, S. Chen, Y. L. Huang, X. Y. Gao, and A. T. S. Wee, Chem. Mater. **20**, 7017 (2008).

[247] D. Dulić, S. J. van der Molen, T. Kudernac, H. T. Jonkman, J. J. D. de Jong, T. N. Bowden, J. van Esch, B. L. Feringa, and B. J. van Wees, Phys. Rev. Lett. **91**, 207402 (2003).

[248] M. Zhuang and M. Ernzerhof, Phys. Rev. B **72**, 073104 (2005).

[249] M. Kondo, T. Tada, and K. A. Yoshizawa, Chem. Phys. Lett. **412**, 55 (2005).

[250] N. Katsonis, T. Kudernac, M. Walko, S. J. van der Molen, B. van Wees, and B. Feringa, Adv. Mater. **18**, 1397 (2006).

[251] K. Matsuda, H. Yamaguchi, T. Sakano, M. Ikeda, N. Tanifuji, and M. Irie, J. Phys. Chem. C **18**, 17005 (2008).

[252] A. J. Kronemeijer, H. B. Akkerman, T. Kudernac, B. J. van Wees, B. L. Feringa, P. Blom, and B. de Boer, Adv. Mater. **20**, 1467 (2008).

[253] S. J. van der Molen, J. Liao, T. Kudernac, J. S. Agustsson, L. Bernard, M. Calame, B. J. van Wees, B. Feringa, and C. Schöneberger, Nano. Lett. **9**, 76 (2009).

[254] Y. Tsuji, A. Staykov, and K. Yoshizawa, Thin Solid Films **518**, 444 (2009).

[255] E. S. Tam, J. J. Parks, W. W. Shum, Y. W. Zhong, M. B. Santiago-Berr´ios, X. Zheng, W. Yang, G. K. L. Chan, H. D. Abruna, and D. Ralph, ACS Nano **5**, 5115 (2011).

[256] J. Ulrich, D. Esrail, W. Pontius, L. Venkataraman, D. Millar, and L. H. Doerrer, J. Phys. Chem. B **110**, 2462 (2006).

[257] J. He, F. Chen, P. A. Liddell, J. Amdreasson, S. D. Straight, D. Gust, T. A. Moore, A. L. Moore, J. Li, O. F. Sankey, and S. M. Linday, Nanotechnology **16**, 695 (2005).

[258] J. Li, G. Speyer, and O. F. Sankey, Phys. Rev. Lett. **93**, 248302 (2004).

[259] A. Odell, A. Delin, B. Johansson, I. Rungger, and S. Sanvito, ACS Nano **4**, 2635 (2010).

[260] A. Odell, A. Delin, B. Johansson, K. Ulman, S. Narasimhan, I. Rungger, and S. Sanvito, Phys. Rev. B **84**, 165402 (2011).

[261] N. Troullier and J. L. Martins, Phys. Rev. B **43**, 1993 (1991).

[262] J. Peralta-Ramos, A. M. Llois, I. Rungger, and S. Sanvito, Phys. Rev. B. **78**, 024430 (2008).

[263] S. Datta, *Quantum Transport: Atom to Transistor*, Cambridge University Press, Cambridge, England (2005).

[264] S. Kobatake, S. Takami, H. Muto, T. Ishikawa, and M. Irie, Nature Lett. **446**, 778 (2007).

[265] H. Dalgleish and G. Kirczenow, Phys. Rev. B. **72**, 184407 (2005).